

DISS. ETH NO. 16414

**HIGH OUTPUT VOLTAGE
SERIES-PARALLEL RESONANT DC-DC
CONVERTER FOR MEDICAL X-RAY IMAGING
APPLICATIONS**

A dissertation submitted to the

SWISS FEDERAL INSTITUTE OF TECHNOLOGY ZURICH

for the degree of
DOCTOR OF SCIENCES

presented by

FABIANA DA SILVEIRA CAVALCANTE
M.Sc. Universidade Federal de Santa Catarina

born 07.09.1976

citizen of Brazil

accepted on the recommendation of

Prof. Dr. J.W. Kolar, examiner
Prof. Dr. K. Fröhlich, co-examiner

2006

Fabiana da Silveira Cavalcante
©2006

For Dominik with love

For my Mom and my Dad

*Para Papy e Mamy,
pelo incentivo, pelo amor
e por sempre acreditarem em mim!*

In Loving Memory of Aurino Mangabinha

ACKNOWLEDGEMENTS

This work has been developed during my research activities at the Power Electronic Systems Laboratory of ETH Zurich from February 2002 to December 2005. I would like to thank many people who made this work possible.

First of all, I would like to thank Professor Dr. Johann W. Kolar for giving me the opportunity to do my Ph.D. at ETH Zurich, for the guidance throughout the course of my research, for our interesting discussions and for his valuable suggestions that helped me a lot improving the quality of this work.

Many thanks are also due to Professor Dr. Klaus Fröhlich for consenting to be the co-examiner and for his critical comments which improved the clarity of the thesis.

On a personal note, I would like to thank my boyfriend Dominik for his love, for being with me also in the darkest days and for his understanding when I had to work instead of spending time with him.

I would not be here without the love, encouragement and support of my parents, Humberto and Ana. Thanks also to my brother Nã and to my little sister Linha for making me laugh, for our friendship and for the wonderful time that we always spend together in Salvador.

I would like to acknowledge Peter Tichy, Walter Beyerlein and Karlheinz Köhler from Siemens Medical AG and Thomas Komma and Professor Eckhard Wolfgang from Siemens Corporate Technology for their cooperation with ETH. This made the realization of this work possible.

I am indebted to Peter Seitz and Hansueli Altorfer for their valuable help with the prototype and for always taking time to answer my questions about hardware and mechanical design. Thanks also to Peter Albrecht for

solving all administrative affairs for me and to Markus Berger who solved all my software problems. I also would like to thank our dear secretaries Roswitha and Gabriela for the good humor, for the talks with them and for being always so helpful.

Many thanks go to my office-mate and good friend Luca for our good time, for our talks and laughs and for retaining his good humor even when I was in a bad mood.

A big acknowledge goes to Gerold for programming the DSP and for helping me with the experimental setup. Furthermore, special thanks go to Marcelo, Simon and Florian for helping me with the prototype. Thanks to all colleagues of the Power Electronic Systems Laboratory for the good moments.

I would like to thank the Brazilian friends in Switzerland that always bring me a piece of home. Thanks also to my special friend Annette.

My gratitude goes to my friend Stephanie. Even being so far away she is always supporting me. Our several endless telephone calls always make me feel better. I am happy that our friendship is stronger than time and distance.

I also would like to acknowledge my former advisor in Brazil Professor Dr. Ivo Barbi for encouraging me and for always believing in my skills. Special thanks also to Professor Dr. Eduardo Deschamps who is the person responsible for introducing me to the world of power electronics.

Finally, I would like to acknowledge the financial support provided by ETH Zurich and Siemens Medical AG.

Fabiana da Silveira Cavalcante

ABSTRACT

A particular application of a high-voltage DC-DC converter is to drive an x-ray tube used in medical x-ray imaging systems like Mammographs and Computed Tomographs (CT). For such application, low ripple voltage waveforms with fast rising time under exact no-overshoot response are required. The x-ray power generator must have the particular capability to adjust its DC output voltages across the x-ray tube in order to assure the best quality image for each specified pattern of body part. Higher output voltages are required to diagnose more dense body parts as all types of bones, and relatively lower high voltages may be adequately used for diagnosing soft tissues of the organs.

The adjustment of the voltage can be implemented by controlling the DC output high-voltage across the x-ray tube over widely specified ranges by using a DC-DC converter. The operation of high output voltage DC-DC converters is considerably affected by transformer non-idealities being caused by the large transformer turns ratio and/or large number of secondary turns. In particular, the leakage inductance and the secondary winding capacitance do take considerable influence on the converter behavior and do potentially reduce efficiency and reliability [EJW88]. Therefore, converter topologies suitable for x-ray imaging applications should integrate the parasitics of the transformer into the circuit operation. Accordingly, resonant converters are frequently employed for the realization of high output voltage DC-DC converter systems. However, the design of resonant converters is involved due to the large number of operating states occurring within a pulse period.

A new high-voltage DC-DC converter for x-ray medical application is proposed in this thesis. The state of the art technology used for x-ray

generators works in the frequency range from 30 kHz to 100 kHz. Due to these low switching frequencies, the magnetic components of these generators are large and heavy. The converter that is proposed in this thesis works at switching frequencies up to 500 kHz in order to reduce volume and weight. However, high frequency operation can generate additional losses in the converter. For this reason, it is important to find a topology and a modulation strategy that allows the converter to operate under soft-switching condition in the entire operating range, in order to reduce the converter losses.

This thesis presents three main contributions for the design of series-parallel resonant converters for high-voltage generation. The first contribution is a straightforward procedure for designing a full-bridge high output voltage series-parallel resonant DC-DC converter for medical x-ray imaging application. The approach is based on an extension of the first harmonic analysis proposed in [IKBY97]. There, the converter output power is controlled by frequency variation at fixed duty-cycle. That means, one has only one control variable. In contrast, for the procedure proposed in this thesis, the output power is controlled by duty-cycle variation while the operating frequency is automatically adjusted for ensuring the commutation of one bridge leg at zero current. As the second bridge leg due to operation above the resonance frequency commutates at zero voltage, soft-switching should be preserved in the entire operating range. Furthermore, in order to guarantee low losses in stand-by mode a control scheme minimizing the converter conduction and switching losses for no load operation is proposed. Also, the transient behavior of the converter is analyzed and a control concept is used, which allows to maintain the converter operation above resonance for all kinds of load changes.

The second contribution of this thesis is the small-signal model for the series-parallel resonant DC-DC converter with capacitive output filter, which models the strong nonlinear behavior of the system as a standard control system. A simple model is still missing in the literature and for this reason many controller designs are performed by trial and error [GSGB04]. The trial and error procedure is not convenient because the small-signal model varies significantly with load changes and the load is normally an

unknown parameter. Therefore, setting of the controller parameters can take a long time until a robust set of parameters are found. The main tool used in this work for deriving the small-signal model is the generalized averaging method proposed in [SNL⁺91]. This method overcomes the limitations of the traditional state-space averaging method because it does not require that the waveforms have small ripple magnitude. Thus, it is able to describe arbitrary types of waveforms. The method is based on the fact that the arbitrary waveform $x(\cdot)$ can be represented on the interval $\tau \in (t-T, t]$ by a Fourier series. The analysis calculates the time-evolution of the Fourier series coefficients as the window of length T slides over the actual waveform [SNL⁺91]. The proposed model simplifies the controller design for series-parallel resonant converters by removing the need of very complex mathematical analysis and saves the time required for measurements in the trial and error design method.

The controller design is the third main contribution of this thesis. This is a very relevant aspect of this work because the controller should meet very restrictive requirements of output voltage rising time and overshoot, which are mandatory for medical x-ray imaging equipments. This work proposes two different adaptive controllers for the series-parallel resonant DC-DC converter with capacitive output filter. The first controller is a gain scheduled controller. Gain scheduling is a feedforward adaptation and it can be regarded as a mapping from process to controller parameters. The main advantage of gain scheduling is the fast dynamic response of the controller. The second controller proposed in this work is a passivity based controller (PBC). This control approach shapes the energy of the system according to a chosen reference trajectory [CdL⁺03]. Passivity based control is a very robust method but the dynamic response is not as fast as the response of the gain scheduled controller because it depends on the speed of the estimate of the load. For medical x-ray imaging systems, fast dynamic response is a very important aspect. Thus, the gain scheduled controller is chosen for the practical implementation.

After concluding the design stage, a prototype is constructed in order to validate the theoretical studies. The prototype is tested at steady-state and under transient conditions and experimental results are presented

and critically analyzed. There is a very good agreement between the results obtained with the theoretical analysis and the experimental results. This shows the validity of the design methods developed in this thesis, which in the meantime have been used as basis for the development of a new generation of Mammography systems.

ZUSAMMENFASSUNG

Eine besondere Anwendung von Hochspannungs- DC-DC Konverters ist die Spannungsversorgung von Röntgenröhren, welche in medizinischen Röntgenanwendungen wie Mammografie oder Computertomografie (CT) verwendet werden. Für diese Einsatzbereiche werden geringe Welligkeit der Röhrenspannung mit schnellen Anstiegszeiten ohne Überschwingen in der Sprungantwort benötigt. Der Röntgengenerator muss in der Lage sein, die erzeugte Gleichspannung für die Röntgenröhre so anzupassen, dass eine optimale Bildqualität für jeden gewünschten menschlichen Körperteil gewährleistet wird. Höhere Ausgangsspannungen werden für die Diagnose von dichteren Körperteilen wie z.B. alle möglichen Arten von Knochen benötigt. Auf der anderen Seite sind tiefere Hochspannungswerte geeigneter für weiche Organgewebe.

Die Spannungsanpassung über den spezifizierten Bereich kann mit Hilfe eines DC-DC Konverters mit Hochspannungsausgang realisiert werden. Der Betrieb von DC-DC Konvertern mit hoher Ausgangsspannung ist sehr abhängig von den Nichtidealitäten des Transformators, welche durch das grosse Windungszahlverhältnis und/oder die grosse Sekundärwindungszahl verursacht werden. Besonders die Streuinduktivität und die Sekundärwicklungskapazität haben einen grossen Einfluss auf das Verhalten des Konverters und können die Effizienz und Zuverlässigkeit beträchtlich reduzieren. Deshalb sind bei der Wahl der Konvertertopologie für medizinische Röntgendiagnostik die Nichtidealitäten des Transformators in den Schaltungsentwurf einzubeziehen. Entsprechend werden häufig Resonanzkonverter für die Realisierung von DC-DC Konvertersystemen mit hoher Ausgangsspannung verwendet. Das Design von Resonanzkonvertern ist wegen der grossen Anzahl von

Betriebszuständen, welche innerhalb einer Pulsperiode auftreten, relativ komplex.

In dieser Arbeit wird ein neuer Hochspannungs-DC-DC-Konverter für medizinische Röntgendiagnostik vorgestellt. Die aktuelle Technologie, welche heute in Röntgengeneratoren verwendet wird, arbeitet in einem Frequenzbereich zwischen 30kHz und 100kHz. Aufgrund dieser tiefen Schaltfrequenzen weisen die magnetischen Komponenten der Generatoren relativ hohes Volumen und Gewicht auf. Der neue, in dieser Arbeit behandelte Konverter arbeitet daher mit Schaltfrequenzen bis zu 500 kHz, so dass das Volumen und das Gewicht erheblich reduziert werden können. Der Einsatz solch hoher Frequenzen würde bei konventionellem Betrieb hohe Verluste des Konverters verursachen. Aus diesem Grund ist es wichtig eine Schaltungstopologie und eine zugehörige Betriebsweise zu finden, welche im ganzen Arbeitsbereich ein *Soft-Switching* der Leistungshalbleiter ermöglicht und so die Konverterschaltverluste reduziert.

Diese Arbeit präsentiert drei Hauptbeiträge für das Design eines Serien-Parallel Resonanzkonverters zur Hochspannungsversorgung von Röntgenröhren. Der erste Beitrag beschreibt ein direktes Verfahren für die Festlegung der Bauelemente des Leistungskreises gestützt auf eine Erweiterung der ersten harmonischen Analyse nach Ivensky et al. [IKBY97]. In der genannten Arbeit wurde die Ausgangsspannung des Konverters durch eine Frequenzvariation bei konstantem Tastverhältnis geregelt. Das bedeutet, dass nur eine Kontrollvariable zur Verfügung steht.

In der vorliegenden Arbeit wird ein Verfahren präsentiert, bei dem die Ausgangsleistung durch die Veränderung des Tastverhältnisses geregelt wird, wobei die Betriebsfrequenz automatisch angepasst wird um sicher zu stellen, dass immer einer der beiden Brückenarme des Konverters im Nulldurchgang des Resonanzstromes schaltet. Da der zweite Brückenarm wegen überresonanten Betriebes unter Nullspannung schaltet, ist *Soft-Switching* über den ganzen Arbeitsbereich gewährleistet. Um weniger Verluste im *Stand-by Mode* zu garantieren, wird zusätzlich eine Betriebsweise angegeben, welche die Verluste des Konverters im Leerlauf reduziert. Weiters wird das Verhalten des Konverters bei spontanen

Laständerungen analysiert und ein Steuerkonzept vorgeschlagen, welches den überresonanten Betrieb für alle möglichen Laständerungen sicherstellt.

Der zweite Beitrag dieser Arbeit ist ein regelungstechnisches Kleinsignalmodell für den Serien-Parallel Resonanzkonverter mit kapazitivem Ausgangsfilter, welches ein stark nichtlineares Regelsystem darstellt. Da ein solches Modell bisher in der Literatur fehlte, wurden die meisten Regelungsverfahren durch *Trial and Error* entworfen [GSGB04]. Diese Vorgehensweise ist aber schwierig, da das dynamische Verhalten stark von der Last abhängt welche normalerweise ein unbekannter Parameter ist. Aus diesem Grund kann sich das Einstellen eines Satzes robuster Reglerparameter relativ zeitaufwendig gestalten. Das in dieser Arbeit vorgeschlagene Modell vereinfacht den Reglerentwurf für den Serien-Parallel Resonanzkonverter, indem es die Notwendigkeit einer sehr komplexen mathematischen Analyse beseitigt und so eine durchgängige regelungstechnische Betrachtung ermöglicht.

Der dritte wesentliche Beitrag dieser Arbeit beschreibt ein neues Regelungsverfahren. Die regelungstechnische Beherrschung des Systems ist ein sehr wichtiger Aspekt, da der Regler restriktive Anforderungen der medizinischen Diagnostik bezüglich Anstiegszeit und Überschwingen der Ausgangsspannung einhalten muss. Um die theoretischen Studien zu validieren wird ein Prototyp aufgebaut, und anschliessend im stationären Betrieb und unter transienten Bedingungen getestet. Danach werden die experimentellen Resultate präsentiert und kritisch analysiert. Es zeigt sich eine sehr gute Übereinstimmung mit den Ergebnissen der theoretischen Analyse. Dies bestätigt die Gültigkeit der Designmethoden, die in dieser Arbeit entwickelt und inzwischen als Grundlage für die Entwicklung einer neuen Generation von Mammographen herangezogen wurden.

CONTENTS

ACKNOWLEDGEMENTS	i
ABSTRACT	iii
ZUSAMMENFASSUNG	vii
NOTATION	1
INTRODUCTION	7
CHAPTER 1	11
1. INTRODUCTION	11
1.1. PRINCIPLES OF X-RAY IMAGING DIAGNOSIS	11
1.1.1. Fundamentals of X-ray	11
1.1.2. X-ray Tubes	14
1.1.3. Mammography	20
1.1.4. X-ray Generator	22
1.2. HIGH-VOLTAGE GENERATION	24
1.2.1. Introduction	24
1.2.2. Main Resonant Converter Configurations	25
1.2.3. State of the Art X-Ray Generator Topologies	34
1.3. THESIS MOTIVATION AND OBJECTIVES	41
1.3.1. Selection of the Converter Topology	41
1.3.2. Main Objectives	43
1.4. SUMMARY	44
CHAPTER 2	47

2. STEADY-STATE ANALYSIS OF THE SERIES-PARALLEL RESONANT CONVERTER.....	47
2.1. INTRODUCTION.....	47
2.2. CIRCUIT DESCRIPTION	48
2.3. THEORETICAL ANALYSIS.....	50
2.3.1. Commutation Zones for Variable Frequency Phase-Shift Control ..	51
2.3.2. Converter Conduction States	55
2.3.3. Design Procedure Based on First Harmonic Analysis	60
2.4. SIMULATION RESULTS	73
2.5. OPEN LOOP CONTROL	74
2.5.1. Current Zero Crossing Synchronization	74
2.5.2. Finite State Machine	75
2.5.3. Operation under No Load Condition	80
2.5.4. Operation above Resonance	82
2.6. SUMMARY	83
CHAPTER 3	85
3. LARGE- AND SMALL-SIGNAL ANALYSIS OF THE SERIES-PARALLEL RESONANT CONVERTER	85
3.1. INTRODUCTION.....	85
3.2. THEORETICAL ANALYSIS.....	86
3.2.1. State of the Art Small-Signal Modeling Techniques	86
3.2.2. Generalized Averaging Method	89
3.3. SMALL-SIGNAL MODEL.....	102
3.4. SIMULATION RESULTS	108
3.5. EXPERIMENTAL RESULTS.....	112
3.6. SUMMARY	114
CHAPTER 4	117
4. ADAPTIVE CONTROLLERS FOR THE SERIES-PARALLEL RESONANT CONVERTER.....	117
4.1. INTRODUCTION.....	117
4.2. ADAPTIVE CONTROL	117
4.2.1. Approaches to Adaptive Control	118

4.2.2.	Direct and Indirect Adaptive Control.....	119
4.2.3.	Selection of the Controller	120
4.3.	GAIN SCHEDULED CONTROLLER.....	120
4.3.1.	Small-Signal Model of the System.....	121
4.3.2.	Gain Scheduling	122
4.3.3.	Gain Scheduled Controller Design.....	123
4.3.4.	Simulation Results.....	128
4.4.	PASSIVITY BASED CONTROLLER	131
4.4.1.	Introduction to Passivity Based Control.....	131
4.4.2.	Passivity Definition	131
4.4.3.	Passivity Based Control.....	132
4.4.4.	Nonlinear Model of the System.....	132
4.4.5.	Passivity Based Controller Design.....	133
4.4.6.	Simulation Results.....	149
4.5.	SUMMARY	155
CHAPTER 5	157
5. EXPERIMENTAL SETUP	157
5.1. INTRODUCTION	157
5.2. SPECIFICATIONS OF THE PROTOTYPE	157
5.3. DESCRIPTION OF THE PRINTED CIRCUIT BOARDS	160
5.3.1.	Power and Control Boards	160
5.3.2.	DSP Board.....	161
5.4. EXPERIMENTAL RESULTS	163
5.4.1.	Results for $P_o = 230W$	163
5.4.2.	Results for $P_o = 1.15kW$	166
5.4.3.	Results for $P_o = 2.3kW$	169
5.4.4.	Results for $P_o = 4.6kW$ (Full Load)	171
5.5. SUMMARY	175
CONCLUSIONS AND OUTLOOK.....	177
REFERENCES.....	181
CURRICULUM VITAE.....	193

NOTATION

SYMBOLS

<i>Symbol</i>	<i>Explanation</i>	<i>Unity</i>
<i>ALPHA</i>	Input signal of the state machine that determines the maximum permissible duty cycle	
α	Ratio of the parallel and series capacitor	
β	Phase displacement of the fundamentals of the voltage across the parallel capacitor and the input current of the output rectifier	rad
$C_{aux}(s)$	Auxiliary controller transfer function	
C_e	Equivalent capacitor of the RC model	F
$C_{h1} - C_{h4}$	Output capacitors	F
$C_{h1'}, C_{h2}'$	Output capacitors referred to the transformer primary side	F
c_k	k th term of the complex Fourier series	
$C_{o1'}, C_{o2'}, C_{o4}'$	Output capacitors referred to the transformer primary side	F
C_p	Parallel resonant capacitor	F
C_s	Series resonant capacitor	F
D	Duty cycle	
$D_1 - D_4$	Intrinsic diodes of the power MOSFETs	
$D_{o1} - D_{o4}$	Output diodes	
e	output voltage error	V
<i>enable</i>	Input of the state machine that enables or disables all gate signals	

<i>Symbol</i>	<i>Explanation</i>	<i>Unity</i>
f_o	Series resonant frequency	Hz
f_s	Switching frequency	Hz
$f_{s,N}$	Normalized switching frequency	
G	$1/R_o$	$1/\Omega$
\hat{G}	Estimate of $1/R_o$	$1/\Omega$
G_{max}	Upper bound of G	$1/\Omega$
$G(s)$	Transfer function	
H	Lyapunov function candidate	
i_{Ls}	Resonant current	A
I_{LsD}	Dynamical magnitude of the resonant current	A
I_{Lsref}	Reference value of the resonant current	A
ILZ	Input of the state machine to detect the zero crossing of the resonant current	
I_o	Output current	A
I_o'	Output current referred to the transformer primary side	A
I_{Qoff}	Turn-off current of the ZVS bridge leg power transistors	A
$I_{QRMSZVS}$	RMS current stress on the ZVS power MOSFETs	A
i_T	Input current of the output rectifier	A
K	Proportional gain	
K_1	Damping injection gain	
K_2	Gain that fixes the adaptation speed of the estimation	
k_{21}	AC voltage transfer ratio	
K_{p1}, K_{p2}	Gains of the sawtooth generator	
k_v	relation between V_o' and the amplitude of the first harmonic of the voltage across the parallel capacitor	
L_s	Resonant inductor	H
n	Transformer turns ratio	
$NENA$	Input signal of the state machine generated by comparing PHI , $ALPHA$ and RP	

<i>Symbol</i>	<i>Explanation</i>	<i>Unity</i>
ϕ	Phase displacement of the first harmonic of v_{AB} and of the first harmonic of i_{Ls}	rad
$\varphi(I)$	Input phase angle	rad
PHI	Input signal of the state machine that determines the duty cycle of the ZVS switches	
P_o	Output power	W
Q	Normalized load	
q_{0-n}	States of the FSM	
R_{AC}	Equivalent AC resistance	Ω
R_{DSon}	Drain-source on-state resistance	Ω
R_e	Equivalent resistance of the RC model	Ω
R_o	Load resistance	Ω
R_o'	Load resistance referred to the transformer primary side	Ω
RP	Reset pulse	
R_{thj-c}	Thermal resistance junction to case	$^{\circ}\text{C}/\text{W}$
$S_1 - S_4$	Power switches	
s_T	Constant amplitude sawtooth-shaped carrier signal	V
s_{T0-n}	States of the state machine	
T	Period	s
T_i	Normalized integrator time constant	
T_{ir}	Integrator time constant	s
T_I	High-voltage transformer	
τ	Time interval	
$u(t)$	Control input of the system	
v_{AB}	Voltage applied to the resonant tank	V
v_{AC}	Equivalent AC voltage	V
v_c	Controller output voltage	V
v_{Cp}	Voltage across the parallel capacitor	V
v_{Cs}	Voltage across the series capacitor	V
V_{in}	Input voltage	V
V_o	Output voltage	V

<i>Symbol</i>	<i>Explanation</i>	<i>Unity</i>
V_o'	Output voltage referred to the transformer primary side	V
$V_o'D$	Dynamical reference value of the output voltage	V
$V_o'ref$	Reference voltage	V
$V(x)$	Energy-like function	
θ	Output rectifier conduction angle	
$\omega C_p R_e$	Dimensionless auxiliary parameter	
ω_s	Angular frequency	rad/s
$x(t)$	State variable	
$\langle x \rangle_k(t)$	Complex Fourier coefficients	
Z	Characteristic impedance	
ZCS_HI	Gate signals of the upper ZCS switch	
ZCS_LO	Gate signals of the lower ZCS switch	
ZVS_HI	Gate signals of the upper ZVS switch	
ZVS_LO	Gate signals of the lower ZVS switch	

SYMBOLS OF UNITIES

<i>Symbol</i>	<i>Explanation</i>
C	Coulomb
Ω	Ohm
A	Ampère
F	Farad
H	Henry
Hz	Hertz
K	Kelvin
rad	Radians
s	Second
V	Volt
W	Watt

ADDITIONAL NOTATIONS

<i>Symbol</i>	<i>Explanation</i>
$x(\cdot)$	Arbitrary waveform
$\langle x \rangle_k$	k th time-varying harmonics of the waveform x
\hat{x}	Peak value of x
x_{SS}	Steady state value of x
Δx	Variation of x
\vec{x}	Vector x
\dot{x}	Time derivative of x
$Proj(x)$	Projection of x
$Re(x)$	Real part of x

LIST OF ACRONYMS

<i>Acronym</i>	<i>Explanation</i>
CPLD	Complex Programmable Logic Device
DC-DC	Direct current- direct current
DSP	Digital Signal Processor
EM	Electromagnetic radiation
FSM	Finite state machine
IGBT	Insulated-gate bipolar transistor
KE	Kinetic energy
LTI	Linear time-invariant
MIT	Massachusetts Institute of Technology
MOSFET	Metal-oxide-semiconductor field-effect-transistor
MRAC	Model reference adaptive control
PDM	Pulse density modulation
PFM	Pulse frequency modulation
PI	proportional-integral controller
PLS	piecewise linear systems
PWM	Pulse width modulation
RMS	Root mean square
RPM	Rotations per minute
STC	Self tuning control

VHDL	VHSIC Hardware Description Language
VHSIC	Very High-Speed Integrated Circuits
ZCS	Zero-current switching
ZVS	Zero-voltage switching

INTRODUCTION

Nowadays, x-ray imaging is a main component of the medical environment. It demonstrates its efficacy for different applications: oncology, cardiovascular analysis, neurology, mammography, and others. Its use for inspecting abnormal diseases of human body as well as in interventional surgery leads to a huge increase of patient recovery chances and to reducing constraints of surgical intervention.

When x-ray tube is in operation, so-called x-ray beams, a type of radiation, are released. Using these beams, the technician can create images of whatever is being examined. This radiation penetrates objects and human bodies, passes through them, and is weakened in the process. In simple terms, this weakening is equivalent to a reduction in the number of individual radioactive particles. A statement concerning the amount of radiation, which is measured at a site, produces the concept of *dose*. Because not all the radiation particles generated during an x-ray are used to produce the resulting images, and because radiation can cause damage to the human body, it is important to try to achieve the greatest possible effect that is the best possible image with the smallest possible dose of radiation [Wip05].

For supplying x-rays tubes, an x-ray generator is connected to its anode-cathode electrodes. In general an x-ray generator is required to properly control the x-ray penetration capability and beam quality as well as the contrast, brightness and resolution of x-ray images. The quality of photographic x-ray image is primarily determined by the x-ray radiated energy, which is proportional to the voltage of the x-ray tube. Higher output voltages are required to diagnose more dense body parts of all types of bones, and relatively lower high voltages may be adequately used for

diagnosing soft tissues of the organs [WH99]. The x-ray generator must have the particular capability to adjust its DC output voltage across the x-ray tube in order to assure the best quality image for each specified pattern of body part.

In addition the contrast of x-ray image is sensitive to the tube voltage ripple and rising time. The total x-ray dose, which determines the photographic density of x-ray image, varies proportionally to the exposure time multiplied by the actual tube current [WH99].

The adjustment of the voltage levels at the operating console has an important effect on the dose, because if a high voltage setting is chosen, the radiation is *harder*, that is, richer in energy and more able to pass through the body. On the other hand, added filters attenuate low energy x-rays in the spectrum, which do not contribute for image production. In both cases, radiation dose is reduced: in case of the high-voltage because tube current is reduced and in case of the filtration because the low energy x-rays are absorbed by the filters instead of the patient. Therefore, high voltage and strong filtration are similar in their dose reduction effects. The difference is that image contrast is not affected by filtration and decreases with high voltage [Wip05], [BSL⁺02].

In order to obtain a good image quality, this application requires low output voltage ripple, fast dynamic response and very restricted voltage overshoot. In addition, the aspects of volume and weight are important to x-ray generators, especially in the applications of x-ray CT scanners, C-arm x-ray systems and portable x-ray machines.

This thesis has as objective the design of a new 5kW high-voltage DC-DC converter for application in mammography devices and it is organized as shown in the following.

Chapter 1 shows fundamental concepts about x-ray imaging diagnosis. It shows the principle of x-ray generation, the main components of a typical x-ray tube, the special requirements for mammography devices and the structure of an x-ray generator. Additionally, it gives a brief overview about resonant converters. They can operate at higher frequencies than comparable PWM converters and integrate the transformer non-idealities. Thus, they are suitable for the realization of x-ray generators.

The selected configuration is the series-parallel resonant converter operating above resonance. This converter takes advantage of the best characteristics of the series and the parallel resonant converter and the operation above resonance improves even more the performance of the system. Additionally, state of the art topologies for this application are presented and the thesis motivation is explained.

Chapter 2 presents a straightforward procedure for designing a full-bridge high output voltage series-parallel resonant DC-DC converter for x-ray imaging diagnosis. The approach is based on an extension of the first harmonic analysis. The output power is controlled by duty-cycle variation while the operating frequency is automatically adjusted for ensuring the commutation of one bridge leg at zero current. The second bridge leg commutates at zero voltage, thus, soft-switching is preserved in the entire operating range. Furthermore, in order to guarantee low losses in stand-by mode a control scheme minimizing the converter conduction and switching losses for no load operation is proposed. Also, the transient behavior for step-like changes from rated load to no load operation is analyzed and a control concept, which guarantees operation above resonance for all kinds of load changes, is described.

Chapter 3 shows a large signal nonlinear model of the series-parallel resonant DC-DC converter that can describe the transient behavior of the converter and is useful in the development of nonlinear controllers. Additionally, this chapter develops a new small-signal model for the series-parallel resonant DC-DC converter with capacitive output filter. The small-signal model is very useful in the control design because it permits that linear control techniques are applied to a nonlinear plant.

Chapter 4 presents two different adaptive control techniques that can be applied in the regulation of the output voltage of the series-parallel resonant converter. Passivity based control and gain scheduling control are two different approaches shown in this chapter. Passivity based control is an energy shaping approach where the closed-loop total energy of the system is modified, and a damping injection stage is added in order to achieve asymptotic stability. Gain scheduling is a feedforward approach and its main principle is to change the parameters of the controller by

monitoring the operating conditions of the plant. The gain scheduled controller shows a better performance than the passivity based control, thus gain scheduling is preferred in the practical implementation.

Chapter 5 shows experimental results of a 5kW constructed prototype. The results confirm that the models and control designs developed along this thesis are valid and the series-parallel resonant converter is a good concept to realize an x-ray generator.

Finally, the design procedures and results of this thesis are critically analyzed and suggestions for the improvement of design procedures and for the extension of the obtained results to other applications are presented.

CHAPTER 1

1. INTRODUCTION

1.1. PRINCIPLES OF X-RAY IMAGING DIAGNOSIS

X-Ray was discovered by the German physicist Wilhelm Conrad Roentgen, in 1895. He was looking for the “invisible high-frequency rays” that Hermann Ludwig Ferdinand von Helmholtz had predicted from the Maxwell theory of electromagnetic radiation. Roentgen named the new kind of ray “X-Strahlen” - X-rays (“X” for unknown). Since then, x-ray has been the most important and most used tool in clinical medicine.

1.1.1. Fundamentals of X-ray

X-ray is a form of electromagnetic radiation (EM) like microwaves, infrared, visible and ultraviolet light. It is characterized by its amplitude and wavelength. Diagnostic x-rays typically have a wavelength from 10nm to 0.01nm as shown in **Fig. 1.1**. They are bounded by ultraviolet light at long wavelengths and gamma rays at short wavelengths. X-rays in the range from 5 to 10 nm are termed soft x-rays because they have lower energies and are easily absorbed.

X-rays are a type of ionizing radiation. Ionization is the ejection of one or more electrons from an atom or molecule to produce a fragment with a net positive charge (positive ion). The classification of radiation as ionizing is essentially a statement that it has enough quantum energy to eject an electron. This is an essential distinction, since ionizing radiation can produce a number of physiological effects, which non-ionizing radiation cannot directly produce at any intensity. X-rays can pass through materials but are absorbed differently depending on the atomic number and thickness of the material. This is the basis of the x-ray image.

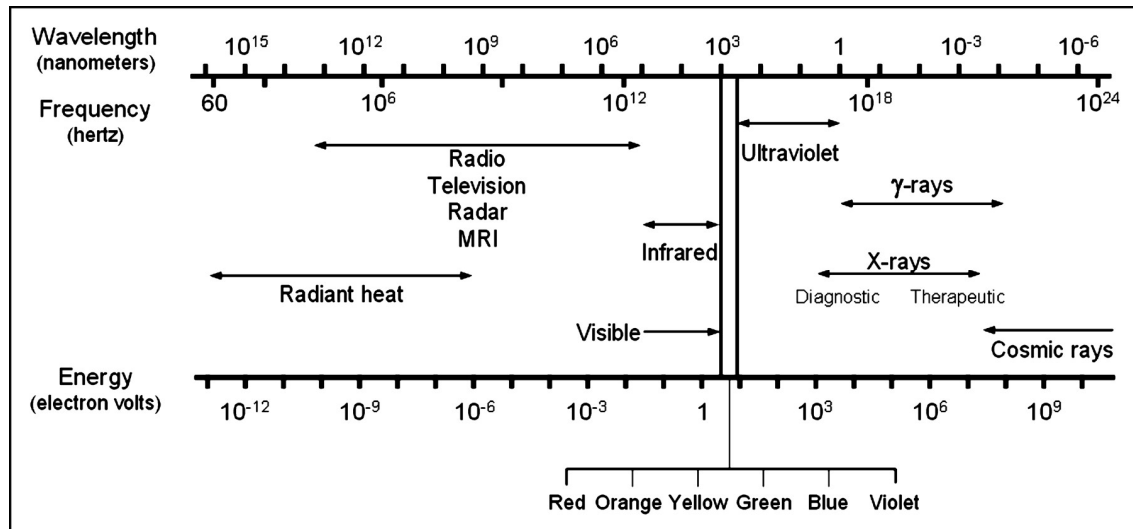


Fig. 1.1: Location of x-ray radiation in the electromagnetic spectrum¹.

1.1.1.1. Bremsstrahlung Spectrum

X-rays are produced by the conversion of electron kinetic energy (KE) into electromagnetic radiation (EM). This occurs when highly energetic electrons strike a target made from materials like tungsten or molybdenum. A large potential difference is applied across two electrodes in an evacuated (usually glass) envelope. Negatively charged cathode is the source of electrons (e^-); the anode is positively charged and is the target of electrons. Electrons released from the cathode are accelerated towards the anode by the electrical potential difference and attain kinetic energy. The kinetic energy gained by an electron is proportional to the potential difference between cathode and anode.

On impact with the target, the kinetic energy of the electrons is converted to other forms of energy. The vast majority of interactions produce unwanted heat by small collisional energy exchanges with electrons in the target. This intense heating limits the number of x-ray photons that can be produced in a given time without destroying the target.

About 99% of the KE is converted to heat via collision like interactions and only about 0.5%-1% of the KE is converted into x-rays. Occasionally (0.5% of the time), an electron comes within the proximity of a positively charged nucleus in the target electrode. Coulombic forces attract and decelerate the electron, causing a significant loss of kinetic

¹ <http://tech.snmjournals.org/cgi/content/full/32/3/139/F2>

energy and a change in the electron's trajectory. An x-ray photon with energy equal to the kinetic energy lost by the electron is produced (conservation of energy). This radiation is termed Bremsstrahlung ("braking radiation"). This process is illustrated in **Fig. 1.2(a)**. The subatomic distance between the bombarding electron and the nucleus determines the energy lost by each electron during the Bremsstrahlung process, because the coulombic force of attraction increases with the inverse square of the interaction distance ($\propto 1/r^2$). A direct impact of an electron with the target nucleus (the rarest event) results in loss of all of the electron's kinetic energy and produces the highest energy x-ray.

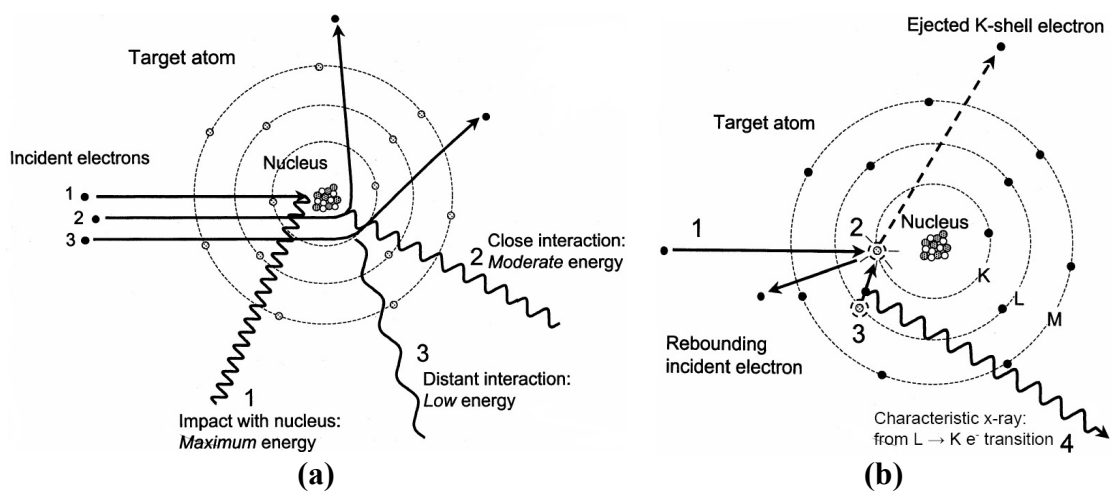


Fig. 1.2: (a) Bremsstrahlung process; (b) Generation of characteristic x-ray [BSL⁺02].

1.1.1.2. Characteristic X-Ray Spectrum

Each electron in the target atom has a binding energy that depends on the shell in which it resides. Closest to the nucleus are two electrons in K shell, which has the highest binding energy. The L shell, with eight electrons has the next highest binding energy and so forth. When the energy of an electron incident on the target exceeds the binding energy of an electron of a target atom, it is energetically possible for a collisional interaction to eject the electron and ionize the atom. The unfilled shell is energetically unstable, and an outer shell electron with less binding energy will fill the vacancy. At this electron transitions to a lower energy state, the excess energy can be released as a characteristic x-ray photon with an energy equal to the difference between the binding energies of the electron shells (**Fig. 1.2(b)**). Binding energies are unique to a given element;

consequently, the emitted x-rays have discrete energies that are characteristic of that element. The most prevalent characteristic x-rays in the diagnostic energy range result from K-shell vacancies. Acceleration potentials must be greater than 69.5kVp for tungsten targets or 20kVp for molybdenum targets to produce K characteristic x-rays.

1.1.2. X-ray Tubes

The x-ray tube provides an environment for x-ray production via Bremsstrahlung and characteristic radiation mechanisms. Major components are the cathode, anode, rotor/stator, glass (or metal) envelope and tube housing. **Fig. 1.3** shows the major components of a modern x-ray tube [BSL⁺02].

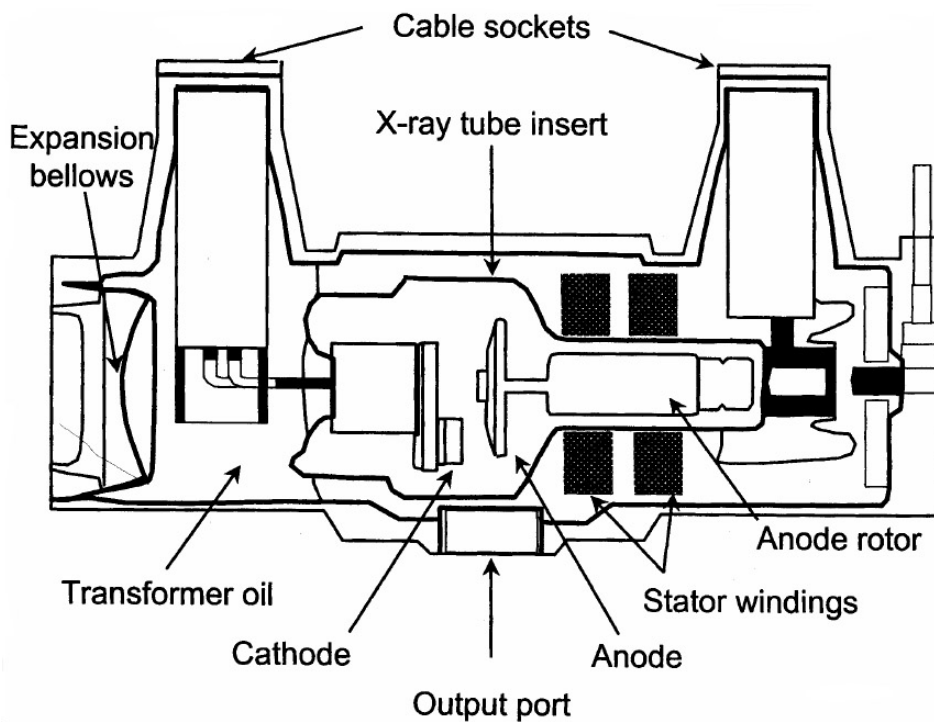


Fig. 1.3: Major components of a modern x-ray tube. [BSL⁺02]

The vast majority of the diagnostic x-ray tubes today are equipped with rotating anodes, with the exception of dental x-ray tubes, which still may use a stationary anode. x-ray tubes are designed for many different purposes ranging from very demanding applications in angiography and computed tomography with short, but heavy-duty and repeated series of exposures to the less demanding but still specific requirements in mammography and in dental imaging. The actual design of the x-ray tube therefore differs vastly. The flow of electrons across the x-ray tube is most

often controlled by external switches [GEH05]. For diagnostic imaging, electrons from the cathode filament are accelerated toward the anode by a peak voltage ranging from 20 to 150 kVp. The tube current is the rate of electron flow from the cathode to the anode, measured in milliamperes (mA), where $1 \text{ mA} = 6.24 \cdot 10^{15}$ electrons/second. The voltage, current and exposure time are the three major selectable parameters on the x-ray generator control panel that determine the x-ray beam characteristics (quality and quantity) [BSL⁺02].

1.1.2.1. Cathode

The source of electrons in the x-ray tube is the cathode, which is a helical filament of tungsten wire surrounded by a focusing cup. This structure, shown in **Fig. 1.4**, is electrically connected to the filament circuit.

The filament circuit provides a voltage up to about 10V to the filament, producing a current up to about 7A through the filament. Electrical resistance heats the filament and releases electrons via a process called thermionic emission. The electrons liberated from the filament flow through the vacuum of the x-ray tube when a positive voltage is placed on the anode with respect to the cathode. Adjustments in the filament current (and thus in the filament temperature) control the tube current.

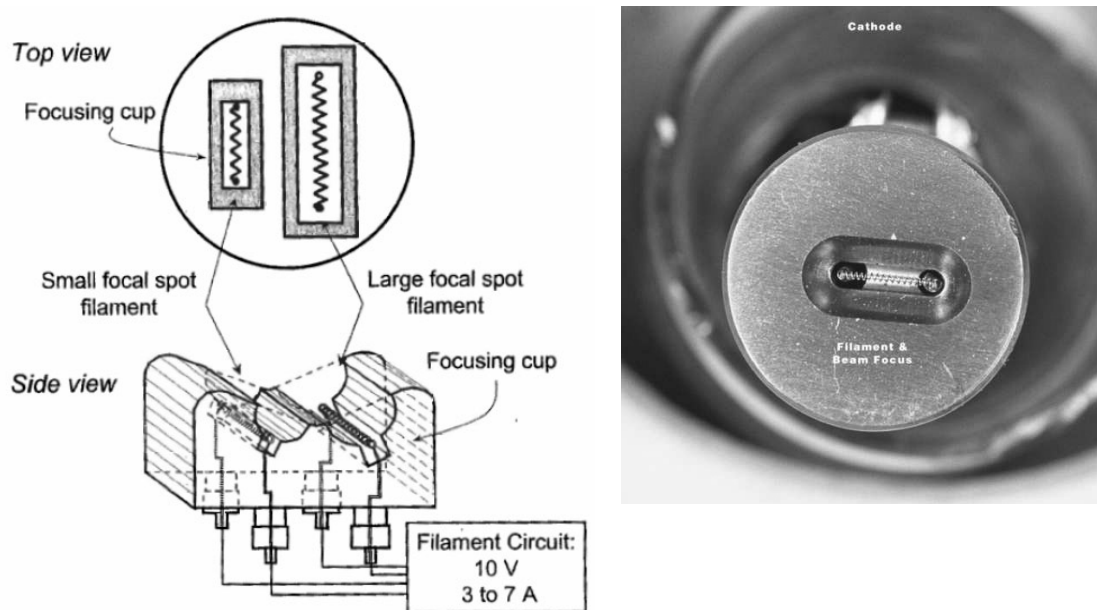


Fig. 1.4: X-ray tube cathode structure [BSL⁺02].

The focusing cup, also called the cathode block, surrounds the filament and shapes the electron beam width. The voltage applied to the cathode block is typically the same as that applied to the filament. This shapes the lines of electrical potential to focus the electron beam to produce a small integration area (focal spot) on the anode.

1.1.2.2. Anode

The anode is a metal target electrode that is maintained at a positive potential difference relative to the cathode. Electrons striking the anode deposit the most of their energy as heat, with a small fraction emitted as x-rays. Consequently, the production of x-rays, in quantities necessary for acceptable image quality, generates a large amount of heat in the anode. To avoid heat damage to the x-ray tube, the rate of x-ray production must be limited. Tungsten is the most widely used anode material because of its high melting point and high atomic number ($Z = 74$). A tungsten anode can handle substantial heat deposition without cracking or pitting of its surface. The high atomic number of tungsten provides better Bremsstrahlung production efficiency compared with low- Z elements. Molybdenum and rhodium are used as material in mammographic x-ray tubes. These materials provide useful characteristic x-rays for breast imaging.

X-ray tubes have stationary and rotating anode configurations. The simplest type of x-ray tube has a stationary anode. Despite their increased complexity in design and engineering, rotating anodes (**Fig. 1.5**) are used for most diagnostic x-ray applications, mainly because of their greater heat loading and consequent higher x-ray output capabilities. Electrons impart their energy on a continuously rotating target, spreading thermal energy over a large area and mass of the anode disk. A bearing-mounted rotor assembly supports the anode disk within the evacuated x-ray tube insert. The rotor consists of copper bars arranged around a cylindrical iron core. A series of electromagnets surrounding the rotor outside the x-ray tube envelope makes up the stator forming an induction motor. Alternating current passes through the stator windings and produces a rotating magnetic field, which induces an electrical current in the rotor's copper bars. This current induces an opposing magnetic field that pushes the rotor and causes it to spin. Rotation speeds are 3000 to 3600 rpm (low speed) or

9000 to 10000 rpm (high speed). X-ray machines are designed such that the x-ray tube will not be energized if the anode is not up to full speed; this is the cause for the short delay when the x-ray tube exposure button is pushed.

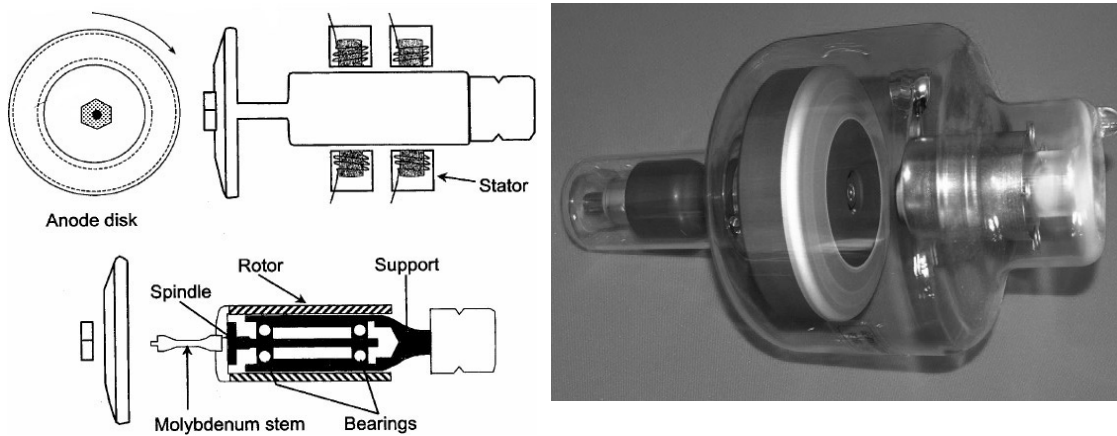


Fig. 1.5: Rotating anode of an x-ray tube.

Rotor bearings are heat sensitive and are often the cause of x-ray tube failure. Bearings are in the high-vacuum environment of the insert and require special heat-insensitive, nonvolatile lubricants. A molybdenum stem attaches the anode to the rotor/bearing assembly, because molybdenum is a very poor heat conductor and reduces heat transfer from the anode to the bearings. Because it is thermally isolated, the anode must be cooled by radiative emission. Heat energy is emitted from the hot anode as infrared radiation, which transfers heat to the x-ray tube insert and ultimately to the surrounding oil bath.

The anode angle is defined as the angle of the target surface with respect to the central ray in the x-ray field. Anode angles in diagnostic x-ray tubes, other than some mammography tubes, range from 7 to 20 degrees, with 12 to 15 degree angles being most common. Focal spot size is defined in two ways. The actual focal spot size is the area on the anode that is struck by electrons, and it is primarily determined by the length of the cathode filament and the width of the focusing cup slot. The effective focal spot size is the length and the width of the focal spot as projected down the central ray in the x-ray field. The effective focal spot size, f , is related to the length of the actual focal spot size, F , on the anode by (1.1),

$$f = F \sin \theta \quad (1.1)$$

where θ is the anode angle. It is evident that a larger anode angle provides a larger area for bombardment but it also produces a larger apparent focal spot. In practice the angle is limited by the so-called Heel effect, which is illustrated in **Fig. 1.6** [CA00].

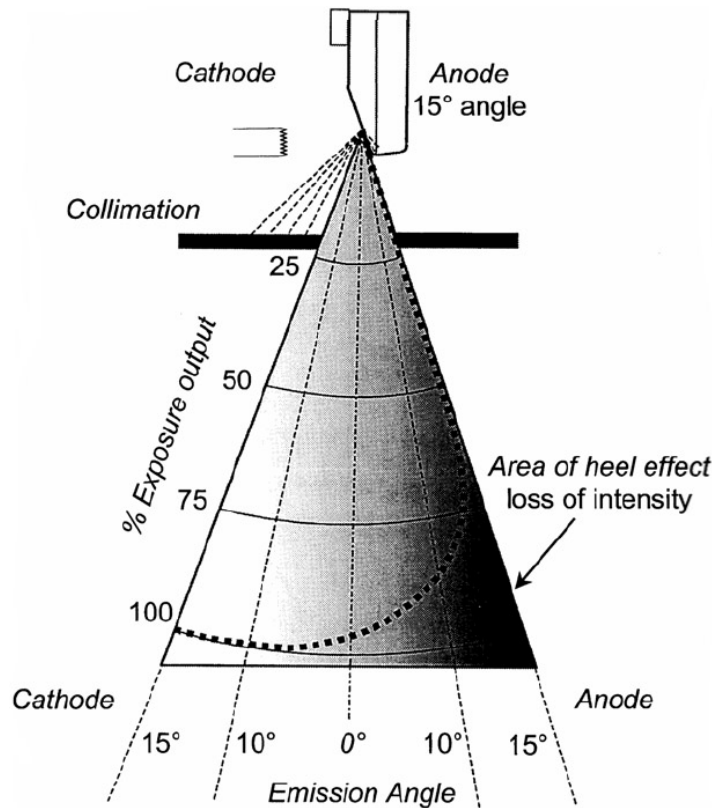


Fig. 1.6: Heel effect [BSL⁺02].

The Heel effect is a reduction in the x-ray beam intensity on the anode side of the x-ray field of view. This effect originates from the facts that 1) the anode angle will make the anode shade the part of the x-ray beam emitted in the anode side of the field, and 2) the focused electron beam from the cathode penetrates the anode surface slightly, especially when the anode is worn and the surface is rugged. In the latter case, the x-rays produced in the anode will have a longer path to penetrate on the anode side of the field, thus affecting both the photon fluence and the spectral distribution. The distance to penetrate on the cathode side is much shorter [GEH05]. For a given field size, the heel effect is less prominent with a longer source-to-image distance (SID), because the image receptor subtends a smaller beam angle. The x-ray tube is best positioned with the cathode over thicker parts of the patient and the anode over the thinner parts, to better balance the transmitted x-ray photons incident on the image receptor.

1.1.2.3. X-Ray Tube Insert

The x-ray tube insert contains the cathode, anode, rotor assembly and support structures sealed in a glass or metal enclosure (see Fig. 1.7) under a high vacuum. The high vacuum prevents electrons from colliding with gas molecules and is required in all electron beam devices.

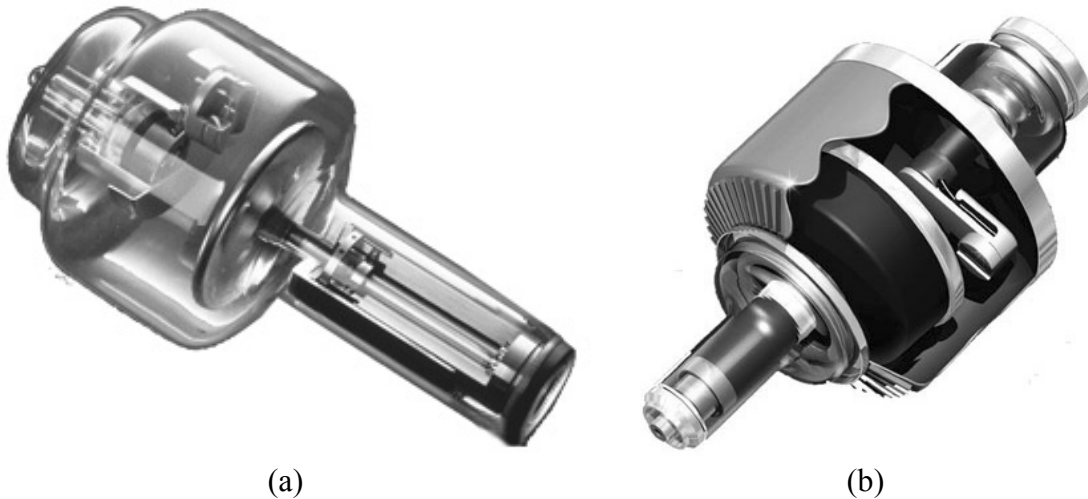


Fig. 1.7: Glass and metal x-ray tube inserts (<http://www.dunlee.com/>)

As x-ray tubes age, trapped gas molecules percolate from tube structures and slightly degrade the vacuum. X-rays are emitted in all directions from the focal spot; however, the x-rays that emerge through the tube port constitute the useful beam. Except for mammography x-ray tubes, the port is typically made of the same material as the tube enclosure. Mammography tubes use beryllium in the port to minimize absorption of the low-energy x-rays used in mammography.

1.1.2.4. X-Ray Tube Housing

The x-ray tube housing supports insulates and protects the x-ray tube insert from the environment. It is bathed in a special oil, contained within the housing, that provides heat conduction and electrical insulation. Lead shielding inside the housing attenuates the x-rays that are emitted in all directions, and of course there is a hole in the shielding at the x-ray tube port. Leakage radiation consists of x-rays that penetrate this lead shielding, and therefore it has a high effective energy. The tube housing must contain sufficient shielding to meet regulations that limit the leakage radiation exposure.

1.1.2.5. Radiation Filtration

The quality of the x-rays also plays a great role in the size of the administered dose. X-ray radiation normally has so-called "hard" and "soft" particles, that is, particles with a lot of energy and particles with little energy. Hard particles are better for the patient, because they pass through the body. Soft particles, by contrast, get caught inside the body because they are too weak to pass through and out of it. Therefore, it is primarily soft radiation that creates unnecessary exposure to the patient. For this reason, copper and aluminum (Molybdenum and Rhodium in the case of Mammography) are used as filters in front of the x-ray tube. The soft radiation is caught in the filter plates, and the remaining radiation emerging from the filter is "harder." This additional filtration can also reduce the dose to the patient without diminishing image quality, because in any case only the *hard* rays reach the image intensifier, film cassette, or Digital Detector [Wip05].

1.1.3. Mammography

X-ray mammography is a radiographic examination that is specially designed for detecting breast pathology. Mammography started in 1960, but modern mammography has existed only since 1969 when the first x-ray units dedicated to breast imaging were available. By 1976, mammography as a screening device became standard practice. Technologic advances over the last several decades have greatly improved the diagnostic sensitivity of mammography.

The requirements for mammography are different from ordinary x-ray examination because the breast is composed of soft tissues and the difference between attenuation coefficients of soft tissues is most pronounced at low x-ray energy levels, that means low energy x-rays in the order of 20keV should be used. **Fig. 1.8** shows that the attenuation differences between normal tissue and cancerous tissue is highest at very low x-ray energies and is poor at higher energies. Low x-ray energies provide the best differential attenuation between the tissues; however, the high absorption results in a high tissue dose and long exposure time.

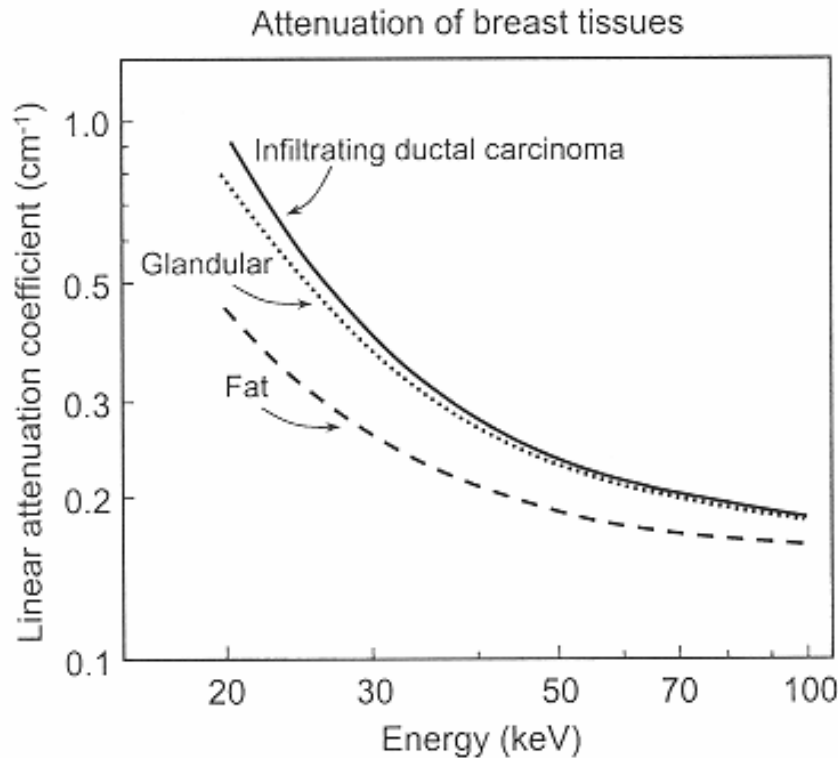


Fig. 1.8: Attenuation of breast tissues as a function of energy [BSL⁺02].

Detection of micro calcifications in breast tissues is also important because of the high correlation of calcification patterns with disease. Detecting micro calcifications while minimizing dose and enhancing low-contrast detection imposes extreme requirements on mammographic equipments and detectors. The imaging system must have a sufficient spatial resolution to delineate the edges of fine structures in the breast. Structural detail small as 50 μm must be resolved adequately. Because the breast is sensitive to ionization radiation, which at least at high doses is known to cause breast cancer, it is desirable to use the lowest radiation dose compatible with excellent image quality have led to the refinement of dedicated x-ray equipment for mammography. The photograph of a modern mammography system and its typical components are shown in **Fig. 1.9**.

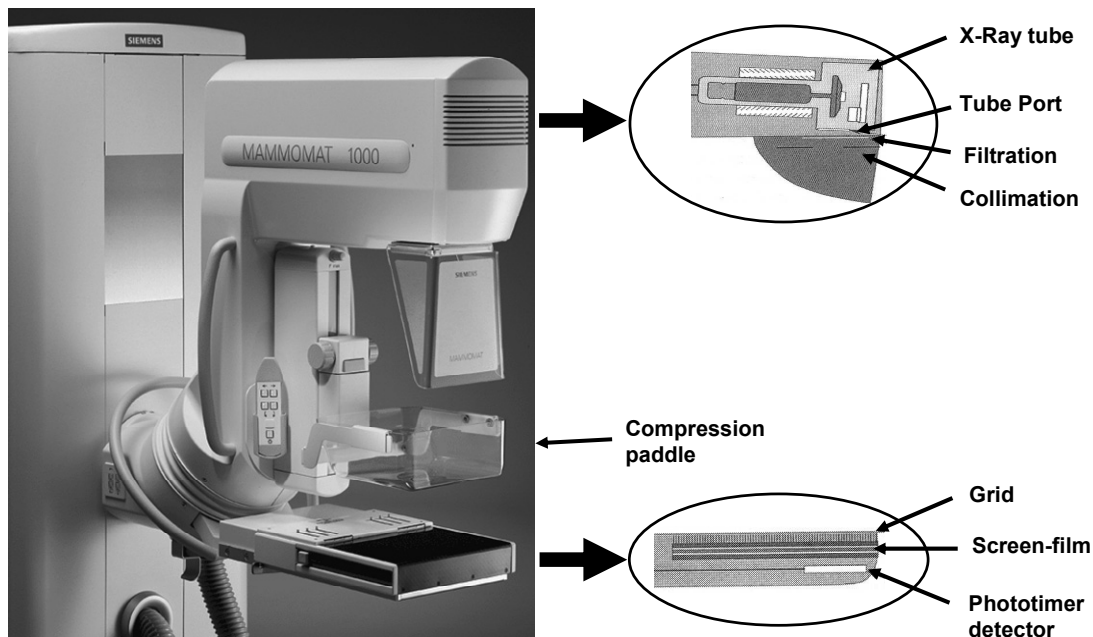


Fig. 1.9: Photograph² of modern mammography system and details of the main components (excluding the generator) [BSL⁺02].

1.1.4. X-ray Generator

X-ray generator is a device, which supplies electric power to the x-ray tube and permits selection of x-ray energy (voltage), x-ray quantity (current) and exposure time. The generator has three main interrelated electric circuits to serve three main functions: 1) The filament circuit supplies the power needed to heat the cathode filament and boil off electrons, 2) the high-voltage circuit supplies the high-voltage needed to accelerate these electrons from the cathode to the anode for production of x-rays, and 3) the timer circuit (exposure timer) controls the length of the x-ray production. **Fig. 1.10** shows a block diagram of a typical x-ray generator.

A generator may be considered to have two main components, the console or control panel, and the transformer assembly. The control panel allows the operator to select the exposure parameters voltage, current and exposure time; the actual current and voltage during exposure are shown by meters on the control panel. There is usually an exposure button with a standby function that starts rotation of the anode and heats the cathode filament prior the actual exposure. The transformer assembly has a low

² Siemens press picture: The copyrights belong to Siemens AG, Munich/Berlin.

voltage filament transformer which is a step-down transformer, and a high-voltage step-up transformer. The transformer assembly also includes rectifiers for the high-voltage circuit. Due to the high potential differences between the high-voltage circuit and filament circuit (up to 150 kV), the transformers and rectifiers are usually immersed in oil which serves as an insulator and prevents sparking [GEH05].

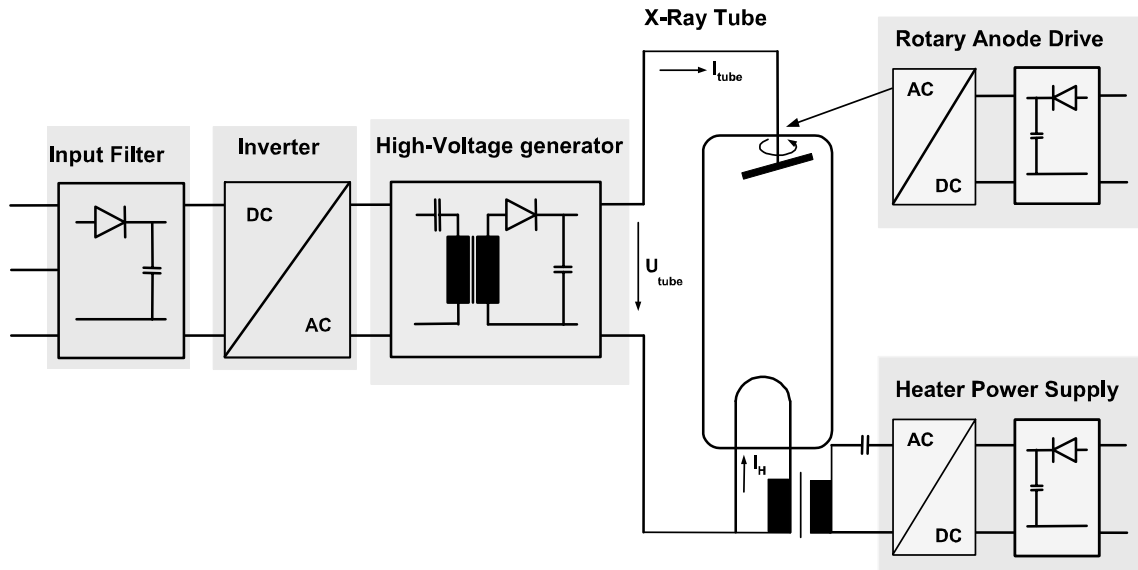


Fig. 1.10: Block diagram of an x-ray generator.

1.2. HIGH-VOLTAGE GENERATION

1.2.1. Introduction

The quality of photographic x-ray image depends on the x-ray absorption by human body. High output voltage of x-ray generator is required to scan dense body parts and low output voltage is used in the diagnosis of soft tissues of the organs [LT01], [SDN⁺00],[WH99]. Short exposure time which is less than a few milliseconds is widely used for the diagnosis of moving organs, such as vessels and heart. In general, relatively lower tube voltage and higher tube current are required for shorter exposure time to acquire the desirable photographic density, as well as enough contrast, and sharpness of images for medical diagnosis [WH99]. In addition, the contrast of x-ray image is sensitive to the tube voltage ripple and rising time [WH99].

In order to avoid imperfections in x-ray images, it is necessary to apply a stable high DC voltage with fast dynamic response across the x-ray tube. Therefore, the power supply for an x-ray generator is required to generate a high voltage during a very short time interval [CFS85], [LT01]. The total x-ray dose, which determines the photographic density of x-ray image, varies proportionally to the exposure time multiplied by the actual tube current [WH99]. The cathode filament of the x-ray tube is controlled by an independent current-regulated heater and as the temperature is varied the x-ray tube behaves as a variable resistor [LT01]. Hence, a high performance x-ray generator needs to provide an output with wide range of voltage and current levels. Furthermore, the aspects of volume and weight are important to x-ray generators, especially in the applications of x-ray CT scanners, C-arm x-ray systems and portable x-ray machines [WH99].

Especially for the case of mammography, dedicated equipment producing images with high contrast and high resolution is required since the radiological signs of many breast cancers are very subtle. An important difference in mammographic tube operation compared to conventional radiographic operation is the low operating voltage, normally below 35 kVp. The reason is that the attenuation difference between normal tissue and cancerous tissue is highest at very low x-ray energies. However the

high absorption results in a high tissue dose and long exposure time. Therefore it is important to minimize radiation dose [BSL⁺02].

A candidate converter to implement an x-ray generator is requested to meet following main specifications: low ripple high output voltage, fast transient response without overshoot and ability to regulate the output voltage over a wide load range. Furthermore, in order to reduce volume and weight, the next generation of x-ray generator is required to have high power density. This is possible by increasing considerably the operating switching frequency of the x-ray generator.

This application also requires a high-voltage transformer with a large turns ratio, which increases the influence of the transformer non-idealities. This leads to a limitation of the number of converter topologies that are suitable for this application. If a conventional hard switching PWM converter is used, in particular, the leakage inductance and the secondary winding capacitance of the transformer will cause parasitic resonances that affect the converter behavior. On the other hand, resonant converters are an attractive choice for this application because they can incorporate the transformer non-idealities [EJW88]. Thus, it is not surprising, that nowadays all topologies found in the literature for this application are resonant converters. In this thesis a resonant converter is also used. The choice of the proper resonant converter topology will be explained in Section 1.3.

1.2.2. Main Resonant Converter Configurations

As mentioned before, in this thesis a resonant converter is selected to implement the high-voltage generator. In this section, the characteristics of the main configurations of resonant converters will be shown, and advantages and weaknesses will be explained. This should be helpful for choosing the proper topology of resonant converter to implement the x-ray power generator.

Resonant converters contain resonant L-C networks whose voltage and current waveforms vary sinusoidally during one or more subintervals of each switching period. The resonant network has the effect of filtering higher harmonic voltages such that a nearly sinusoidal current appears at the input of the resonant network [Ste88]. There are three main types of

resonant networks, which are shown in **Fig. 1.11**: series resonant, parallel resonant and series-parallel resonant [Ras01]. Depending on how the resonant networks are combined with other circuit configurations, one can obtain several types of resonant converters. The more common configurations are: DC-to-high-frequency-AC inverters, resonant DC-DC converters and resonant link converters. In this work, the focus will be on the resonant DC-DC converters.

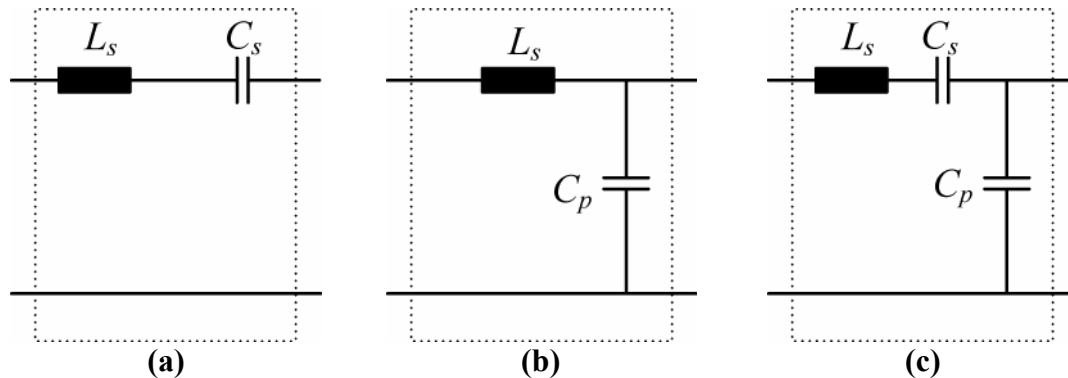


Fig. 1.11: Resonant networks: (a) Series Resonant; (b) Parallel Resonant; (c) Series-Parallel Resonant.

A main advantage of resonant converters is the reduced switching losses. Resonant converters can run in either the zero-current-switching (ZCS) or zero-voltage-switching (ZVS) mode [Ste01]. That means that turn-on or turn-off transitions of semiconductor devices can occur at zero crossings of tank voltage or current waveforms, thus reducing or eliminating some of the switching loss mechanisms. Since the losses are proportional to switching frequency, converters can operate at higher switching frequencies than comparable PWM converters [EM01].

Resonant converters are widely used in industrial applications, for example, as supplies for CO₂ lasers, x-rays tubes, and radars [ZCA00]. In high-voltage applications, such as x-ray generators and electrostatic precipitators, resonant networks are frequently used because transformer leakage inductance and winding capacitance lead to resonant network. Thus, it is necessary to integrate these parasitics such that they will not have negative influence on the converter behavior [EM01], [Ste01].

1.2.2.1. Series Resonant Converter

The main structure of a series resonant DC-DC converter is shown in **Fig. 1.12**. The major advantage of this converter is that the series resonant

capacitor on the primary side blocks the DC component. Hence the converter can easily be used in full-bridge arrangements without any additional mechanisms to control unbalance in the switching times of the power switches and it also avoids the transformer saturation. For this reason the series resonant converter is suitable for high-power applications where a full-bridge converter is desirable [Bha91],[Ste88].

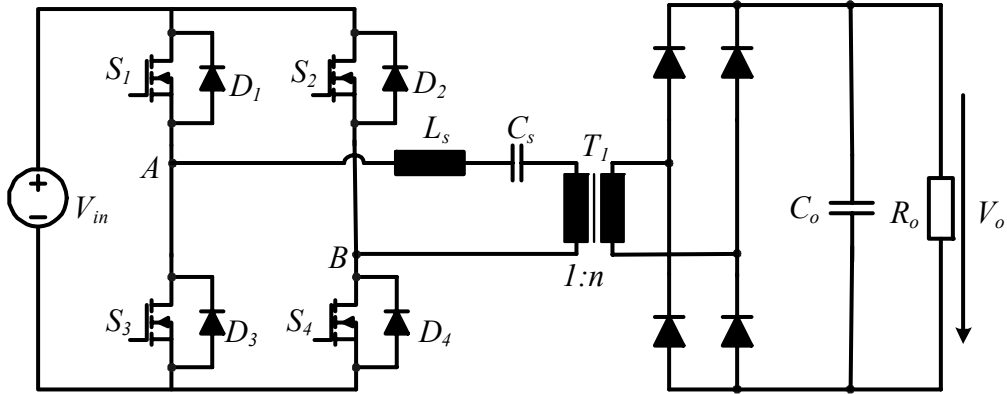


Fig. 1.12: Schematics of a series resonant DC-DC converter.

The equation (1.2) describes the voltage conversion ratio of a series resonant converter using the approximation proposed by Steigerwald in [Ste88].

$$\frac{V_o}{nV_{in}} = \frac{1}{1 + j \frac{\pi^2}{8} Q \left[f_{s,N} - \frac{1}{f_{s,N}} \right]} \quad (1.2)$$

where

$Q = Z/R_o$ – normalized load,

$Z = \sqrt{L_s/C_s}$ – characteristic impedance of the resonant network,

n – transformer turns ratio

$f_{s,N} = f_s/f_o$ – normalized switching frequency,

f_s – switching frequency and

$f_o = (2\pi\sqrt{L_s C_s})^{-1}$ – series resonant frequency.

Another advantage of the series resonant converter is the decrease in current of the power devices with a decrease in load. This leads to a reduction of the power device conduction losses as the load decreases, consequently preserving high part load efficiency [Ste88].

The major disadvantage of the series resonant converter is the difficulty to regulate the output voltage for the no load case. This fact can

be observed in the DC characteristic of the series resonant converter shown in **Fig. 1.13**. The voltage conversion ratio is the graphical representation of Eq. (1.2). One can see that when the load becomes lower, the DC characteristic becomes very flat and consequently the curves have less selectivity. This means that this converter can only be used without auxiliary mechanisms, in applications where a no load regulation is not required.

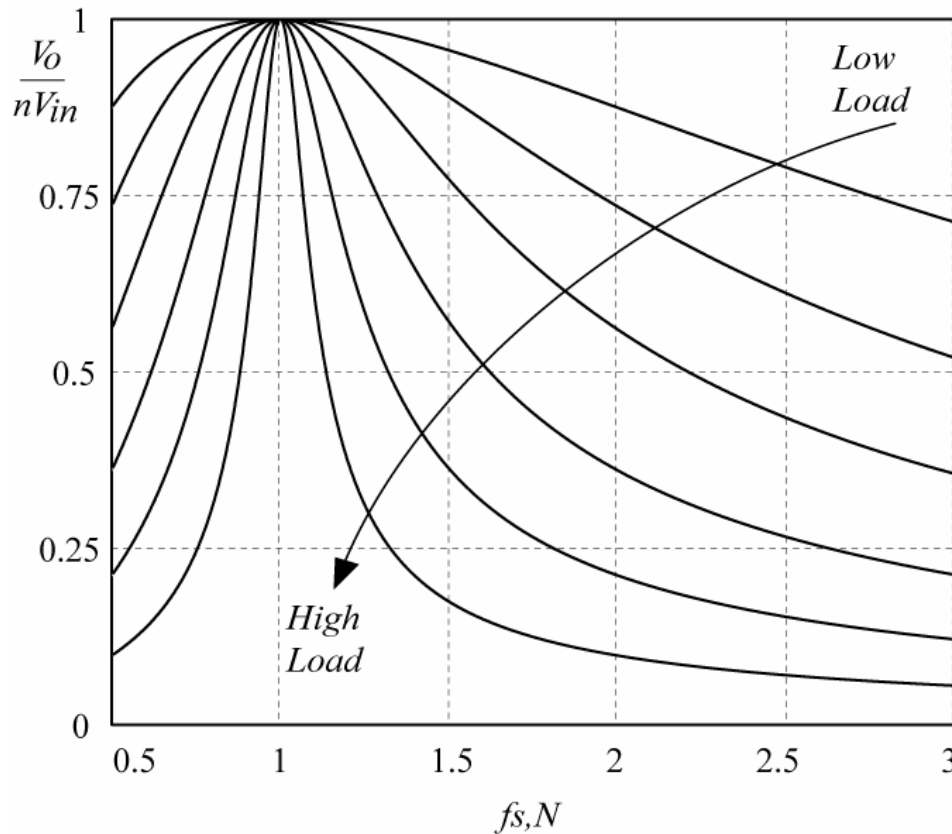


Fig. 1.13: Voltage conversion ratio curves of the series resonant converter; $f_{s,N} = f_s/f_o$ (normalization with reference to the series resonant frequency $f_o = (2\pi\sqrt{L_s C_s})^{-1}$).

Another disadvantage of this converter is that the output DC filter capacitor must carry high ripple current [Bha91],[Ste88]. This is a significant disadvantage for applications with low output voltage and high current. For this reason the series resonant converter is not considered suitable for low-output-voltage high-output-current converters but rather is more suitable for high-output-voltage low-output-current converters. For the high-output-voltage case, no magnetic components are needed on the high-voltage side of the converter. X-ray generators could make use of this advantage because they have a pure capacitive output filter.

1.2.2.2. Parallel Resonant Converter

The characteristics of the parallel resonant converter are quite different from those of the series resonant converter, and from those of conventional PWM converters. The parallel topology can both step up and step down the DC voltage. Although the output characteristics are elliptical, near resonance they exhibit a current-source characteristic [EM01]. **Fig. 1.14** shows the structure of a parallel resonant DC-DC converter.

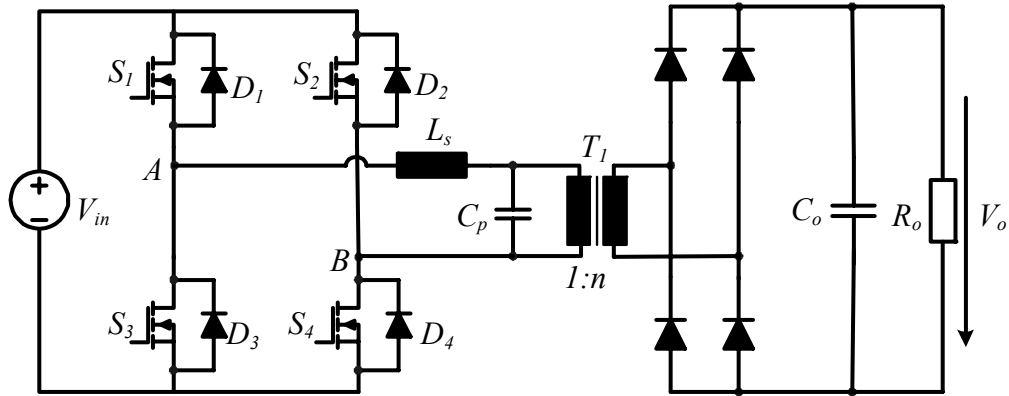


Fig. 1.14: A full-bridge parallel resonant DC-DC converter with capacitive output filter.

The voltage conversion ratio of the parallel resonant converter, using the approximation proposed by Ivensky et al. in [IKBY97], is given by equation (1.3).

$$\frac{V_o}{nV_{in}} = \frac{4}{\pi} \cdot \frac{k_{21}}{k_v} \quad (1.3)$$

where

$$k_{21} = \frac{1}{\sqrt{[(1 - f_{s,N}^2) \cdot (1 + \frac{\tan(|\beta|)}{\omega C_p R_e})]^2 + [f_{s,N}^2 \cdot \frac{1}{\omega C_p R_e}]^2}} \quad (1.4)$$

$$k_v = 1 + 0.27 \cdot \sin\left(\frac{\theta}{2}\right) \quad (1.5)$$

θ – output rectifier conduction angle (proportional to the load; see [IKBY97] for more details),

β and $\omega C_p R_e$ – see [IKBY97] for details,

n – transformer turns ratio,

$f_{s,N} = f_s/f_o$ – normalized switching frequency,

f_s – switching frequency and

$f_o = (2\pi\sqrt{L_s C_p})^{-1}$ – parallel resonant frequency.

The voltage conversion ratio curves of the parallel resonant converter are shown in **Fig. 1.15**. From these curves one can see that, in contrast to the series resonant converter, the parallel converter can regulate the output voltage at no load by running at a frequency above resonance. It is also important to point out that the output voltage at resonance is a function of load and can rise to very high values at no load if the operating frequency is not raised by the controller [Ste88].

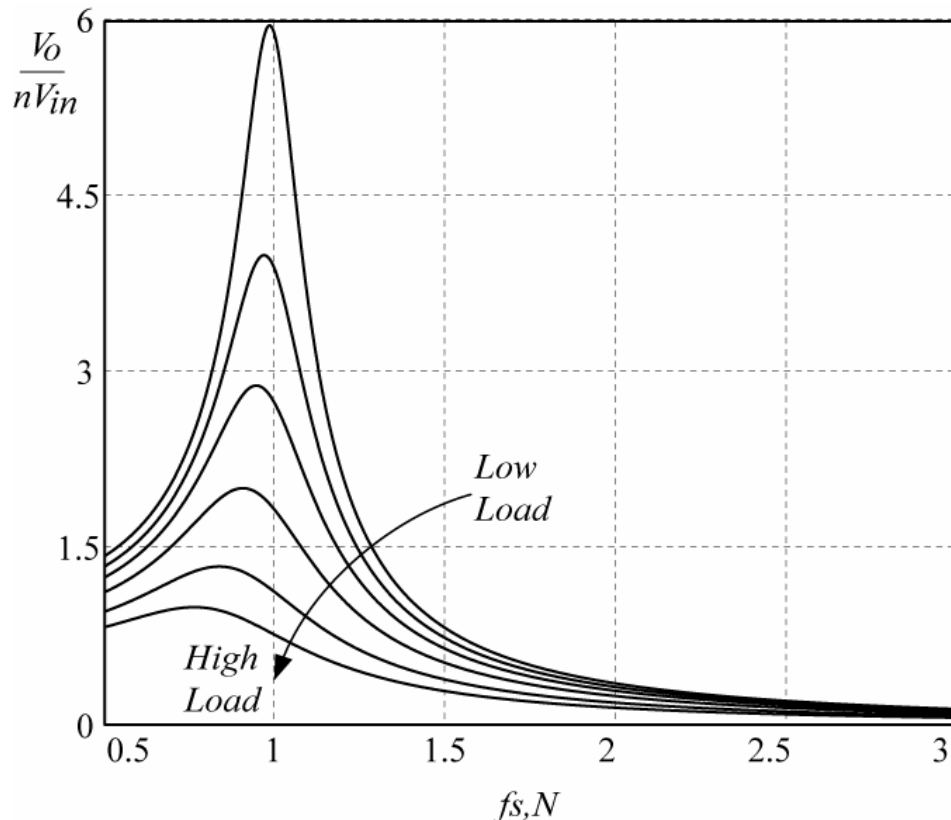


Fig. 1.15: Voltage conversion ratio curves of the parallel resonant converter in dependency on the load and on the normalized switching frequency.

The parallel resonant converter is physically protected against short circuit. This property can be seen by applying a short circuit directly across the resonant capacitor. For that case, the entire voltage applied by the inverter is directly across the resonant inductor and, therefore, the current is limited by the impedance of the inductor. For this reason the parallel resonant converter is particularly desirable for applications with severe short circuit requirements [Ste88].

The major disadvantage of the parallel resonant converter is the higher device current that is relatively independent of load. As the load resistance increases (load decreases), the frequency of operation increases to regulate the output voltage, but the current into the resonant circuit stays almost constant. The consequence of this behavior is that the conduction losses in the semiconductor devices and the reactive components also stay almost fixed as the load decreases, such that the efficiency of the converter descends at light load. In addition, this circulating current increases as the input DC voltage to the converter increases. Hence, this converter is normally better suited for applications which run from a relatively narrow input voltage range and that exhibit an approximately constant load near the maximum power [Ste88]. Even if in the literature, the parallel resonant converter is normally used with inductive output filter for low-output-voltage high-output-current applications, it can be shown that this converter is also suitable for high-voltage applications by removing the output filter inductor [EJW88]. This removal modifies the waveforms of the resonant circuit but the performance of the converter remains the same.

1.2.2.3. Series-Parallel Resonant Converter

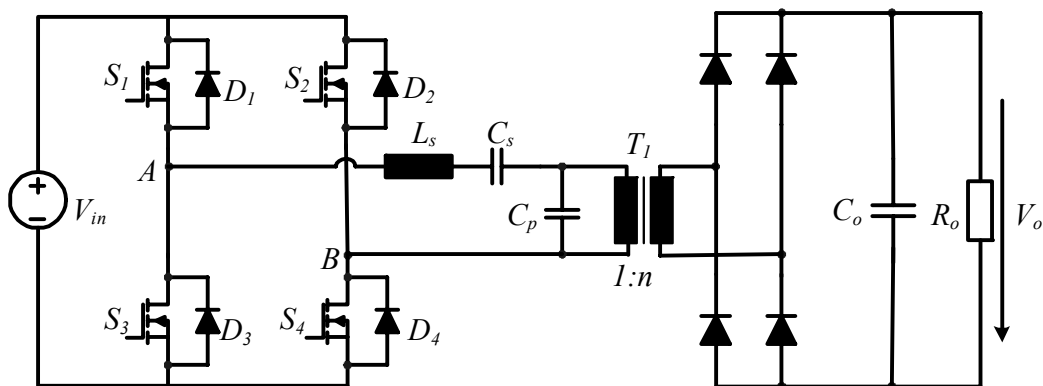


Fig. 1.16: Series-parallel resonant DC-DC converter with capacitive output filter.

The series-parallel resonant DC-DC converter with capacitive output filter is shown in **Fig. 1.16**. In the literature, this converter has also been often used with inductive output filter [Bha91],[Ste88]. However, in the current work the focus will be on the converter with capacitive output filter because this configuration is better suited for high-voltage applications.

Eq. (1.6) gives the voltage conversion ratio of the series-parallel resonant converter, using the approximation proposed by Ivensky et al. in [IKBY97].

$$\frac{V_o}{nV_{in}} = \frac{4}{\pi} \cdot \frac{k_{21}}{k_v} \quad (1.6)$$

$$k_{21} = \frac{1}{\sqrt{[1 - \alpha \cdot (f_{s,N}^2 - 1) \cdot (1 + \frac{\tan(|\beta|)}{\omega C_p R_e})]^2 + [\alpha \cdot (f_{s,N}^2 - 1) \cdot \frac{1}{\omega C_p R_e}]^2}} \quad (1.7)$$

$$k_v = 1 + 0.27 \cdot \sin\left(\frac{\theta}{2}\right) \quad (1.8)$$

where

$\alpha = C_p/C_s$ – ratio of the parallel to the series capacitor,

θ – output rectifier conduction angle (proportional to the load; see Chapter 2 for more details),

β and $\omega C_p R_e$ – see Chapter 2 for details,

n – transformer turns ratio,

$f_{s,N} = f_s/f_o$ – normalized switching frequency,

f_s – switching frequency and

$f_o = (2\pi\sqrt{L_s C_s})^{-1}$ – series resonant frequency.

The real resonant frequency of the circuit changes with the load as shown in **Fig. 1.17**. This happens because the load defines the influence of C_p on the resonant frequency. For high load the resonant current flows for only a small part of the switching period through C_p . Thus, the converter behaves as a series resonant converter and the resonant frequency is almost equal the series resonant frequency f_o . On the other hand, for low load the resonant current flows almost the whole switching period through C_p . Therefore, the converter behaves as a parallel resonant converter. When operating above resonance, the converter behaves as a series resonant converter at lower frequencies (high load operation) and as a parallel resonant converter at higher frequencies (low load operation) [DRS00]. At higher switching frequencies the series capacitance becomes so small that it behaves just as a DC blocking capacitance. The resonant inductor then resonates with the parallel capacitor and the converter operates in the parallel resonant mode [EJW88]. By proper selection of the resonant

elements, the series-parallel resonant converter has better control characteristics than the resonant converters with only two resonant elements [Bar94] being less sensitive to component tolerances.

This configuration aims to take advantage of the desirable characteristics of the series and the parallel converter while reducing or eliminating their drawbacks. Unlike the series resonant converter, the series-parallel resonant converter is capable of both step-up and step-down operation [FM98]. This capability can be observed in the voltage conversion ratio curves of the series-parallel resonant converter as shown in **Fig. 1.17**.

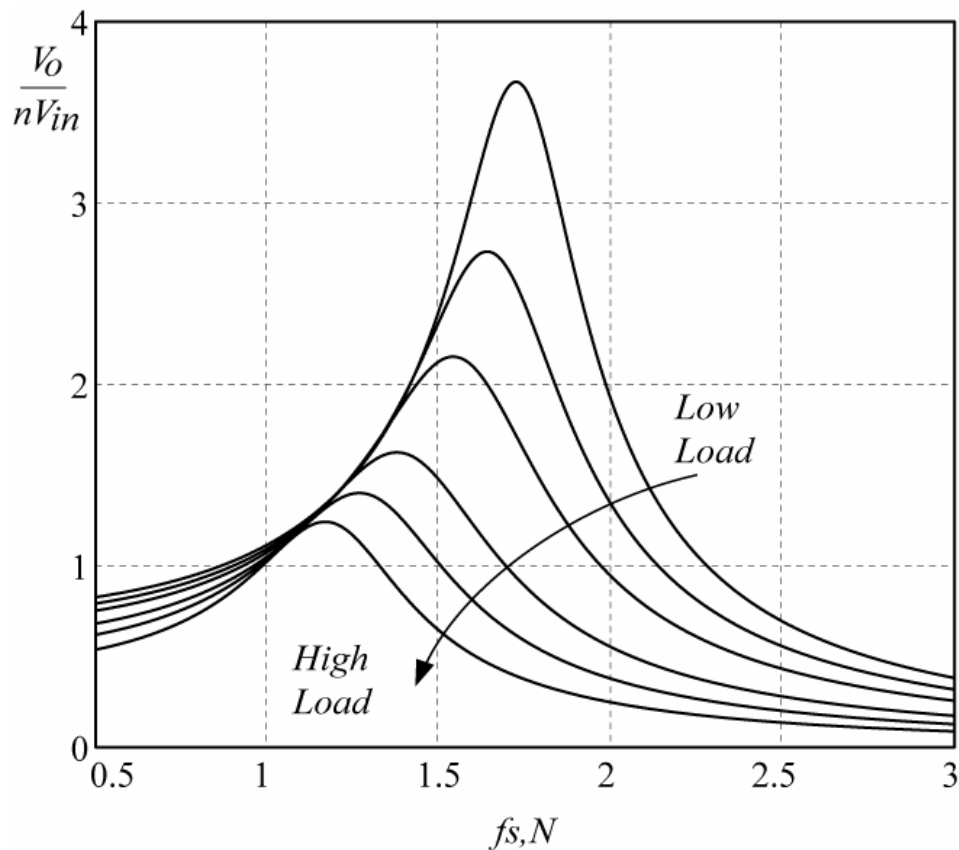


Fig. 1.17: Voltage conversion ratio of a series-parallel resonant converter in dependency on the load and on the normalized switching frequency. $f_{s,N} = f_s/f_o$ (normalization with reference to the series resonant frequency $f_o = (2\pi\sqrt{L_s C_s})^{-1}$).

The voltage conversion ratio curves also show that the output voltage can be regulated at no load. Thus, the main disadvantage of the series resonant converter is successfully eliminated with this configuration. It is important to note that the lower the value of the parallel resonant capacitor C_p the more the circuit will have the characteristic of a series resonant converter. Therefore, the value of the parallel resonant capacitor C_p may

not be too low in order to permit that the converter takes the characteristic of the parallel resonant converter at light load. When the resonant current flows for a long interval of the switching period through C_p (and this is the case at light load operation), it is increased above the level expected in the series resonant converter, producing a higher output voltage. Therefore the presence of C_p in combination with L_s results in boosting of the converter output voltage at light load [FM98].

The main disadvantage of the parallel resonant converter, i.e. the high device current independent on the load is supposed to be eliminated in the series-parallel resonant converter. Unfortunately this drawback cannot be totally removed but, with the proper choice of the resonant elements, it can be considerably reduced for certain load levels [Bha91], [Ras01]. The limiting factor in reducing C_p , to reduce circulating current is the upper switching frequency limit. As the value of C_p gets lower relative to C_s , the ratio $\alpha = C_p/C_s$ also gets lower and consequently the converter operating frequency range gets wider. As very high switching frequencies are not desirable due to practical implementation limitations, one has to find a compromise between reducing the circulating current for low loads and having a reasonable limit for the upper switching frequency. Normally one designs the converter such that it operates essentially as a series resonant converter so that the circulating current will decrease as the load decreases to a certain level. Below this level, the converter behaves like a parallel resonant converter, and the circulating current no longer decreases with load [Ste88]. Unfortunately, in the case of high-voltage generation, where high voltage conversion ratio is required, the value of C_p cannot be significantly reduced. Thus, the circulating current does not decrease considerably with the load and losses remain almost unchanged. In order to reduce the losses at light load operation, one can use other concepts like discontinuous operation mode as will be shown in Chapter 2.

1.2.3. State of the Art X-Ray Generator Topologies

Many converter topologies have been proposed in order to supply the high output voltage that is necessary to drive an x-ray tube. In order to choose a proper topology for the next generation of x-ray generators, it is important to know the state of the art technology that is employed in this

application. As mentioned before, nowadays all topologies found in the literature for this application are resonant converters. The advantages of these converters over conventional PWM converters are already explained in the previous section. The most relevant types of resonant converters, which have been published in the last years for x-ray imaging application, are: the LCC series-parallel resonant converter, the LCLC resonant converter and the multilevel series resonant converter. These converters are briefly described in the following.

A. LCC Series-Parallel Resonant Converter

The structure of the full-bridge LCC resonant DC-DC converter is shown in **Fig. 1.18**. This converter is called LCC because of the structure of its resonant tank with one resonant inductor and two resonant capacitors.

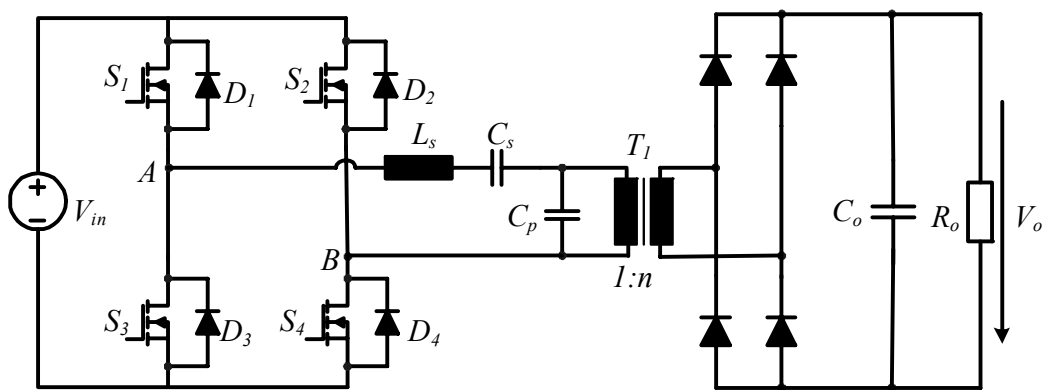


Fig. 1.18: LCC series-parallel resonant converter.

The LCC resonant converter has been used in high output voltage applications for more than twenty years. As already pointed out, this configuration takes advantage of the attractive characteristics of the series and the parallel converter while reducing or eliminating their drawbacks. By proper selection of the resonant elements, the series-parallel resonant converter has better control characteristics than the resonant converters with only two resonant elements [Bar94] being less sensitive to component tolerances. In addition, the converter is protected against short circuit and can regulate the output voltage at no load.

Many authors used this topology with different combination of control strategies: PFM operating below resonance [OCI⁺02], [SDN⁺00], PFM operating above resonance [CFS85], [VGS⁺95] and phase-shifted

PWM above resonance with fixed [LT01], or variable frequency [GRS⁺94b]. It has been shown that operation above resonance has many advantages like the use of lossless snubbers, elimination of turn-on losses, reduction in the size of magnetics and operation with medium speed diodes [Bha91], [Ste88]. Regarding the different control strategies, normally the pulse frequency modulation (PFM) is associated with resonant converters. In this type of modulation the output voltage is controlled by varying the switching frequency. This method has the drawback that it can produce a wide band EMI noise. Moreover, when PFM is used with operation below resonance, the magnetic components cannot be optimized because they have to be designed for the lowest frequency of operation. By phase-shifted PWM operation, the converter output is controlled by varying the pulse width of the quasi-square voltage v_{AB} applied to the resonant tank. This variation of duty cycle of the voltage v_{AB} can be realized by operating the bridge legs with a phase-shift [TML88]. This operation is also called clamped-mode operation because the voltage v_{AB} is clamped at zero during the time delay between both bridge legs [ARB⁺95], [SL91], [TML88]. One of the main advantages of this method is that it simplifies the design of the gate drivers of the switches. This is due to the fact that the switches are always driven with a fixed 50% duty cycle [SJL⁺95], [TML88].

The voltage v_{AB} and the resonant current i_{Ls} for the LCC resonant converter when operating above resonance with phase-shifted PWM are shown in **Fig. 1.19**.

The maximum switching frequency found in the literature for this type of converter operating with high output voltage is 170 kHz [VGS⁺95]. However, the converter proposed in [VGS⁺95] is for Travelling Wave Tube (TWT) systems, thus it has a relative low power level. For high output voltage and high power level, the maximum switching frequency published in the literature for the LCC converter is 100 kHz [LT01].

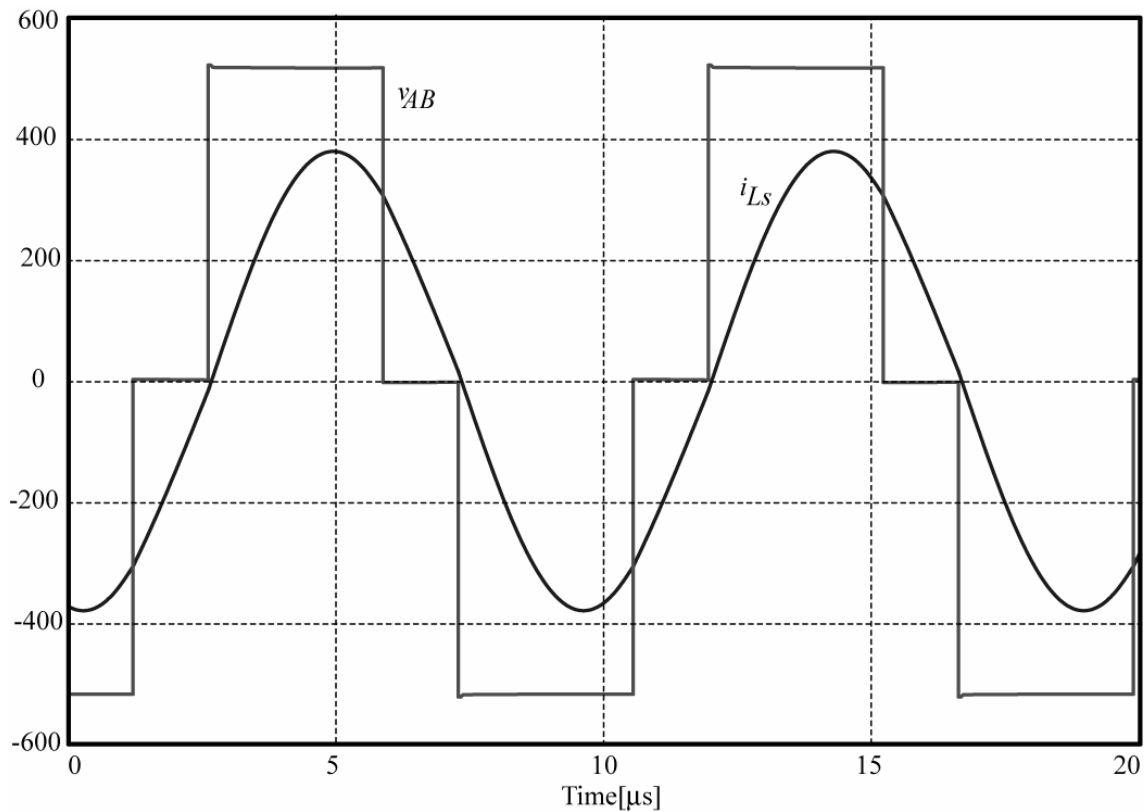


Fig. 1.19: Voltage V_{AB} and resonant current for the LCC resonant converter.

B. LCLC Resonant Converter

The topology of a full-bridge LCLC resonant DC-DC converter is shown in **Fig. 1.20**. This converter operates for low power close to the parallel resonant frequency $(2\pi\sqrt{L_p C_s})^{-1}$ and for full load, close to the series resonant frequency $(2\pi\sqrt{L_s C_s})^{-1}$.

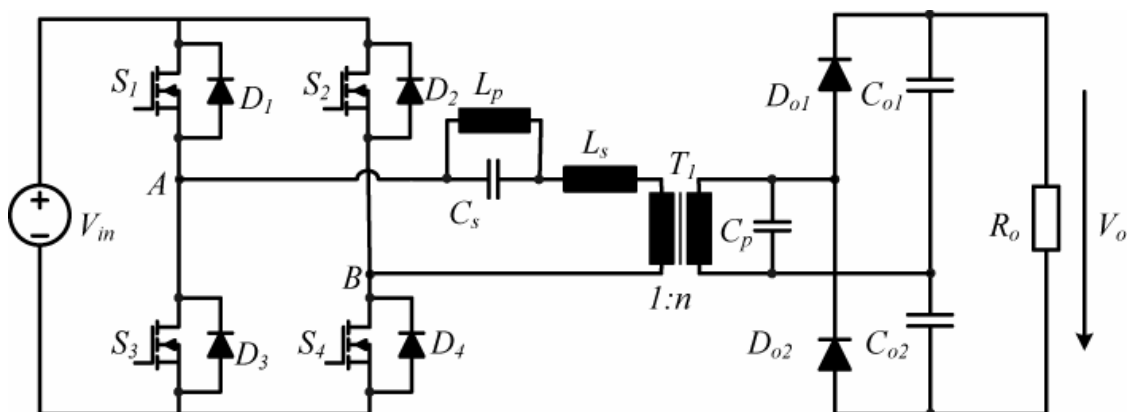


Fig. 1.20: LCLC-type resonant converter.

One can see that in this converter a voltage doubler circuit is used instead of a full-bridge rectifier. This alteration is useful to reduce the

transformer turns ratio and will be discussed in Chapter 2. The advantages of this converter are basically adjustable slope of the voltage transmission curves and zero current switching [ZPv00]. Moreover, an advantage of converters with more than one resonance is the reduced operating frequency range and, thus, the high operating frequency even at low power [CBG⁺99], [LGP⁺97]. In the literature a frequency range from 25 kHz to 65 kHz is used. **Fig. 1.21** shows typical waveforms of the voltage v_{AB} and the resonant current of the LCLC resonant converter.

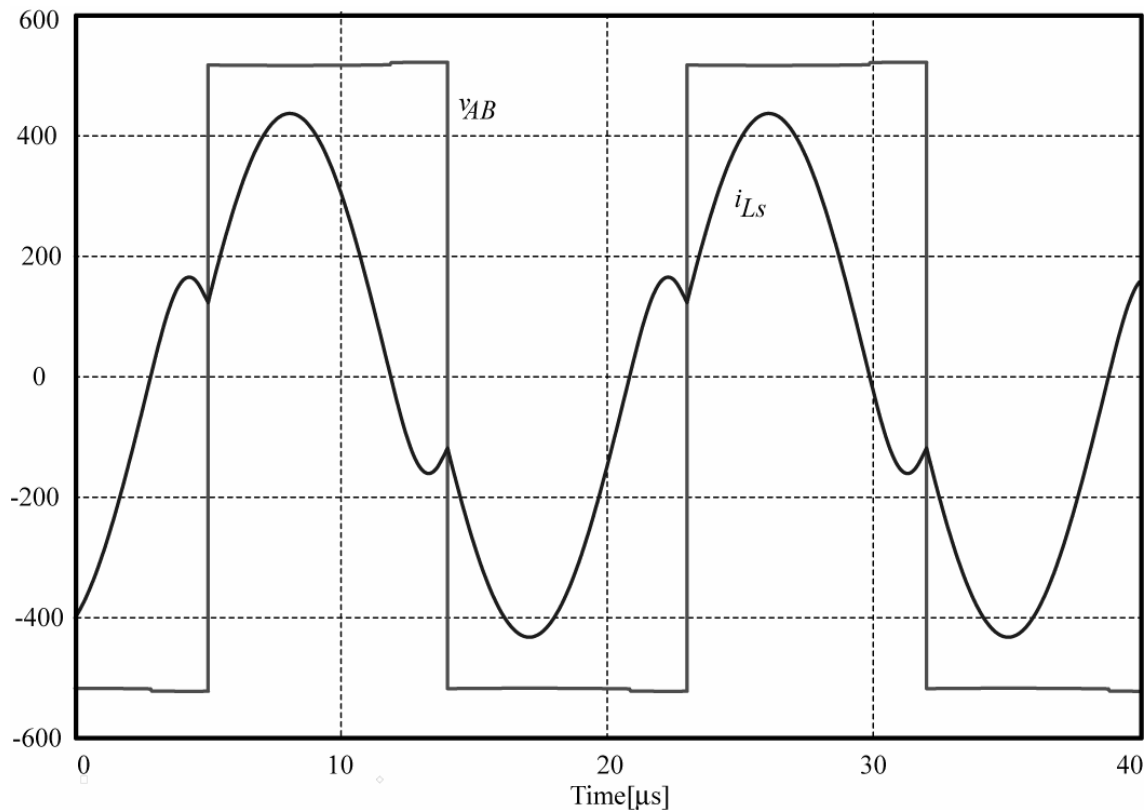


Fig. 1.21: Voltage V_{AB} and resonant current for the LCLC resonant converter.

C. Multilevel Series Resonant Converter

Fig. 1.22 shows the series resonant multilevel DC-DC converter for high output voltage application proposed in [WH99]. This converter has the advantage that the voltage imposed to the switches is only half of the input voltage. Thus, power switches with lower drain-source breakdown voltage and, consequently, lower drain-source on-state resistance (R_{DSon}) can be used. This fact reduces costs and conduction losses of the converter. Furthermore, using several voltage doublers connected in series, the transformer turns ratio and, accordingly, the secondary winding

capacitance can be reduced. However, this is not an exclusive advantage of this topology because the association of voltage multipliers can be used for any other resonant DC-DC topology in order to reduce the transformer turns ratio.

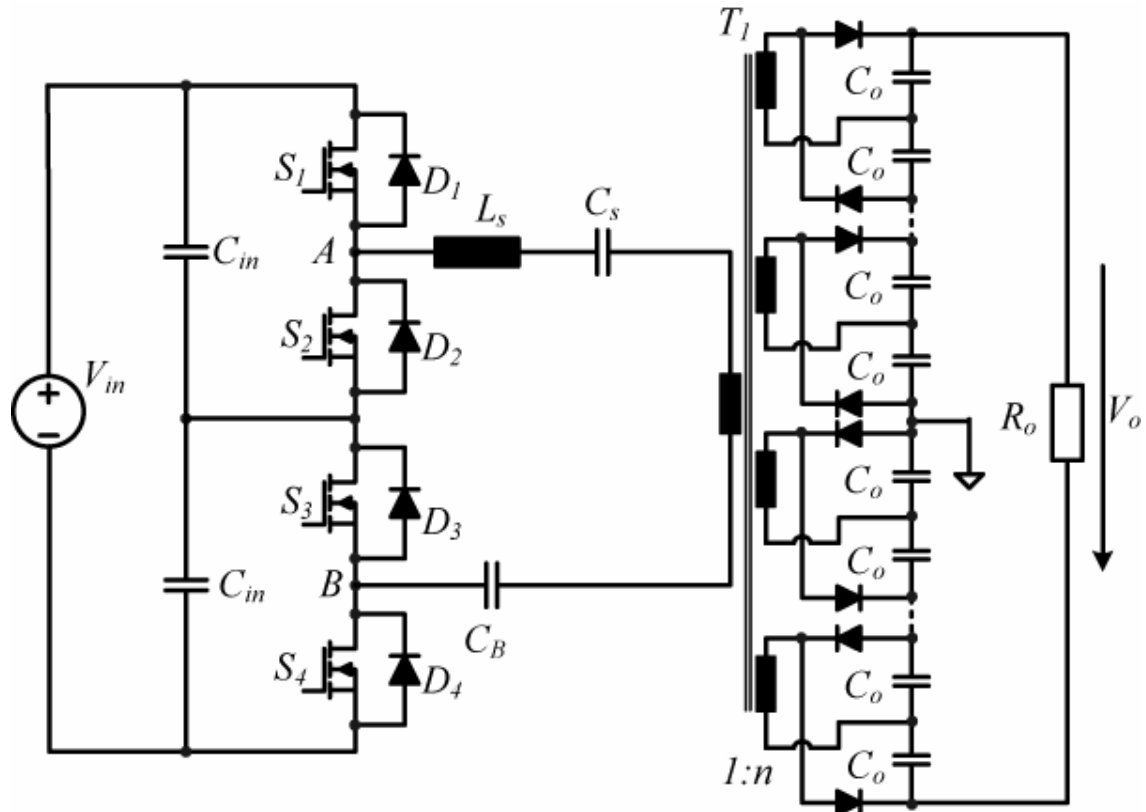


Fig. 1.22: Series resonant multilevel converter.

Typical waveforms of voltage v_{AB} and of the resonant current of the series resonant multilevel converter are shown in Fig. 1.23.

The series resonant multilevel converter is operated with pulse density modulation (PDM) at fixed switching frequency and above resonance that allows zero voltage switching. Using pulse density modulation, the output voltage is controlled by combining the powering stages and free wheeling stages of the converter. This is possible by changing the pulse density of voltage v_{AB} . That means, one defines a PDM pattern with “0” or “1”, where “0” corresponds to the absence of a v_{AB} pulse and “1” corresponds to the occurrence of a v_{AB} pulse. One advantage of this type of modulation is that the PDM control allows obtaining a linear input to output voltage transfer characteristic. Therefore, a simple controller design is possible [KC94].

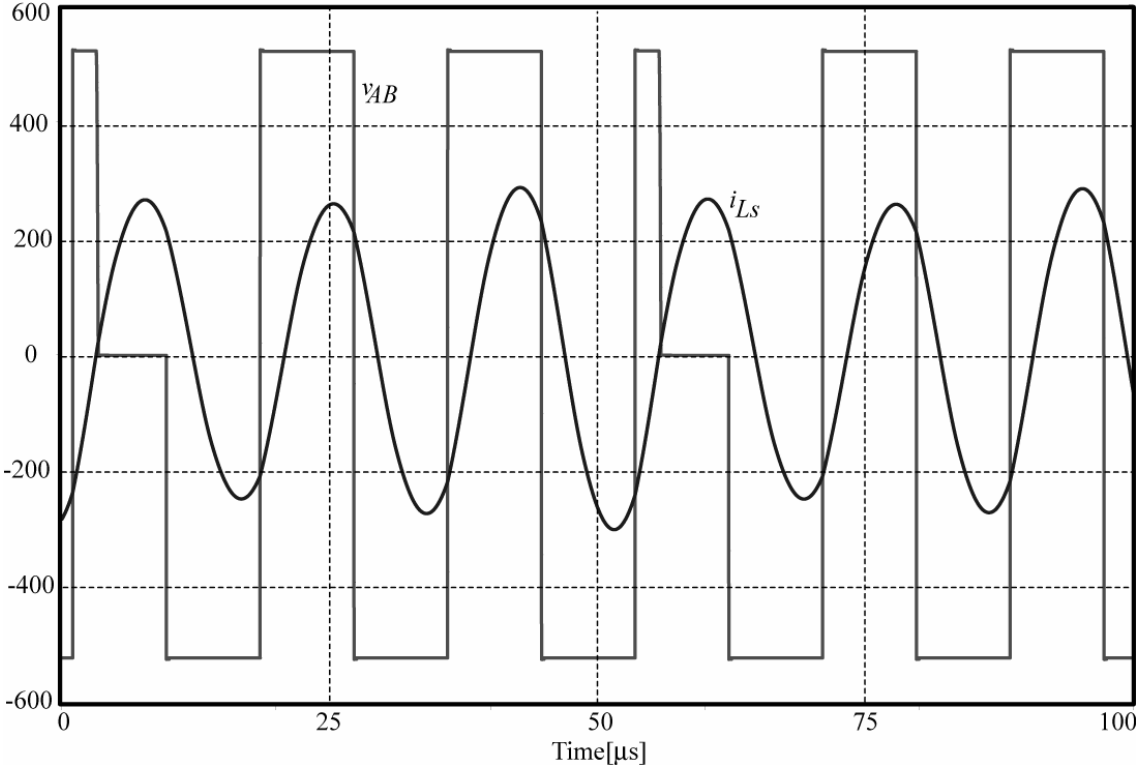


Fig. 1.23: Typical waveforms of the multilevel converter with PDM modulation.

1.3. THESIS MOTIVATION AND OBJECTIVES

The primary motivation of this thesis is the design of the next generation of high-voltage generators for medical x-ray imaging. This design includes some challenging tasks, namely: choice of a proper topology, design of the power circuit, steady-state and dynamic model of the converter and control design. The high-voltage generator should work at very high switching frequency in order to reduce volume and weight of the x-ray power generator.

If one examines the three converter types that have been used as x-ray generators so far, the maximum switching frequency in use is 100 kHz. This is a relatively low frequency and if one would be able to increase the switching frequency, the volume of the converter would be significantly reduced. In the past, increasing the switching frequency was problematic because power switching devices, which should have the capability to switch high current at very high frequency with low losses, have not been available. IGBTs would have high switching losses caused by the large current tail and MOSFETs would have high conduction losses due to the high drain-source on-state resistance. Nowadays, with the new technology of power MOSFETs called CoolMOS™, it is possible to switch the power devices at very high frequency with low losses. This is due to the fact that CoolMOS™ virtually combines the low switching losses of a MOSFET with the low on-state losses of an IGBT [LDK⁺99]. Thus, the utilization of CoolMOS™ power devices associated with the advantages of resonant topologies, which reduce or eliminate the switching losses, should allow the increase of the switching frequency of the converter.

The maximum switching frequency of the converter proposed in this thesis should be five times higher than the maximum switching frequency of state of the art converters. That means the converter works at very high switching frequency up to 500 kHz in order to reduce volume and weight of the x-ray power generator.

1.3.1. Selection of the Converter Topology

The basic structure of resonant converter selected to implement the medical x-ray imaging system proposed in this thesis is the LCC series-

parallel resonant converter shown in **Fig. 1.18** operating above resonance with phase-shifted PWM control and variable switching frequency. The selection of the converter is explained in details in the following.

There are a large number of resonant converter configurations with two, three, four or more resonant elements. The behavior of converters with more than three resonant elements is described by very complex equations such that their steady analysis becomes more involved. In addition the increase in the performance is very small compared with the increase in the complexity of the system. Therefore, the three major candidate converters are: series resonant converter (two resonant elements), parallel resonant converter (two resonant elements) and series-parallel resonant converter (three resonant elements) [Bha91]. The advantages and drawbacks of the series, parallel and series-parallel resonant converter have been explained in details in Section 1.2.2.

The series resonant converter lacks from the main disadvantage of difficulty in regulating the output voltage at light or no load operation. This is a significant weak point because the x-ray generator is requested to operate also at no load. This problem can be solved by adding extra switches to the circuit [VSS96] but this increases complexity and costs of the converter. Additionally due to the large winding capacitance of the high-voltage transformer, resulting from the high number of secondary turns, necessary to produce the high-voltage for the x-ray tube, it is impossible to obtain an ideal series resonant converter. The parallel resonant converter has the main disadvantage that the device currents do not decrease with the load resulting in reduced efficiency for decreasing load. The series-parallel resonant converter has the desirable characteristics of the series and the parallel resonant converters: Short-circuit and no load regulation are possible and high efficiency is achieved with a good selection of the resonant parameters [Bha91]. These are enough reasons to select the series-parallel resonant converter for the current design.

The operation above resonance has been preferred because it offers better possibility to reduce the size of the magnetic components, mainly the high-voltage transformer compared with operation below resonance. This is due to the fact that full load operation occurs at minimum switching

frequency. The maximum switching frequency chosen by the designer could be theoretically unlimited. However, in practice, one has to limit the maximum switching frequency in order to restrict the influence of the gate drive and signal electronics delay times on the operating behavior of the converter, and the complexity of the gate drive and control circuits.

The choice of the PWM phase-shifted control is justified because it simplifies the design of gate drivers due to the 50% fixed duty cycle of the power switches. Moreover, applying the optimum commutation strategy proposed by [GRS⁺94b], where the duration of the clamped interval is determined by the resonant current, the reactive power circulation in the bridge legs is minimized, reducing conduction and switching losses.

1.3.2. Main Objectives

Once the topology has been chosen, there are three main steps of the design of the high-voltage generator, which have to be considered. These steps are the main focus of this thesis:

- the design of the resonant tank elements and steady state model;
- the small-signal model that provides the starting point for control oriented analysis;
- the controller design that should be able to meet very restrictive specifications.

The first step is the design of the resonant tank elements in order to define the operating frequency range and to calculate the stresses of the main components. One of the main contributions of this thesis is a straightforward method to design the power circuit of the series-parallel resonant converter with capacitive output filter and optimum commutation based on the RC load model. With the proposed method, one can easily design the resonant tank elements. Additionally, one is able to calculate the voltage and current stresses of the main components of the power circuit, and duty cycle and switching frequency that ensure optimum commutation for each operating point of the converter. In **Chapter 2**, a detailed description of the proposed method is presented.

Resonant DC-DC converters are nonlinear and time varying systems. Since they do not satisfy the small-ripple condition, state space averaging cannot be applied to resonant converters. For this reason, the control

oriented model of resonant converters is not easy to obtain. Regarding the small-signal model of the series-parallel resonant converter, several models for the converter with inductive output filter are presented in the literature. However, the small-signal model of the converter with capacitive output filter is still missing in the literature so that many controllers are designed by trial and error or fuzzy-controllers are used. In order to design a robust controller, the small-signal model for this converter has to be derived. In **Chapter 3** of this thesis, the small-signal model of the series-parallel resonant DC-DC converter with capacitive output filter model is derived. This model simplifies the controller design task by modeling the converter as a piecewise linear system.

The last but not least challenging task concerning the design of the x-ray generator is the controller design. In order to regulate the output voltage over a wide load range and to meet the very restrictive requirements of rising time and overshoot a robust control should be used. The objective is to implement a digital adaptive controller that covers the whole operating range of the converter. The converter should verify how much current is available to reach a predetermined output voltage. In this manner, the adaptive gains are recalculated for each sampling time such that the controller can impress an accurate output voltage for any operation point. The controller design is shown in **Chapter 4**.

1.4. SUMMARY

This chapter presents a brief overview about x-ray medical diagnosis. It is shown how x-rays are generated and x-ray images are produced and the structure of an x-ray tube. Furthermore, the special case of mammography is briefly described and the block diagram of an x-ray generator is presented. The knowledge of the operation of an x-ray generator is very important for the designer in order to select a proper topology that fulfills all the requirements of medical imaging application.

A brief overview about resonant converters is shown in order to allow a better understanding of the choice of the converter topology for the realization of the x-ray power generator.

State of the art converters for x-ray imaging are presented and the need of further development towards designing the next generation of

medical x-ray generators with high efficiency and high power density is explained. The selected configuration for the design of the x-ray generator is the series-parallel resonant converter operating above resonance. This converter takes advantage of the best characteristics of the series and the parallel converter and the operation above resonance improves even more the performance of the system. The design of the resonant components for the selected configuration will be shown in the next chapter.

Finally, the objectives of this thesis are presented. They are, namely, to propose: a straightforward procedure for designing the converter, a small-signal model of the converter and an adaptive controller that complies with the strict requirements of this application.

CHAPTER 2

2. STEADY-STATE ANALYSIS OF THE SERIES-PARALLEL RESONANT CONVERTER

2.1. INTRODUCTION

The operation of high output voltage DC-DC converters is considerably affected by transformer non-idealities being caused by the large transformer turns ratio and/or large number of secondary turns. The large number of secondary turns is necessary to step up the voltage and as a consequence the secondary winding capacitance of the transformer is increased. Besides, the leakage inductance between the windings of a high-voltage transformer is difficult to minimize, because due to isolation requirements the windings cannot be kept very close together. Both parasitic elements, the leakage inductance and the secondary winding capacitance do take considerable influence on a conventional converter behavior and potentially reduce efficiency and reliability [EJW88]. Therefore, converter topologies suitable for high-voltage applications should integrate the parasitics of the transformer into the circuit operation. Accordingly, resonant converters are frequently employed for the realization of high output voltage DC-DC converter systems because they can make use of the leakage inductance and of the secondary winding capacitance as resonant tank elements. Furthermore, a series-parallel resonant converter is preferred because it has the attractive characteristics of the series and the parallel resonant converters while minimizing or eliminating their drawbacks [EJW88], [Ste88]. However, the design of resonant converters is involved due to the large number of operating states occurring within a pulse period.

This chapter presents a straightforward procedure for designing a full-bridge high output voltage series-parallel resonant DC-DC converter for x-ray imaging diagnosis. The approach is based on an extension of the

first harmonic analysis proposed in [IKBY97]. There, the converter output power is controlled by frequency variation at fixed duty-cycle. In contrast, in the case at hand the output power is controlled by duty-cycle variation while the operating frequency is automatically adjusted for ensuring the commutation of one bridge leg at zero current. As the second bridge leg due to operation above the resonance frequency commutates at zero voltage, soft-switching is preserved in the entire operating range.

In the following, the converter power circuit will be described and subsequently an analytical description of the operating behavior will be given based on the first harmonic concept [IKBY97]. Furthermore, the stresses on the main power components as determined by a numerical solution of the nonlinear implicit analytical system description will be shown in graphical form. In addition, simulation results of a 5kW, 23-62.5kV output converter operating at 260 kHz at full load and 500 kHz at low load will be given, which fully verify the theoretical considerations. Finally, a control concept guaranteeing low no-load losses and operation above resonance also in case of highly dynamic load changes will be described.

The contents of this chapter have been published by the author in short form in the Proceedings of the 34th IEEE Power Electronics Specialists Conference (PESC'03) under the title *Design of a 5kW High Output Voltage Series-Parallel Resonant DC-DC Converter* (cf. [CK03]).

2.2. CIRCUIT DESCRIPTION

The topology of the 5kW series-parallel resonant full-bridge DC-DC converter with impressed output voltage operating above resonance is shown in **Fig. 2.1**.

The (parasitic) capacitors C_1 , C_3 serve for zero-voltage switching of power transistors S_1 and S_3 , the resonant inductor L_s is formed by the transformer stray inductance in combination with an auxiliary inductor connected in series. The parallel resonant capacitor C_p is formed by the parasitic capacitance of the high-voltage transformer T_1 secondary winding. As free-wheeling diodes D_1 , D_2 , D_3 , D_4 , the intrinsic diodes of the power MOSFETs are employed.

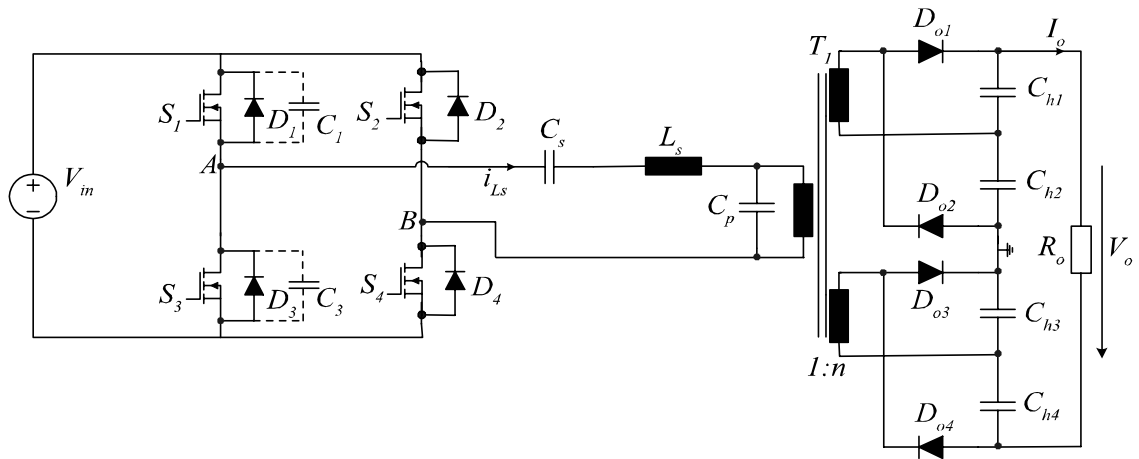


Fig. 2.1: Structure of the power circuit of a series-parallel resonant DC/DC converter with impressed output voltage; C_p denotes the equivalent capacitance of the secondary winding referred to the primary.

As will be shown in detail in section 2.3 the bridge leg S_1, S_3 is operating under zero voltage switching (ZVS) condition, and the bridge leg S_2, S_4 is commutating at zero current (ZCS). Due to ZCS, it should be possible to realize the bridge leg S_2, S_4 with IGBTs. The (parasitic) capacitors of the switches S_2, S_4 are not shown because they are not relevant for the commutation of these switches.

If one compares the structure of the series-parallel resonant converter in **Fig. 2.1** with its basic structure shown in **Fig. 1.18** (Chapter 1), one can see two main differences: the transformer has two secondary windings and, at the output, a voltage doubler circuit is used instead of a full bridge rectifier. Both modifications serve to reduce the transformer turns ratio and consequently reduce the influence of the parasitics of the transformer. Additionally, reduction of the transformer turns ratio allows reduction of the size of the transformer because due to the lower secondary voltages the isolation distances can be reduced.

The equivalent circuit of the series-parallel resonant converter is depicted in **Fig. 2.2** where the output quantities are referred to the transformer primary side. There, $V_o' = V_o/2n$, $I_o' = I_o \cdot 2n$ and $R_o' = R_o/4n^2$ where n is the transformer turns ratio.

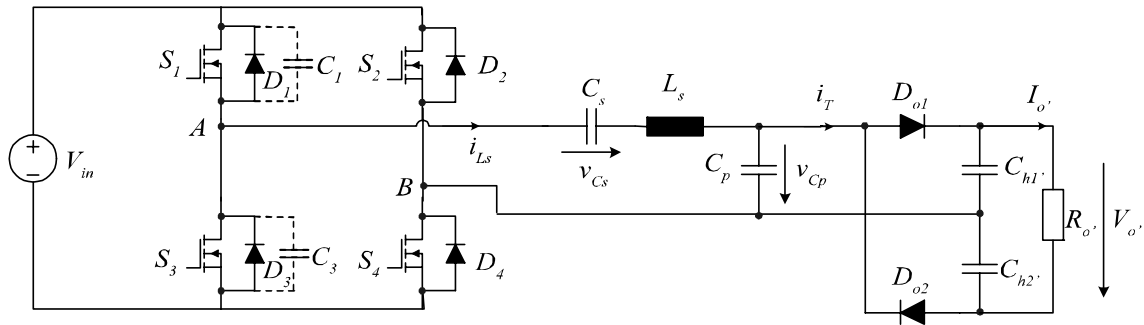


Fig. 2.2: Equivalent circuit of the converter circuit shown in Fig.2.1 for referring the output quantities to the transformer primary side. For the actual system, the rectifier circuits connected in series on the secondary side are supplied in parallel by the primary winding.

2.3. THEORETICAL ANALYSIS

The voltage transfer ratio of a series-parallel resonant converter in dependency on the load and on the normalized switching frequency is depicted in **Fig. 2.3**.

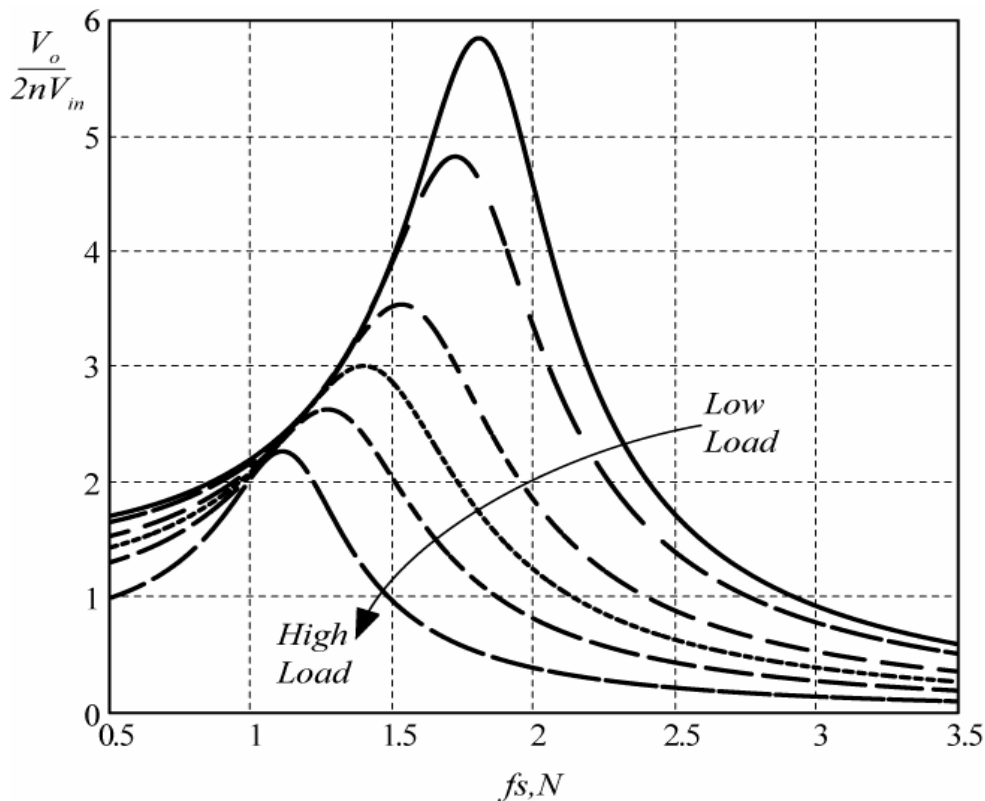


Fig. 2.3: Voltage transfer ratio of a series-parallel resonant converter in dependency on the load and on the normalized switching frequency $f_{s,N} = f_s/f_o$ (normalization with reference to the series resonant frequency $f_o = (2\pi\sqrt{L_s C_s})^{-1}$); n denotes the transformer turns ratio.

As already explained in **Chapter 1**, the converter behaves as a series resonant converter at high load and as a parallel resonant converter at low load [DRS00]. This occurs because for high output power the parasitic winding capacitance in a first approximation can be assumed as being short-circuited by the equivalent load resistance [Ste88], accordingly the system shows the characteristic of a series resonant converter.

In the following, operation of the series-parallel resonant converter above resonance with variable frequency and phase-shift control is assumed.

2.3.1. Commutation Zones for Variable Frequency Phase-Shift Control

Depending on the duty cycle, the operation frequency and the output load, the series-parallel resonant converter can operate in three different commutation modes: natural, forced and mixed.

A. Natural Commutation Mode

In the natural commutation mode, the switches turn on with the current of the anti-parallel diode of the opposite power transistor of a bridge leg (t_0 , t_2) as shown in **Fig. 2.4**. The turn on process has high switching losses if slow reverse recovery diodes are used because the diodes are forced to turn-off due to the inverse voltage applied by the transistors. Therefore, this mode has the drawbacks of large current spikes during the diode turn-off process, and the need of fast-recovery diodes [ABL⁺95], [ABL⁺98], [ARB⁺95].

However, the switches present zero-current switching (ZCS) in the turn off process (t_1 , t_3). That means, they turn off when the current changes its sign and begins to flow through their anti-parallel diodes [ABL⁺98].

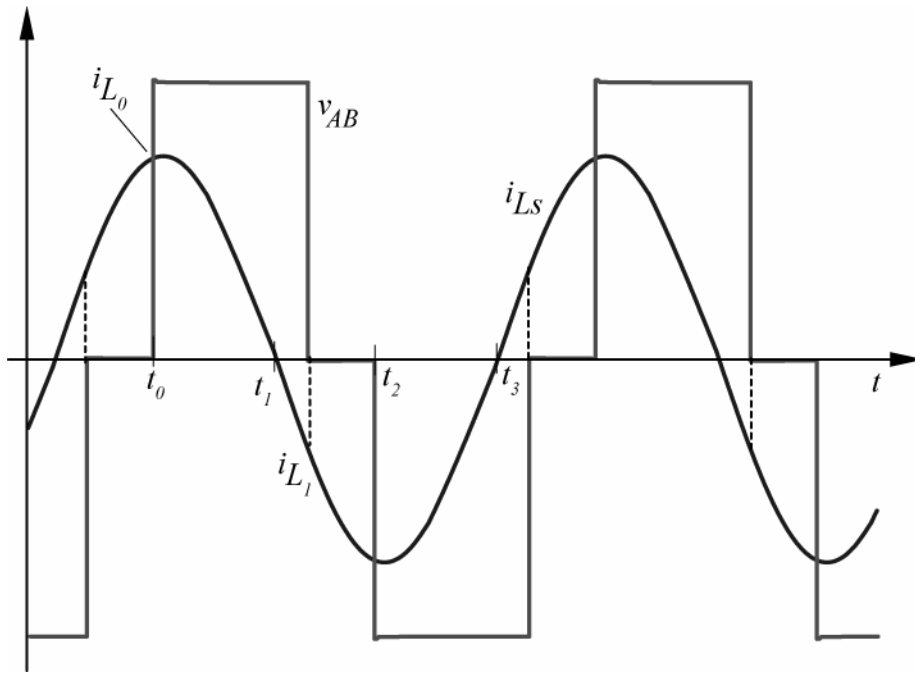


Fig. 2.4: Voltage v_{AB} and resonant current for natural commutation mode.

B. Forced Commutation Mode

In the forced commutation mode, the four transistors operate with zero-voltage switching (ZVS). They turn on when their anti-parallel diodes are in conduction mode (t_0, t_2) and turn off with current (t_1, t_3) as shown in **Fig. 2.5**. Therefore, losses are generated in the turn-off process.

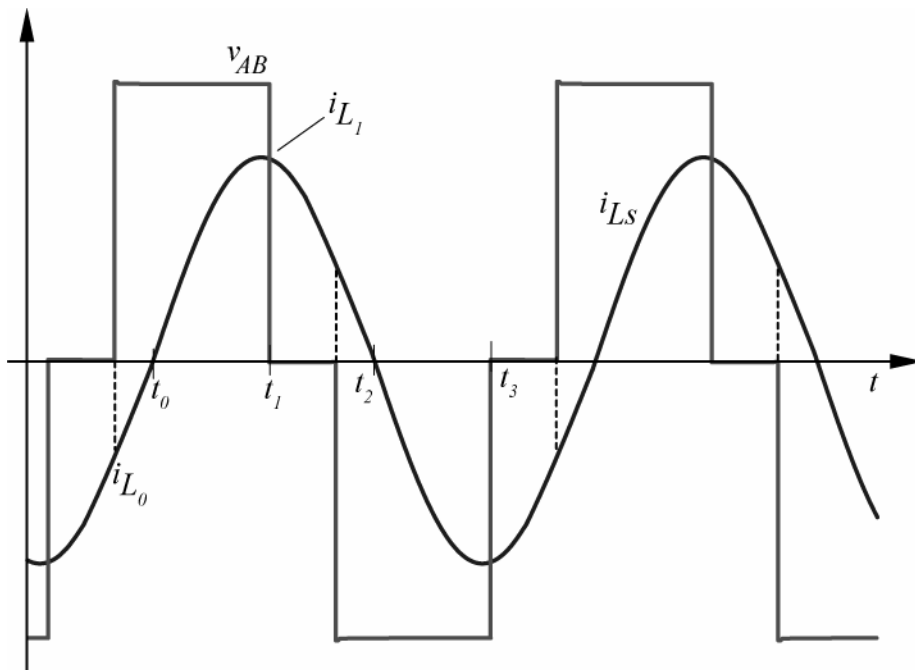


Fig. 2.5: Voltage v_{AB} and resonant current for the LCC resonant converter with forced commutation.

In this mode, it is possible to use capacitors as lossless snubbers in order to reduce the turn-off losses. Another advantage of this operation mode is that the anti-parallel diodes turn off naturally when the resonant current reaches zero and they have all the transistor conduction intervals to pass toward the off state. This means that slow-recovery diodes may be used. Thus, this mode presents some characteristics that make the MOSFET a good switch to be used [ABL⁺95], [ABL⁺98], [ARB⁺95].

C. Mixed Commutation Mode

In the mixed commutation mode, one of the legs (S_1, S_3) presents ZVS in the turn on process (t_0, t_3), and the other leg (S_2, S_4) operates with ZCS in the turn off process (t_0, t_3). The characteristics from the ZVS and ZCS commutations are the same as for forced and natural commutations, respectively. The main waveforms of the circuit when operated in mixed commutation mode are shown in **Fig. 2.6**.

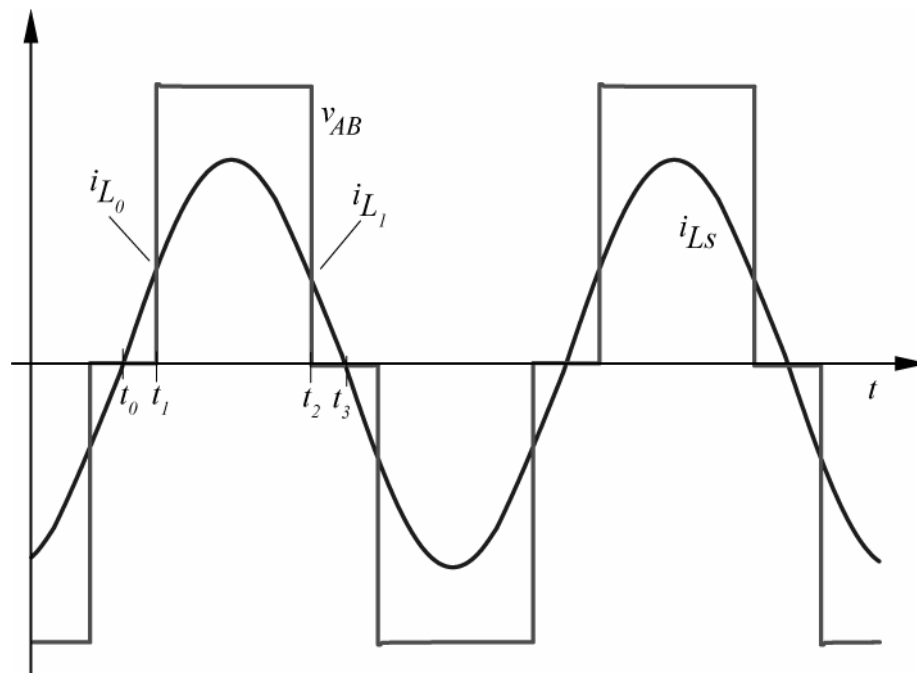


Fig. 2.6: Voltage v_{AB} and resonant current for mixed commutation mode.

This mode has the advantage that the energy is always delivered to the tank circuit and to the load at steady-state operation. Thus, the reactive energy handled by the inverter is reduced and in the ideal case, is equal to zero. Therefore, operation in the mixed mode will be preferred since the conduction losses are minimized. In contrast, in forced and natural commutation modes, there are intervals in which the energy flows from the

input DC voltage source to the resonant tank and intervals in which the energy is returned from the resonant tank to the input DC voltage source. This means that the inverter is handling some reactive energy and the conduction losses increase.

The boundary between mixed and forced commutation modes is considered an optimum commutation boundary because this operation point because combines the advantages of mixed and forced commutation. The voltage v_{AB} and the resonant current waveforms operating with optimum commutations are shown in **Fig. 2.7**.

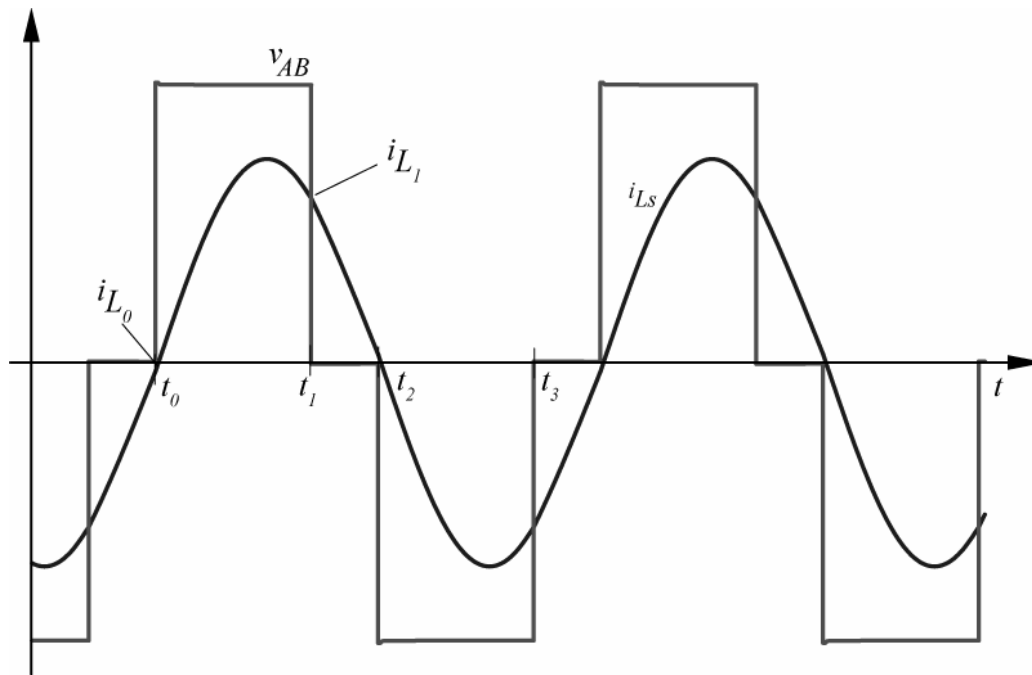


Fig. 2.7: Voltage v_{AB} and resonant current for optimum commutation boundary.

At this operating point, the transistors S_2 and S_4 turn on and off with zero current (t_0 , t_2), and thus without switching losses. Anti-parallel diodes D_2 and D_4 never conduct and theoretically it would not be necessary to implement them in the bridge. However, in practical implementation the commutation cannot be triggered exactly at zero current and a dead-time between both switches is necessary. Thus, D_2 and D_4 have to be implemented but they conduct only during a very short time.

The switches S_1 and S_3 turn on with zero-voltage switching and turn off with losses (t_1 , t_3) because they have to switch current. But the parasitic capacitance of the MOSFETs can be used as lossless snubbers in order to reduce the losses. Diodes D_1 and D_3 can be implemented with slow diodes

because no direct current commutation from a free-wheeling diode to a power transistor does occur. For this reason, the (intrinsic) anti-parallel diodes of the power MOSFETs which are characterized by a relatively slow reverse recovery behavior can be employed as free-wheeling diodes [Ste88]. Thus, at this operating point there are only switching losses due to the S_1 and S_3 turn-off process, and since it also belongs to the mixed mode the conduction losses are minimized [ABL⁺95], [ABL⁺98], [ARB⁺95].

For the reasons presented before, the analysis of the converter will be based on the operation with optimum commutation.

2.3.2. Converter Conduction States

For simplifying the analysis of the converter stationary operating behavior, in the following all components are considered ideal and the voltage V_{in} is assumed to show a constant value. Furthermore, the switching frequency ripple of the output voltage is neglected and the load is modeled by an equivalent resistor.

The conduction states of the converter occurring within the first half switching period are compiled in **Fig. 2.9** with reference to **Fig. 2.10**.

First State ($t_0 - t_1$): This state begins at t_0 when the resonant current i_{Ls} crosses zero. Switch S_2 turns off just before the resonant current crosses zero. The turn off has been synchronized with a threshold level $-V_{th}$ determined by the designer. After a short dead time, S_4 turns on exactly when i_{Ls} crosses zero. In the previous stage, S_1 was turned on under ZVS when its anti-parallel diode was conducting, accordingly in this state S_1 and S_4 conduct the resonant current. The voltage v_{AB} is positive, the resonant current is positive sinusoid and the output rectifier is turned off as v_{Cp} decreases cosinusoidally from $-V_o/4n$ to zero and continues to increase to positive values. The state ends when v_{Cp} reaches $+V_o/4n$ and the output rectifier starts to conduct again.

Second State ($t_1 - t_2$): In t_1 the resonant current still flows through S_1 and S_4 . The voltage v_{Cp} is clamped to $+V_o/4n$ and v_{AB} is still positive.

Third State ($t_2 - t_3$): At the beginning of this state S_1 is turned off, accordingly i_{Ls} is directed to the capacitors C_1 and C_3 and charging C_1 and discharging C_3 . When the voltage across C_3 reaches zero in t_3 the commutation of S_1 to D_3 is completed.

Fourth State ($t_3 - t_4$): At time t_3 , S_4 and D_3 are conducting. S_3 is turned on at zero voltage (ZVS). The resonant current i_{Ls} is positive and the inverter output voltage v_{AB} is zero. Immediately before the i_{Ls} reaches zero, S_4 is turned off in t_4 synchronized with a threshold level V_{th} .

Fifth State ($t_4 - t_5$): This state corresponds to the dead time between switches S_2 and S_4 . As S_4 has been turned off i_{Ls} flows through D_2 and D_3 . Accordingly, one has $v_{AB} = -V_{in} < 0$. When i_{Ls} reaches zero in t_5 , a half switching period is completed.

The steady state trajectory for the series-parallel resonant converter operating at full load is shown in **Fig. 2.8**. The instants shown in the diagram are referred to **Fig. 2.10**. One can see that the shape of the trajectory is almost circular like for a resonant network without switching operations. That means, for the converter analyzed in this thesis, the resonant current i_{Ls} and the voltage across the series resonant capacitor v_{Cs} , which are state variables of the system, have almost a sinusoidal evolution.

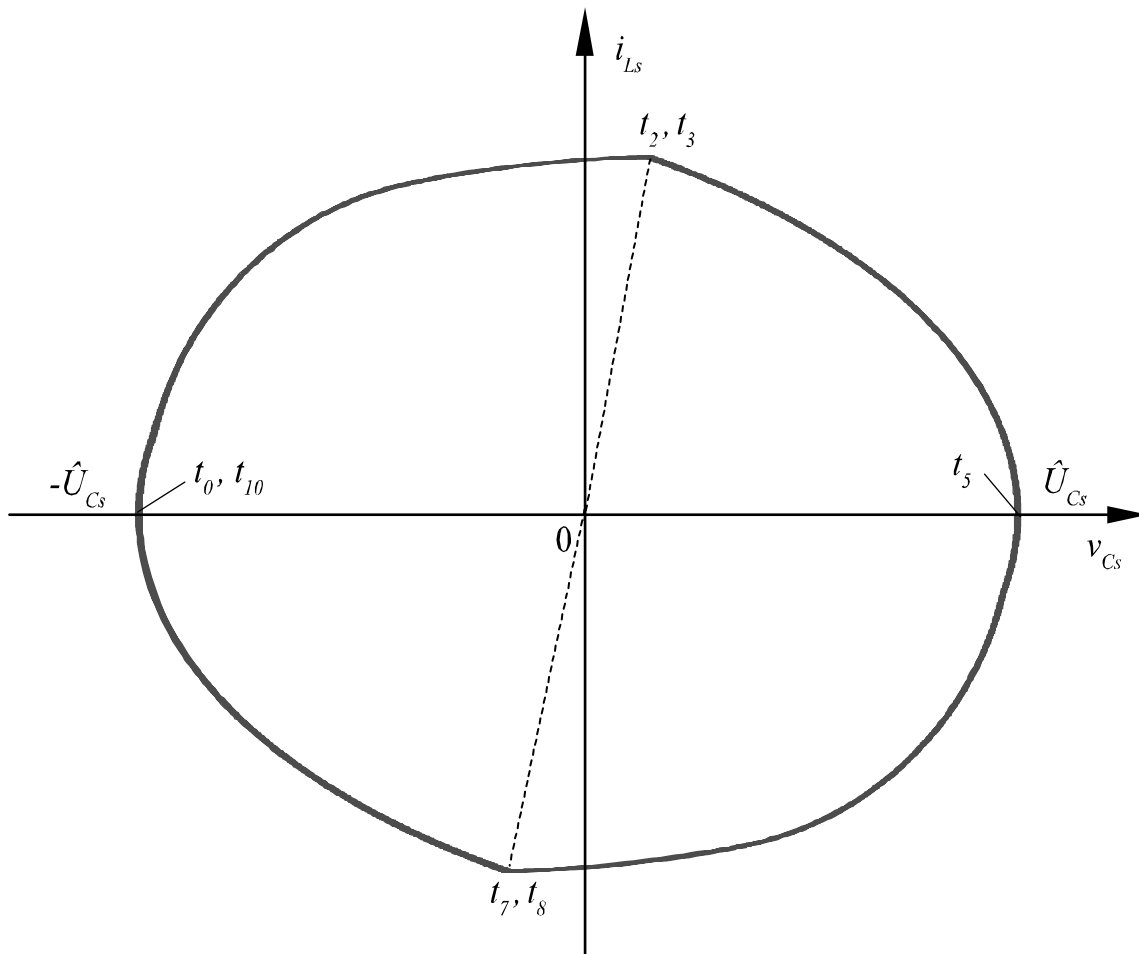


Fig. 2.8: Steady state trajectory of the series-parallel resonant converter for one switching period.

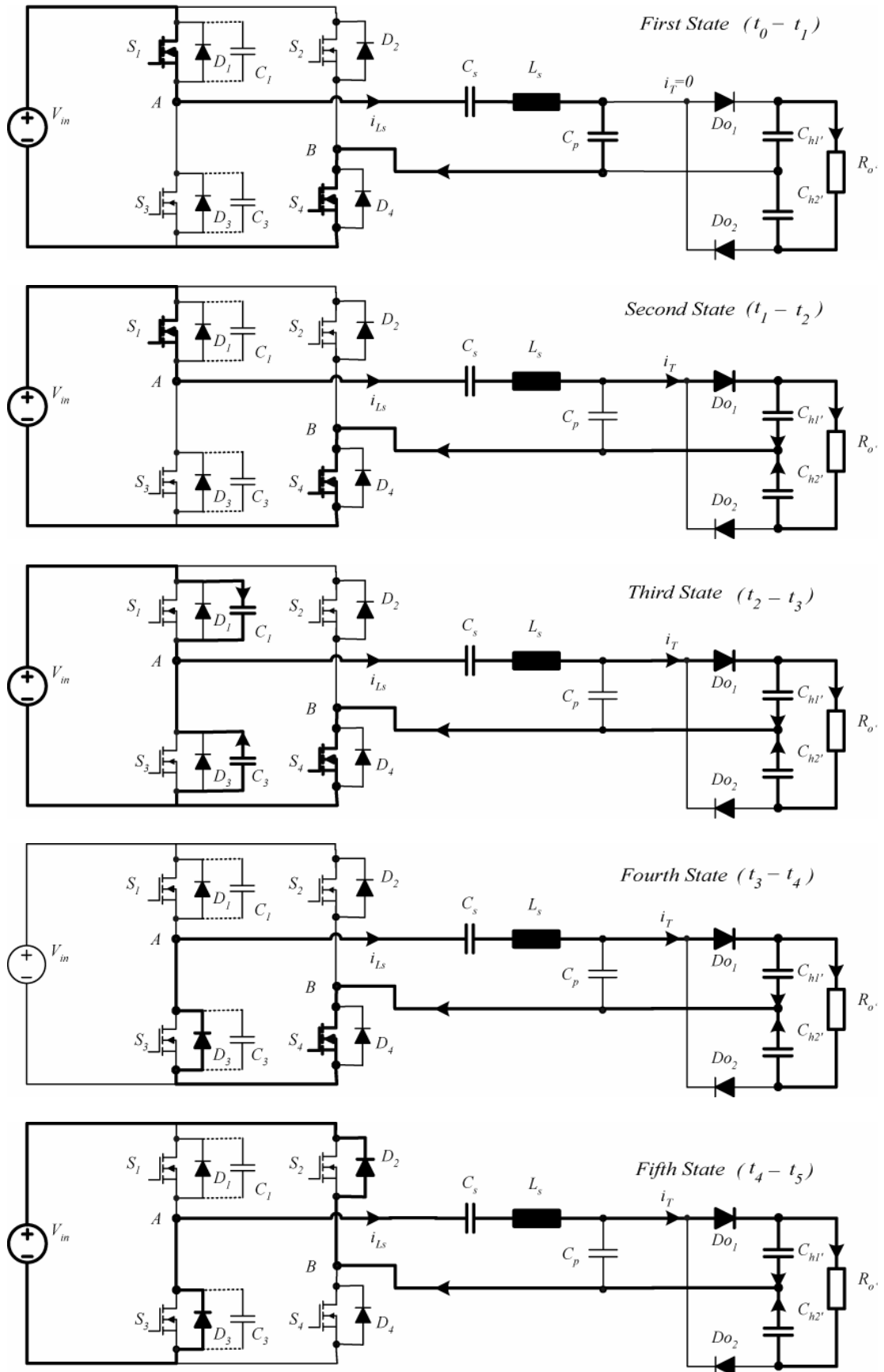


Fig. 2.9: Conduction States of the series-parallel resonant converter within a half pulse period (cf. Fig. 2.10).

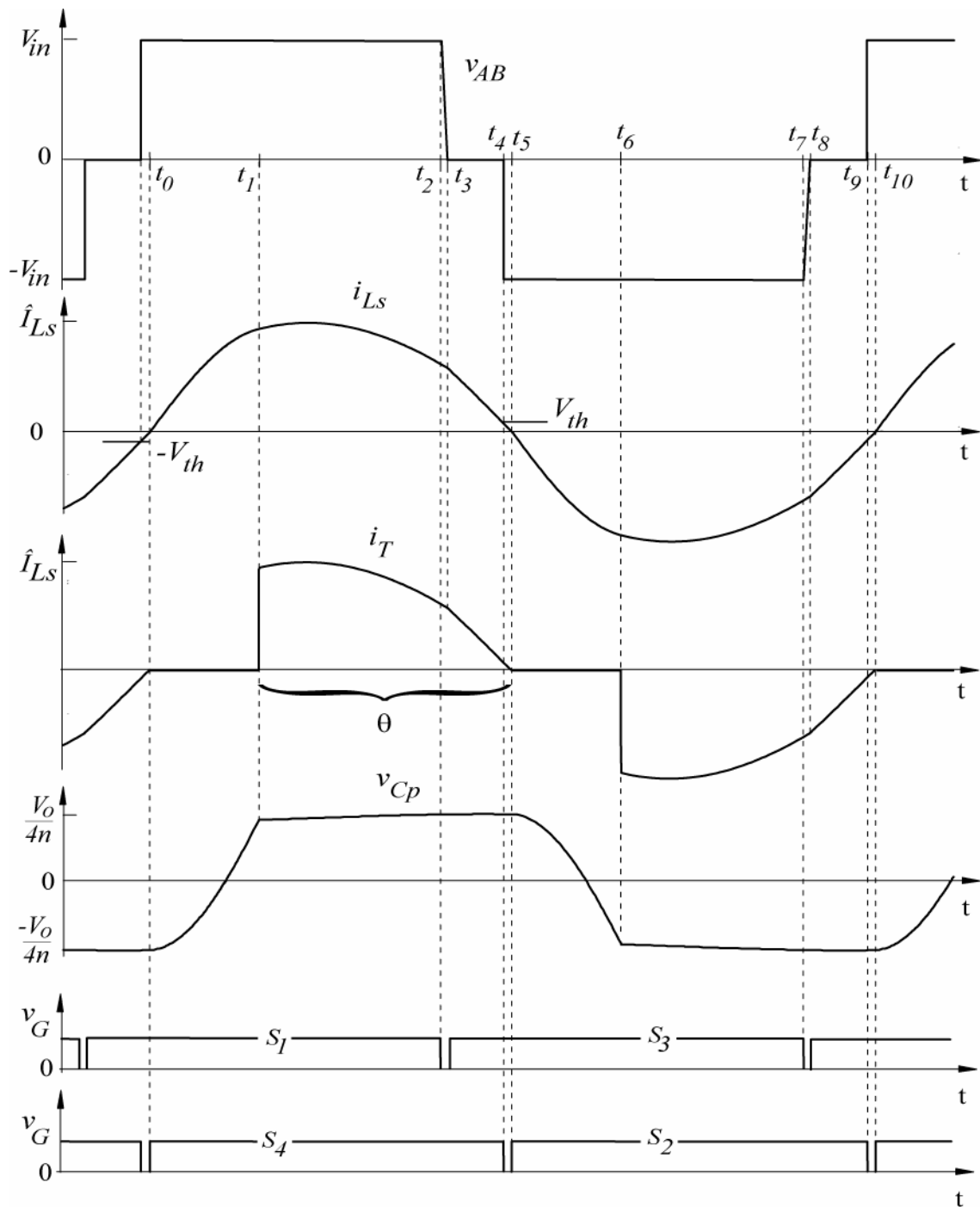


Fig. 2.10: Time behavior of characteristic voltages and currents and of the transistor switching functions (gate drive signals) of a series-parallel resonant converter within a pulse period (t_0 – t_{10}).

The system behavior for the second half switching period is analog to the first half period with replacing S_1 and S_4 by S_3 and S_2 . Therefore, the second half period will not be described, but only the conduction states are shown in **Fig. 2.11**(cf. (t_5 – t_{10})).

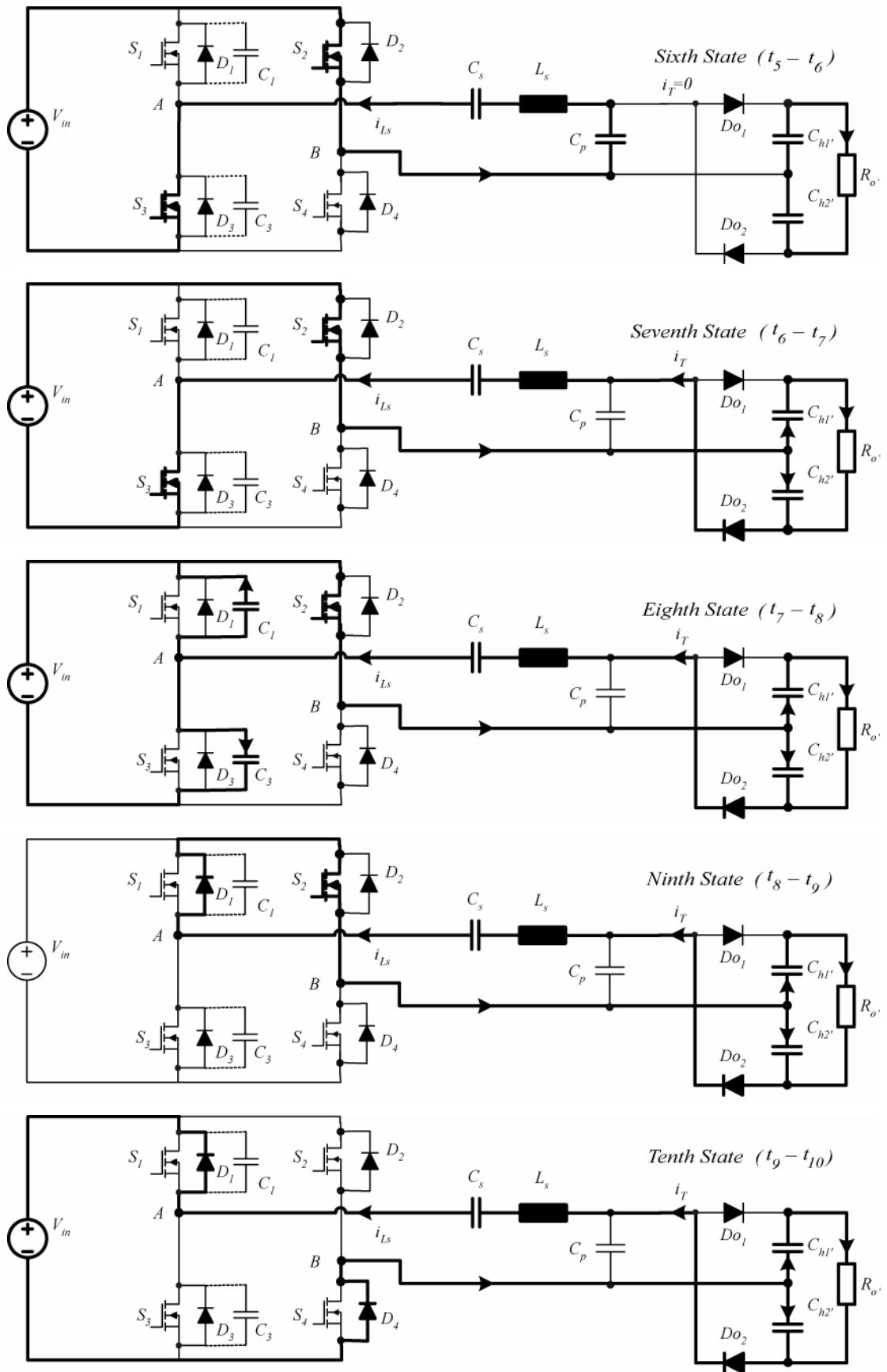


Fig. 2.11: Conduction states of the series-parallel resonant converter within the second half pulse period.

2.3.3. Design Procedure Based on First Harmonic Analysis

If one observes the waveforms of to **Fig. 2.10** one can see that the resonant current i_{L_s} is almost sinusoidal. However, waveforms v_{AB} , i_T and v_{C_p} do not have sinusoidal shape. That means their spectrum have high-order harmonics. For this reason it is important to explain why a design procedure based on the first harmonic analysis produces good results even if the high-order harmonics are not included in the model. The explanation is the following. The active power transferred to the load is dependent on the voltage v_{AB} and the resonant current i_{L_s} . As the resonant current is (almost) sinusoidal, i.e., only has the first harmonic component in its spectrum, the high-order harmonics of v_{AB} will be multiplied by zero when one calculates the instantaneous power. Thus, the high-order harmonics of v_{AB} do not contribute to the power transfer to the load. For this reason, the design procedure based on the first harmonic analysis accurately predicts the power output and stresses on the components.

The simplest model used in the analysis of the series-parallel resonant converter is the AC resistance model proposed by Steigerwald [Ste88]. There, the output rectifier and the load are substituted by an equivalent AC resistance that expresses the effect of the dissipative nature of the load [BYR96] as shown in **Fig. 2.12**.

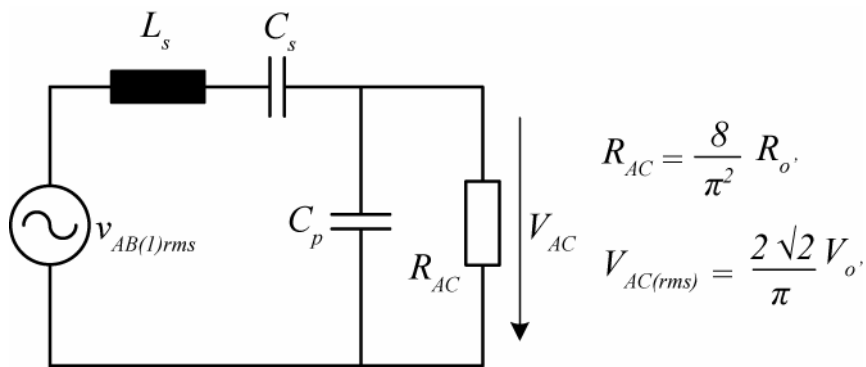


Fig. 2.12: Equivalent AC resistance model [Ste88]. $V_o' = V_o/2n$, and $R_o' = R_o/4n^2$ where n is the transformer turns ratio with reference to **Fig. 2.1**.

This model produces good results for the converter with inductive output filter. However, for the capacitive loaded series-parallel resonant converter, the AC resistance model cannot be successfully applied. This is due to the fact that the input current of the output rectifier flows for only a

part of the switching period. Consequently, the equivalent load cannot be considered as being purely resistive as it will be explained later.

The exact analysis of the series-parallel resonant converter with capacitive output filter is very complex due to the fact that the output rectifier operates in discontinuous current mode [IKBY97]. For this reason, the design procedures proposed in the literature are frequently very involved.

The only simple and efficient method found in the literature for the analysis of the series-parallel resonant converter with capacitive output filter has been proposed by Ivensky et al. in [IKBY97]. There, output rectifier, filter capacitor and load are substituted by an RC load model. The starting point of the model is the assumption that the resonant current is purely sinusoidal. This assumption is reasonable, if one observes the resonant current steady state trajectory in **Fig. 2.8**. Observing the waveforms of the voltage across the parallel capacitor and the input current of the output rectifier and their respective fundamental components shown in **Fig. 2.13**, one can see that the fundamental components are not in phase. The first harmonics of the rectifier input current leads the first harmonics of the voltage across the parallel capacitor (rectifier input voltage) [IKBY97]. Thus, the equivalent load can be approximated by an RC equivalent circuit such as shown in **Fig. 2.14**.

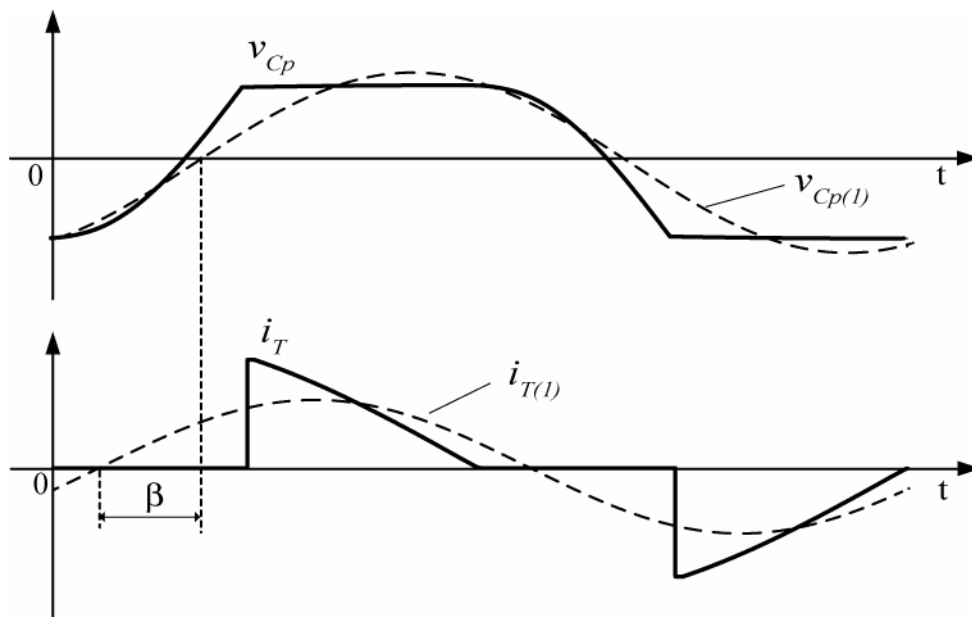


Fig. 2.13: First harmonics approximation of i_T and v_{Cp} .

The coefficient k_v defines the relation between the output voltage V_o referred to the primary and the amplitude of the first harmonics of the voltage across the parallel capacitor C_p . The coefficient k_v will be explained in details later.

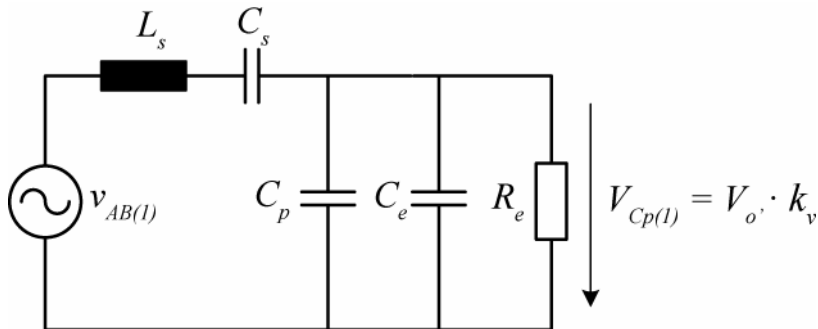


Fig. 2.14: Equivalent RC circuit model according to [IKBY97].

The RC load model proposed in [IKBY97] supplies accurate results for the capacitive loaded series-parallel resonant converter. However, the method covers only the case with constant duty cycle and variable frequency control (PFM). In this thesis phase-shifted-PWM control with optimum commutation is intended to be used. Thus, the RC load model will be extended in order to include the optimum commutation behavior and employed for a straightforward system design and/or for analyzing the influence of parameter variations in the following. There, the main specifications of the converter are assumed as:

- output voltage range $V_o = 23 \dots 62.5 \text{ kV}$;
- output current range $I_o = 0 \dots 200 \text{ mA}$;
- output power range $P_o = 0 \dots 5 \text{ kW}$.

In a first step of the system design, the components of the resonant circuit have to be determined under consideration of limitations caused by maximum admissible stresses on power components or by parasitic component values. In the case at hand

- the converter switching frequency f_s should not exceed 500kHz in order to limit the complexity of the gate drive and control circuits and to have only a limited influence of the gate drive and signal electronics delay times on the operating behavior;
- the maximum voltage stress on the (low capacitance) series capacitor C_s should be lower than 1kV with respect to the

capacitor technology available for high frequency high-current applications;

- the capacitance C_p/n^2 of the parallel resonant capacitor referred to the secondary must be larger than 50pF with respect to the minimum achievable winding capacitance of the high-voltage transformer employed in the case at hand.

The procedure for designing the resonant circuit components is iterative and starts from initial values for C_p , α and n (C_p is the capacitance of the parallel resonant capacitor, $\alpha = C_p/C_s$, n denotes the transformer turns ratio). The choice of C_p and n is correlated via $C_p/n^2 \geq 50\text{pF}$, accordingly any values which satisfy this condition can be taken as starting values. There, one has to consider that the choice of α takes a large influence on the converter operating frequency range. For lower values of α , the frequency range will be wider than for higher values. This means that the choice of α is related to the upper switching frequency limit. As the value of C_p gets lower relative to C_s , the ratio $\alpha = C_p/C_s$ also gets lower and consequently the converter behaves more as a series resonant converter. The series resonant converter, compared with the series-parallel resonant converter, needs at low load higher switching frequency to achieve the same operating point. Thus, for lower values of α , the operating frequency range gets wider. As very high switching frequencies are not desirable due to practical implementation limitations, one has to find a compromise between reducing the circulating current for low loads and having a reasonable limit for the upper switching frequency. Following the procedure described in [IKBY97] and considering the starting values for C_p , α and n and the effect of the output rectifier stage, we have for the rectifier conduction angle θ (cf. **Fig. 2.10**)

$$\theta = 2 \cdot \tan^{-1} \sqrt{\frac{4 \cdot n^2}{f_s \cdot C_p \cdot R_o}}. \quad (2.1)$$

For the sake of clearness, notations of quantities defined in [IKBY97] will be maintained in the following. With reference to [IKBY97] (cf. Eqs. (17), (21) and section V in [IKBY97]) one has

$$k_v = 1 + 0.27 \cdot \sin\left(\frac{\theta}{2}\right) \quad (2.2)$$

$$\beta = -0.4363 \cdot \sin(\theta) \quad (2.3)$$

$$\omega C_p R_e = \frac{k_v^2 \cdot \pi}{4 \cdot \tan\left(\frac{\theta}{2}\right)^2} \quad (2.4)$$

where

k_v – is a coefficient defining the relation between V_o transferred to the primary and the amplitude of the first harmonic of the voltage across the parallel capacitor,

β – denotes the phase displacement of the fundamentals of the voltage across the parallel capacitor and the input current of the output rectifier, and

$\omega C_p R_e$ – is a dimensionless parameter.

For the AC voltage transfer ratio, i.e. for the ratio of the amplitudes of first harmonics of the transformer primary voltage and of the voltage v_{AB} one has (cf. Eq. (34) in [IKBY97])

$$k_{21} = \frac{v_{Cp(1)}}{v_{AB(1)}} = \frac{1}{\sqrt{\left[1 - \alpha \cdot (f_{s,N}^2 - 1) \cdot \left(1 + \frac{\tan(|\beta|)}{\omega C_p R_e}\right)\right]^2 + \left[\alpha \cdot (f_{s,N}^2 - 1) \cdot \frac{1}{\omega C_p R_e}\right]^2}} \quad (2.5)$$

in dependency of θ and of the normalized switching frequency $f_{s,N} = f_s/f_o$ where $f_o = (2\pi\sqrt{L_s C_s})^{-1}$ is the series resonant frequency.

The time behavior of characteristic waveforms as assumed for the analysis in [IKBY97] is depicted in **Fig. 2.15(a)**. In the case at hand (cf. **Fig. 2.15(b)**) we have for the amplitude of the first harmonic of the converter output voltage v_{AB}

$$V_{AB(1)} = \frac{4}{\pi} \cdot V_{in} \cdot \cos(\phi). \quad (2.6)$$

Furthermore, according to **Fig. 2.15(b)** the phase displacement ϕ of the first harmonic $v_{AB(1)}$ of the converter output voltage v_{AB} and of the first harmonic $i_{Ls(1)}$ of the inverter output current and/or resonant circuit input current i_{Ls} is

$$\phi = \frac{\pi}{2} - \frac{D \cdot \pi}{2} \quad (2.7)$$

where $D = \gamma/\pi$ denotes the converter output voltage duty cycle.

Considering (2.7) and (2.6) we obtain

$$V_{AB(1)} = \frac{4}{\pi} \cdot V_{in} \cdot \sin\left(\frac{D \cdot \pi}{2}\right). \quad (2.8)$$

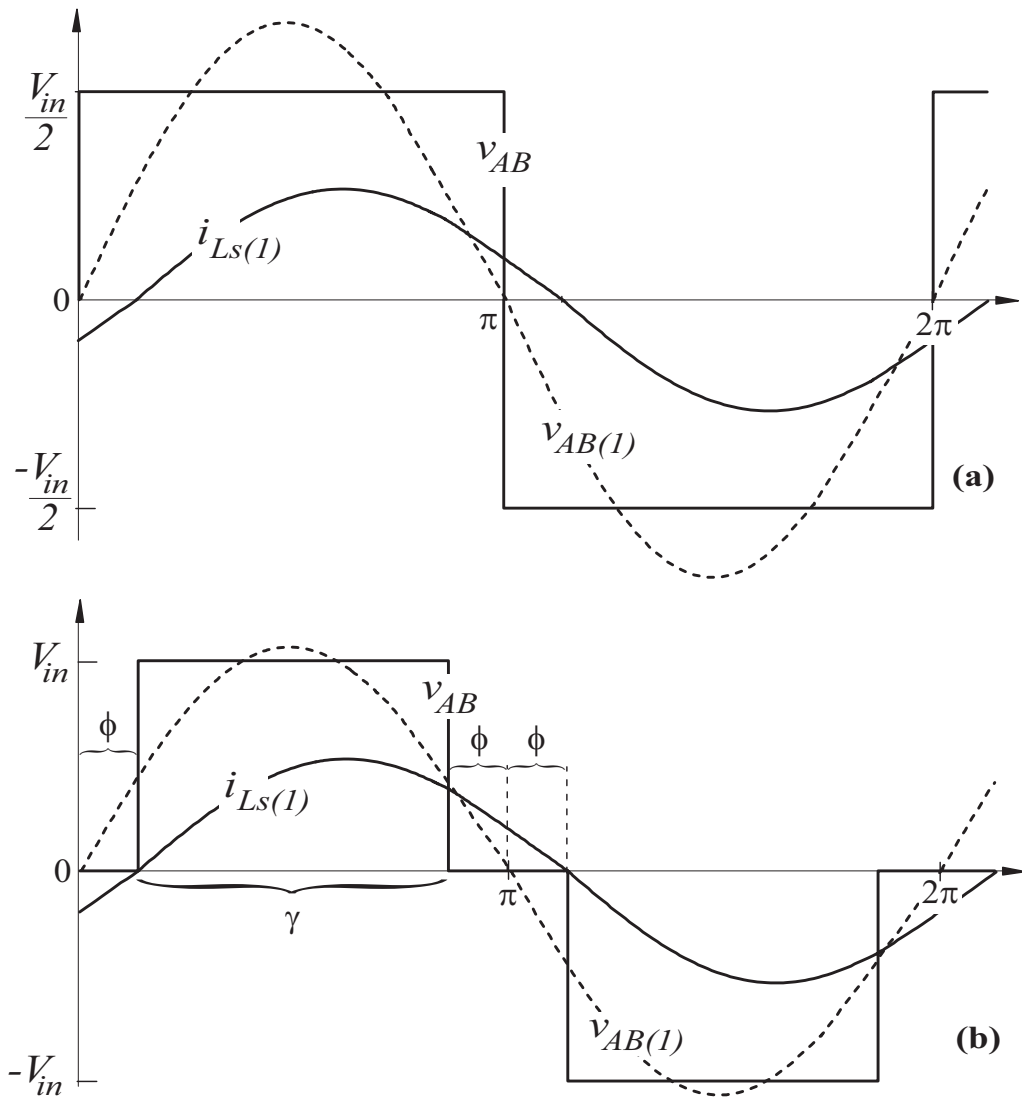


Fig. 2.15: Time behavior of the actual converter output voltage, of the output voltage fundamental (shown dashed) and of the resonant current fundamental as considered for the first harmonic analysis in [IKBY97] (cf. (a)) and in this work (cf. (b)), one the bridge leg is switching at the zero crossing of the resonant current, i.e. at $i_{Ls}=0$ (ZCS).

With the relation for the input phase angle $\phi(I)$ given in [IKBY97] (cf. Eq.(39) in [IKBY97]), and considering $\phi(I) = \phi$, the duty cycle D can

be represented as a function of the normalized switching frequency $f_{s,N}$ and of the rectifier conduction angle θ

$$D = 1 - \frac{2}{\pi} \cdot \tan^{-1} \left(\frac{1}{\omega C_p R_e} \cdot \alpha \cdot \{f_{s,N}^2 \cdot [1 + (\omega C_p R_e + \tan(|\beta|)^2)] - 1\} \right) - [\omega C_p R_e + \tan(|\beta|)] \cdot \left[1 + \alpha \cdot \left(1 + \frac{\tan(|\beta|)}{\omega C_p R_e} \right) \right] \quad (2.9)$$

Finally, also the output voltage can be given as function of $f_{s,N}$ and θ resulting in the voltage transfer characteristic

$$V_o = \frac{16}{\pi} \cdot \frac{k_{21}}{k_v} \cdot n \cdot V_{in} \cdot \sin\left(D \cdot \frac{\pi}{2}\right) \quad (2.10)$$

which is depicted in **Fig. 2.16** for the specifications given in section 2.4 as a function of $f_{s,N}$ and θ .

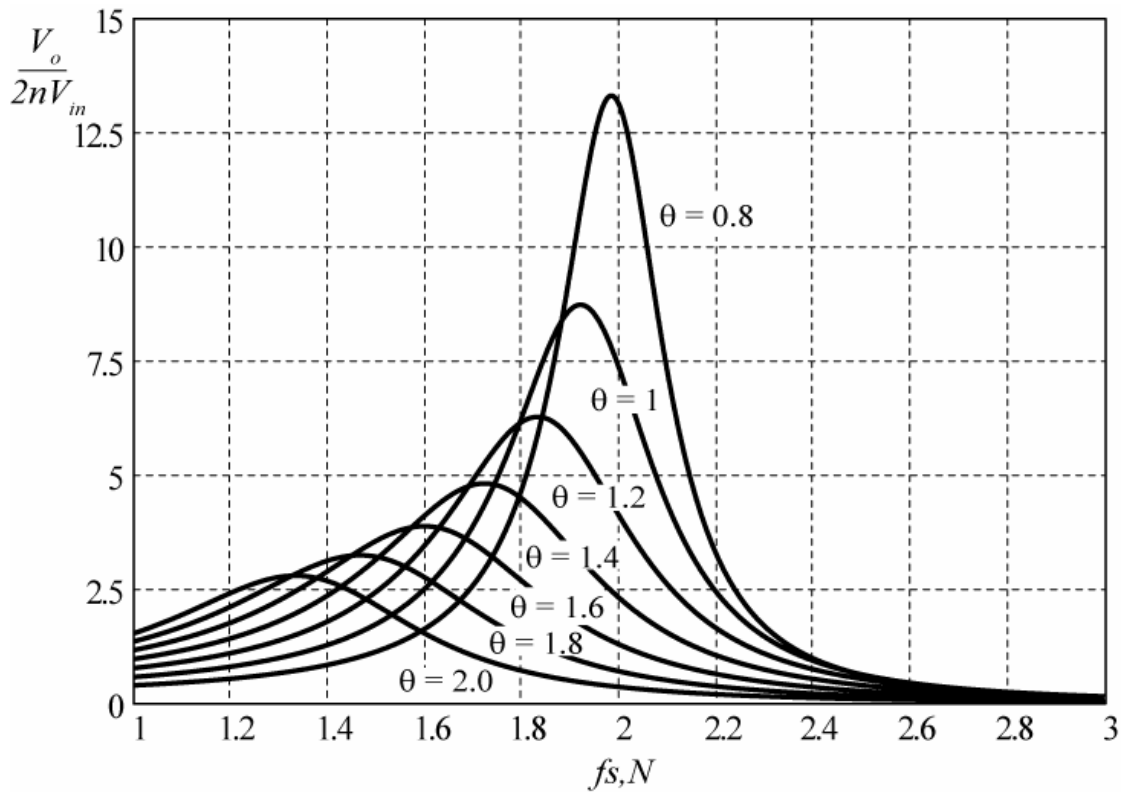


Fig. 2.16: Voltage transfer characteristic of the series-parallel resonant converter in dependency of the normalized switching frequency and the rectifier conduction angle θ .

With decreasing load and/or decreasing output rectifier conduction angle θ , the peak of the resonant characteristic shown in **Fig. 2.16** moves to higher frequencies. The converter operating (switching) frequency, which has to be adjusted accordingly in order to ensure operation above resonance

therefore, shows a pronounced dependency on the load condition. The converter control scheme will be described in detail in section 0.

Now, based on the characteristics shown in **Fig. 2.16**, with the starting values $C_p = 15\text{nF}$, $n = 17$ and $\alpha = 0.3$, the resonant components can be specified. The starting value for n can be derived with reference to **Fig. 2.3** by assuming high output power where the DC gain $V_o/(2nV_{in})$ approaches 2.25; for the given operating conditions ($V_{in}=325\text{V}$, $V_o=25\text{kV}$) this results in $n \approx 17$. As already said, the choice of C_p and n is correlated via $C_p \geq 50\text{pF}$, accordingly any values which satisfy this condition can be taken as starting values. Taking the minimum value $C_p = 50\text{pF} \cdot n^2$, and the starting value for n , one obtains $C_p \approx 15\text{nF}$. Finally the choice of α was 0.3, which is in the range of typical values of α proposed in the literature [EJW88], [Ste88].

As can be seen from a finished design (cf. **Fig. 2.17(a)**) the maximum duty cycle occurs in a first approximation at the minimum output voltage at maximum output current, i.e. at maximum output current and rated power ($I_o=200\text{mA}$, $P_o=5\text{kW}$ and/or $V_o=25\text{kV}$, cf. specifications given in section 2.4).

Ideally, the maximum duty cycle should be set to $D = 1$, the operating point for the maximum output power then would be placed at the peak of the resonant characteristic. However, as for a practical circuit a dead time has to be considered for the switch-over of an inverter bridge leg and delay times of the gate drive circuits and the signal electronics do occur, $D < 0.8$ is selected with respect to the high switching frequency. Another reason for choosing a maximum duty cycle lower than $D = 1$ for steady state operation, is the improvement of the dynamic response of the system.

The voltage transfer characteristic (cf. **Fig. 2.16**) gives a rough idea about the possible operating points. It can be seen that for $\theta = 2$ and $f_{s,N} \approx 1.5$ it would be possible to achieve $V_o=25\text{kV}$ at high output power. Based on (2.9) and (2.10) one obtains $\theta = 1.964$, $f_{s,N} = 1.516$ and $D = 0.697$ for operation at $25\text{kV}/5\text{kW}$. Substituting $\theta = 1.964$ and $R_o = 125\text{k}\Omega$ (equivalent to $P_o=5\text{kW}@V_o=25\text{kV}$) in (2.1), the switching frequency becomes $f_s = 275\text{kHz}$. Based on that, the series resonant frequency f_o can be calculated and, finally, the inductance of the resonant inductor L_s can be determined.

Afterwards, the design proceeds with determining the stresses on the components.

For the above described design of the resonant tank components, the variables R_o and θ were employed. However, these variables do not provide a clear representation of the system operating point. For this reason the equations, which describe the system operating behavior, will be given in dependency of the output voltage and output current in the following. From a first harmonic analysis of the dependency of the system operating behavior one gets for a defined output voltage V_o and output current I_o

$$Q = \frac{V_o}{4 \cdot n^2 \cdot Z_s \cdot I_o} \quad (2.11)$$

$$\theta = 2 \cdot \tan^{-1} \sqrt{\frac{2 \cdot \pi}{f_{s,N} \cdot \alpha \cdot Q}} \quad (2.12)$$

$$k_v = 1 + 0.27 \cdot \sin\left(\frac{\theta}{2}\right) \quad (2.13)$$

$$\beta = -0.4363 \cdot \sin(\theta) \quad (2.14)$$

$$\omega C_p R_e = \frac{k_v^2 \cdot \pi}{4 \cdot \tan\left(\frac{\theta}{2}\right)^2} \quad (2.15)$$

$$k_{21} = \frac{v_{Cp(1)}}{v_{AB(1)}} = \frac{1}{\sqrt{[1 - \alpha \cdot (f_{s,N}^2 - 1) \cdot (1 + \frac{\tan(|\beta|)}{\omega C_p R_e})]^2 + [\alpha \cdot (f_{s,N}^2 - 1) \cdot \frac{1}{\omega C_p R_e}]^2}} \quad (2.16)$$

$$D = 1 - \frac{2}{\pi} \cdot \tan^{-1} \left(\frac{1}{\omega C_p R_e} \cdot \alpha \cdot \{ f_{s,N}^2 \cdot [1 + (\omega C_p R_e + \tan(|\beta|)^2)] - 1 \} \right. \\ \left. - [\omega C_p R_e + \tan(|\beta|)] \cdot [1 + \alpha \cdot (1 + \frac{\tan(|\beta|)}{\omega C_p R_e})] \right) \quad (2.17)$$

$$V_o = \frac{16}{\pi} \cdot \frac{k_{21}}{k_v} \cdot n \cdot V_{in} \cdot \sin\left(D \cdot \frac{\pi}{2}\right) \quad (2.18)$$

with the parameters

$Z_s = \sqrt{L_s/C_s}$ – characteristic impedance of the series resonant circuit

Q – normalized load resistance,

$f_o = (2\pi\sqrt{L_s C_s})^{-1}$ – series resonant frequency

$$f_{s,N} = f_s/f_o \quad - \quad \text{normalized switching frequency}$$

$$\alpha = C_p/C_s.$$

Some of the above given relations were already presented but are shown again in order to compile the whole set of equations (cf. (2.11)-(2.18)) which can be condensed into one nonlinear equation $V_o = f(V_o, I_o, f_{s,N})$. Hence, for given values of V_{in} , V_o , I_o , n , α , and for specified resonant circuit components, an unique switching frequency $f_{s,N}$ can be determined numerically. Also, substituting equations (2.11)-(2.16) in (2.17), this last equation can be rewritten as $D = f(V_o, I_o, f_{s,N})$. Thus, taking the value of $f_{s,N}$ calculated before, D can be analytically determined. Taking a set of values V_o and I_o which covers the whole operating range the variables D and $f_{s,N}$ can be graphically represented as shown in **Fig. 2.17(a)** and **(b)**.

Based on the solutions for D and $f_{s,N}$ and on the time behavior of the voltages and currents shown in **Fig. 2.10** and/or **Fig. 2.15**, now the stresses on all power components can be calculated. There results, e.g., for the peak value of the fundamental component of the resonant inductor current

$$\hat{I}_{Ls} = \frac{f_{s,N} \cdot \alpha}{2 \cdot n \cdot (1 + \cos(\theta))} \cdot \frac{V_o}{Z_s}, \quad (2.19)$$

for the turn-off current of the ZVS bridge leg power transistors

$$I_{Qoff} = \hat{I}_{Ls} \cdot \sin(D \cdot \pi), \quad (2.20)$$

for the peak value of the fundamental component of series capacitor voltage

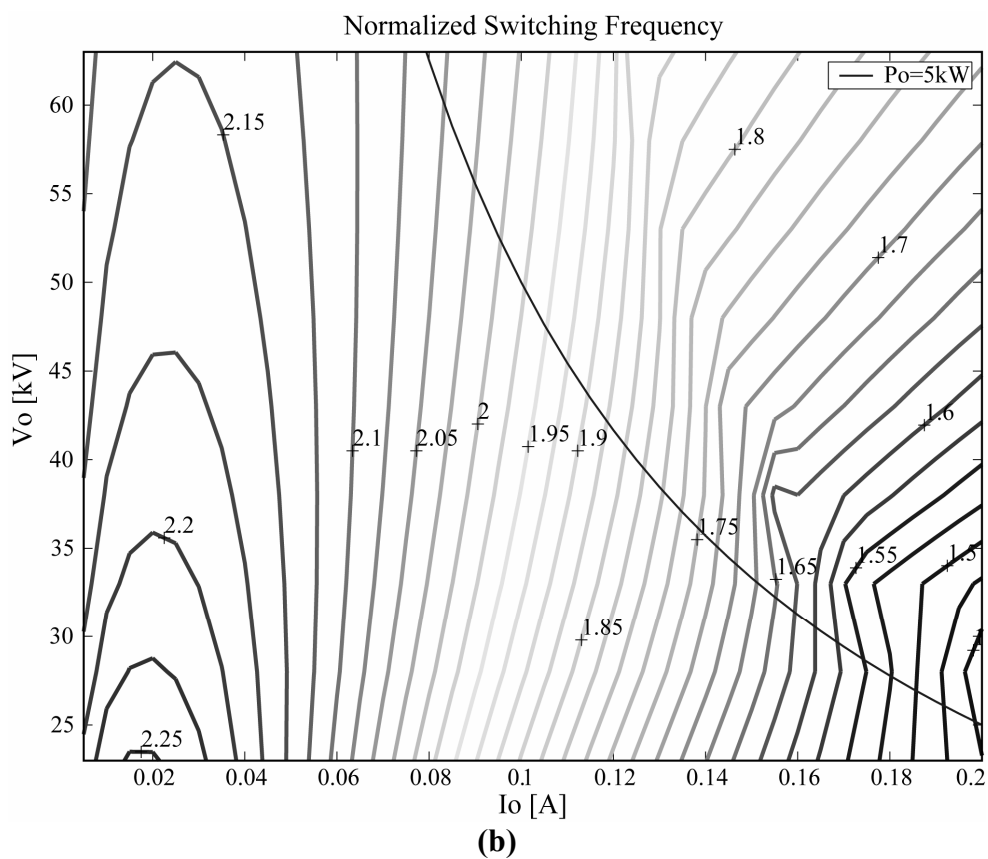
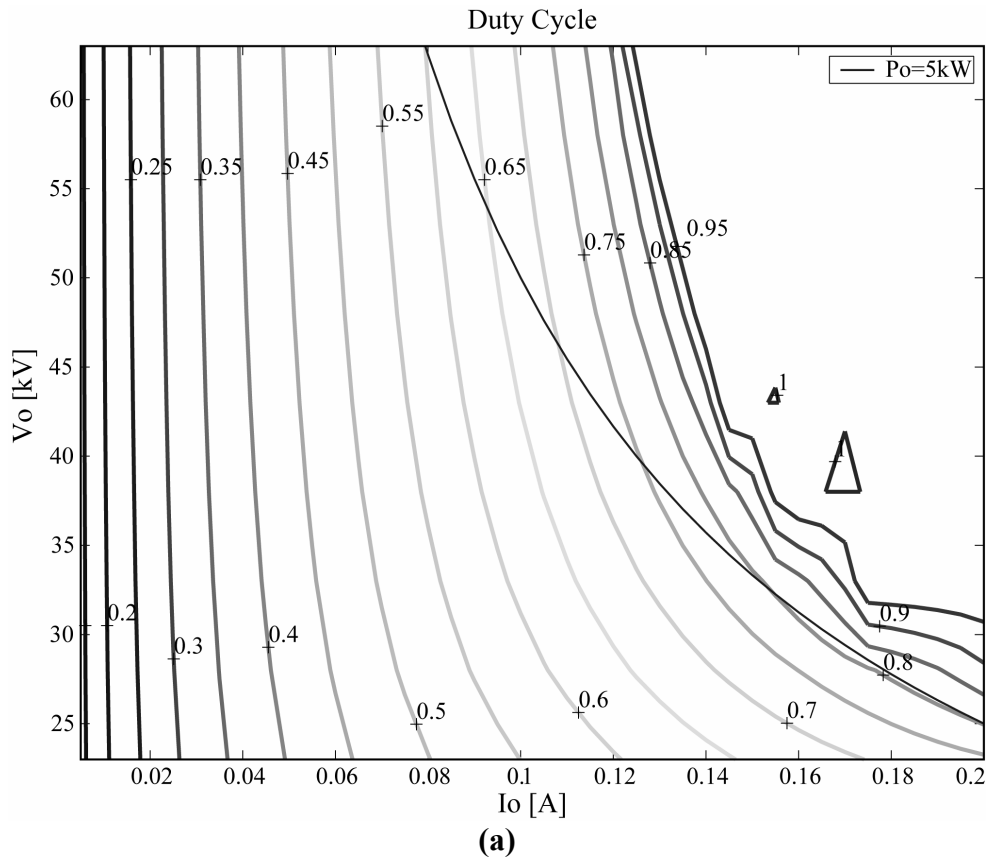
$$\hat{U}_{Cs} = \frac{\hat{I}_{Ls}}{2 \cdot \pi \cdot C_s} \quad (2.21)$$

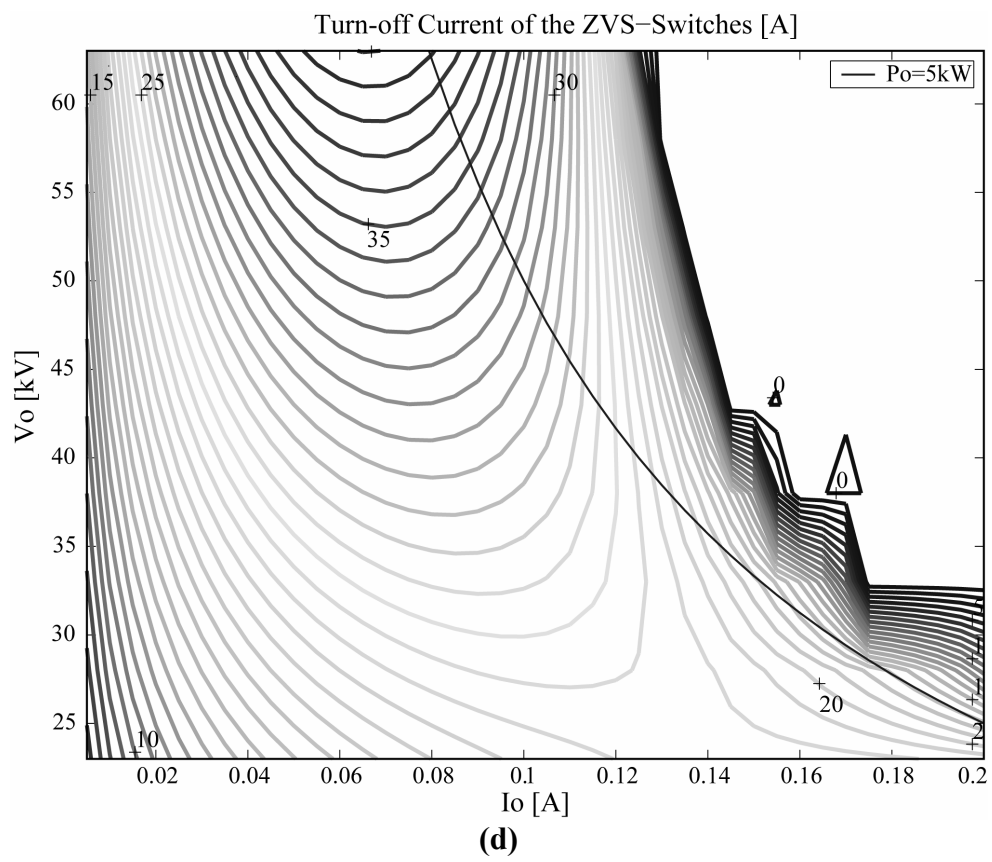
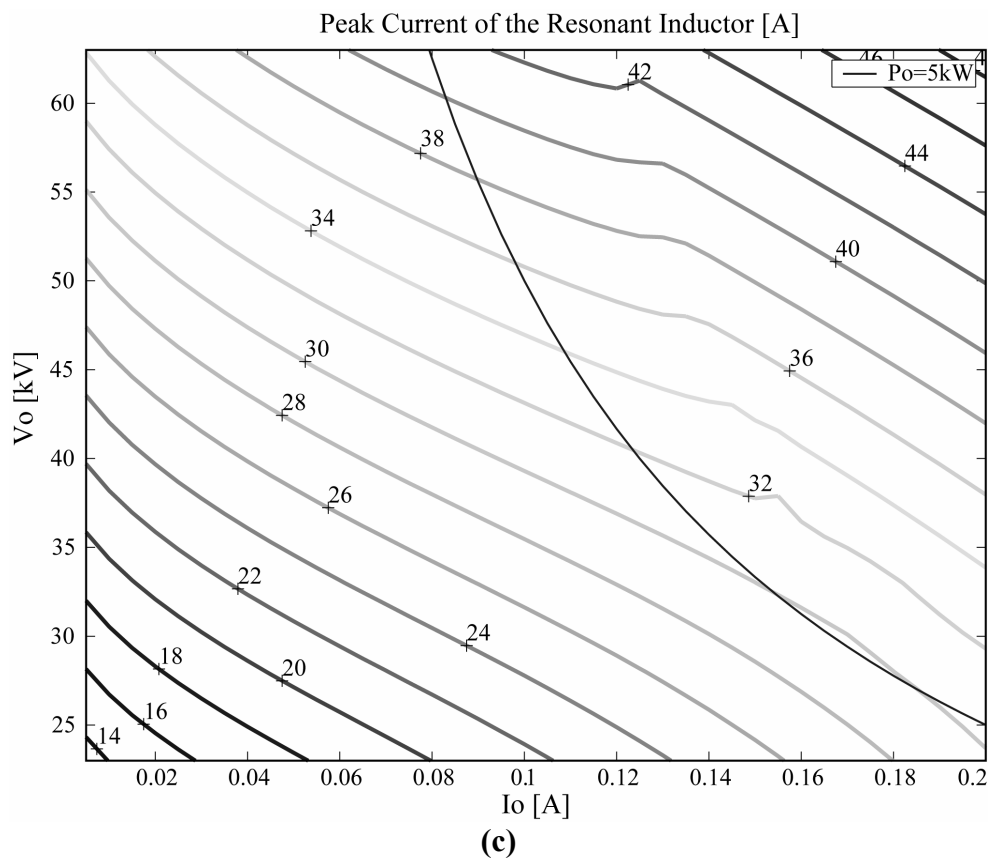
and for the RMS current stress on the ZVS power MOSFETs

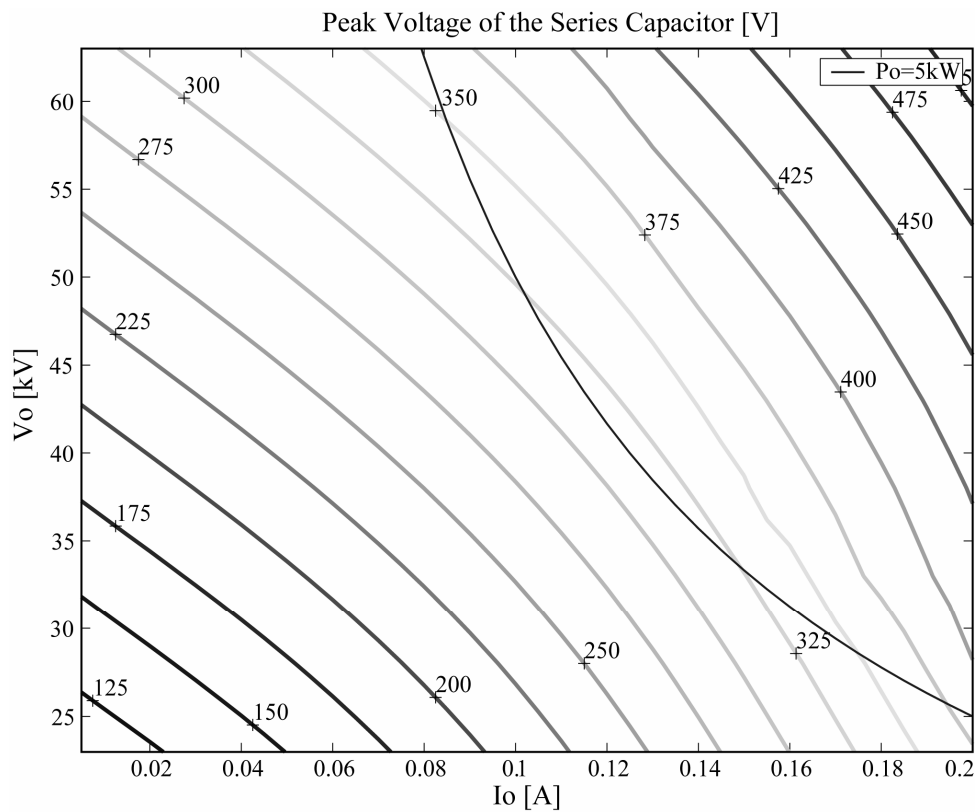
$$I_{QRMS_{ZVS}} = \frac{\hat{I}_{Ls}}{2} \cdot \sqrt{D - \frac{\sin(2 \cdot D \cdot \pi)}{2 \cdot \pi}}. \quad (2.22)$$

A graphical representation of (2.19)-(2.22) is depicted in **Fig. 2.17(c)** - **(f)**, for the parameters specified in section 2.4. There, it can be verified that the maximum switching frequency is lower than 500 kHz, and the maximum voltage across the series capacitor is lower than 1 kV. Accordingly the design does meet the specifications. In the case of the

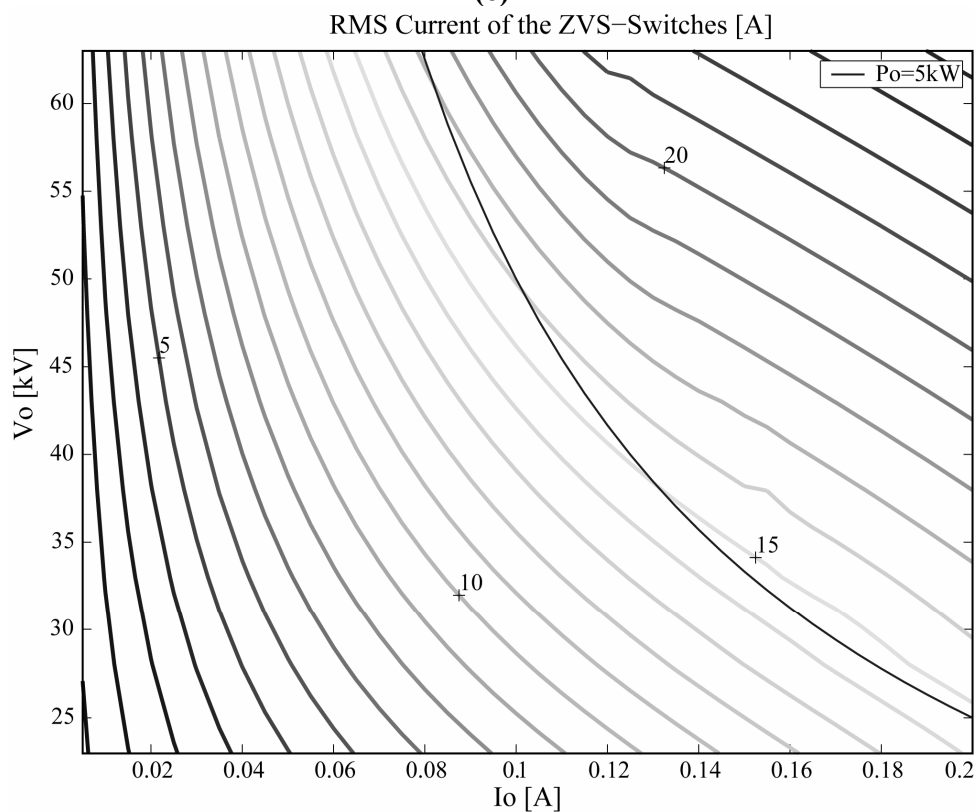
specifications would not be met the design procedure would have to be repeated with modified initial values C_p , α and n .







(e)



(f)

Fig. 2.17: Duty cycle (cf. (a)), switching frequency (cf. (b)) and stresses on the selected power components (cf. (c)-(f)) in dependency of the output current I_o and output voltage V_o . Parameters: $C_p = 15 \text{ nF}$, $n = 17$ and $\alpha = 0.3$.

2.4. SIMULATION RESULTS

Based on the converter design described in section 2.3 digital simulations were performed for minimum and maximum output voltage and full load and light load condition. The resulting time behavior of the inverter output voltage v_{AB} and of the resonant current i_{Ls} is shown in **Fig. 2.18** for operation at rated power and $V_o=62.5\text{kV}$ (cf. (a)) and $V_o=23\text{kV}$ (cf. (c)). The system behavior for operation at light load $P_o < 500\text{W}$ is depicted in **Fig. 2.18(b)** ($V_o=62.5\text{kV}$) and (d) ($V_o=23\text{kV}$). The parameters used for the simulations (cf. **Fig. 2.2**) are:

$$\begin{array}{llll} V_o = 23 \dots 62.5\text{kV} & I_o = 0 \dots 200\text{mA} & P_o = 0 \dots 5\text{kW} & V_{in} = 325\text{V} \\ n = 17 & C_1, C_3 = 200\text{pF} & C_s = 48\text{nF} & \\ C_p = 15\text{nF} & L_s = 16\mu\text{H} & C_{h1}', C_{h2}' = 1\mu\text{F} & \end{array}$$

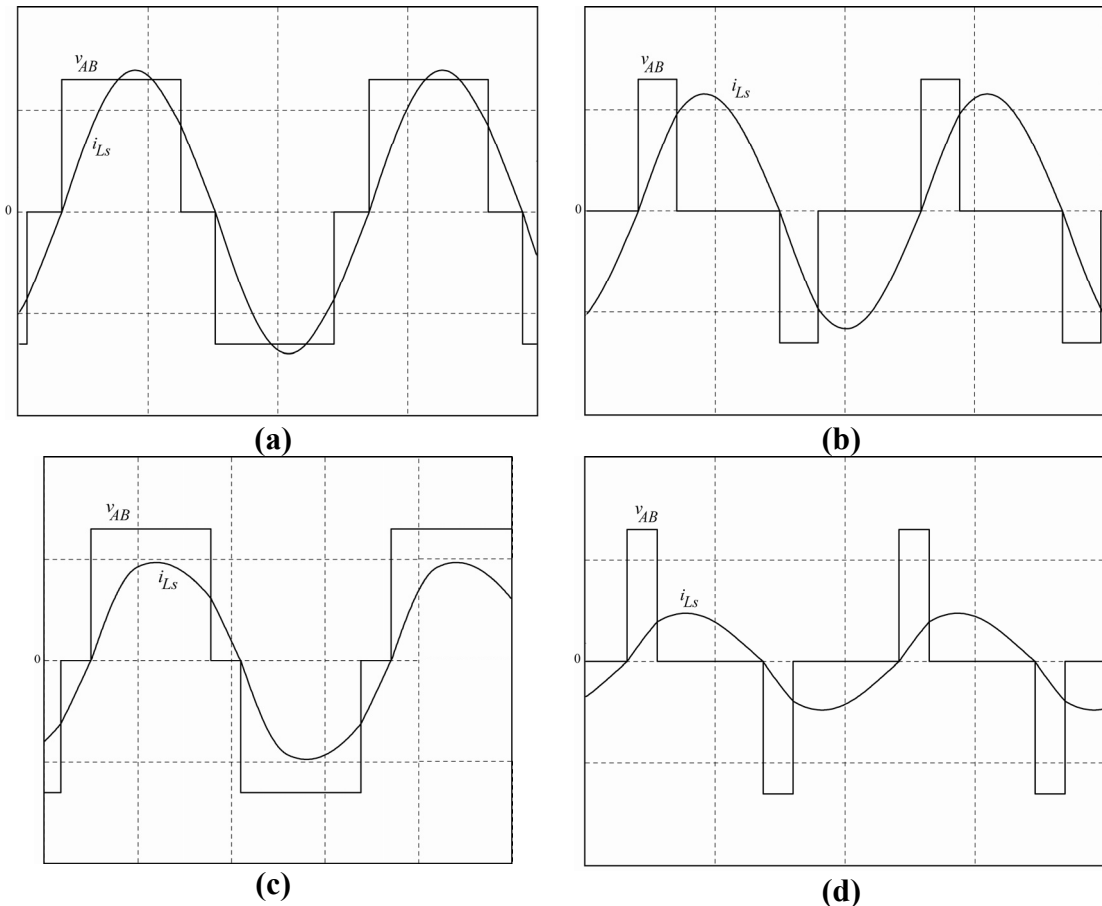


Fig. 2.18: Digital simulation of the stationary operating behavior; inverter output voltage v_{AB} (250V/div) and resonant current i_{Ls} (25A/div); time scale: $1.25\mu\text{s}/\text{div}$.

The simulation results agree well with the calculated values. Additionally, one can observe the operation with optimum commutation where the switching of one bridge leg is synchronized with the zero

crossing of the resonant current. Another important point, which has been verified by the simulations (cf. **Fig. 2.18**), is that the amplitude of the resonant current does not decrease significantly with the load, particularly for higher output voltage. This drawback of the series-parallel resonant converter has been explained in **Chapter 1** and a solution to reduce losses for operation at light load will be shown in Section 2.5.3.

2.5. OPEN LOOP CONTROL

2.5.1. Current Zero Crossing Synchronization

The turn-on and turn-off of the ZCS power transistors is synchronized with the zero crossing of i_{Ls} . The gate drive signals of the ZVS power transistors are generated by comparing a constant amplitude sawtooth-shaped carrier signal s_T and the controller output voltage v_c . The sawtooth frequency has to be properly adjusted for different points of operation, whereas the amplitude of the sawtooth remains constant for all frequency variations. To generate a sawtooth with those characteristics, a concept proposed in [PJJ99] is employed. According to this concept, a closed loop is used to regulate the average value of s_T and the reset pulse RP is synchronized with the zero crossing of i_{Ls} . A basic schematic of the sawtooth generator is depicted in **Fig. 2.19**.

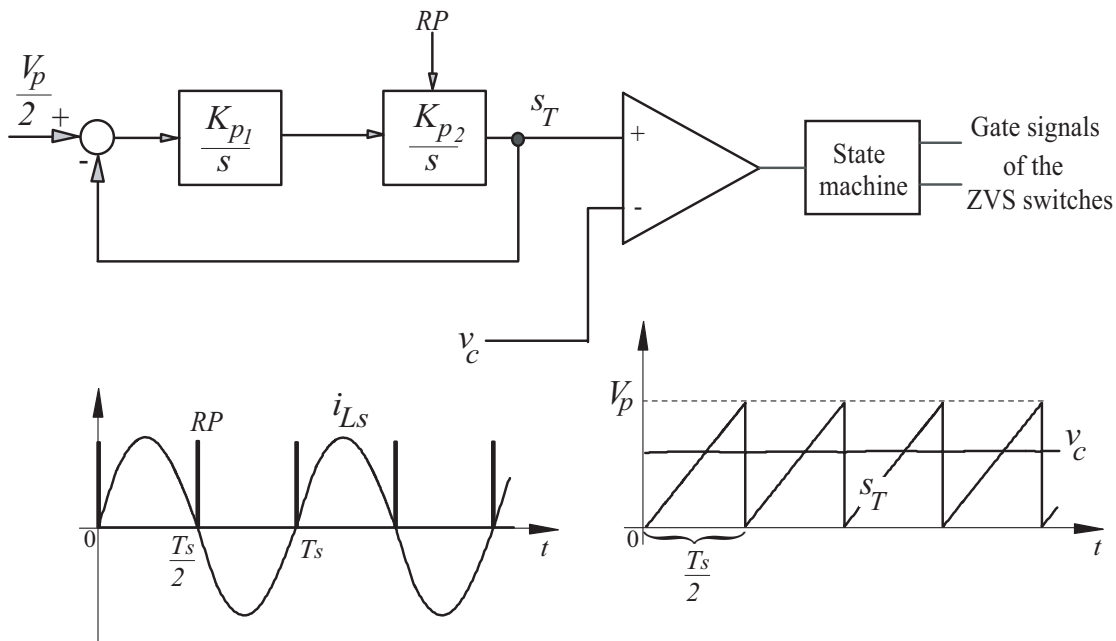


Fig. 2.19: Constant amplitude sawtooth generator for the control of a series-parallel resonant converter according to [PJJ99].

In order to design the constants of the sawtooth generator, the equations that describe its behavior have to be derived. These equations can be found by solving the differential equation associated with the closed loop. In order to design the gains K_{p1} and K_{p2} of the sawtooth generator, a tradeoff between speed of response, which is required to reject the variations in the switching frequency, and distortion in the sawtooth waveform must be considered. The variable s_T approaches an ideal sawtooth waveform for decreasing values of K_{p1} and K_{p2} . However, by increasing K_{p1} and K_{p2} faster transient responses are achieved.

2.5.2. Finite State Machine

For system control and protection, a finite state machine is employed. A finite state machine (FSM) or finite automaton is an abstract machine composed of a finite number of states, actions and functions that determines transitions from one state to another. A state stores information about the past, i.e. it reflects the input changes from the system start to the current state. A transition indicates a state change and is described by a condition that needs to be satisfied to allow the transition. An action is a description of an activity that is to be performed at a given moment. The finite state machine is associated with a graph called state diagram as represented in **Fig. 2.20**. State q_0 is the initial state, in which the state machine starts and for each condition there is exactly one transition out of each state.

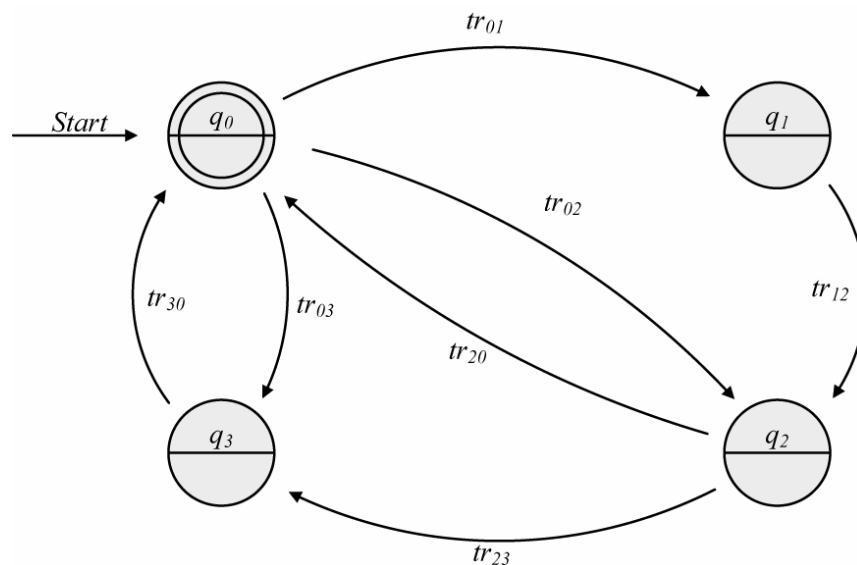


Fig. 2.20: State diagram of a finite state machine.

The transition functions are given by a state transition table. This function controls what state the state machine will move to, given a condition to the machine. **Table 2.1** shows the state transition table that corresponds to the state diagram shown in **Fig. 2.20**

Current State \ Condition	q_0	q_1	q_2	q_3
tr_{01}	q_1	—	—	—
tr_{02}	q_2	—	—	—
tr_{03}	q_3	—	—	—
tr_{12}	—	q_2	—	—
tr_{20}	—	—	q_0	—
tr_{23}	—	—	q_3	—
tr_{30}	—	—	—	q_0

Table 2.1: State transition table related to **Fig. 2.20**.

In the series-parallel resonant converter analyzed in this work, the state machine is responsible to provide the gate signals for the power switches and the reset pulse for the sawtooth generator described in the previous section. A block diagram of the state machine with the inputs and outputs is shown in **Fig. 2.21**. The state machine is implemented using the method proposed in [Aig05].

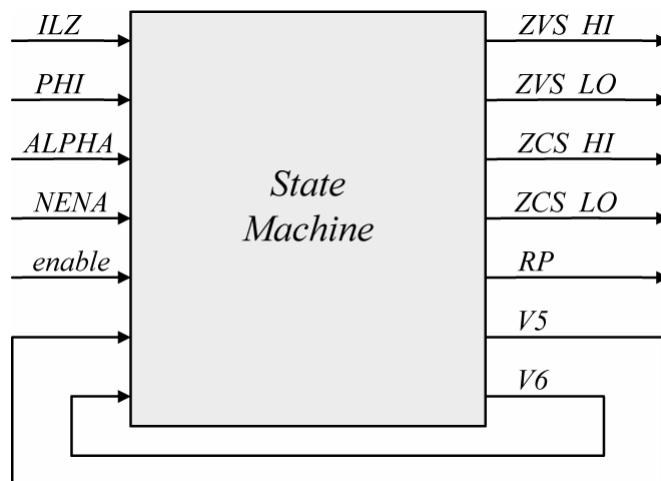


Fig. 2.21: Block diagram showing inputs and outputs of the state machine.

The input ILZ is associated with the zero crossing of the resonant current as shown in **Fig. 2.22**. If the resonant current i_{Ls} is positive, ILZ has logic level 1 (high) and if i_{Ls} is negative ILZ has logic level 0 (low). Thus,

ILZ is responsible for the commutation of the bridge leg S_2, S_4 (refer to **Fig. 2.1**) that is commutating at zero current (ZCS). The ZCS switches have fixed duty cycle equal to half switching period.

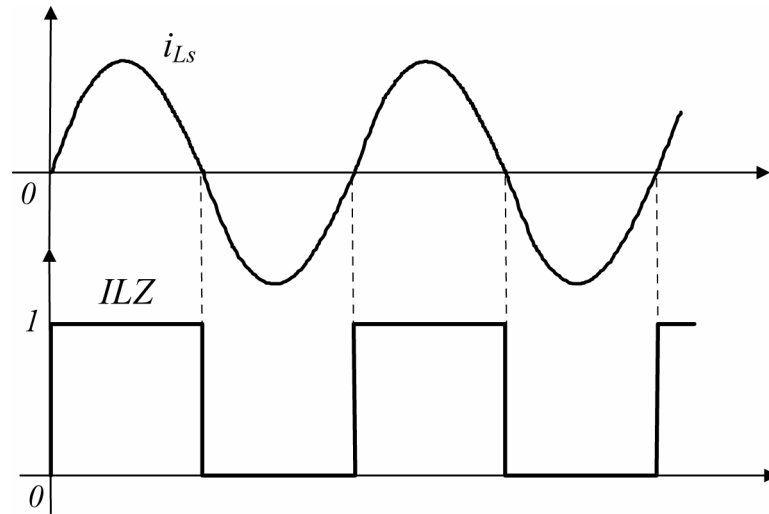


Fig. 2.22: Input ILZ .

The bridge leg S_1, S_3 (refer to **Fig. 2.1**) is operating under zero voltage switching (ZVS) condition. The ZVS switches have variable duty cycle because they are governed by the controller output voltage v_C as shown in the previous section. The input signal PHI is associated with the duty cycle of the ZVS switches. PHI is generated by comparing the sawtooth signal s_T and the controller output voltage v_C as shown in **Fig. 2.23**.

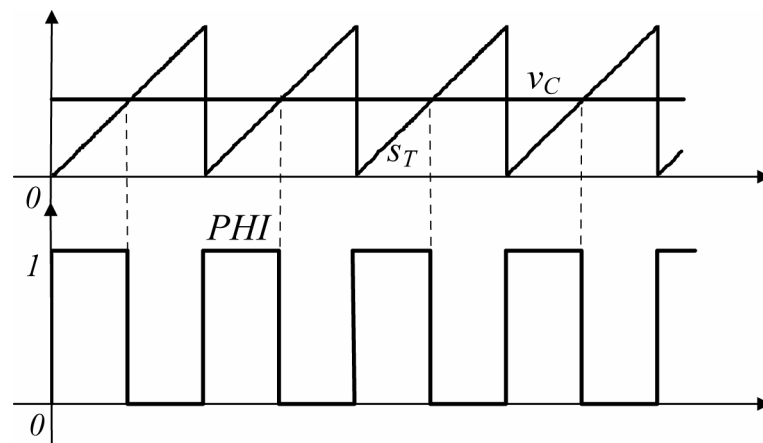


Fig. 2.23: Generation of the input signal PHI .

Additionally, as shown in the design in Section 2.3.3 it is necessary to define a maximum duty cycle for the circuit. The input $ALPHA$ is related with the maximum permissible duty cycle and is generated by comparing

the sawtooth signal s_T with a constant voltage v_{Dmax} that can be adjusted by the designer. **Fig. 2.24** shows how $ALPHA$ is generated.

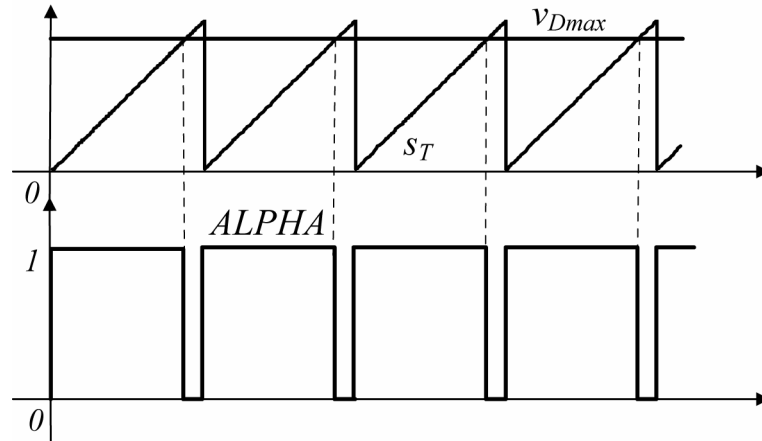


Fig. 2.24: Input signal that represents the maximum duty cycle for the ZVS switches.

The $NENA$ input is generated by comparing PHI , $ALPHA$ and the reset pulse, RP . This signal is given by the logical combination

$$NENA = (\text{NOT}(PHI) \text{ AND } \text{NOT}(ALPHA)) \text{ OR } RP \quad (2.23)$$

The *enable* input is given by an external switch that is manually controlled by the operator. This switch applies the logic levels 0 or 1 to the respective input. When *enable* is set to 0 (low), the state machine disables all gate signals. That means, all switches are turned off. Additionally, it holds the reset pulse RP permanently at logic level 1 (high). In this way, the sawtooth generator is continually reset.

The reset pulse RP for the sawtooth generator is synchronized with the zero crossing of i_{Ls} as shown in **Fig. 2.25**.

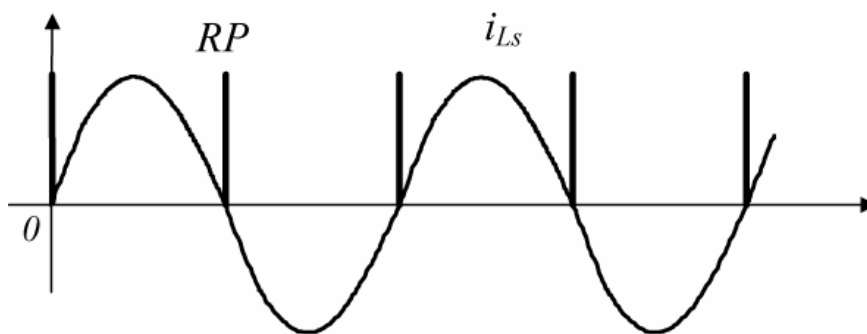


Fig. 2.25: Generation of the reset pulse.

The outputs ZVS_HI , ZVS_LO , ZCS_HI and ZCS_LO are the gate signals of the power switches. The complete state machine has eight states and is presented in **Fig. 2.26**.

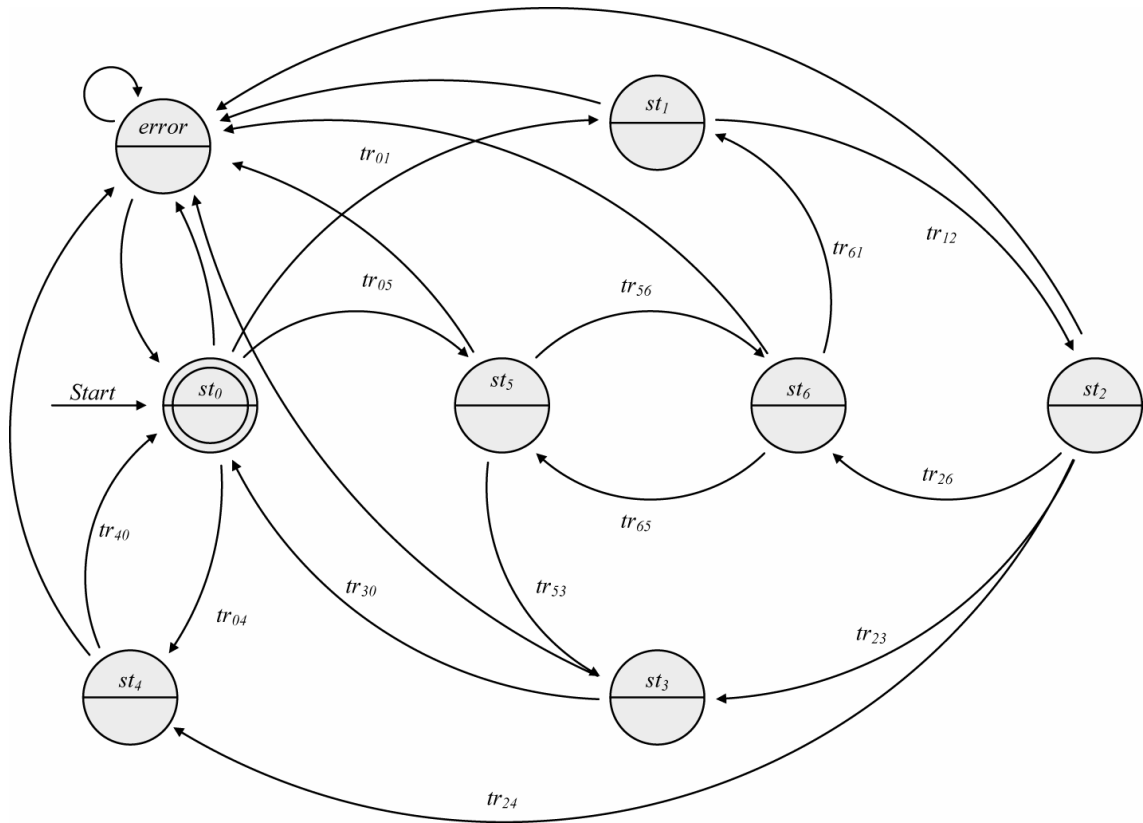


Fig. 2.26: State machine for control the series parallel resonant converter [Aig05].

Table 2.2 shows which switches are turned on or off for each state of the automaton.

Current State \ Switch	<i>ZVS_HI</i>	<i>ZVS_LO</i>	<i>ZCS_HI</i>	<i>ZCS_LO</i>
<i>st₀</i>	OFF	ON	ON	OFF
<i>st₁</i>	ON	OFF	ON	OFF
<i>st₂</i>	ON	OFF	OFF	ON
<i>st₃</i>	OFF	ON	OFF	ON
<i>st₄</i>	OFF	OFF	OFF	OFF
<i>st₅</i>	OFF	OFF	OFF	ON
<i>st₆</i>	OFF	OFF	ON	OFF
<i>error</i>	OFF	OFF	OFF	OFF

Table 2.2: State transition table.

The automaton starts at state st_0 with a power transfer state. In the power transfer state, two diagonal switches are on. This applies the full input voltage across the resonant circuit, transferring power to the load. The normal operation states are st_0 , st_1 , st_2 and st_3 . st_4 is the discontinuous mode state that will be described in the next section. st_5 and st_6 are special states

to prevent operation below resonance. Furthermore, if some abnormal behavior occurs, there is a transition from each state to the *error* state. In the *error* state, all switches are turned off and the state machine can be reinitialized from state st_0 . The state machine is implemented in practice on a CPLD (Complex Programmable Logic Device using VHSIC (Very High-Speed Integrated Circuits) Hardware Description Language (VHDL).

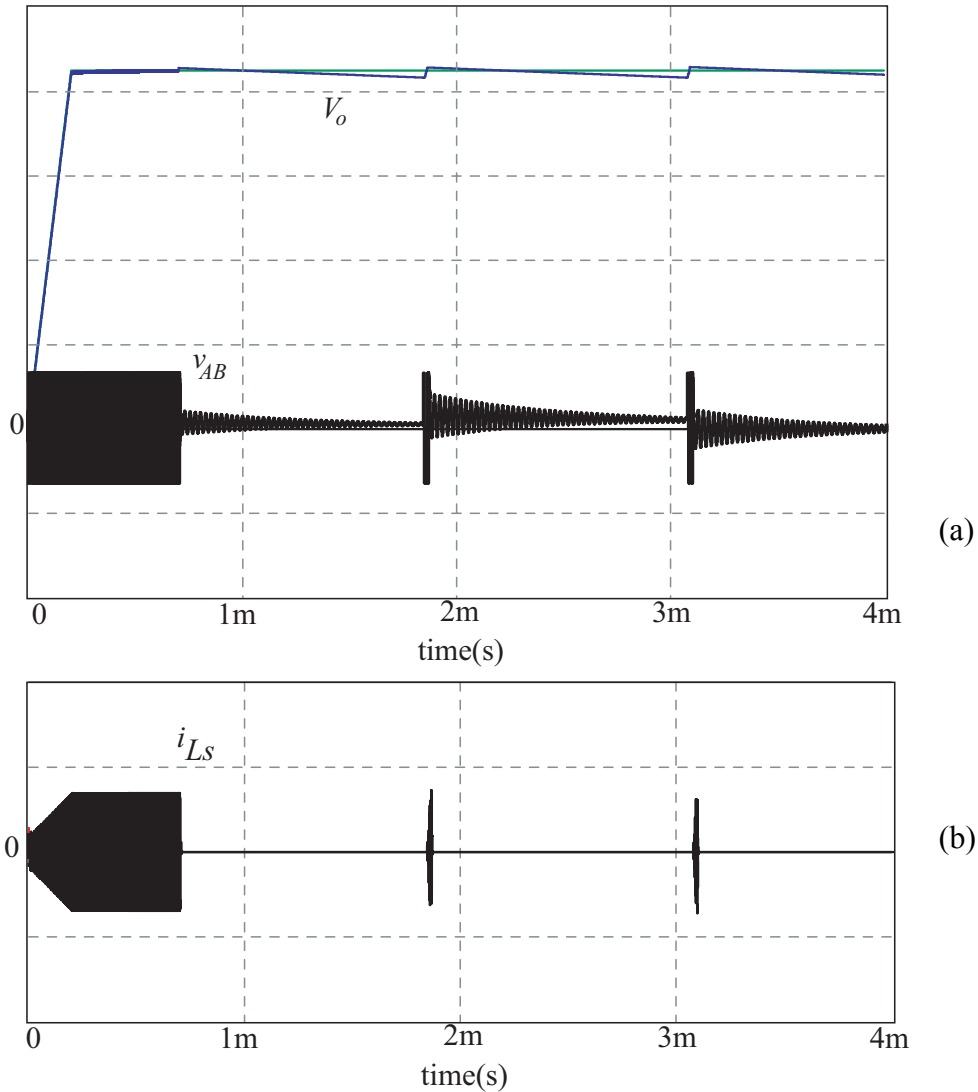


Fig. 2.27: Discontinuous operation at no load for an output voltage reference value of $V_o^* = 62.5\text{kV}$; (a) output voltage V_o (15kV/div) and the voltage v_{AB} (500V/div); (b) resonant current i_{Ls} (50A/div).

2.5.3. Operation under No Load Condition

According to Fig. 2.17(c) the amplitude of the resonant current does not change significantly with the output power level for higher output voltages. That means that the conduction losses under no load condition

will be almost as high as for full load. This is an inherent drawback of series-parallel resonant converter systems having a large output voltage range. To solve this problem, the converter operation is switched to discontinuous mode at low load condition. There, the output voltage is maintained in a determined tolerance band around the reference value and the power losses are reduced due to the low relative on-time of the power transistors (cf. **Fig. 2.27**) [CK03].

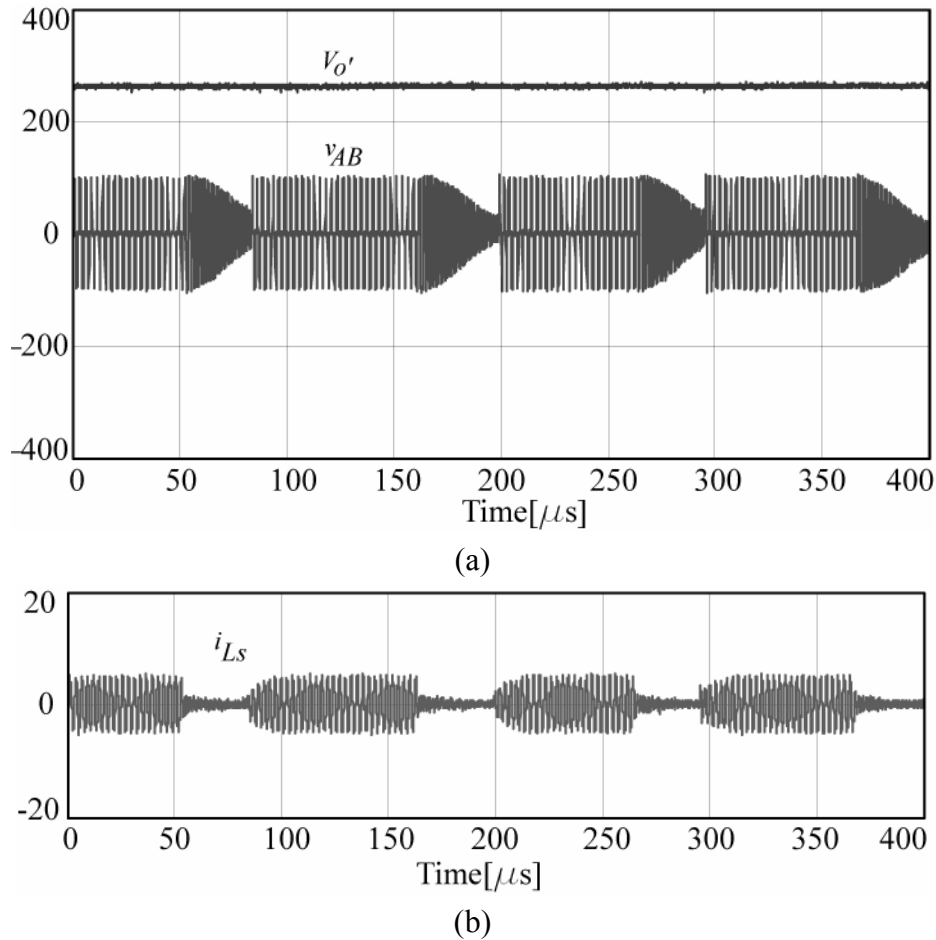


Fig. 2.28: Experimental waveforms of discontinuous operation. **(a)** output voltage V_o' (200V/div) and the voltage v_{AB} (200V/div); **(b)** resonant current i_{Ls} (20A/div).

In order to verify the results obtained theoretically and with simulations, a 5kW prototype was built (see **Chapter 5**). The prototype was constructed with all elements referred to the primary side of the transformer as shown on **Fig. 2.2**. The resonant elements L_s and C_p that normally would be integrated in the transformer were replaced with external elements. **Fig. 2.28** shows experimental waveforms of the output voltage V_o' ($V_o' = V_o/2n$), the voltage v_{AB} and the resonant current i_{Ls} for

discontinuous operation and a reference voltage value of $V_o^* = 285\text{V}$. One can see that the principle of discontinuous operation works very well in the practical implementation.

2.5.4. Operation above Resonance

As mentioned before, the resonant frequency of the series-parallel resonant converter is strongly dependent on the load and one has to ensure that the circuit remains operating above resonance and/or with lagging current as otherwise the free-wheeling diodes would be conducting current at the turn-on of the opposite power transistor of a bridge leg. This would result in a large reverse recovery current and/or in excessive switching losses due to the slow reverse recovery behavior of the power MOSFET internal diodes.

Operation below resonance might occur for a large load step. If a step-like increase of the load occurs, the converter remains operating above resonance. However, for step-like reduction of the load operation below resonance is likely to occur. Therefore, in order to ensure operation above resonance for all operating conditions a turn-on of a power transistor is only allowed if the opposite free-wheeling diode is not conducting current.

Operation below resonance could be prevented by monitoring the polarities of the voltage v_{AB} and of i_{Ls} . For regular operation, the voltage v_{AB} is always positive or equal to zero when i_{Ls} is positive. For operation below resonance, for $i_{Ls} > 0$ v_{AB} can be positive or negative. Thus, if the current goes negative and v_{AB} is still positive the system is operating below resonance. In this case the power transistors S_1 and S_4 will be turned-off but S_2 and S_3 will not be turned-on as for regular operation; all switches will remain in the off-state until the next zero-crossing of i_{Ls} , where S_1 and S_4 will be turned-on again, restoring the regular operation above resonance.

However, the problem is alleviated by the output capacitor, which does prevent an immediate influence of the load change on the resonant circuit and does provide time for the system control to adjust to the load condition by properly changing the duty cycle.

The system behavior in case of changing from full load to low load is shown in **Fig. 2.29** where the smooth transition of the control voltage v_C and the sawtooth signal s_T can be observed. It is important to point out that

if a very faster controller is employed, operation below resonance could become critical again because the controller does not respond immediately to a load change [CK03].

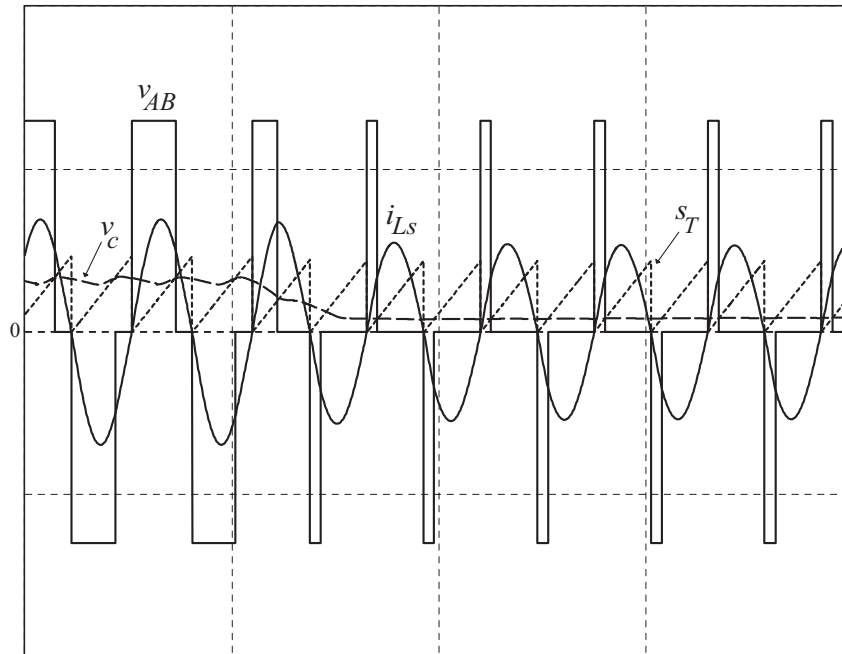


Fig. 2.29: Converter behavior for load change. Scales: v_{AB} : 250V/div; i_{LS} : 50A/div; v_C : 25V/div; s_T : 25V/div.

2.6. SUMMARY

This chapter presents a detailed procedure for determining the characteristic values of the power components of a high output voltage DC-DC series-parallel resonant converter. The theoretical considerations are verified by digital simulations. Furthermore, the dynamic control behavior is discussed and a concept for ensuring operation above resonance also in case of large load transients is described.

CHAPTER 3

3. LARGE- AND SMALL-SIGNAL ANALYSIS OF THE SERIES-PARALLEL RESONANT CONVERTER

3.1. INTRODUCTION

An x-ray power generator requires the capability to adjust its DC output voltage across the x-ray tube in a short time over a wide operating range without any voltage overshoot. Therefore, the controller design is a very important part of the design procedure of imaging power generators. However the controller design task is very involved because the small-signal transfer function is extremely dependent on the operating point of the converter. Many controller designs were performed by trial and error because a simple small-signal model of the capacitive loaded series-parallel resonant converter up to now was missing in the literature. The trial and error procedure is not convenient because the small-signal model varies significantly with load changes and the equivalent load of the x-ray tube is normally an unknown parameter. Therefore, setting of the controller parameters can take a long time until a robust set of parameters is found.

This chapter shows a large-signal model for the series-parallel resonant DC-DC converter that can describe the transient behavior of the converter and it will be useful to develop a nonlinear controller shown in the next chapter. The large-signal model of the series-parallel resonant converter with capacitive output filter has been originally proposed in [MRDP⁺02] and it will be reviewed here because it is useful for obtaining the small-signal converter model. Moreover, this chapter develops a novel small-signal model for the series-parallel resonant DC-DC converter with capacitive output filter in order to make the controller design for this type of converter easier.

The contents of this chapter have been published by the author in short form in the Proceedings of the 36th IEEE Power Electronics Specialists Conference (PESC'05) under the title *Small-Signal Model of a*

5kW High-Output Voltage Capacitive-Loaded Series-Parallel Resonant DC-DC Converter (cf. [CK05]).

3.2. THEORETICAL ANALYSIS

The topology of the 5kW series-parallel resonant full-bridge DC-DC converter with impressed output voltage, operating above resonance, is shown in **Fig. 2.1** (Chapter 2).

In order to simplify the analysis it will be assumed that: all the components are ideal and have no losses and that the voltage V_{in} supplied by an input pre-regulator is constant and has no ripple. Furthermore, the magnetizing inductance of the transformer will not be considered for the analysis. In addition, capacitors C_1, C_3 will not be included in the analysis because idealized switching waveforms are assumed. The x-ray tube is modeled as a pure resistance. All output quantities are referred to the transformer primary side. According to these considerations, the simplified model of the converter is represented by the circuit of the **Fig. 3.1**. The equivalent output voltage, output current and output resistance, referred to the primary side of transformer, are respectively: $V_{o'} = V_o / 2n$, $I_{o'} = I_o \cdot 2n$ and $R_{o'} = R_o / 4n^2$ where n is the transformer turns ratio.

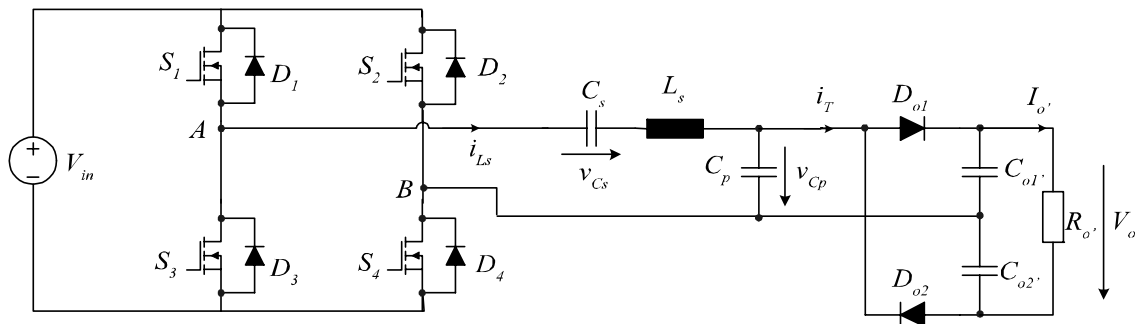


Fig. 3.1: Simplified converter circuit for referring the output quantities to the transformer primary side.

3.2.1. State of the Art Small-Signal Modeling Techniques

Resonant DC-DC converters are nonlinear dynamic systems. This nonlinear aspect is one of the reasons of the difficulties encountered when calculating control laws for this type of converters [HBB⁺92].

A dynamic model is helpful for determining the analytical small-signal model of the converter, which allows the application of classical

linear feedback technique, for example Bode plots and root locus method, to design control schemes in a fast and reliable way. In addition, it allows the comparison of dynamics of different converters [EVK88].

The four main methods used to calculate the small-signal model for resonant converters are: sampled-data modeling technique [VEK86], extended describing function technique [YLJ92a], approximate technique [Vor84], [Vor89] and AC resistance technique [Ste88].

Many works have been published about the small-signal modeling and control of the series-parallel resonant converter with inductive output filter but in the case of the capacitive loaded series-parallel resonant converter, there is a sparse number of publications. In [MF99], a small-signal model based on the fundamental frequency analysis is described. However, the method presented by [MF99] covers only the case with fixed duty cycle. Thus, it cannot be applied to the converter proposed here, because in the case at hand the control variable is the duty cycle. Afterwards, a method based on a sampled-data technique [VEK86], which covers the case of variable duty cycle, has been proposed by [YPJ03]. This method produces accurate solutions but it requires an explicit solution of equations that govern the behavior of the converter in each conduction state. Therefore, it has the disadvantage of being mathematically complex [FH96]. The sampled-data technique leads to a discrete-time model that is not easy to use in the controller design [YLJ92b]. Explicit expressions for the small-signal model can only be obtained for simple converters. In most cases the transfer functions must be calculated for each separate operating condition [FH96]. Due to the third-order resonant tank, an explicit solution of the converter equations is quite complex and the model has to be calculated numerically. The complexity of the equations could be the reason why the explicit matrices A and B of the state space model and the explicit small-signal transfer function of the series-parallel resonant converter are not presented in [YPJ03].

In fact, continuous models are preferred in comparison with discrete models, when the first harmonic approximation is sufficient to obtain the desired accurate waveforms, and when the order of the system makes the explicit solution of the converter equations complex [PJJ97]. Both

conditions apply in the case of the converter analyzed in this thesis. For this reason a continuous model will be developed.

The approximate method proposed by Vorpérian in [Vor84], [Vor89] is a good combination of accuracy and simplicity. However, this approach is an intuitive rather than a formal approximation [WHE91]. The main assumption of this method is that for the series-parallel resonant converter the dominant behavior is given by a single pole and the high-frequency behavior is given by a conjugate complex pole pair. Based on this assumption, the output filter is supplied by a voltage source $H_o H_h(s) \hat{f}(s)$ through a series resistance r_{in} . $\hat{f}(s)$ represents the small-signal change in the normalized switching frequency and H_o is the low frequency gain that can be calculated by differentiating the converter steady state equations. The resistance r_{in} is defined as the negative partial derivative of the average output voltage with respect to the average output current. $H_h(s)$ represents the high-frequency complex pole pair which occurs in the transfer functions of resonant converters [FHO94].

The complete control to output transfer function is expressed as $\hat{v}_o(s) / \hat{f}(s) = H_o H_h(s) H_f(s)$, where $H_f(s)$ is the transfer function of the output filter including the resistor r_{in} .

By using the AC resistance approach proposed by Steigerwald [Ste88], the converter is described as a resonant network with a load dependent damping factor. There, the output rectifier and the load are substituted by an equivalent AC resistance that expresses the effect of the dissipative nature of the load [BYR96]. A brief explanation about this approach is shown in **Chapter 2**. In [Ste88] the DC voltage transfer ratio is presented but the small-signal model is not presented. The AC resistance approach has been extended and successfully applied to obtain the small-signal model of the series-parallel resonant converter with inductive filter [BYR96], [PJJ97]. However, the AC resistance approach does not provide accurate results for the series-parallel resonant converter with capacitive output filter. This is due to the fact that the input current of the output rectifier flows for only a part of the switching period. As a result, the first harmonic of the rectifier input current leads the first harmonic of the

rectifier input voltage [IKBY97]. Thus, the equivalent load cannot be considered as purely resistive.

The extended describing function method assumes that the resonant waveforms may be approximated by their fundamental components. The derivation of the small-signal model starts from the non-linear differential equation for the converter. There are two discontinuous terms in the equation, the first representing the output voltage of the full-bridge, and the second representing the current waveform drawn by the rectifier from the parallel resonant capacitor. The discontinuous functions are eliminated by first assuming that they are quasi-square waves, and then second by assuming that the quasi-square waves may be approximated by their respective fundamental components. Also, by assuming the resonant waveforms to be sinusoidal a non-linear steady-state equation is derived for the converter. Small perturbations are introduced to linearize the steady-state equation resulting in a continuous-time small-signal model.

This method can be used to calculate the Fourier coefficients for the generalized averaging method [SNL⁺91] in order to obtain large and small-signal model of the converter. The only limitation of the generalized averaging method occurs when the voltages and currents cannot be described with sufficient accuracy by their first harmonics. However, for the operating modes intended in this work, the voltages and currents are predominantly sinusoidal. Thus, the generalized averaging method will be preferred in the calculation of the large and small-signal model.

3.2.2. Generalized Averaging Method

State-space averaging approximation, widely used in the analysis and design of power electronic systems, is fundamentally a large signal method. This method is often used for fast simulation of large-signal power converter transients. However, small and large-signal dynamics cannot be followed by the averaging method that means, continuous-time averaging methods do not provide any information about the current and voltage waveform ripple, i.e., detail within each switching cycle [BS98]. Thus, the accuracy of the approximation deteriorates as the ripple magnitudes in the current and voltage waveforms increase, or equivalently as the switching frequency decreases [CGV⁺00].

However, the method cannot be applied to a wide range of power circuits that includes the resonant type converters. The basic limitation concerning resonant converters is that these circuits have state variables with a predominantly oscillatory behavior. The generalized averaging method overcomes limitations of the state-space averaging method because it can describe arbitrary types of waveforms. It is based on a time-dependent Fourier series representation for a sliding window of a given waveform [SNL⁺91].

The method is based on the fact that the waveform $x(\cdot)$ can be approximated on the interval $\tau \in (t-T, t]$ with a Fourier series representation of the form

$$x(\tau) = \sum_k \langle x \rangle_k(t) e^{jk\omega_s \tau} \quad (3.1)$$

where the sum is over all integers k , $\omega_s = 2\pi/T$ and $\langle x \rangle_k(t)$ are complex Fourier coefficients.

These Fourier coefficients are time dependent since the interval under consideration slides as a function of time [MST⁺01]. However, $\langle x \rangle_k(t)$ are assumed to be varying very slowly compared to $e^{jk\omega_s \tau}$, so that they can be considered as constant coefficients. The k th coefficient is obtained by integrating the waveform within the period T , i.e. by averaging the waveform as shown in (3.2) [MST⁺01], [SNL⁺91].

$$\langle x \rangle_k(t) = \frac{1}{T} \int_{t-T}^t x(\tau) e^{-jk\omega_s \tau} d\tau \quad (3.2)$$

If one maintains only the DC coefficient of the Fourier series, the traditional state-space averaging method is recovered.

The time derivative of the k th coefficient is computed to be

$$\frac{d}{dt} \langle x \rangle_k(t) = \left\langle \frac{d}{dt} x \right\rangle_k(t) - jk\omega_s \langle x \rangle_k(t). \quad (3.3)$$

It is important to point out that (3.3) corresponds to the exact derivative of the k th coefficient only in the case that ω_s is constant. When the frequency is not constant, (3.3) is only a good approximation if ω_s is a slowly varying variable [SNL⁺91].

A state-space model of a switching circuit like a resonant converter can be expressed as:

$$\frac{d}{dt}x(t) = f\{x(t), u(t)\} \quad (3.4)$$

where $x(t)$ is a state variable, $u(t)$ some input of the system represented by a time-dependent function with period T and f is a scalar function. In order to apply the generalized averaging method to the state-space model, one has to calculate the relevant Fourier coefficients of (3.4) [SNL⁺91], i.e.

$$\left\langle \frac{d}{dt}x \right\rangle_k = \langle f(x, u) \rangle_k \quad (3.5)$$

The derivative of the k th coefficient is given by

$$\frac{d}{dt}\langle x \rangle_k = \langle f(x, u) \rangle_k - jk\omega_s \langle x \rangle_k \quad (3.6)$$

The term $\langle f(x, u) \rangle_k$ can be calculated as a function of state variables and of inputs of the circuit using describing functions.

Describing function method is a quasi-linearization method. That means it represents an approximation of a nonlinear operation by a linear one, which depends on some properties of the input [GVV68]. The basic idea of this approach is to replace the nonlinearities with quasi-linear describing functions whose gains depend on the amplitude of the input signal. As a result, a quasi-linear system is obtained, to which linear control system analysis and design techniques can be applied [GVV68]. The main limitation on the use of describing functions is the requirement that the actual input signal of the nonlinearity approximates the form of the signal used to derive the describing functions [GVV68].

The generalized averaging method is applied to the series-parallel resonant converter, shown in **Fig. 3.1**. Using the notation given in the figure and choosing $C_{o1'} = C_{o2'} = C_{o'}$, the differential equations that describe the circuit can be written as:

$$L_s \frac{di_{L_s}(t)}{dt} = -v_{C_s}(t) - v_{C_p}(t) + v_{AB}(t) \quad (3.7)$$

$$C_s \frac{dv_{C_s}(t)}{dt} = i_{L_s}(t) \quad (3.8)$$

$$C_{o'} \frac{dv_{o'}(t)}{dt} = abs(i_T) - \frac{2 \cdot v_{o'}(t)}{R_{o'}} \quad (3.9)$$

The state vector is given by $x(t) = [i_{L_s}(t) \ v_{C_s}(t) \ v_{o'}(t)]^T$. At this point, it is important to notice why the voltage in the parallel capacitor v_{C_p} is not used as a state variable even though C_p is an energy storing element. In fact the v_{C_p} waveform is not differentiable and its dynamic behavior is completely defined by the energy stored in L_s and in both output capacitors [MRDP⁺02].

Fig. 3.2 shows the main waveforms of the simplified circuit of **Fig. 3.1** for a typical operating point.

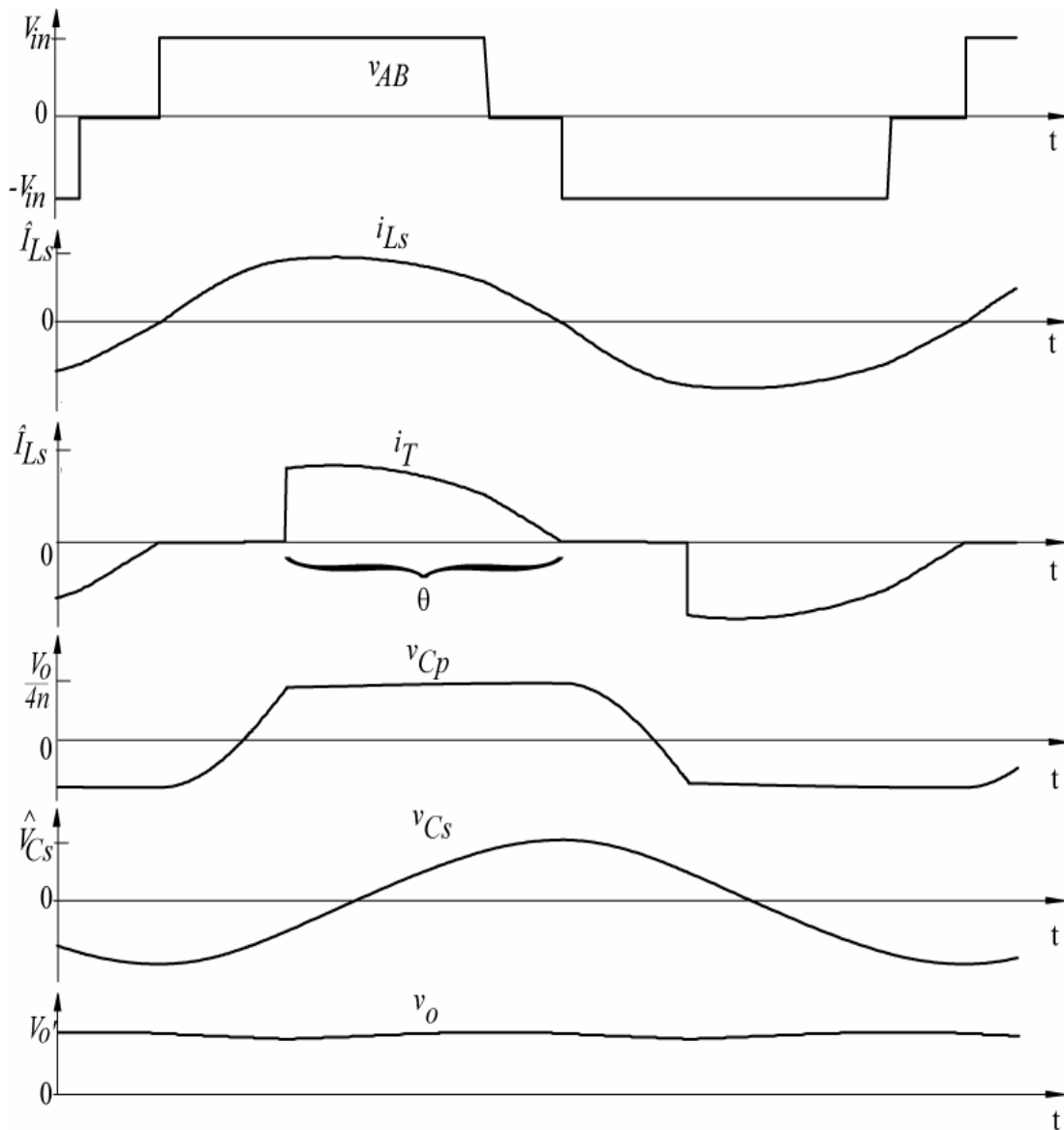


Fig. 3.2: Time behavior of the characteristic voltages and currents of a series-parallel resonant converter within a pulse period (t_0 - t_{10}).

Fig. 3.2 is similar to **Fig. 2.10** with the difference that the waveforms of the voltage across the series capacitor and of the output voltage have

been added. The objective here is to show that the voltages and currents of the circuit are predominantly sinusoidal with exception of the output voltage that is a DC voltage with small ripple. Thus, it can be assumed that the resonant current i_{Ls} and the voltage in the series capacitor v_{Cs} are well approximated by their first time-varying harmonic i.e. with the fundamental term of the Fourier series. Since the output voltage v_o is a DC voltage with slow dynamical behavior, it is assumed that it can be approximated with sufficient accuracy with the DC coefficient of the complex Fourier series.

The procedure to determine the dynamical large-signal model of the system includes two steps. First, one describes the instantaneous switched variables with a standard state-space description and afterward the state space equations are averaged using complex Fourier series. Later the averaged model will be linearized around an equilibrium operating point in order to obtain the small-signal model of the converter. As said before, the state variables of the system are $i_{Ls}(t)$, $v_{Cs}(t)$ and $v_o(t)$. However, if one observes equations (3.7)-(3.9), one can see that the three equations contain three other variables in addition to the state variables. Thus, one has to find a way to express the remaining variables as a function of the state variables and the control inputs. In the following, it will be shown how to calculate the remaining variables $v_{AB}(t)$, $abs(i_T)$ and $v_{Cp}(t)$.

The complex Fourier series is simpler to calculate than the real Fourier series when the function has no odd or even symmetry, i.e. when the function has sine and cosine terms in its expansion.

The complex form of the Fourier series of a periodic function $f(\varepsilon)$ with period 2π is given by (3.10).

$$f(\varepsilon) = \sum_{k=-\infty}^{+\infty} c_k \cdot e^{jk\varepsilon} \quad (3.10)$$

The coefficient of the k th term of the series c_k is calculated as

$$c_k = \frac{1}{2\pi} \int_{-\pi}^{\pi} f(\varepsilon) e^{-jk\varepsilon} d\varepsilon \quad (3.11)$$

In order to exemplify, how the complex Fourier representation can be applied to the waveforms in the case at hand, the fundamental component of the voltage v_{AB} will be calculated in the following.

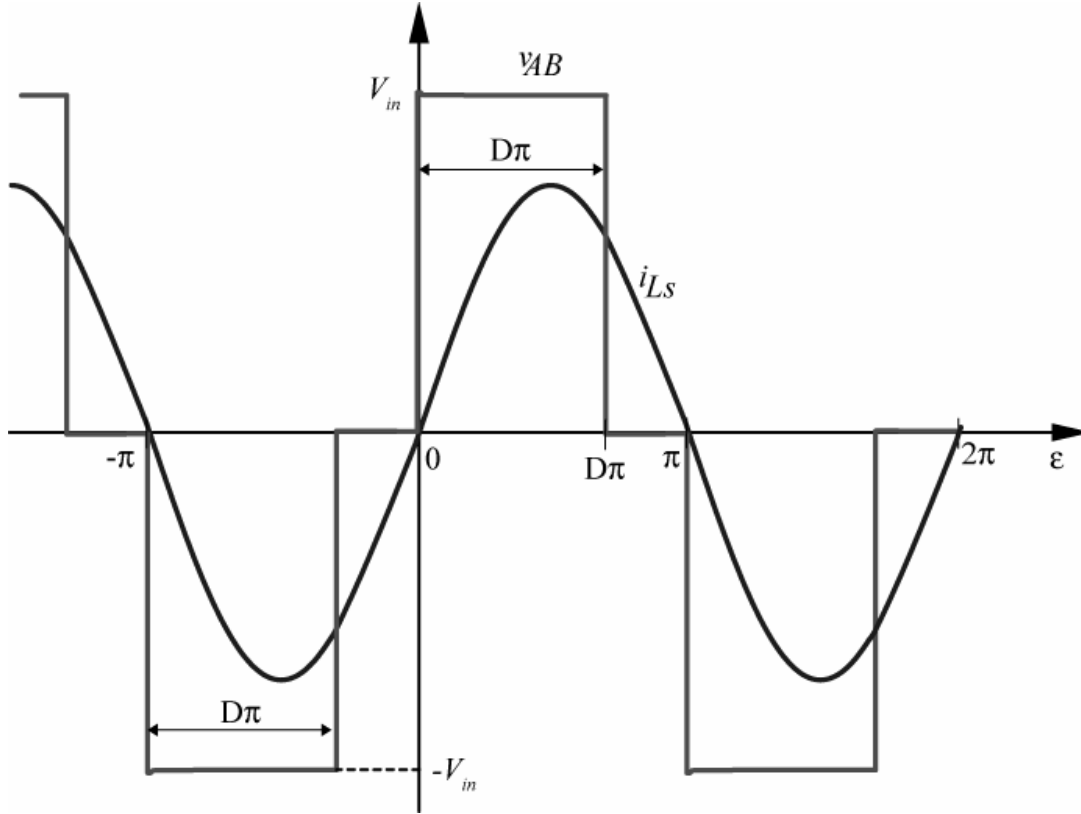


Fig. 3.3: Voltage v_{AB} and resonant current i_{LS} .

Given the waveforms v_{AB} and i_{LS} shown in **Fig. 3.3**, the zero crossing of the resonant current is taken as the reference $\varepsilon = 0$. The k th time-varying harmonic of v_{AB} is calculated as

$$\langle V_{AB} \rangle_k = \frac{1}{2\pi} \int_{-\pi}^{\pi} v_{AB}(\varepsilon) e^{-jk\varepsilon} d\varepsilon \quad (3.12)$$

If one observes the v_{AB} waveform in **Fig. 3.3**, the instantaneous values of v_{AB} for the different intervals from $-\pi$ to π are given by

$$v_{AB} = \begin{cases} -V_{in} & \text{if } -\pi < \varepsilon < -\pi + D\pi \\ 0 & \text{if } -\pi + D\pi < \varepsilon < 0 \\ V_{in} & \text{if } 0 < \varepsilon < D\pi \\ 0 & \text{if } D\pi < \varepsilon < \pi \end{cases} \quad (3.13)$$

Substituting these values in Eq. (3.12), following expression is obtained

$$\langle V_{AB} \rangle_k = \frac{1}{2\pi} \left[\int_{-\pi}^{-\pi+D\pi} -V_{in} e^{-jk\varepsilon} d\varepsilon + \int_0^{D\pi} V_{in} e^{-jk\varepsilon} d\varepsilon \right] \quad (3.14)$$

then

$$\langle V_{AB} \rangle_k = \frac{V_{in}}{2\pi} \left[- \int_{-\pi}^{-\pi+D\pi} e^{-jk\varepsilon} d\varepsilon + \int_0^{D\pi} e^{-jk\varepsilon} d\varepsilon \right]. \quad (3.15)$$

Solving the integral terms, one gets,

$$\langle V_{AB} \rangle_k = \frac{V_{in}}{2\pi} \left[\left(\frac{e^{-jkD\pi} - 1}{-jk} \right) - \left(\frac{e^{-jk(-\pi+D\pi)} - e^{jk\pi}}{-jk} \right) \right]. \quad (3.16)$$

After some manipulations and assuming that k is an odd number, one obtains

$$\langle V_{AB} \rangle_{k(odd)} = V_{in} \cdot j \left[\frac{(e^{-j\pi})^{kD} - 1}{k\pi} \right]. \quad (3.17)$$

Assuming that v_{AB} can be well approximated by its first time-varying harmonics, the fundamental term $\langle V_{AB} \rangle_1$ is calculated as

$$\langle V_{AB} \rangle_1 = V_{in} \cdot j \left[\frac{(e^{-j\pi})^D - 1}{\pi} \right]. \quad (3.18)$$

The term $e^{-j\pi}$ is defined as

$$e^{-j\pi} = \cos(\pi) - j \sin(\pi). \quad (3.19)$$

Substituting (3.19) in (3.18), and after some manipulations, the final expression of the fundamental term of the Fourier series $\langle V_{AB} \rangle_1$ for the voltage v_{AB} is given by

$$\langle V_{AB} \rangle_1 = \frac{V_{in}}{\pi} [\sin(D\pi) + j(\cos(D\pi) - 1)]. \quad (3.20)$$

After obtaining the Fourier representation of the voltage v_{AB} , the next step is to find the Fourier representation of the term $\text{abs}(i_T)$, which represents the average current of the output rectifier. The input current of the output rectifier i_T is depicted in **Fig. 3.4**. As shown in **Fig. 3.2**, the current i_T is equal to the resonant current i_{Ls} when the voltage across the parallel capacitor is clamped to $V_o/2$ ($V_o' = V_o/2n$) and is equal to zero, otherwise.

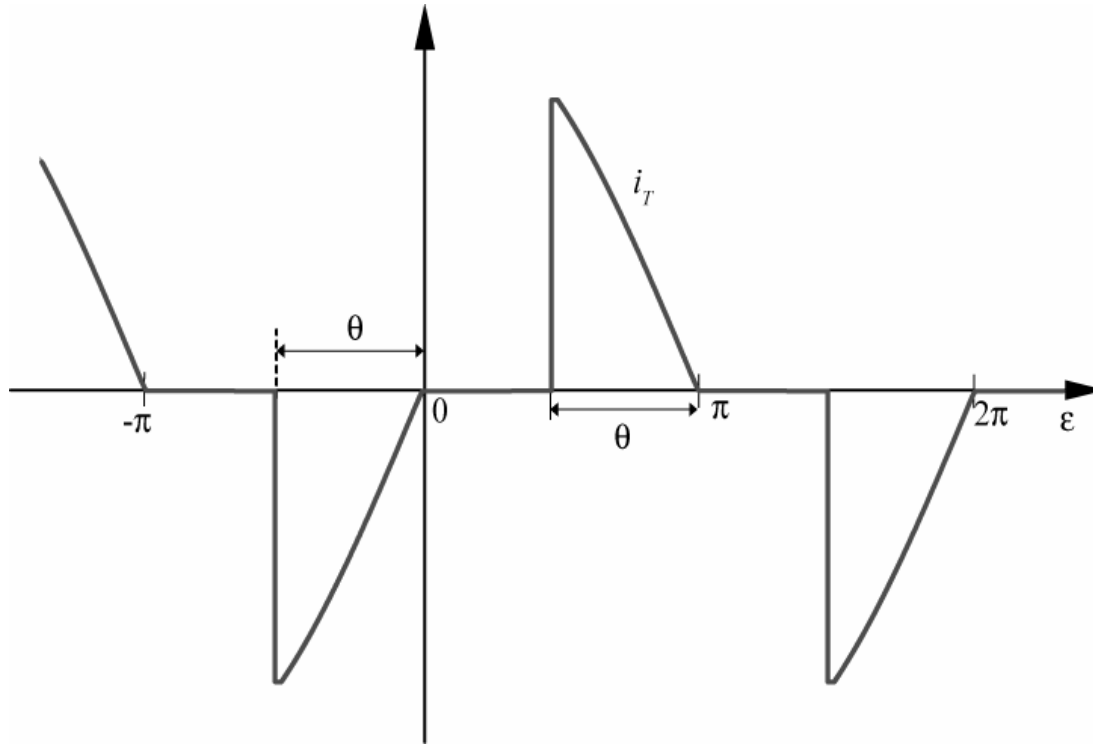


Fig. 3.4: Output rectifier input current i_T .

The values of i_T for the different intervals from $-\pi$ to π are given by

$$i_T = \begin{cases} 0 & \text{if } -\pi < \varepsilon < -\theta \\ \hat{I}_{Ls} \sin(\varepsilon) & \text{if } -\theta < \varepsilon < 0 \\ 0 & \text{if } 0 < \varepsilon < \pi - \theta \\ \hat{I}_{Ls} \sin(\varepsilon) & \text{if } \pi - \theta < \varepsilon < \pi \end{cases} \quad (3.21)$$

where \hat{I}_{Ls} is the peak value of the resonant current.

One is interested in the rectified value of the current i_T . The rectified value $\text{abs}(i_T)$ is shown in **Fig. 3.5** and is described as

$$\text{abs}(i_T) = \begin{cases} -i_T & \text{if } -\pi < \varepsilon < 0 \\ i_T & \text{if } 0 < \varepsilon < \pi \end{cases} \quad (3.22)$$

The DC coefficient of the Fourier series of $\text{abs}(i_T)$ is given by

$$\langle \text{abs}(i_T) \rangle_0 = \frac{1}{2\pi} \int_{-\pi}^{\pi} \text{abs}(i_T(\varepsilon)) e^{-j0\varepsilon} d\varepsilon \quad (3.23)$$

Simplifying (3.23), one gets

$$\langle \text{abs}(i_T) \rangle_0 = \frac{1}{2\pi} \int_{-\pi}^{\pi} \text{abs}(i_T(\varepsilon)) d\varepsilon \quad (3.24)$$

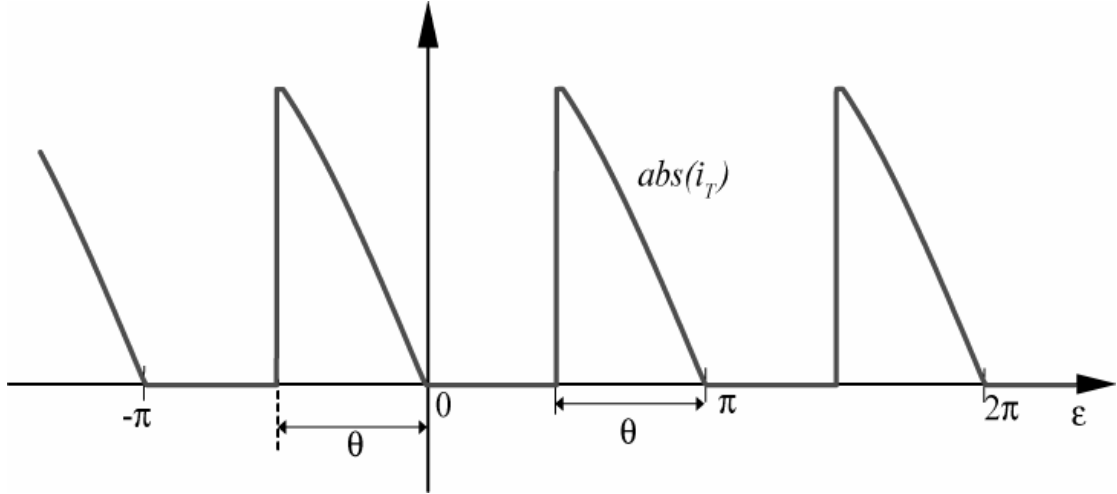


Fig. 3.5: Rectified i_T waveform.

Using the functions (3.21) and (3.22), one has

$$\langle abs(i_T) \rangle_0 = \frac{1}{2\pi} \left[\int_{-\theta}^0 -\hat{I}_{Ls} \sin(\varepsilon) d\varepsilon + \int_{\pi-\theta}^{\pi} \hat{I}_{Ls} \sin(\varepsilon) d\varepsilon \right] \quad (3.25)$$

Solving (3.25), the DC coefficient is given by

$$\langle abs(i_T) \rangle_0 = \frac{\hat{I}_{Ls}}{\pi} [1 - \cos(\theta)] \quad (3.26)$$

As it has been assumed that the resonant current i_{Ls} is purely sinusoidal, it can be written as the sum of the first harmonics of the complex Fourier series, i.e., the coefficients $\langle \bullet \rangle_{-1}$ and $\langle \bullet \rangle_1$. Thus,

$$i_{Ls} = \langle I_{Ls} \rangle_1 e^{j\varepsilon} + \langle I_{Ls} \rangle_{-1} e^{-j\varepsilon} \quad (3.27)$$

The coefficients $\langle I_{Ls} \rangle_{-1}$ and $\langle I_{Ls} \rangle_1$ are complex conjugate, thus they have the same magnitude. Therefore, the peak value of the resonant current may be written as

$$\hat{I}_{Ls} = 2 \left| \langle I_{Ls} \rangle_1 \right| \quad (3.28)$$

Eq. (3.29) is the final equation of the Fourier series DC coefficient that represents the average current of the output rectifier.

$$\langle abs(i_T) \rangle_0 = \frac{2 \cdot \left| \langle I_{Ls} \rangle_1 \right|}{\pi} \cdot [1 - \cos(\theta)] \quad (3.29)$$

The rectifier conduction angle θ is defined in **Chapter 2** for steady-state operation. In order to apply the generalized averaging method, it is necessary to write θ as a function of state variables, inputs and circuit parameters.

The resonant current flows through the parallel capacitor in the interval $0 - \pi - \theta$, as shown in **Fig. 3.6**. During this interval no power is transferred from the resonant tank to the output rectifier.

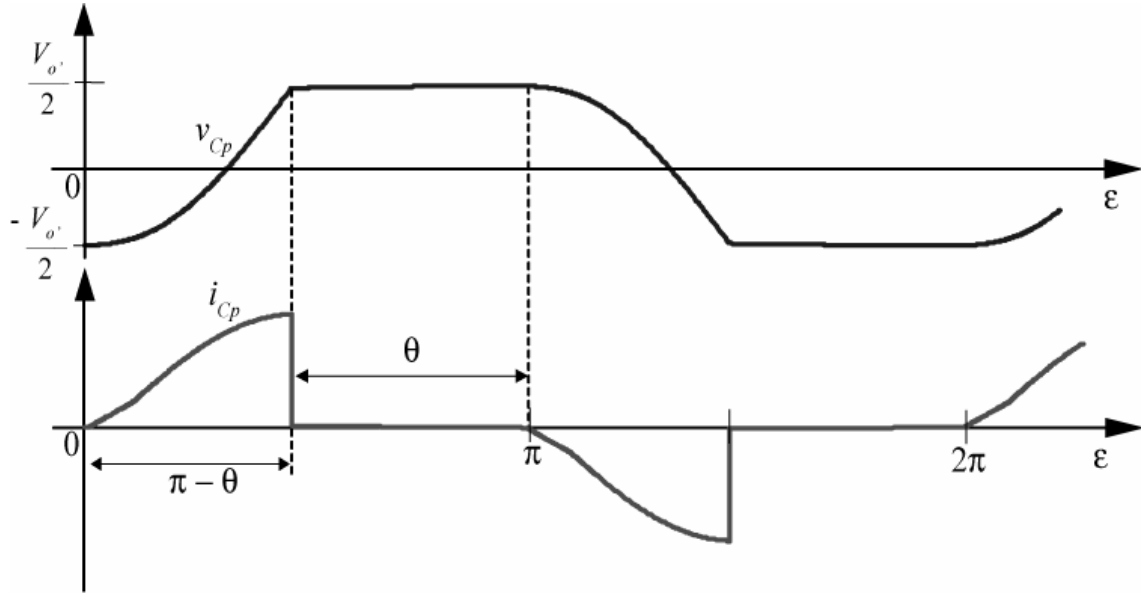


Fig. 3.6: Voltage and current waveforms of the parallel capacitor.

Assuming that $\varepsilon = \omega_s t$, the time evolution of the current in the parallel capacitor during this interval may be approximated by

$$i_{Cp}(t) = \hat{I}_{Ls} \sin(\omega_s t) \quad (3.30)$$

During the interval $(0 - \pi - \theta)$, the voltage across the parallel capacitor C_p increases from $-V_o'/2$ to $+V_o'/2$. The time evolution of the voltage v_{Cp} within this interval is given by

$$v_{Cp}(t) = v_{Cp}(0) + \frac{1}{C_p} \int_0^t \hat{I}_{Ls} \sin(\omega_s t) dt \quad (3.31)$$

Solving this equation, one obtains

$$v_{Cp}(t) = -\frac{V_o'}{2} + \frac{\hat{I}_{Ls}}{\omega_s C_p} (1 - \cos(\omega_s t)) \quad (3.32)$$

In the following, one can apply this equation to the point $\omega_s t_1 = \pi - \theta$. There, one knows from **Fig. 3.6** that $v_{Cp}(t_1) = V_o'/2$. Thus, (3.32) becomes

$$\frac{V_o'}{2} = -\frac{V_o'}{2} + \frac{\hat{I}_{Ls}}{\omega_s C_p} (1 - \cos(\pi - \theta)). \quad (3.33)$$

After some manipulations, the equation of the rectifier conduction angle θ becomes

$$\theta = \cos^{-1} \left(\frac{\omega_s C_p V_{o'}}{\hat{I}_{L_s}} - 1 \right). \quad (3.34)$$

As shown in (3.28), the amplitude of the resonant current is twice the first harmonics of the complex Fourier series. In addition, the output voltage is assumed to be represented with the DC coefficient of the complex Fourier series. Thus, (3.34) can be rewritten as

$$\theta = \cos^{-1} \left(\frac{\omega_s C_p \langle V_{o'} \rangle_0}{2 \cdot |\langle I_{L_s} \rangle_1|} - 1 \right). \quad (3.35)$$

The complete nonlinear model for the dynamics of the local harmonics, assuming that the switching frequency varies slowly from one switching period to the next, is given by

$$\frac{d \langle I_{L_s} \rangle_1}{dt} = -j\omega_s \langle I_{L_s} \rangle_1 + \frac{1}{L_s} \left\{ -\langle V_{C_s} \rangle_1 - \langle V_{C_p} \rangle_1 + \langle V_{AB} \rangle_1 \right\} \quad (3.36)$$

$$\frac{d \langle V_{C_s} \rangle_1}{dt} = -j\omega_s \langle V_{C_s} \rangle_1 + \frac{1}{C_s} \langle I_{L_s} \rangle_1 \quad (3.37)$$

$$\frac{d \langle V_{o'} \rangle_0}{dt} = \frac{1}{C_{o'}} \left\{ \langle abs(i_T) \rangle_0 - \frac{2 \cdot \langle V_{o'} \rangle_0}{R_{o'}} \right\} \quad (3.38)$$

where

$$\langle V_{AB} \rangle_1 = \frac{V_{in}}{\pi} [\sin(D\pi) + j(\cos(D\pi) - 1)] \quad (3.39)$$

$$\theta = \cos^{-1} \left(\frac{\omega_s C_p \langle V_{o'} \rangle_0}{2 \cdot |\langle I_{L_s} \rangle_1|} - 1 \right) \quad (3.40)$$

$$\langle abs(i_T) \rangle_0 = \frac{2 \cdot |\langle I_{L_s} \rangle_1|}{\pi} \cdot [1 - \cos(\theta)] \quad (3.41)$$

The new state variables are: $\langle I_{L_s} \rangle_1$, $\langle V_{C_s} \rangle_1$ and $\langle V_{o'} \rangle_0$. The state variables $\langle I_{L_s} \rangle_1$ and $\langle V_{C_s} \rangle_1$ are complex Fourier coefficients that can be rewritten with real variables by separating the real and imaginary parts of

the equations (3.36) and (3.37). Thus, the state variables can be written as: $\langle I_{L_s} \rangle_1 = x_1 + jx_2$, $\langle V_{C_s} \rangle_1 = x_3 + jx_4$ and $\langle V_o \rangle_0 = x_7$. Therefore, a fifth order state space model with real variables is obtained. The terms x_1 and x_3 represent the cosine components of the waveforms and the terms x_2 and x_4 , the sinusoidal parts. The voltage across the parallel capacitor can be also written as a function of real variables: $\langle V_{C_p} \rangle_1 = x_5 + jx_6$ [MRDP⁺02].

Eq. (3.40) and (3.41) can be rewritten as:

$$\theta = \cos^{-1} \left(\frac{\omega_s C_p x_7}{2 \cdot \sqrt{x_1^2 + x_2^2}} - 1 \right) \quad (3.42)$$

$$\langle abs(i_T) \rangle_0 = \frac{2 \cdot \sqrt{x_1^2 + x_2^2}}{\pi} \cdot [1 - \cos(\theta)]. \quad (3.43)$$

As already stated, the voltage across the parallel capacitor is not considered as a state variable. Therefore, one needs to express this voltage as a function of the state variables. x_5 and x_6 are expressed as a function of the existing state variables x_1 and x_2 by

$$x_5 = \frac{1}{\pi \omega_s C_p} [x_1 \delta + x_2 \gamma] \quad (3.44)$$

$$x_6 = \frac{1}{\pi \omega_s C_p} [x_2 \delta - x_1 \gamma] \quad (3.45)$$

where

$$\gamma = \pi - \theta + \frac{1}{2} \sin(2\theta) \quad (3.46)$$

$$\delta = \sin^2(\theta). \quad (3.47)$$

The new state vector is given by $x = [x_1 \ x_2 \ x_3 \ x_4 \ x_7]^T$ and the model with real variables is

$$\frac{dx_1}{dt} = \omega_s x_2 - \frac{x_3}{L_s} - \frac{x_5}{L_s} + \frac{V_{in}}{\pi \cdot L_s} \sin(D\pi) \quad (3.48)$$

$$\frac{dx_2}{dt} = -\omega_s x_1 - \frac{x_4}{L_s} - \frac{x_6}{L_s} + \frac{V_{in}}{\pi \cdot L_s} [\cos(D\pi) - 1] \quad (3.49)$$

$$\frac{dx_3}{dt} = \omega_s x_4 + \frac{x_1}{C_s} \quad (3.50)$$

$$\frac{dx_4}{dt} = -\omega_s x_3 + \frac{x_2}{C_s} \quad (3.51)$$

$$\frac{dx_7}{dt} = \frac{2 \cdot \sqrt{x_1^2 + x_2^2}}{\pi \cdot C_{o'}} \cdot [1 - \cos(\theta)] - \frac{2 \cdot x_7}{R_{o'} \cdot C_{o'}} \quad (3.52)$$

The switching frequency ω_s and duty cycle D are defined as the control inputs u_1 and u_2 , respectively. The output voltage, the amplitude of the resonant current and the amplitude of the voltage in the series-capacitor are defined as the outputs y_1 , y_2 and y_3 , respectively.

$$u_1 = \omega_s \quad (3.53)$$

$$u_2 = D \quad (3.54)$$

$$y_1 = x_7 \quad (3.55)$$

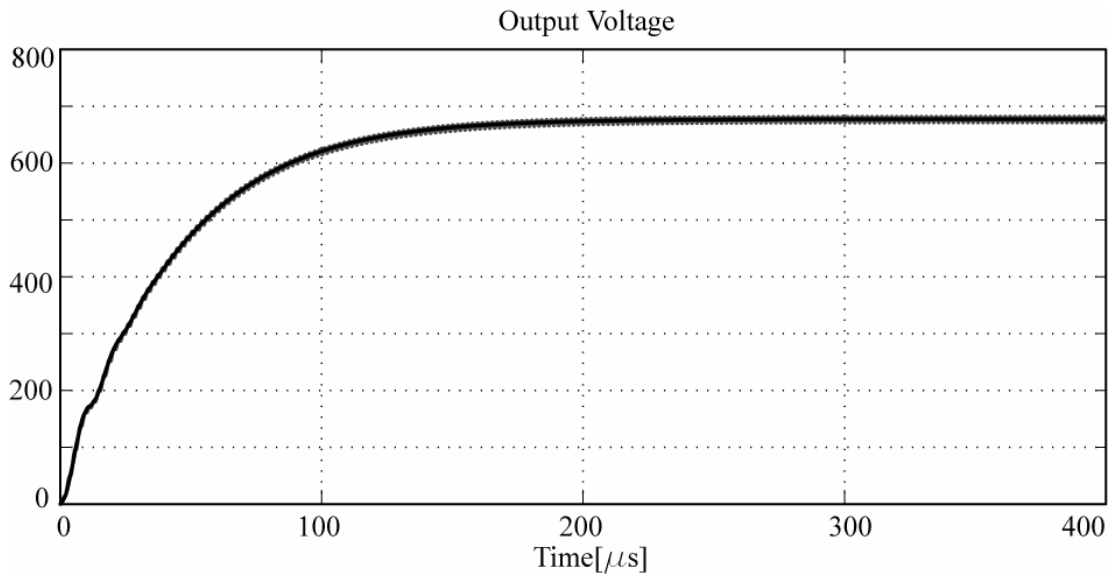
$$y_2 = 2 \cdot \sqrt{x_1^2 + x_2^2} \quad (3.56)$$

$$y_3 = 2 \cdot \sqrt{x_3^2 + x_4^2} \quad (3.57)$$

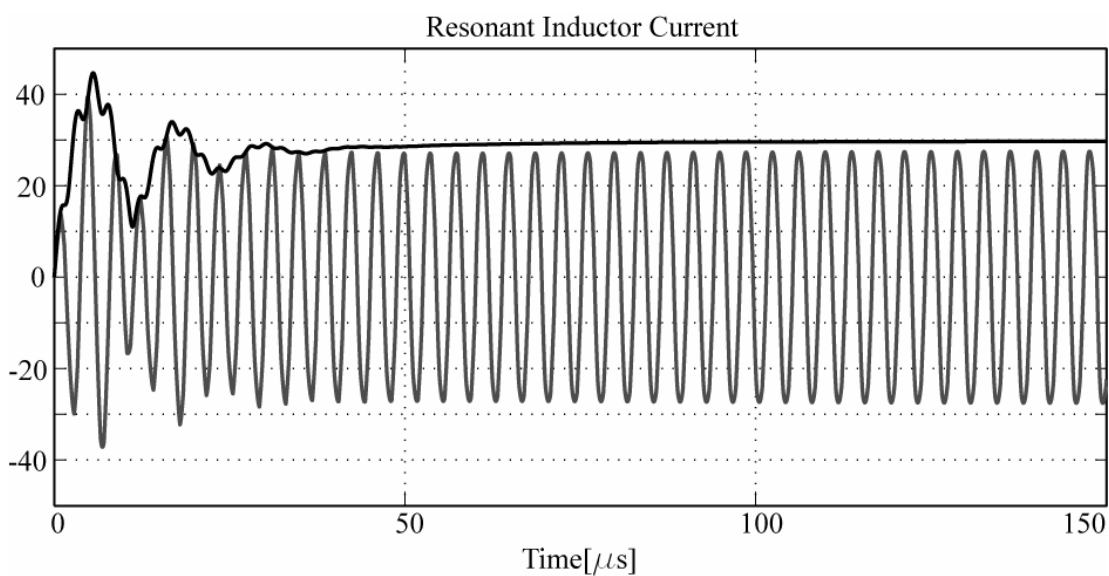
The converter system is designed with following parameters, which is representative of the experimental system of **Chapter 5**: $V_{in} = 325\text{V}$, $V_{o'} = 677\text{V} \dots 1838\text{V}$, $I_{o'} = 0 \dots 6.8\text{A}$, $P_o = 0 \dots 5\text{kW}$, $f_s = 260\text{kHz} \dots 410\text{kHz}$, $L_s = 16\mu\text{H}$, $C_s = 48\text{nF}$, $C_p = 15\text{nF}$, C_{o1}' , $C_{o2}' = 1\mu\text{F}$, $n = 17$.

Based on the generalized averaging model, digital simulations using MATLAB/SIMULINK are performed. The parameters used for the simulation are: $V_{o'} = 677\text{V}$, $P_o = 4.6\text{kW}$, $D = 0.741$, $f_s = 265\text{kHz}$ and $R_{o'} = 100\Omega$. The simulation compares the magnitude of the complex coefficients obtained with the averaging method with the amplitude of the waveforms obtained simulating the switching circuit when the system starts up in open-loop with predetermined duty cycle and switching frequency (see parameters specified before). The results for the resonant current and the equivalent output voltage referred to the primary side of the transformer are shown in **Fig. 3.7**. The results show that the correspondence between the waveforms obtained with the model and with the simulated circuit is excellent. For example in **Fig. 3.7(a)** the correspondence of the $V_{o'}$ waveforms is so good, that one almost cannot distinguish between model and simulation results except for a small ripple in the simulated waveform. The model characterizes the dynamic behavior of the system using

amplitude modulation and frequency $f_s + f_o$. This is clearly observed in the start up transient of the resonant current in **Fig. 3.7(b)**. Due to the good results obtained, the large signal model based on generalized averaging method is a good starting point to derive the small-signal model of the converter.



(a)



(b)

Fig. 3.7: Comparison of the amplitude of the model variables with the simulated waveforms: (a) output voltage V_o (100V/div); (b) resonant current i_{Ls} (10A/div).

3.3. SMALL-SIGNAL MODEL

In order to find the small-signal model for the series-parallel resonant converter with capacitive output filter the first step is to obtain a

steady state solution of the system. This can be done by setting the derivatives of Eq. (3.48)-(3.52) equal to zero. Furthermore, the steady-state value θ_{ss} of the angle θ is taken from [CK03]. The equations that represent the steady-state solution are given by

$$\theta_{ss} = 2 \cdot \tan^{-1} \sqrt{\frac{2\pi}{\omega_s C_p R_o}} \quad (3.58)$$

$$\gamma_{ss} = \pi - \theta_{ss} + \frac{1}{2} \sin(2\theta_{ss}) \quad (3.59)$$

$$\delta_{ss} = \sin^2(\theta_{ss}) \quad (3.60)$$

$$\alpha = \frac{C_p}{C_s} \quad (3.61)$$

$$K = \frac{\omega_{s_{ss}} \cdot C_p \cdot V_{in}}{\delta_{ss}} \quad (3.62)$$

$$M = \frac{\delta_{ss}}{\gamma_{ss} + \pi \cdot \alpha - \pi \cdot \omega_{s_{ss}}^2 \cdot L_s \cdot C_p} \quad (3.63)$$

$$x_{1_{ss}} = -\frac{x_{2_{ss}}}{M} + K \cdot \sin(D\pi) \quad (3.64)$$

$$x_{2_{ss}} = \frac{K \cdot M^2}{(1 + M^2)} \left\{ \frac{\sin(D\pi)}{M} + [\cos(D\pi) - 1] \right\} \quad (3.65)$$

$$x_{3_{ss}} = \frac{x_{2_{ss}}}{\omega_{s_{ss}} \cdot C_s} \quad (3.66)$$

$$x_{4_{ss}} = -\frac{x_{1_{ss}}}{\omega_{s_{ss}} \cdot C_s} \quad (3.67)$$

$$x_{5_{ss}} = \frac{1}{\pi \omega_{s_{ss}} C_p} [x_{1_{ss}} \delta_{ss} + x_{2_{ss}} \gamma_{ss}] \quad (3.68)$$

$$x_{6_{ss}} = \frac{1}{\pi \omega_{s_{ss}} C_p} [x_{2_{ss}} \delta_{ss} - x_{1_{ss}} \gamma_{ss}] \quad (3.69)$$

$$x_{7_{ss}} = \frac{R_o' \sqrt{x_{1_{ss}}^2 + x_{2_{ss}}^2}}{\pi} [1 - \cos(\theta_{ss})] \quad (3.70)$$

After obtaining the steady-state solution, the model can be linearized around the steady state in order to obtain the small-signal transfer functions

from any desired input to any desired output. After the linearization one obtains a linearized model of the type given by Eq. (3.71).

$$\begin{cases} \dot{\vec{\Delta x}} = A\vec{\Delta x} + B\vec{\Delta u} \\ \vec{\Delta y} = C\vec{\Delta x} + D\vec{\Delta u} \end{cases} \quad (3.71)$$

where A , B , C and D are matrices that describe the system, \vec{x} is the state vector, \vec{u} is the input vector, \vec{y} is the output vector and Δ means the small changes of the respective parameter.

Matrix A is a 5x5 system matrix and it gives the relation between the derivative of states and the states.

$$A = \begin{bmatrix} a_{11} & a_{12} & a_{13} & 0 & a_{15} \\ a_{21} & a_{22} & 0 & a_{24} & a_{25} \\ a_{31} & 0 & 0 & a_{34} & 0 \\ 0 & a_{42} & a_{43} & 0 & 0 \\ a_{51} & a_{52} & 0 & 0 & a_{55} \end{bmatrix}$$

where

$$I_{1_{ss}} = \sqrt{x_{1_{ss}}^2 + x_{2_{ss}}^2} \quad (3.72)$$

$$G_1 = \frac{x_{9_{ss}}^2 \cdot \omega_s \cdot C_p}{4 \cdot \pi \cdot L_s \cdot I_{1_{ss}}^2} - \frac{x_{9_{ss}}}{\pi \cdot L_s \cdot I_{1_{ss}}} \quad (3.73)$$

$$G_2 = \left(\frac{x_{9_{ss}}}{\pi \cdot L_s \cdot I_{1_{ss}}} - \frac{x_{9_{ss}}^2 \cdot \omega_s \cdot C_p}{2 \cdot \pi \cdot L_s \cdot I_{1_{ss}}^2} \right) \quad (3.74)$$

$$G_3 = \frac{2}{\pi \cdot \omega_s \cdot C_p \cdot L_s \cdot I_{1_{ss}}^2 \cdot \tan\left(\frac{\theta_{ss}}{2}\right)} + \frac{x_{9_{ss}}^2 \cdot \omega_s \cdot C_p \cdot \tan\left(\frac{\theta_{ss}}{2}\right)}{2 \cdot \pi \cdot L_s \cdot I_{1_{ss}}^4} \quad (3.75)$$

$$- \frac{x_{9_{ss}}}{2 \cdot \pi \cdot L_s \cdot I_{1_{ss}}^3} \left(\tan\left(\frac{\theta_{ss}}{2}\right) + \frac{1}{\tan\left(\frac{\theta_{ss}}{2}\right)} \right)$$

$$G_4 = \omega_s - \frac{1}{\omega_s \cdot C_p \cdot L_s} + \frac{\theta_{ss}}{\pi \cdot \omega_s \cdot C_p \cdot L_s} \quad (3.76)$$

$$a_{11} = G_1 + \frac{x_{1_{ss}}^2}{I_{1_{ss}}^2} \cdot G_2 + x_{1_{ss}} \cdot x_{2_{ss}} \cdot G_3 \quad (3.77)$$

$$a_{12} = \left[\frac{x_{1_{ss}} \cdot x_{2_{ss}}}{I_{1_{ss}}^2} + \frac{1}{2} \tan\left(\frac{\theta_{ss}}{2}\right) \right] \cdot G_2 + x_{2_{ss}}^2 \cdot G_3 + G_4 \quad (3.78)$$

$$a_{13} = -\frac{1}{L_s} \quad (3.79)$$

$$a_{15} = -\frac{x_{1_{ss}}}{x_{9_{ss}}} \cdot G_2 - \frac{x_{2_{ss}} \cdot I_{1_{ss}}^2}{x_{9_{ss}}} G_3 \quad (3.80)$$

$$a_{21} = \left[\frac{x_{1_{ss}} \cdot x_{2_{ss}}}{I_{1_{ss}}^2} - \frac{1}{2} \tan\left(\frac{\theta_{ss}}{2}\right) \right] \cdot G_2 - x_{1_{ss}}^2 \cdot G_3 - G_4 \quad (3.81)$$

$$a_{22} = G_1 + x_{2_{ss}}^2 \cdot G_2 - x_{1_{ss}} \cdot x_{2_{ss}} \cdot G_3 \quad (3.82)$$

$$a_{24} = -\frac{1}{L_s} \quad (3.83)$$

$$a_{25} = -\frac{x_{2_{ss}}}{x_{9_{ss}}} \cdot G_2 + \frac{x_{1_{ss}} \cdot I_{1_{ss}}^2}{x_{9_{ss}}} G_3 \quad (3.84)$$

$$a_{31} = \frac{1}{C_s} \quad (3.85)$$

$$a_{34} = \omega_s \quad (3.86)$$

$$a_{42} = \frac{1}{C_s} \quad (3.87)$$

$$a_{43} = -\omega_s \quad (3.88)$$

$$a_{51} = \frac{4 \cdot x_{1_{ss}}}{\pi \cdot C_{o'} \cdot I_{1_{ss}}} \quad (3.89)$$

$$a_{52} = \frac{4 \cdot x_{2_{ss}}}{\pi \cdot C_{o'} \cdot I_{1_{ss}}} \quad (3.90)$$

$$a_{55} = -\frac{1}{C_{o'}} \left(\frac{\omega_s \cdot C_p}{\pi} + \frac{2}{R_{o'}} \right) \quad (3.91)$$

B is the input matrix and it relates the derivative of the states with the system inputs. Inputs D and ω_s have been chosen for the system. This means that B is a 5x2 matrix.

$$B = \begin{bmatrix} b_{11} & b_{12} \\ b_{21} & b_{22} \\ b_{31} & 0 \\ b_{41} & 0 \\ b_{51} & 0 \end{bmatrix}$$

where

$$H_1 = \frac{x_{9_{ss}}^2 \cdot C_p}{4 \cdot \pi \cdot L_s \cdot I_{1_{ss}}^2} \quad (3.92)$$

$$H_2 = 1 + \frac{1}{\omega_s^2 \cdot C_p \cdot L_s} - \frac{\theta_{ss}}{\pi \cdot \omega_s^2 \cdot C_p \cdot L_s} - \frac{2}{\pi \cdot \omega_s^2 \cdot C_p \cdot L_s \cdot \tan\left(\frac{\theta_{ss}}{2}\right)} - \frac{x_{9_{ss}}^2 \cdot C_p \cdot \tan\left(\frac{\theta_{ss}}{2}\right)}{4 \cdot \pi \cdot L_s \cdot I_{1_{ss}}^2} + \frac{x_{9_{ss}}}{2 \cdot \pi \cdot \omega_s \cdot L_s \cdot I_{1_{ss}} \cdot \tan\left(\frac{\theta_{ss}}{2}\right)} \quad (3.93)$$

$$b_{11} = x_{1_{ss}} \cdot H_1 + x_{2_{ss}} \cdot H_2 \quad (3.94)$$

$$b_{21} = x_{2_{ss}} \cdot H_1 - x_{1_{ss}} \cdot H_2 \quad (3.95)$$

$$b_{31} = x_{4_{ss}} \quad (3.96)$$

$$b_{41} = -x_{3_{ss}} \quad (3.97)$$

$$b_{51} = -\frac{x_{9_{ss}} \cdot C_p}{\pi \cdot C_o} \quad (3.98)$$

$$b_{12} = \frac{V_{in}}{L_s} \cos(D\pi) \quad (3.99)$$

$$b_{22} = -\frac{V_{in}}{L_s} \sin(D\pi) \quad (3.100)$$

The matrix that relates the states with the output is the C matrix. There are three outputs and five states thus C is a 3x5 matrix.

$$C = \begin{bmatrix} 0 & 0 & 0 & 0 & 1 \\ c_{21} & c_{22} & 0 & 0 & 0 \\ 0 & 0 & c_{33} & c_{34} & 0 \end{bmatrix}$$

where

$$V_{1_{ss}} = \sqrt{x_{3_{ss}}^2 + x_{4_{ss}}^2} \quad (3.101)$$

$$c_{21} = \frac{2 \cdot x_{1_{ss}}}{I_{1_{ss}}} \quad (3.102)$$

$$c_{22} = \frac{2 \cdot x_{2_{ss}}}{I_{1_{ss}}} \quad (3.103)$$

$$c_{33} = \frac{2 \cdot x_{3_{ss}}}{V_{1_{ss}}} \quad (3.104)$$

$$c_{34} = \frac{2 \cdot x_{4_{ss}}}{V_{1_{ss}}}. \quad (3.105)$$

Finally, matrix D is called the direct transmission matrix and it represents the elements that transmit an input directly to the output of the system. For our case D is a 3x2 zero matrix.

It is important to point out that the steady state solution is dependent on the operating point of the system (desired output voltage and load). Thus, there is one steady state solution for each operating point of the system. This makes the symbolic linearization of the system complex but it is still possible to obtain analytical solutions for all equations. And if one is interested in a specific operation point then the numerical explicit solutions are easily computed with software such as MATLAB. Therefore this procedure can be used to calculate transfer functions for desired operating points in a fast and reliable way.

With the linear system formed by the matrices A , B , C , D one is in position to obtain the six transfer functions that relate the control input u_1 (switching frequency) or u_2 (duty cycle, D) to the outputs y_1 (output voltage), y_2 (amplitude of the resonant current) or y_3 , (amplitude of the voltage in the series capacitor). The transfer functions that relate the inputs u_1 , u_2 with the output y_1 , are particularly interesting because the main control purpose is to adjust the output voltage to any desired reference

value for all kind of load changes. The switching frequency of the converter is automatically adjusted to ensure zero-current switching of one bridge leg while the output power is controlled by duty cycle variation. Therefore, the transfer function that is essential for the controller design is the transfer function that relates duty cycle with output voltage $G(s) = \Delta V_o / \Delta D = \Delta y_1 / \Delta u_2$.

The fact that the variation of the switching frequency is not modeled in $G(s)$ is justified by the assumption that changes in the switching frequency are instantaneous when compared with dynamics of the output voltage. For this reason the variation of the switching frequency can be modeled as a constant disturbance w added to the output of $G(s)$ as shown in Fig. 3.8.

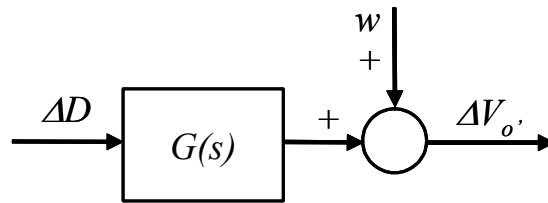


Fig. 3.8: Block diagram of the open loop system including the effect of the switching frequency variation.

This constant disturbance does not have significant influence on the high-frequency behavior and stability of the closed loop system. However, it is important to design a controller $C(s)$ that increase the open loop gain $G(s)C(s)$ at low frequencies to improve the disturbance rejection at low frequencies.

3.4. SIMULATION RESULTS

Fig. 3.9 presents the Bode magnitude and phase plots of the transfer function that relates duty cycle with output voltage. They represent the transfer function $G(s)$ for different load conditions from full power to very low power. The five different output voltage / output power operating points are: 23kV/4.6kW, 46kV/5kW, 62.5kV/5kW, 62.5kV/0.5kW and 46kV/2.5kW. These points are arbitrarily chosen just in order to show how the transfer function changes within the operating range of the converter.

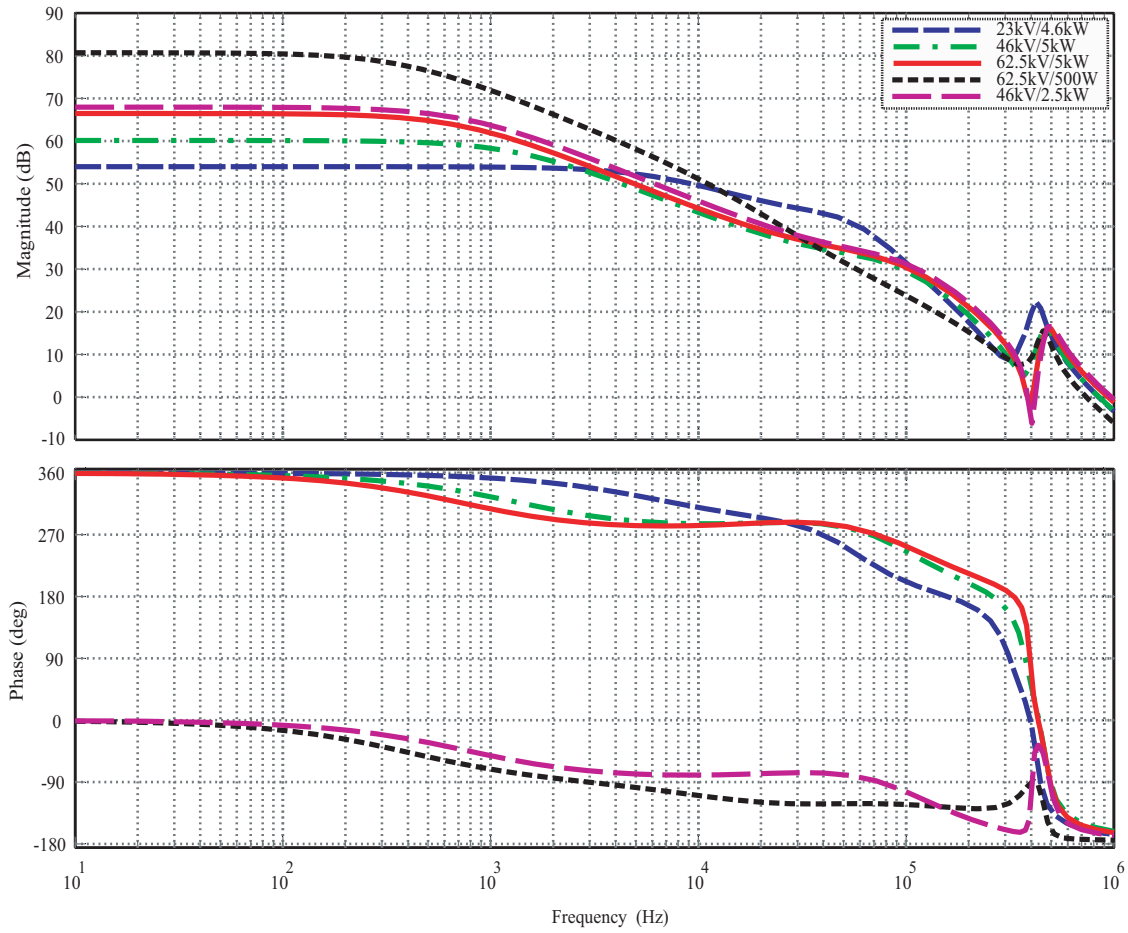


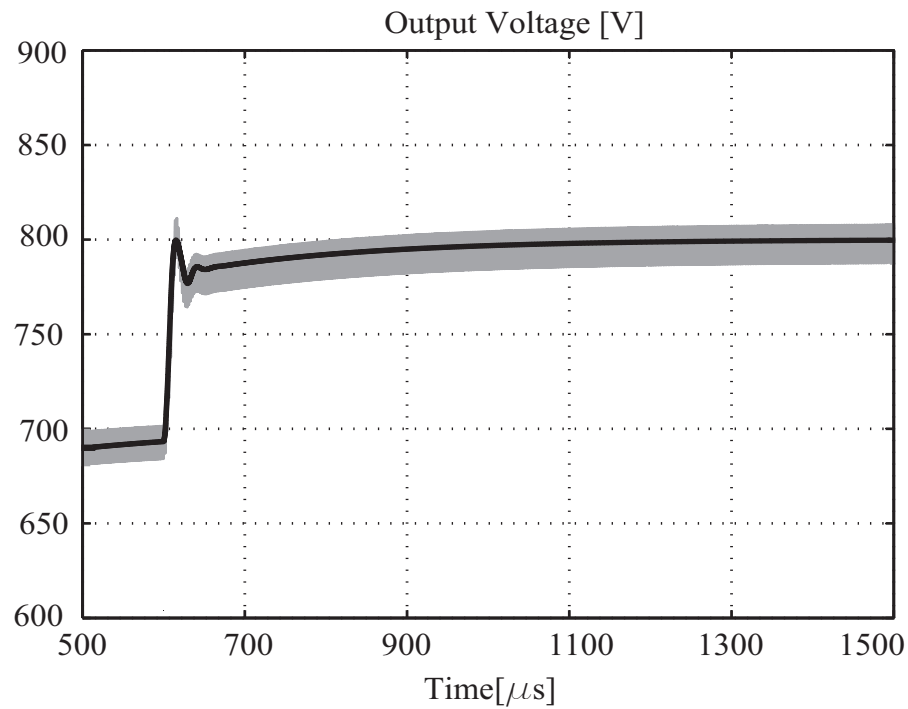
Fig. 3.9: Bode plots of $G(s)$ for different operating points of the system.

If one observes the phase plot of **Fig. 3.9**, it is observed that for three operating points the phase starts at 360° for $s \rightarrow 0$. Of course, this phase is not real. The diagrams are calculated using MATLAB® and this software has its own way to display the waveforms. It adds 360° to the phase of a given transfer function until the minimum phase in the scale is -180° .

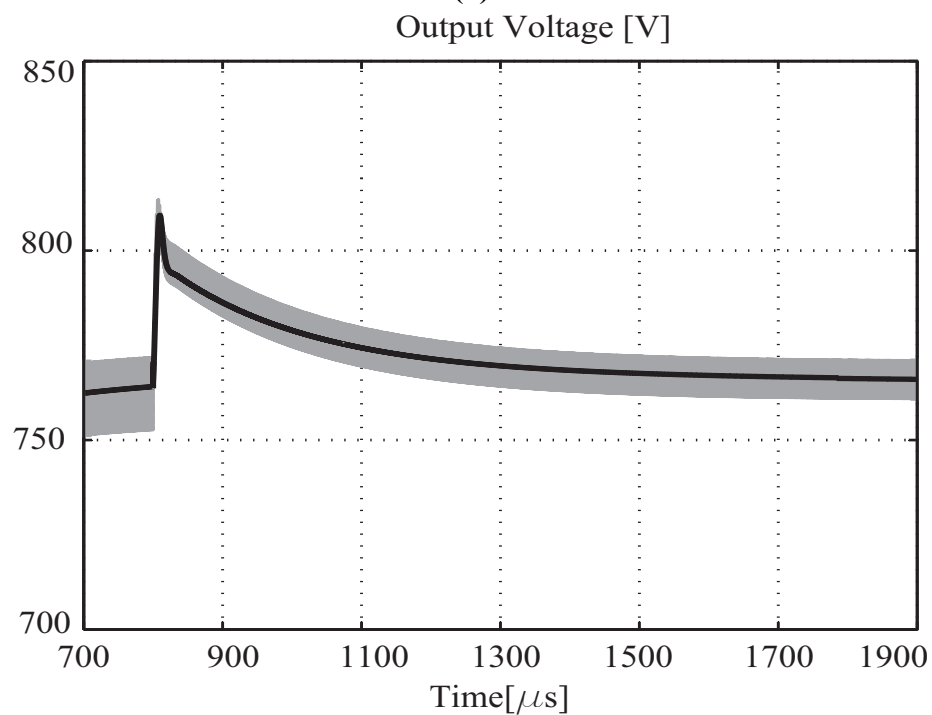
One can see that the DC gain of the transfer function $G(s)$ changes significantly with the load. The model is accurate up to the switching frequency [YLJ92a] of each operating point. The phase plot shows that for some load conditions the transfer function has two non minimum phase zeros, which indicates that the system could be difficult to control. This characteristic is evident comparing phase transitions for the same output voltage, 62.5kV, and different output power, 5kW and 500W. For 5kW the system is non minimum phase and for 500W is minimum phase. However, the phase dropping occurs at very high-frequency. Hence, it does not take influence on the control loop design.

In order to prove that the small-signal model well approximates the converter, simulations using MATLAB® were undertaken for various loads and reference output voltage steps. **Fig. 3.10(a)** shows a comparison between the simulated switching circuit with a constant load ($R_o = 128\Omega$) and the linearized model about the point $V_o = 767\text{V}$. It represents the closed loop response (using a PI controller with fixed parameters) to a step change in the reference voltage referred to the primary side of the transformer $V_{o,ref}$ from 700V to 800V. Considering the definitions of Section 3.2: $V_o = V_o/2n$ and $n =$ transformer turns ratio, and taking $n = 17$, which is the value chosen for the experimental system, the previous values, referred to the high-voltage side of the transformer, correspond to a step change from 23.8kV to 27.2kV. For the simulations, maximum duty cycle is $D = 1$ and ideal components (without losses) are used. **Fig. 3.10(b)** shows a comparison between the simulated switching circuit and the linearized model when a load change occurs. This represents the step response when the reference voltage (referred to the primary side of the transformer) is held constant at 767V and the output power is reduced from 4.6kW to 2.3kW.

From the results shown in **Fig. 3.10**, one can conclude that the linearized model agrees well with the dynamics of the simulated converter. Therefore, the calculation method is valid and is a very helpful tool for the control design.



(a)



(b)

Fig. 3.10: Comparison between step response of the linearized model and of the circuit (a) with a step change in the value of reference voltage and (b) with a step change in the value of the load resistance. Scale: output voltage V_o (50V/div).

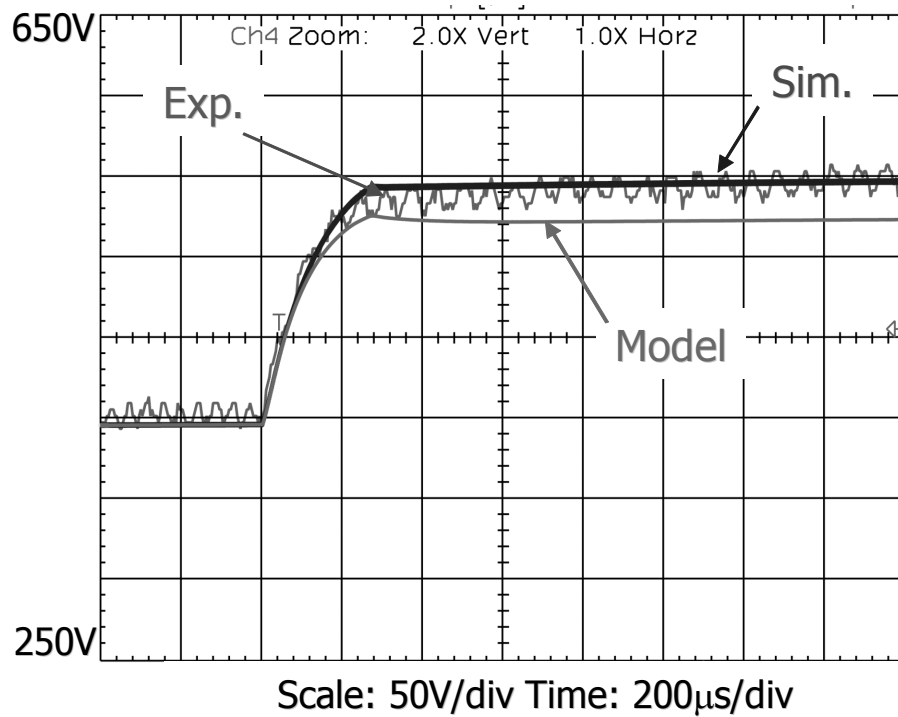
3.5. EXPERIMENTAL RESULTS

In order to verify if results obtained theoretically and with digital simulations are reproducible in practice, a 5kW prototype is built. For details about the prototype please refer to **Chapter 5**.

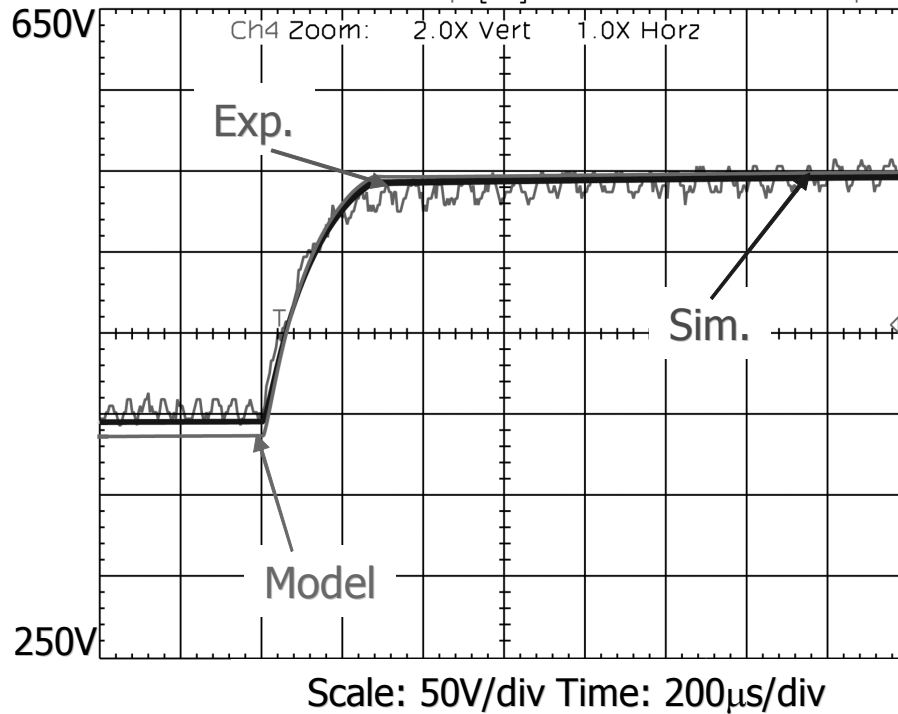
Fig. 3.11 shows the comparison between the results obtained with simulation of the small-signal model, simulation of the circuit and laboratory tests without the high-voltage transformer. This represents the closed loop response of the system using an adaptive PI controller when a step change in the reference voltage occurs. The adaptive PI controller is DSP based and the gate signals of the switches are generated using a PLD. In practice the step change in the reference voltage passes through a first-order low-pass filter with a time constant equal to $14\mu\text{s}$ included in the implementation of the system. Thus, the reference voltage slowly steps up. The experiments have been carried out at low load ($R_o = 455\Omega$) and with reduced input voltage $V_{in} = 170\text{V}$. Additionally the maximum duty cycle is limited to 0.7 in order to operate the converter with optimum commutation (see **Chapter 2** for details). The presence of the low-pass filter, the reduced input voltage and the limited duty cycle explains the slow dynamics of the output voltage compared with the simulations using idealized conditions shown in **Fig. 3.10**. At time of $400\mu\text{s}$ the reference voltage is changed from 397V to 550V. In **Fig. 3.11(a)** the model is developed with linearization about the point $V_o = 397\text{V}$, $D = 0.57$, $f_s = 443\text{ kHz}$. One can see that as long as the actual value of the output voltage is not too far from this point, the model gives good results because the consideration that the system is linear in the surrounds of this point is still valid. Once the output voltage achieves a point where the assumption of linear behavior is not valid anymore, the quality of the model deteriorates and its results do not agree well with simulation and experimental results anymore. The same is observed in **Fig. 3.11(b)** where the model is linearized about the point $V_o = 470\text{V}$, $D = 0.63$, $f_s = 425\text{ kHz}$.

The best way to eliminate this limitation of the model is to use several models. That means the system is linearized about a definite number of points and one switches between the different models in order to always have the best model for the actual operating point. The parameters,

which are adapted in the several models, are the values of the switching frequency f_s and duty cycle D , which are the control inputs of the circuit.



(a)



(b)

Fig. 3.11: Closed-loop response of the output voltage for a step change in the reference from 397V to 550V: Simulation result using the proposed model linearized about the point (a) $V_o = 397V$ and (b) $V_o = 470V$.

One example of an adaptive model is shown in **Fig. 3.12**. This adaptive scheme switches between two models dependent on the output voltage level. At the begin, the model is linearized about the point $V_o = 397\text{V}$ and when the output voltage reaches 470V the model is switched to the second model linearized about the point $V_o = 470\text{V}$. One can see that adaptive model works well for the whole transitory.

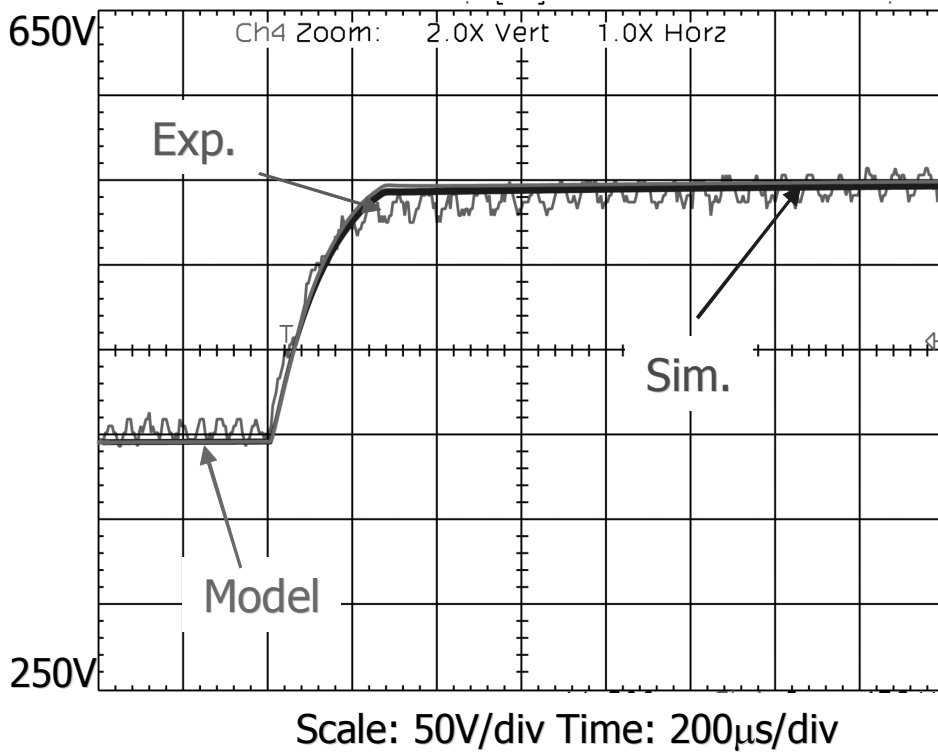


Fig. 3.12: Closed-loop response of the output voltage for a step change in the reference from 397V to 550V: Simulation result using the proposed model linearized about the point $V_o = 397\text{V}$ for $V_o < 470\text{V}$ and about the point $V_o = 470\text{V}$ for $V_o \geq 470\text{V}$.

There is a good agreement between the simulation results using the proposed small-signal model, using the circuit and the experimental results. Thus, the adaptive scheme will be used in the next chapter for the design of an adaptive controller for the series-parallel resonant converter.

3.6. SUMMARY

This chapter presents an accurate method, based on first harmonic analysis, to derive the small-signal model of the series-parallel resonant DC-DC converter with capacitive output filter. The model provides a fast and reliable way to obtain desired small-signal transfer functions of the system for each operating point. For this reason, the small-signal model

simplifies the controller design task for resonant converters by removing the need of complex mathematical analysis and saves the time required for measurements in the trial and error design method.

CHAPTER 4

4. ADAPTIVE CONTROLLERS FOR THE SERIES-PARALLEL RESONANT CONVERTER

4.1. INTRODUCTION

Resonant converters are linear piecewise systems whose global behavior is strongly nonlinear. This nonlinear aspect is one of the reasons of the difficulties encountered when calculating control laws for this type of converters [HBB⁺92]. One possible solution is to make use of adaptive controllers. According to Merriam-Webster's dictionary, “to adapt” means “to change (something) so as to make it suitable for a new use or situation” [IS96]. Intuitively, an adaptive controller is thus a controller that can modify its behavior in response to changes in the dynamics of the process and the character of the disturbances [AW95]. This chapter shows two different adaptive controllers for the series-parallel resonant DC-DC converter with capacitive output filter: a gain scheduled controller and a passivity based controller.

4.2. ADAPTIVE CONTROL

The research on control techniques in connection with the design of autopilots for high-performance aircraft in the early 1950s was one of the first motivations for the development of adaptive control. An adaptive controller is a special type of controller with adjustable parameters and a mechanism for adjusting the parameters [AW95]. The basic objective of adaptive control is to maintain consistent performance of a system in the presence of disturbances or unknown variation in plant parameters [SB03]. An adaptive control system can be thought of as having two loops. One loop is a normal feedback with the process and the controller and the other loop is the parameter adjustment loop [AW95]. The elements of a typical adaptive control system are shown in **Fig. 4.1**.

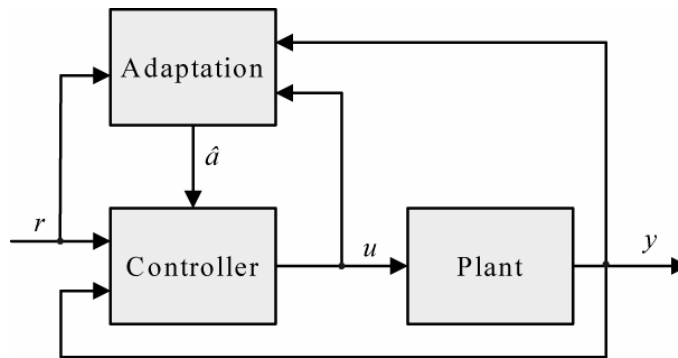


Fig. 4.1: Basic Adaptive Control Schematics.

4.2.1. Approaches to Adaptive Control

A. GAIN SCHEDULING

One of the earliest and most intuitive approaches to adaptive control is gain scheduling. This concept was introduced in the context of flight control systems in the 1950s and 1960s. The idea is to find auxiliary process variables (other than the plant outputs used for feedback) that correlate well with the changes in process dynamics. These auxiliary variables are used to change the parameters of the controller thus compensating plant parameter variations [AW95], [SB89].

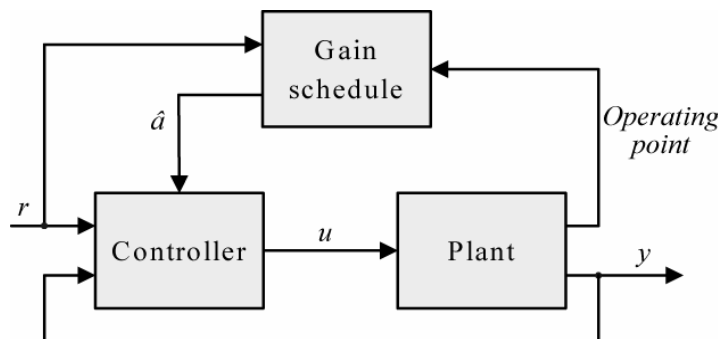


Fig. 4.2: Gain Scheduled Controller.

Gain scheduling can be regarded as a mapping from process parameters to controller parameters. It can be implemented as a function or a lookup table [AW95]. Although gain scheduling is extremely popular in practice, the disadvantage of gain scheduling is that it is a feed forward adaptation scheme, with no real “learning” or intelligence [SB89]. The main advantage of gain scheduling is that parameters can be altered fast (as fast as the auxiliary measurements) in response to changes in the plant dynamics. It is convenient particularly if the plant dynamics depend in a well-known way on easily measurable variables [SB89].

B. SELF TUNING CONTROL (STC)

Self tuning controllers estimates system parameters and then compute the control input \hat{a} using the estimated parameters. A block diagram of a self-tuning controller is shown in **Fig. 4.3**.

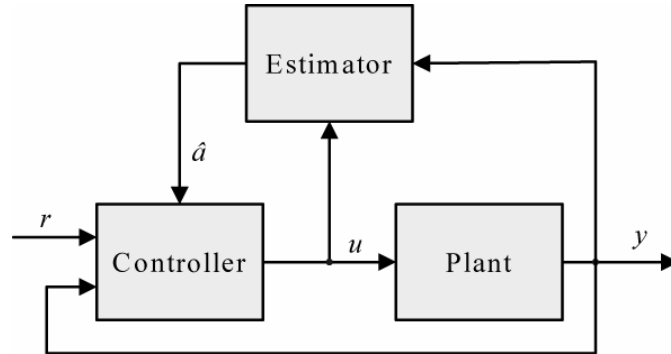


Fig. 4.3: Self-Tuning Control (STC).

The controller is called self tuning, since it has the ability to tune its own parameters; that means the controller parameters or the process parameters are estimated in real time. The estimates are used as if they are equal to the true parameters i.e., the uncertainties of the estimates are not considered. This is called the *certainty equivalence principle* [AW95], [SB89].

The self tuning controller is very flexible with respect to the choice of the design methodology and estimation methods [AW95], [SB89]. An interesting new method to implement self-tuning controllers is the so called passivity based control (PBC). The basic idea behind PBC design is to shape the energy of the system and its variations according to a chosen state trajectory. The major advantage of PBC approach is its intrinsic stability. The PBC design is independent of the dimension of the state space because it is based on the physical structure of the system. This fact has the advantage that nonlinear behavior is directly incorporated in the model. [CdL⁺03].

4.2.2. Direct and Indirect Adaptive Control

In standard adaptive control, it is assumed that the controller has been designed off-line, but may contain some uncertain parameters. The way the parameter estimator is combined with the control law results in two different approaches: indirect adaptive control, in which the uncertain parameters are actually parameters of an uncertain plant model that appear

in the controller design, or direct adaptive controller in which the parameters are estimated directly without intermediate calculations involving plant parameters estimates [CFG⁺01], [IS96]. The STC can be designed using both direct and indirect approaches.

4.2.3. Selection of the Controller

The main requirements of the controller for the x-ray generator are no overshoot and fast dynamic response over the entire converter operating range. Additionally, the system must be stable also in case of large load changes. In order to meet the dynamic response requirements, the gain scheduled controller is the best option because of its fast dynamics. However, as the method uses linearization techniques, it could happen that it is difficult to tune as to ensure robust performance. For this reason, it is also reasonable to investigate an alternative for the case that the gain scheduled controller would not be stable over the entire converter operating range. This alternative should be an adaptive controller that handles directly with the nonlinear model of the system. Normally, this type of controller is more robust and stable than controllers derived from linear techniques. A good option to implement a nonlinear adaptive controller is a self-tuning controller using the passivity based control (PBC) methodology. The PBC has high stability but its dynamic response is slower compared with the gain scheduled controller because it requires an estimator. The gain scheduling approach and the passivity based control approach will be investigated in details in order to compare both performances so that one can find the best balance between stability and dynamics. The gain scheduling approach will be discussed in details in Section 4.3 and the passivity based controller will be shown in Section 4.4.

4.3. GAIN SCHEDULED CONTROLLER

Nonlinear systems can be often linearized, that means, it is possible to obtain a linear representation of its behavior. That representation approximates the true dynamics well in a small region. For example, the equations that describe the behavior of the series-parallel resonant converter are nonlinear but, as it is shown in Chapter 3, for very small deviations from the operating point, they may be adequately replaced by

linear equations. This approximation stops working, however, for large deviations and, in dealing with these, one must consider the nonlinear equation itself and not only a linear representation [GMD03].

Resonant converters are variable structure systems. In fact they are piecewise linear systems (PLS) whose global behavior is strongly nonlinear [HBB⁺92]. PLS are characterized by a finite number of linear dynamical models together with a set of rules for switching among these models. Therefore, this model description causes a partitioning of the state space into cells. These cells have distinctive properties in that the dynamics within each cell are described by linear dynamic equations. The boundaries of each cell are in effect switches between different linear systems. Those switches come up from the breakpoints in the piecewise linear functions of the model [GMD03]. A major advantage of piecewise linear characteristics is that they admit linear parameterization with unknown breakpoint and slope parameters [TK96]. Making use of definition of piecewise linear systems and of the small-signal model of the series-parallel resonant DC-DC converter developed in **Chapter 3**, an adaptive controller based on gain scheduling approach will be designed.

4.3.1. Small-Signal Model of the System

The complete small-signal model of the series-parallel resonant converter has been depicted in **Chapter 3**. For this reason the whole procedure is not repeated here. The linearized model of the system is given by

$$\begin{cases} \overline{\Delta \dot{x}} = A \overline{\Delta x} + B \overline{\Delta u} \\ \overline{\Delta y} = C \overline{\Delta x} + D \overline{\Delta u} \end{cases} \quad (4.1)$$

where A , B , C and D are matrices that describe the system, \vec{x} is the state vector, \vec{u} is the input vector, \vec{y} is the output vector and Δ means the small changes of the respective parameter (cf. Eq. 3.71).

However, for the controller design one is interested to control the output voltage V_o by means of duty cycle D and switching frequency f_s . Thus, the model has only one output. The switching frequency of the converter is automatically adjusted to ensure zero-current switching of one

bridge leg where the output power is controlled by duty cycle variation. Hence, the control variable of the controller is the duty cycle D . For this reason the control input f_s is set to zero in the controller design. Considering the changes in the number of control inputs (one instead of two) and outputs (one instead of three) of the system compared with the generic model shown in Chapter 3, matrices B , C and D will be accordingly defined as shown in following (the coefficients of the matrices are presented in Chapter 3). The state matrix A remains the same but it will be shown again for the sake of completeness

$$A = \begin{bmatrix} a_{11} & a_{12} & a_{13} & 0 & a_{15} \\ a_{21} & a_{22} & 0 & a_{24} & a_{25} \\ a_{31} & 0 & 0 & a_{34} & 0 \\ 0 & a_{42} & a_{43} & 0 & 0 \\ a_{51} & a_{52} & 0 & 0 & a_{55} \end{bmatrix} \quad (4.2)$$

$$B = [b_{12} \quad b_{22} \quad 0 \quad 0 \quad 0]^T \quad (4.3)$$

$$C = [0 \quad 0 \quad 0 \quad 0 \quad 1] \quad (4.4)$$

$$D = 0 \quad (4.5)$$

The small-signal model of the series-parallel resonant converter is then calculated for nine different operating points. These points are shown in Fig. 4.4 and they will be used in the controller design.

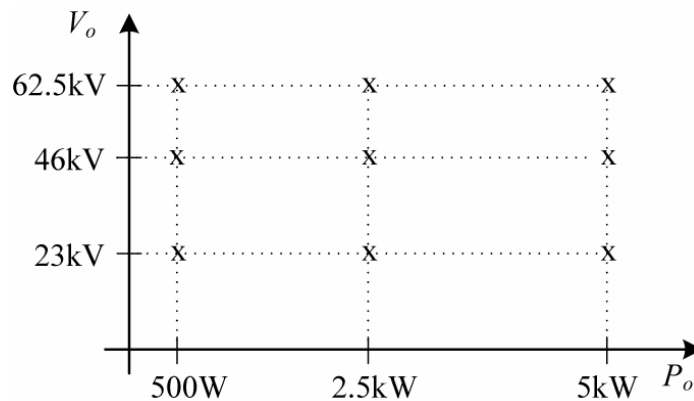


Fig. 4.4: Operating points where the small-signal models are calculated.

4.3.2. Gain Scheduling

In many situations it is known how the dynamics of a plant change with the operating conditions. It is then possible to change the parameters of the controller by monitoring the operating conditions of the plant

[AW95]. This approach is called gain scheduling and it is a common engineering practice used to design controllers for systems with widely varying nonlinear dynamics [LL00], [SA92], [SA91].

Gain scheduling is a feedforward adaptation and it can be implemented as a look-up table or as a function [AW95], [IN02]. In recent years the interest for gain scheduled methods has increased. This can be explained with the evolution of digital techniques because before digital implementation of controllers was possible, gain scheduling was expensive and difficult to realize in hardware [Bru04], [RS00]. Nowadays gain scheduling is an efficient and inexpensive procedure for nonlinear control design.

A typical gain scheduled design procedure for nonlinear plants is as follows: 1) one selects several operating points that cover the range of the plant's dynamics; 2) at each of these operating points, a linear time-invariant (LTI) model of the nonlinear plant is derived and a linear controller is designed for each linearized model and 3) between operating points, the controller parameters are interpolated, thus resulting in a non-local controller containing a family of linear controllers such that the controller coefficients are scheduled according to the current value of the scheduling variables [RS00], [SA90], [SA92], [SA88]. Usually, the local stability and performance properties of the gain scheduled controller might be subjected to analytical investigation, while the nonlocal performance evaluation is based on simulation studies [RS00].

4.3.3. Gain Scheduled Controller Design

A gain scheduled controller for the equivalent circuit of the series-parallel resonant converter already shown in **Fig. 3.1** will be designed. The plant is linearized about nine points previously shown in **Fig. 4.4**, remembering that $V_{o'} = V_o/2n$ and $I_{o'} = I_o \cdot 2n$. The specifications of the equivalent circuit have been shown in Chapter 3, section 3.2.2.

The objective is to find a gain scheduled controller using the measured output current $I_{o'}$ and the reference output voltage $V_{o'_{ref}}$ as scheduling variables. That means, the controller verifies how much current is available to reach a predetermined output voltage. In this way the gain of

the controller can be adapted to each operating point. Fig. 4.5 shows the block diagram of the closed loop system.

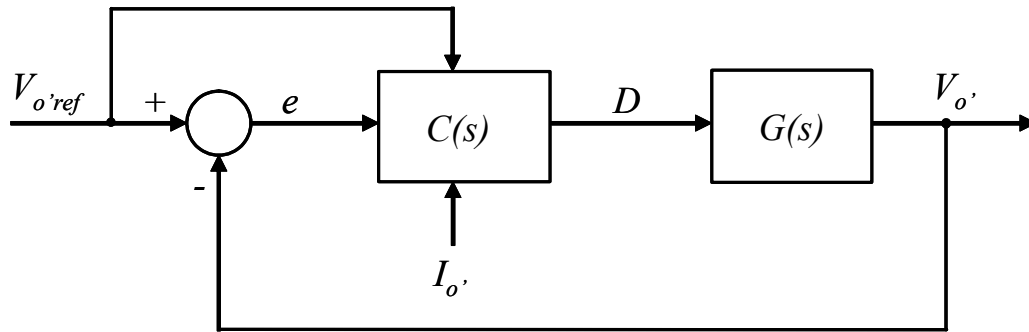


Fig. 4.5: Block diagram of the closed loop system.

For the sake of simplicity, the gain scheduled controller $C(s)$ is defined to have the structure of a proportional-integral (PI) controller as shown in (4.6) where the proportional gain K and the integrator time constant T_{ir} are functions of the scheduling variables.

$$C(s) = K(I_{o'}, V_{o'}'_{ref}) + \frac{1}{T_{ir}(I_{o'}, V_{o'}'_{ref})s} \quad (4.6)$$

Table 4.1 shows the values of K and T_{ir} for the nine operating points where the small-signal model is calculated. The corresponding output current is calculated as $I_{o'} = P_o / V_{o'}$. K is a dimensionless parameter while T_{ir} is given in seconds. The parameters K and T_{ir} are selected in order to guarantee that the transient response of the output voltage has no overshoot and the rise time is less than $300\mu\text{s}$.

$V_{o'}'_{ref}(V)$	$P_o(W)$	K	$T_{ir}(s)$
677	4600	12.576	4.822e-5
677	2500	15.597	1.043e-4
677	500	16.456	2.283e-4
1353	5000	26.896	2.234e-4
1353	2500	27.414	2.873e-4
1353	500	24.810	5.147e-4
1838	5000	31.073	2.673e-4
1838	2500	31.363	4.964e-4
1838	500	20.723	6.279e-4

Table 4.1: Coefficients K and T_{ir} .

As said before a gain scheduled controller can be implemented as a look-up table or as a function. In order to calculate the coefficients K and

Tir , a polynomial function with degree two is preferred, that means, the sum of exponents of all variables in any term is less than or equal to two. One has to find a way to fit a polynomial of the type shown in (4.7) to data in **Table 4.1**,

$$z(x, y) = a_0 + a_1x + a_2y + a_3xy + a_4x^2 + a_5y^2 \quad (4.7)$$

where a_0, a_1, a_2, a_3, a_4 and a_5 are the coefficients to be determined.

The best way to find the coefficients is to use a method called multivariate polynomial regression. Multivariate polynomial regression determines a minimum squared error polynomial for given data. It applies least squares method to fit a multivariable polynomial to tabulated data. In doing so, any noise or inaccuracies in the observed data are expected to have less effect on the accuracy of the mathematical model [AW95], [IS96].

The values of tabulated data must be taken for values of the independent variables belonging to a rectangular grid which may be not uniformly spaced, that is, a function of n variables must be tabulated at the nodes of an n -dimensional rectangular grid.

The built-in function *regress* from MathCAD performs regression analysis and function *interpret* defines a polynomial function using the vector returned as output from *regress*. Before the MathCAD's functions are applied, coefficient Tir will be normalized, because in practice the controller will be implemented via 16-bit fixed point DSP with a sampling time of $6.4\mu\text{s}$. The normalized integrator time constant is called Ti and is defined by (4.8).

$$Ti(I_o', V_{o',ref}) = \frac{6.4\mu\text{s}}{Tir(I_o', V_{o',ref})} \cdot 32768 \quad (4.8)$$

The number 32768 is the maximum number that the 16-bit DSP can represent for signed mode. Signed mode is used because as it will be shown in the following the expressions for K and Ti also include negative coefficients. Hence, the DSP should be able to represent negative numbers.

After applying functions *regress* and *interpret* the obtained expressions for K and Ti are represented by (4.9) and (4.10) respectively.

$$\begin{aligned} K(I_o', V_{o',ref}) = & 2.544 - 1.258 \cdot 10^{-3} I_o' + 5.82 \cdot 10^{-3} V_{o',ref} \\ & + 6.052 \cdot 10^{-7} I_o' V_{o',ref} - 1.845 \cdot 10^{-7} I_o'^2 - 4.043 \cdot 10^{-7} V_{o',ref}^2 \end{aligned} \quad (4.9)$$

$$Ti(I_o', V_{o'ref}) = 2010 + 0.208I_o' - 0.506V_{o'ref} - 3.645 \cdot 10^{-5} I_o' V_{o'ref} + 6.57 \cdot 10^{-5} I_o'^2 + 3.857 \cdot 10^{-5} V_{o'ref}^2 \quad (4.10)$$

The values of $V_{o'ref}$ and I_o' used in the equations (4.9) and (4.10) are not the original values in Volts and Amperes, respectively, but normalized DSP numbers. Hence, the values of K and Ti are dimensionless DSP numbers. It has been chosen to normalize the values of $V_{o'ref}$ and I_o' using only one-fourth of the full scale of the DSP, i.e. the maximum DSP number used to scale $V_{o'ref}$ and I_o' is 8192. This is due to the fact that this scale already provides sufficient resolution for displaying the values of $V_{o'ref}$ and I_o' while keeping the DSP computation effort low. The scale for $V_{o'ref}$ is $1853V = 8192$ and for I_o' is $8.5A = 8192$. Thus, the resolution of $V_{o'ref}$ is 226mV and of I_o' is about 1mA.

Fig. 4.6 shows how the proportional gain K behaves in the whole operating range of the converter.

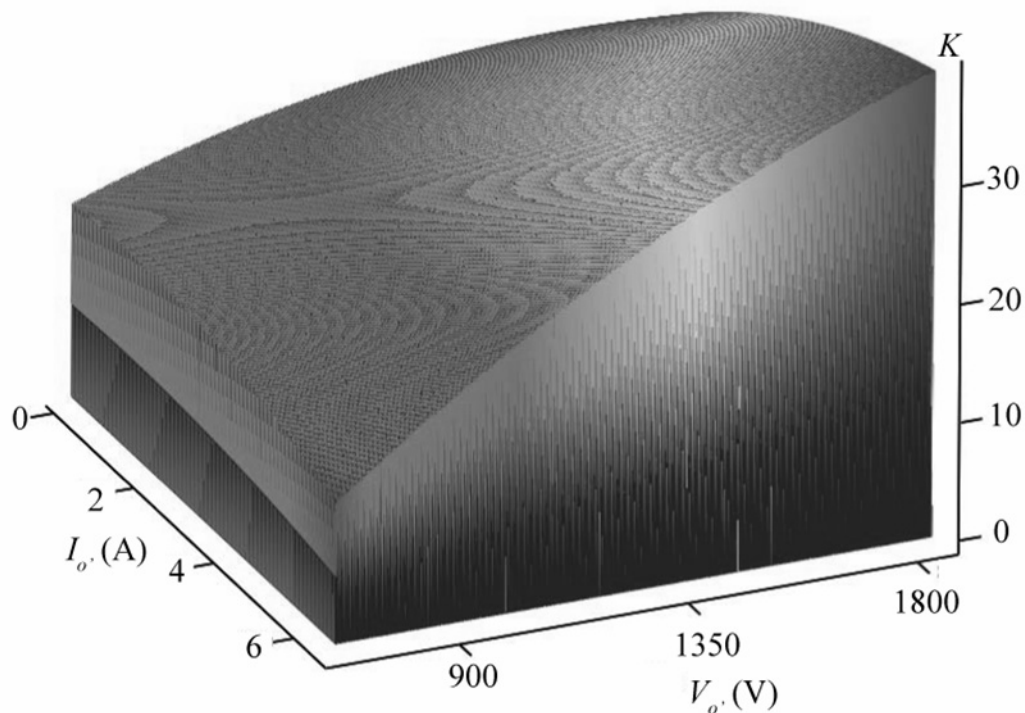


Fig. 4.6: Graphical representation of the proportional gain K as a function of the output reference voltage and the output current.

The variation of the polynomial function that represents the normalized integrator time constant Ti for the whole operating range of the converter is shown in **Fig. 4.7**.

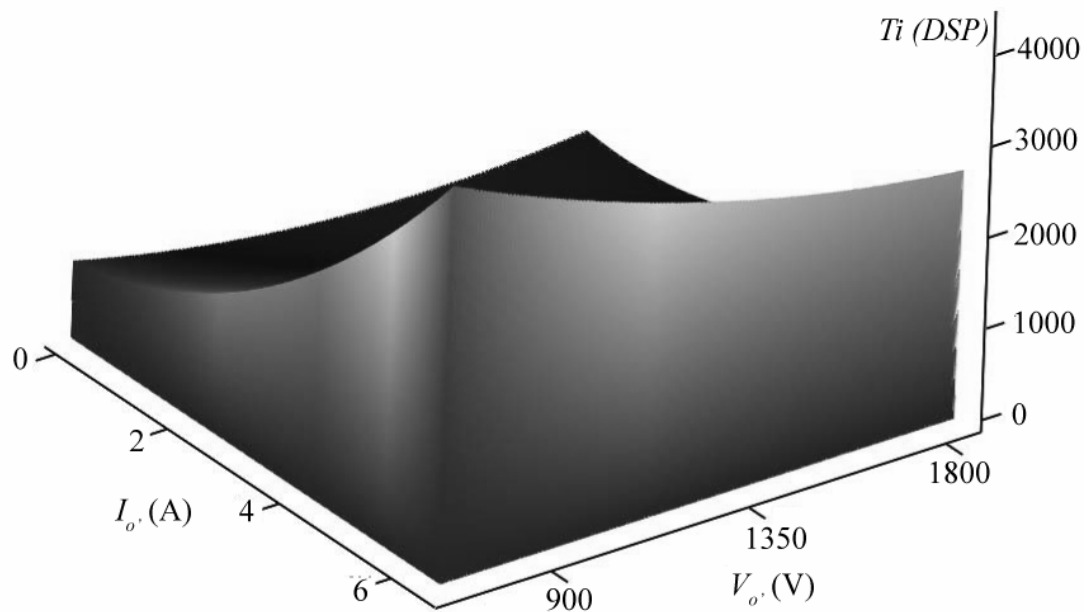


Fig. 4.7: 3D representation of the normalized integrator time constant T_i as a function of the output reference voltage and output current.

The small-signal transfer function that relates duty cycle with output voltage of the series-parallel resonant converter $G(s) = \Delta V_o / \Delta D$ has five poles. However, one pair of complex conjugate poles is located at very high frequency so that it does not have a relevant influence on the behavior of the converter. For this reason, $G(s)$ can be reduced to a third order transfer function. Nevertheless, the influence of the variation of the switching frequency is not included in the calculation of $G(s)$, because this would make $G(s)$ far too complex. Thus, the switching frequency variation can be seen as an unmodeled constant disturbance (for more details, please refer to **Chapter 3**). Since the adaptive controller has an integrator, the steady-state error is zero for a step input. However, simulations with the adaptive controller $C(s)$ showed that the unmodeled constant disturbance caused by the switching frequency variation affects the settling time (slow dynamics) and makes it slower. On the other hand, the unmodeled constant disturbance does not affect the rise time (fast dynamics). This is a sign that the disturbance rejection at low frequencies is bad. To improve the disturbance rejection at low frequencies, one has to increase the open loop gain $G(s)C(s)$ at low frequencies. This can be easily done by adding a second PI controller with fixed parameters to the circuit. The addition of the second integrator assures better disturbance rejection at low

frequencies. The controller has been selected with the purpose of increasing the gain of the system at low frequencies without having influence on the high-frequency behavior of the system. The controller with fixed parameters is given by (4.11).

$$C_{aux}(s) = 1 + \frac{6775}{s} \quad (4.11)$$

4.3.4. Simulation Results

Digital simulations using MATLAB/Simulink are performed, in order to validate the design of the gain scheduled controller described in the previous section. The circuit is simulated as shown in **Fig. 3.1**, all components are considered ideal and additionally, $V_{o'ref} = 677V$.

In the first simulation, the start up of the converter is simulated at rated power and at light load ($P_o = 1.15kW$). The corresponding values of $R_{o'}$ are, respectively, $R_{o'} = 99.5\Omega$ (full load) and $R_{o'} = 398\Omega$ (light load).

Fig. 4.8 shows start up response of the measured output voltage $V_{o'}$ and reference voltage $V_{o'ref}$, respectively, at rated power and at light load. One can see that in both cases, the voltages converge without overshoot within about $300\mu s$ to the reference voltage $V_{o'ref} = 677V$. A step like change of the reference voltage $V_{o'ref}$ does not occurs because a first-order low-pass filter with a time constant equal to $14\mu s$ has been included in the implementation of the system in order to provide soft-start. Thus, when a step like change occurs in the reference voltage, this step input passes through the filter, so that the reference voltage slowly steps up.

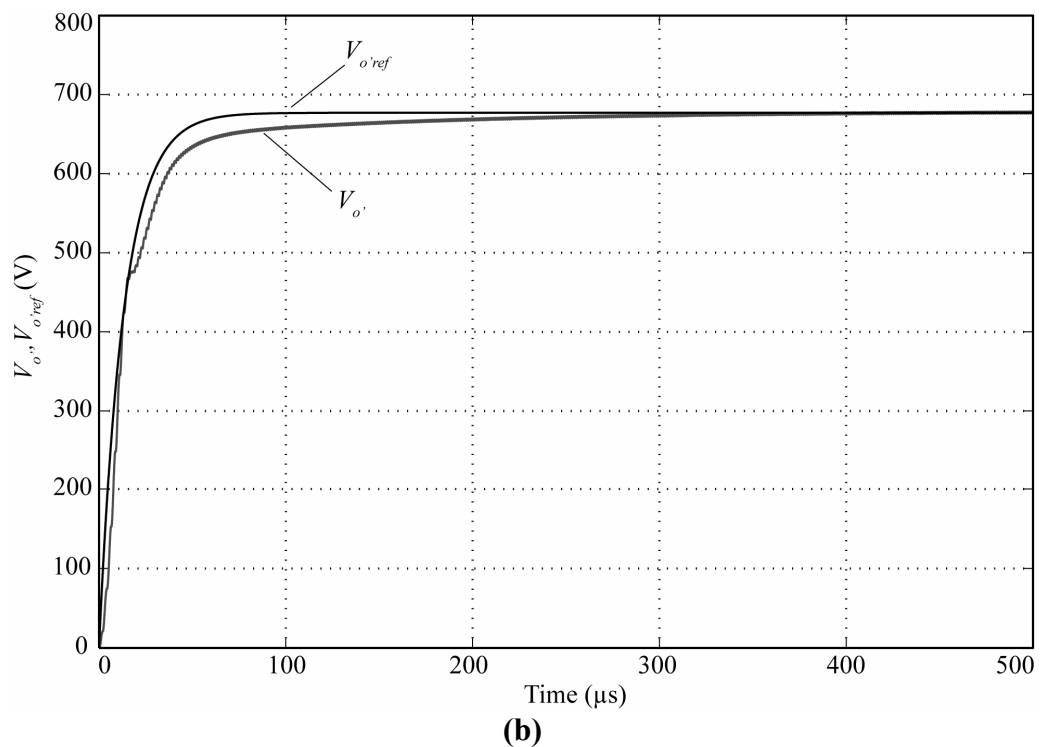
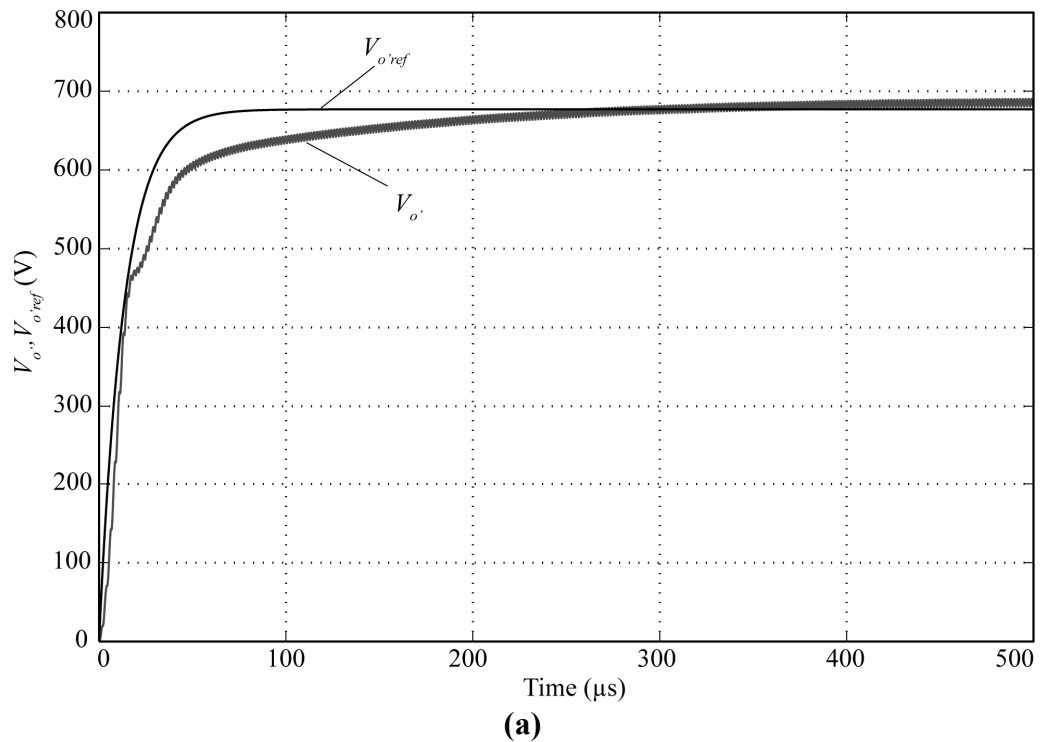


Fig. 4.8: Start up response of the measured output voltage, $V_{o'}$ and reference voltage $V_{o'ref}$ for operation at rated power (a) and at light load (b).

Fig. 4.9 represents the closed loop response of the measured output voltage $V_{o'}$ to a step change in the reference voltage $V_{o'ref}$ from 377V to 677V respectively, at rated power and at light load. One can see that the controller reacts very fast to the step-like change in the reference voltage and adjusts the output voltage to the new reference value within about

150 μ s. It is also important to note that the performance of the controller is almost the same, independent of load level. This independence is a relevant advantage of the controller because the load is normally an unknown parameter.

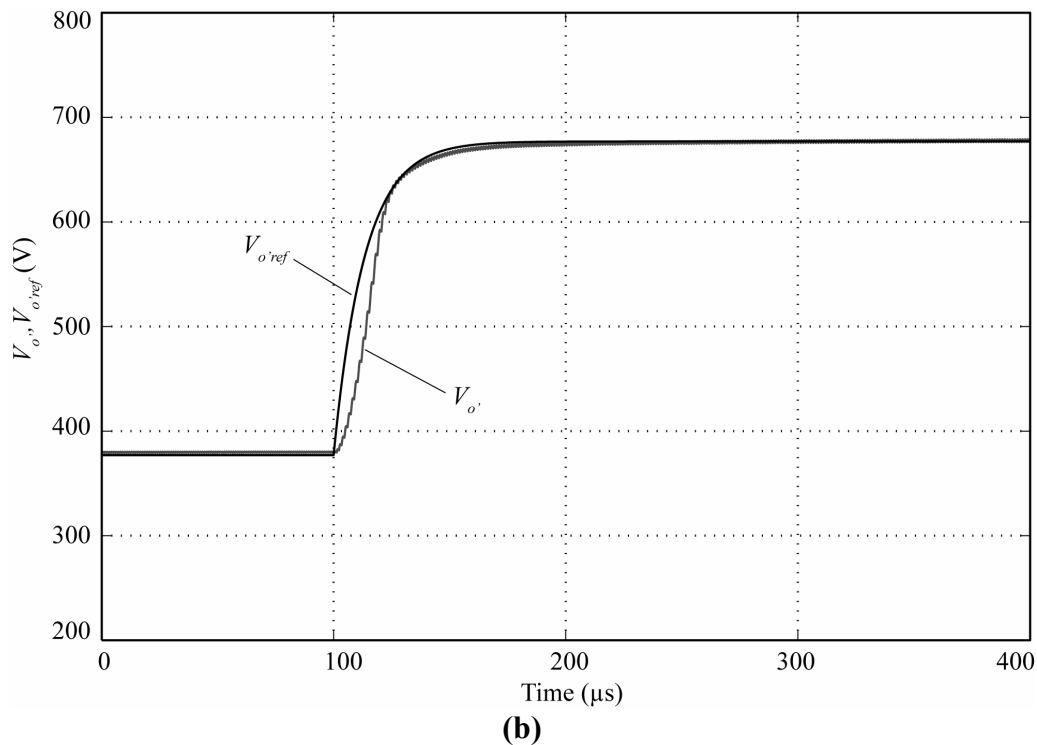
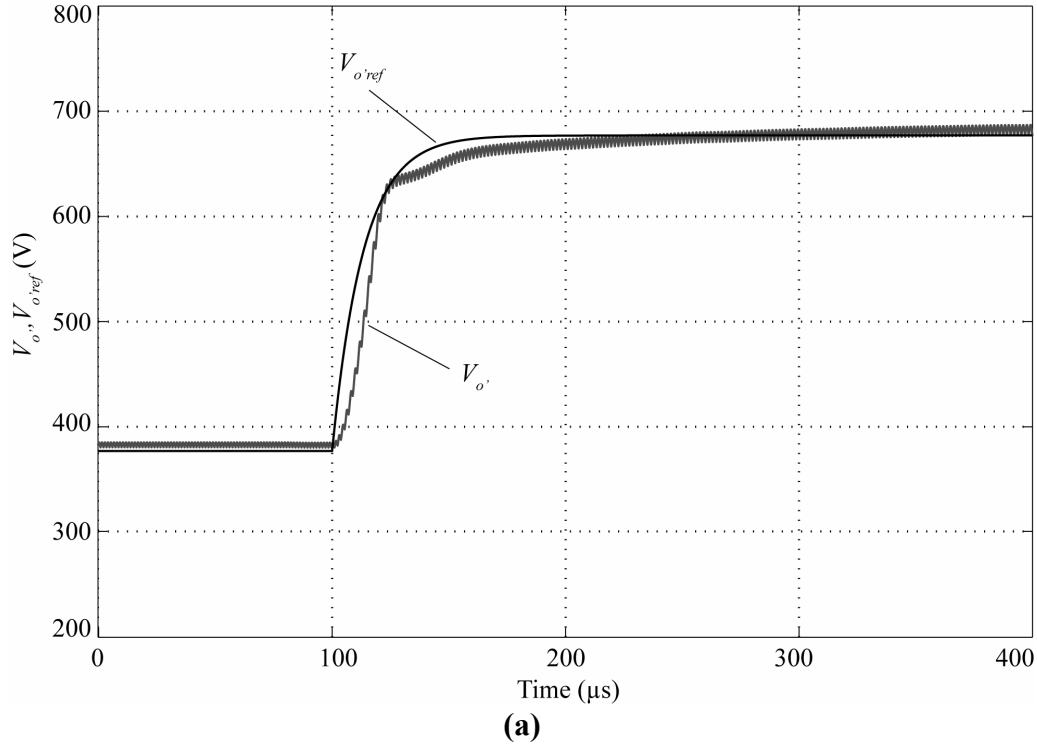


Fig. 4.9: Measured output voltage, V_o and reference voltage $V_{o,ref}$ with a step change in the value of reference voltage from 377V to 677V for operation at rated power (a) and at light load (b).

4.4. PASSIVITY BASED CONTROLLER

4.4.1. Introduction to Passivity Based Control

Energy is one of the fundamental concepts in science and engineering practice, where it is common to view dynamical systems as energy-transformation devices. This perspective is particularly useful in studying complex nonlinear systems by decomposing them into simpler subsystems that, upon interconnection, add up their energies to determine the full system's behavior. The action of a controller may also be understood in energy terms as another dynamical system interconnected with the process to modify its behavior. The control problem can then be recast as finding a dynamical system and an interconnection pattern such that the overall energy function takes the desired form. This energy-shaping approach is the essence of passivity-based control (PBC), a controller design technique that is very well known in mechanical systems [OLNSR98].

4.4.2. Passivity Definition

Passivity is a fundamental property of many physical systems which may be roughly defined in terms of energy dissipation and transformation. It is an inherent input-output property in the sense that it quantifies and qualifies the energy balance of a system when stimulated by external inputs to generate some output. Passivity is therefore related to the property of stability in an input-output sense, that is, the system is stable if bounded input energy supplied to the system, yields bounded output energy. This is in contrast to Lyapunov stability which concerns the internal stability of a system, that is, how far the state of a system is from a desired value. In other words, how differently a system behaves with respect to a desired performance [LN02].

From an energetic viewpoint one can define passive systems as a class of dynamical systems in which the energy exchanged with the environment plays a central role. In passive systems the rate at which the energy flows into the system is not less than the increase in storage. In other words, a passive system cannot store more energy than is supplied to it from outside, with the difference being the dissipated energy [OLNSR98].

4.4.3. Passivity Based Control

Passivity based control is a feedback control design method for nonlinear systems that exploits the physical restrictions of the system, and, in particular, its energy properties [OLNSR98].

This method consists of two stages: an energy shaping stage and a damping injection stage. The energy shaping stage modifies the potential energy of the closed-loop of the system and the damping injection stage modifies the dissipation properties of the system in order to achieve asymptotic stability [GGRD98], [SRO95].

The passivity based controller shapes the energy of the system according to a chosen state trajectory [CdL⁺03]. This approach differs from the feedback linearization and similar approaches as it avoids some intrinsically non-robust operations, such as exact cancellations of nonlinearities. The control approach utilizes the physical laws underlying energy conversion and the model structure in a fundamental way, as it consists of: 1) specification of the desired energy function of the closed-loop system (which contains incremental terms around the intended operating mode, i.e., desired output voltage and estimated load), and desired (periodic) steady-state trajectories that provide output voltage regulation and 2) addition of damping around this nominal trajectory (i.e., dissipation of undesirable deviations of stored energy) that assures exponential convergence toward the nominal trajectory, thus guaranteeing robust operation [Sta96], [SPS97].

4.4.4. Nonlinear Model of the System

The control of resonant converters is not a trivial problem because they are strongly nonlinear systems. It is common that one tries to overcome the nonlinearity problem by linearizing the system around a steady point and then applying linear control techniques like in the gain scheduling controller shown in the previous section. However, some authors insist that if the nonlinearities are not considered, the performance of the controller will be poor [HBB⁺92]. The previous results are very good and demonstrate that it is possible to obtain a good controller applying linear control techniques. Even so, it is important to calculate a controller using nonlinear techniques, in order to compare the nonlinear controller

with the previous one and see which are the advantages and drawbacks of each one.

In [CGV⁺00], the dynamics of a series resonant converter are described by a third order nonlinear system, consisting of an oscillator and a first order linear filter interconnected via various static nonlinearities. The series-parallel resonant converter can be also described in a similar way.

The nonlinear model based on the generalized averaging method was already described in Chapter 3, thus only the main equations will be shown again here. For more details, please refer to **Chapter 3**.

$$\frac{d\langle I_{Ls} \rangle_1}{dt} = -j\omega_s \langle I_{Ls} \rangle_1 + \frac{1}{L_s} \left\{ -\langle V_{Cs} \rangle_1 - \langle V_{Cp} \rangle_1 + \langle V_{AB} \rangle_1 \right\} \quad (4.12)$$

$$\frac{d\langle V_{Cs} \rangle_1}{dt} = -j\omega_s \langle V_{Cs} \rangle_1 + \frac{1}{C_s} \langle I_{Ls} \rangle_1 \quad (4.13)$$

$$\frac{d\langle V_{o'} \rangle_0}{dt} = \frac{1}{C_{o'}} \left\{ \langle abs(i_T) \rangle_0 - \frac{2 \cdot \langle V_{o'} \rangle_0}{R_{o'}} \right\} \quad (4.14)$$

where

$$\langle V_{AB} \rangle_1 = \frac{V_{in}}{\pi} [\sin(D\pi) + j(\cos(D\pi) - 1)] \quad (4.15)$$

$$\langle abs(i_T) \rangle_0 = \frac{2 \cdot |\langle I_{Ls} \rangle_1|}{\pi} \cdot [1 - \cos(\theta)] \quad (4.16)$$

$$\theta = \cos^{-1} \left(\frac{\omega_s C_p \langle V_{o'} \rangle_0}{2 \cdot |\langle I_{Ls} \rangle_1|} - 1 \right) \quad (4.17)$$

The system state variables are: $\langle I_{Ls} \rangle_1$, $\langle V_{Cs} \rangle_1$ and $\langle V_{o'} \rangle_0$. They are complex Fourier coefficients that can be written as a fifth order state space model with real variables: $\langle I_{Ls} \rangle_1 = x_1 + jx_2$, $\langle V_{Cs} \rangle_1 = x_3 + jx_4$ and $\langle V_{o'} \rangle_0 = x_7$. The voltage on the parallel capacitor can be also written as a function of real variables: $\langle V_{Cp} \rangle_1 = x_5 + jx_6$ [CK05].

4.4.5. Passivity Based Controller Design

Following the PBC approach proposed by [CGV+00], one has to add some damping to the system in order to dissipate undesirable deviations of energy. Observing the dynamics of the series-parallel resonant converter,

one can see that the output voltage (variable to be controlled) has very slow dynamical behavior compared with the resonant elements. It is reasonable to say that transients in the resonant elements are instantaneous compared with the transients in the output capacitors. That means the amount of energy stored in the output capacitors is considerably larger than the energy stored in the resonant elements. Thus, only (4.14) will be evaluated because dynamics of the output voltage is the only relevant dynamics for the controller design. The control action of the PBC consists of transferring energy from one energy storage element to another one. For this reason, it is not possible to control the output voltage directly with the duty cycle. Instead of this, an intermediate stage has to be included in the controller. In this stage the energy of the output capacitor is controlled using another state variable, in this case the resonant current. The resonant current has been selected as intermediate control input because it determines, associated with the duty cycle, the active power that is transferred to the load. Hence, the first step of control design is to shape the energy stored in the output capacitor taking the amplitude of the first harmonic of the resonant current $\langle I_{L_s} \rangle_1$ as control input. For doing this, first it is necessary to generate the correspondent reference resonant current for a given reference output voltage $V_{o,ref}$. The amplitude I_{L_sref} of the reference resonant current is dependent on the reference output voltage, on the switching frequency f_s and on the load. For a constant reference output voltage $V_{o,ref}$, different switching frequencies and/or different load resistances result in different output power. The switching frequency is easily measurable because the sawtooth generator is synchronized with the zero crossing of the resonant current (c.f. **Chapter 2**). However, the load is an unknown parameter. For this reason, it is necessary to build an estimator that predicts the load value. In order to reduce the complexity of the equation that describes the estimator, the conductance $G = 1/R_o$ is usually estimated instead of the resistance R_o . This guideline is followed in the present work. Thus, the estimate \hat{G} of the conductance G will be calculated. It is important to point out that I_{L_sref} is a dynamical reference, which is constantly adapted when the switching frequency or the load resistance changes. This dynamical reference is also used to generate a dynamical reference $V_{o,D}$ for the output

voltage. The dynamical reference $V_{o'D}$ helps preventing overshoot in the step response of the output voltage. After I_{Lsref} is computed, the second step is to calculate the corresponding duty cycle using the steady-state relationship between the duty cycle and the amplitude of the fundamental term of the resonant current [SPS99] and evaluating this relationship for $|\langle I_{Ls} \rangle_1| = I_{Lsref}$. In order to simplify the notation in the controller design, the amplitude of the state variables will be redefined as: $I_{Ls} = |\langle I_{Ls} \rangle_1|$, $V_{Cs} = |\langle V_{Cs} \rangle_1|$ and $V_{o'} = \langle V_{o'} \rangle_0$. A simplified block diagram of the passivity based controller is shown in **Fig. 4.10**. The variables that appear in the diagram will be defined in the following.

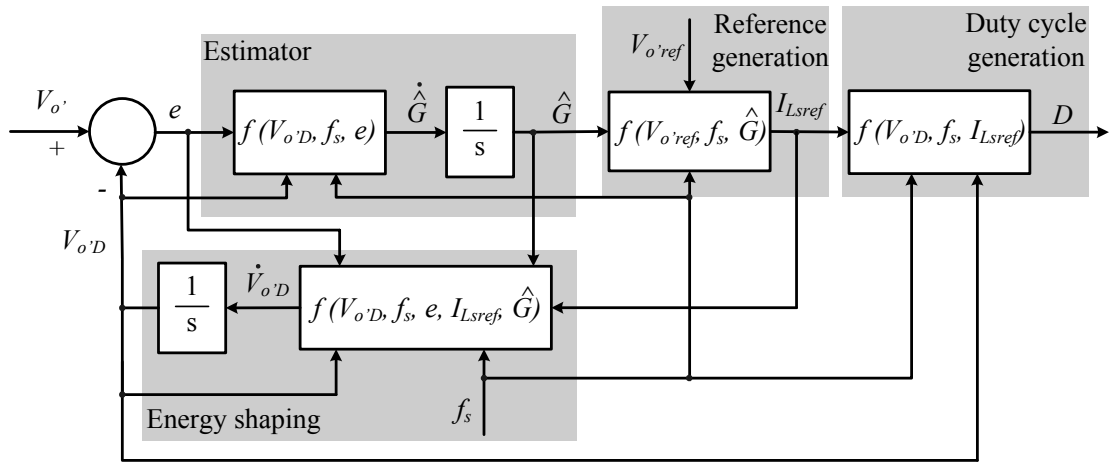


Fig. 4.10: Simplified block diagram of the passivity based controller.

4.4.5.1. First Step – Reference Generation

The objective of this step is to define the amplitude I_{Lsref} of the reference resonant current as a function of the output reference voltage $V_{o'ref}$, switching frequency f_s and estimate of the load \hat{G} . The reference resonant current is calculated setting the derivative of Eq. (4.14) to zero and evaluating the resulting expression for the equilibrium point $V_{o'} = V_{o'ref}$, where $V_{o'ref}$ represents the static (steady-state) reference value of the output voltage.

$$0 = \frac{1}{C_{o'}} \left\{ \frac{2 \cdot I_{Lsref}}{\pi} \cdot [1 - \cos(\theta)] - \frac{2 \cdot V_{o'ref}}{R_{o'}} \right\} \quad (4.18)$$

After some manipulations one obtains

$$\frac{I_{Lsref}}{\pi} \cdot [1 - \cos(\theta)] = V_{o'ref} \cdot \widehat{G} \quad (4.19)$$

Equation (4.17) can be rewritten as

$$\cos \theta = \left(\frac{\pi f_s C_p V_{o'ref}}{I_{Lsref}} - 1 \right) \quad (4.20)$$

Substituting (4.20) in (4.19), the equation for the reference current is obtained

$$I_{Lsref} = \frac{V_{o'ref} \pi}{2} (f_s C_p + \widehat{G}). \quad (4.21)$$

4.4.5.2. Second Step – Energy Shaping

The objective of this step is to determine the error dynamics of the output voltage and of the intermediate control input namely, the resonant current. The information about the error dynamics is later necessary to find the adaptive law and to analyze the stability of the system. Now, we will rewrite the equation that describes the dynamics of the output voltage (4.14) as a function of the parameters used in the energy shaping design namely, the amplitude of the resonant current I_{Ls} , the switching frequency f_s and load conductance G . Substituting (4.16) and (4.17) in (4.14) one obtains

$$C_o \frac{dV_{o'}}{dt} = \frac{4}{\pi} I_{Ls} - 2f_s C_p V_{o'} - 2V_{o'} G \quad (4.22)$$

Based on the PCB methodology, one creates a copy of the dynamic behavior of the output voltage given by (4.22), evaluating this equation for the dynamical parameters I_{LsD} , $V_{o'D}$ and \widehat{G} [CGV⁺00]. This is called the dynamical copy of the system. Additionally, a damping term K_I is added to the error. This damping term implements the adaptive control action of the passivity based control. The dynamical copy of the system with damping injection is shown in (4.23).

$$C_o \frac{dV_{o'D}}{dt} = \frac{4}{\pi} I_{LsD} - 2f_s C_p V_{o'D} - 2V_{o'D} \widehat{G} + K_I e \quad (4.23)$$

where

$$e = V_{o'} - V_{o'D},$$

$V_{o'D}$ – dynamical reference value of the output voltage,

$V_{o'}$ – output voltage,

I_{LsD} – dynamical magnitude of the resonant current,

f_s – switching frequency,

C_p – parallel resonant capacitor,

\hat{G} – estimate of $1/R_{o'}$ and

K_I – damping injection gain.

The error dynamics of the output voltage is obtained subtracting (4.23) from (4.22).

$$C_o \dot{e} = \frac{4}{\pi} \tilde{I}_{Ls} + 2V_{o'D} \tilde{G} - (2f_s C_p + K_I + 2G)e \quad (4.24)$$

where

$$\dot{e} = \frac{de}{dt} \quad (4.25)$$

$$\tilde{I}_{Ls} = I_{Ls} - I_{LsD} \quad (4.26)$$

$$\tilde{G} = \hat{G} - G \quad (4.27)$$

The error dynamics of the amplitude of the resonant current \tilde{I}_{Ls} , which appears in (4.24), is still unknown. Thus, it is necessary to calculate \tilde{I}_{Ls} in order to solve the equation. For this purpose, first one has to find a steady-state relationship for I_{Ls} as a function of G (parameter to be estimated) and of the output voltage $V_{o'}$ (parameter to be controlled). Afterwards, one evaluates this steady-state relationship for the dynamical parameters $V_{o'D}$ and \hat{G} in order to obtain the dynamical magnitude of the resonant current I_{LsD} .

Following the model developed in **Chapter 3**, it was assumed that $\langle I_{Ls} \rangle_1 = x_1 + jx_2$ and $\langle V_{Cs} \rangle_1 = x_3 + jx_4$. Assuming that $\langle I_{Ls} \rangle_1$ is predominantly sinusoidal and $\langle V_{Cs} \rangle_1$ is predominantly cosinusoidal these expressions are reduced to $\langle I_{Ls} \rangle_1 = jx_2$ and $\langle V_{Cs} \rangle_1 = x_3$. These assumptions are reasonable if one observes the time behavior of both variables shown in **Fig. 3.2**. Using the previous assumptions, the phasor diagram of the main voltages and currents of the system at an equilibrium point is shown in **Fig. 4.11**.

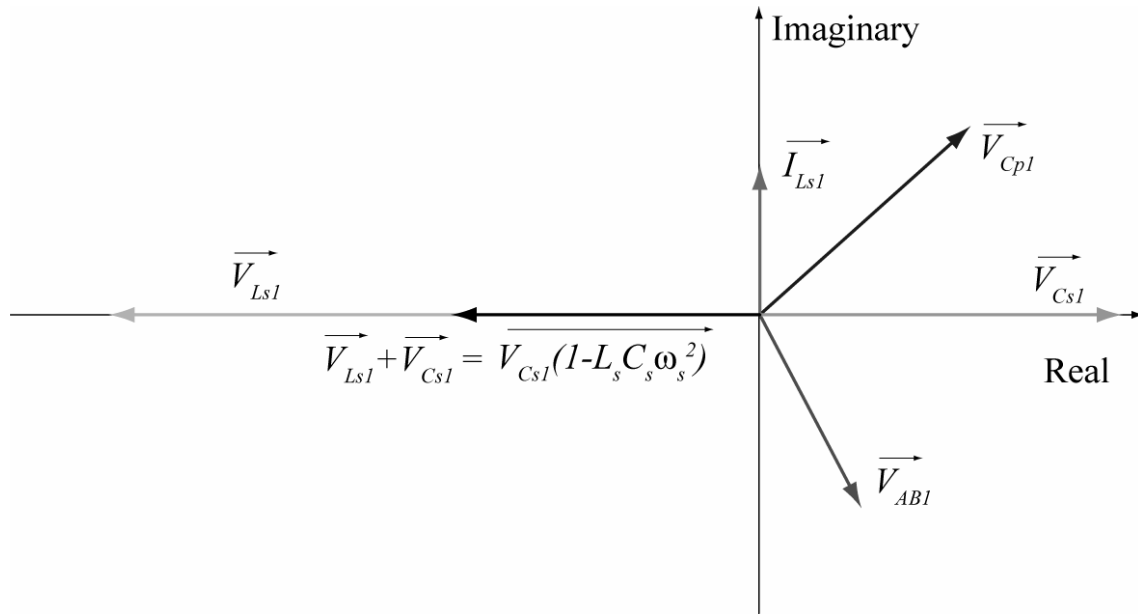


Fig. 4.11: Current and voltages phasor diagram

In the phasor diagram different notations than those used in Chapter 3 are utilized. The correspondence to the past notations used in Chapter 3 are: $I_{Ls1} = \langle I_{Ls} \rangle_1$, $V_{Cs1} = \langle V_{Cs} \rangle_1$, $V_{Cp1} = \langle V_{Cp} \rangle_1$ and $V_{Ab1} = \langle V_{Ab} \rangle_1$.

The voltage across the resonant inductor is given by

$$\overrightarrow{V_{Ls1}} = j\omega_s L_s \overrightarrow{I_{Ls1}} \quad (4.28)$$

From the resonant circuit structure (c.f. **Fig.3.1**), one can see that the current of the resonant inductor and of the series resonant capacitor is the same, namely i_{Ls} . Thus, the first harmonic I_{Ls1} of the resonant current is given by

$$\overrightarrow{I_{Ls1}} = j\omega_s C_s \overrightarrow{V_{Cs1}} \quad (4.29)$$

Substituting (4.29) in (4.28), one obtains

$$\overrightarrow{V_{Ls1}} = -\omega_s^2 L_s C_s \overrightarrow{V_{Cs1}} \quad (4.30)$$

Thus, the sum of the phasors $\overrightarrow{V_{Ls1}}$ and $\overrightarrow{V_{Cs1}}$ is given by

$$\overrightarrow{V_{Ls1}} + \overrightarrow{V_{Cs1}} = \overrightarrow{V_{Cs1}} (1 - L_s C_s \omega_s^2) \quad (4.31)$$

From the phasor diagram, one can see that

$$\overrightarrow{V_{Cs1}} (1 - L_s C_s \omega_s^2) = -\overrightarrow{V_{Ab1}} - \overrightarrow{V_{Cp1}}, \quad (4.32)$$

where $\omega_s = 2\pi f_s$ and f_s is the switching frequency.

As the phasor $\overrightarrow{V_{Cs1}} (1 - L_s C_s \omega_s^2)$ is a cosine, that means, it has only real part, the magnitude is given by

$$|V_{Cs1}| |(1 - L_s C_s \omega_s^2)| = \left| -|V_{AB1}| \cos(\angle V_{AB1}) - |V_{Cp1}| \cos(\angle V_{Cp1}) \right| \quad (4.33)$$

$$|V_{Cs1}| |(1 - L_s C_s \omega_s^2)| = \left| -\left[\operatorname{Re}(V_{AB1}) + \operatorname{Re}(V_{Cp1}) \right] \right| \quad (4.34)$$

$$|V_{Cs1}| = \frac{\operatorname{Re}(V_{AB1}) + \operatorname{Re}(V_{Cp1})}{|(1 - L_s C_s \omega_s^2)|} \quad (4.35)$$

where

$$\operatorname{Re}(V_{AB1}) = \frac{V_{in}}{\pi} \sin(D\pi) \quad (4.36)$$

$$\operatorname{Re}(V_{Cp1}) = \frac{|I_{Ls1}| \gamma_{ss}}{2\pi^2 f_s C_p} \quad (4.37)$$

The steady-state solution of the output voltage is given by

$$V_{o'ss} = \frac{R_{o'}}{\pi} |I_{Ls1}| [1 - \cos(\theta_{ss})] \quad (4.38)$$

Rewriting (4.38), one obtains

$$|I_{Ls1}| = \frac{V_{o'ss} \pi}{R_{o'} [1 - \cos(\theta_{ss})]} \quad (4.39)$$

where

$$\cos(\theta_{ss}) = 1 - \frac{2}{f_s C_p R_{o'} + 1} \quad (4.40)$$

The steady state value of the variable γ is defined as

$$\gamma_{ss} = \pi - \theta_{ss} + \frac{1}{2} \sin(2\theta_{ss}) \quad (4.41)$$

For $30^\circ \leq \theta \leq 150^\circ$ this function can be well approximated by

$$\gamma_{ss} = 1.8 \cos(\theta_{ss}) + 1.6. \quad (4.42)$$

Fig. 4.12 shows the graphical representation of (4.41) and (4.42). The solid line represents the exact solution and the dashed line represents the approximation. Both curves agree well, thus the approximation will be applied.

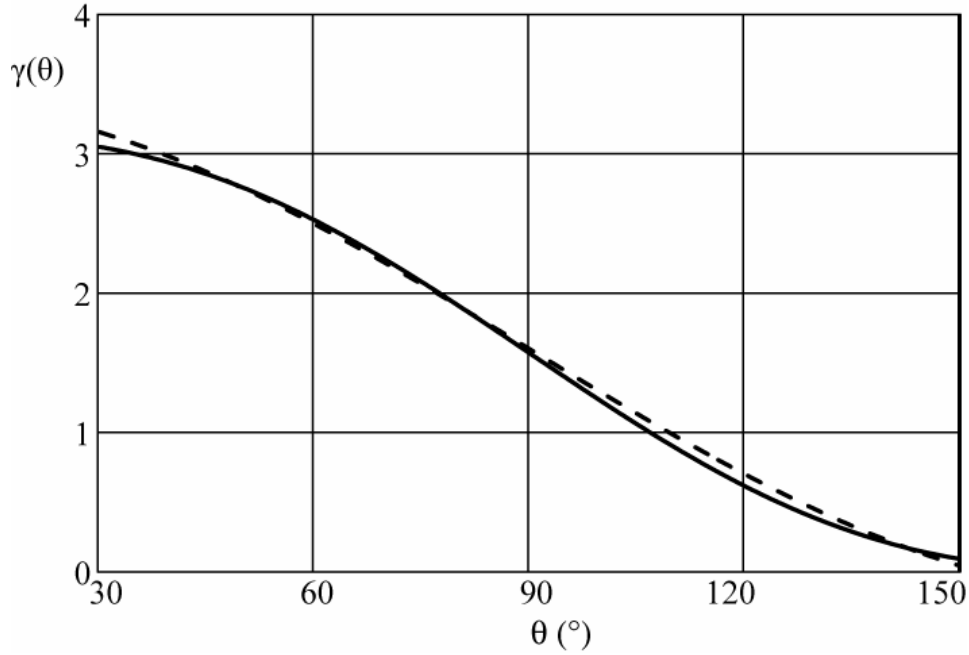


Fig. 4.12: The parameter γ as a function of the output rectifier conduction angle θ .

Substituting (4.39), (4.40) and (4.42) in (4.37) and after some manipulations one has

$$\operatorname{Re}(V_{Cp1}) = \frac{V_{o'}(17f_s C_p - G)}{20\pi f_s C_p}. \quad (4.43)$$

Thus, equation (4.35) becomes

$$|V_{Cs1}| = \frac{1}{|(1 - L_s C_s \omega_s^2)|} \left[\frac{V_{in} \sin(D\pi)}{\pi} + \frac{V_{o'}(17f_s C_p - G)}{20\pi f_s C_p} \right]. \quad (4.44)$$

Taking the relationship $|I_{Ls1}| = \omega_s C_s |V_{Cs1}|$, one obtains the steady-state equation of the amplitude of the resonant current.

$$|I_{Ls1}| = \frac{\omega_s C_s}{|(1 - L_s C_s \omega_s^2)|} \left[\frac{V_{in} \sin(D\pi)}{\pi} + \frac{V_{o'}(17f_s C_p - G)}{20\pi f_s C_p} \right] \quad (4.45)$$

Taking (4.45) one can calculate the error dynamics of the resonant current $\tilde{I}_{Ls} = I_{Ls} - I_{LsD}$

$$I_{Ls} = \frac{\omega_s C_s}{|(1 - L_s C_s \omega_s^2)|} \left[\frac{V_{in} \sin(D\pi)}{\pi} + \frac{V_{o'}(17f_s C_p - G)}{20\pi f_s C_p} \right] \quad (4.46)$$

$$I_{LSD} = \frac{\omega_s C_s}{\left| (1 - L_s C_s \omega_s^2) \right|} \left[\frac{V_{in} \sin(D\pi) + \frac{V_{o'D} (17 f_s C_p - \hat{G})}{20 \pi f_s C_p}}{\pi} \right] \quad (4.47)$$

$$\tilde{I}_{Ls} = \frac{1}{10\alpha \left| 1 - \left(\frac{f_s}{f_o} \right)^2 \right|} (17 f_s C_p e - G e + V_{o'D} \tilde{G}). \quad (4.48)$$

Once the error dynamics of the output voltage and of the resonant current have been calculated, let us propose the following Lyapunov function candidate intending to shape the energy of the output capacitor

$$H = \frac{1}{2} C_o e^2 + \frac{1}{2K_2} \tilde{G}^2. \quad (4.49)$$

The time derivative is given by

$$\dot{H} = C_o \cdot \dot{e} \cdot e + \frac{1}{K_2} \tilde{G} \cdot \dot{\tilde{G}}. \quad (4.50)$$

Substituting (4.24) in (4.50) leads to

$$\dot{H} = \frac{4}{\pi} \tilde{I}_{Ls} e + 2V_{o'D} \tilde{G} e - (2f_s C_p + K_1 + 2G) e^2 + \frac{1}{K_2} \tilde{G} \cdot \dot{\tilde{G}}. \quad (4.51)$$

Substituting (4.48) in (4.51) one obtains

$$\begin{aligned} \dot{H} = & \frac{4}{\pi} (17 f_s C_p Y e - Y G e + Y V_{o'D} \tilde{G}) e + 2V_{o'D} \tilde{G} e \\ & - (2f_s C_p + K_1 + 2G) e^2 + \frac{1}{K_2} \tilde{G} \cdot \dot{\tilde{G}} \end{aligned} \quad (4.52)$$

where

$$Y = \frac{1}{10\alpha \left| 1 - \left(\frac{f_s}{f_o} \right)^2 \right|} \quad (4.53)$$

As the converter will always operate above resonance, the normalized switching frequency $f_{s,N} = f_s/f_o$ is always greater than one. That leads to (4.54).

$$\left| 1 - \left(\frac{f_s}{f_o} \right)^2 \right| = \left(\frac{f_s}{f_o} \right)^2 - 1 \quad (4.54)$$

Rewriting (4.52) one has

$$\begin{aligned} \dot{H} = & \left(\frac{68}{\pi} f_s C_p Y - 2f_s C_p - K_1 \right) e^2 - \left(\frac{4}{\pi} Y + 2 \right) G e^2 \\ & + \left(\frac{4}{\pi} Y + 2 \right) V_{o,D} \tilde{G} e + \frac{1}{K_2} \tilde{G} \cdot \dot{\tilde{G}} \end{aligned} \quad (4.55)$$

With (4.55), one is able to calculate the adaptive law of the estimator. The adaptive law should be selected aiming the elimination of the terms of \dot{H} , which are dependent on the error of the estimate \tilde{G} .

4.4.5.3. Third Step – Estimator Design

The next step is to find an adaptive law for the estimator that properly updates \hat{G} in order to drive the output voltage error e to zero. The adaptive law is based on the gradient method. This method has an update law of the form,

$$\dot{\Psi} = -k \cdot e \cdot \frac{\partial e}{\partial \Psi} \quad (4.56)$$

where

k – adaptation gain ($k > 0$),

e – error signal and

Ψ – parameter to be updated.

The gradient method is a descent method in which a function $f(\Psi)$ is minimized while the parameter Ψ is updated in the direction of the negative gradient of $f(\Psi)$.

The adaptive law is selected with the purpose of eliminating the terms of \dot{H} , which are dependent on the error of the estimate \tilde{G} . The adaptive law based on the gradient method is given by

$$\dot{\tilde{G}} = \hat{G} = -K_2 \left[\frac{4}{10\alpha\pi \left(\left(\frac{f_s}{f_o} \right)^2 - 1 \right)} + 2 \right] V_{o,D} e \quad (4.57)$$

where K_2 is a design constant that fixes the adaptation speed [CdL⁺03].

Substituting (4.57) in (4.55) the derivative of the Lyapunov function is given by (4.58).

$$\dot{H} = \left(\frac{68}{\pi} f_s C_p Y - 2f_s C_p - K_1 - \frac{4}{\pi} YG - 2G \right) e^2. \quad (4.58)$$

In order to analyze the stability of the previous function it is important to introduce some basic concepts about Lyapunov stability theory.

A. STABILITY ANALYSIS USING LYAPUNOV'S SECOND METHOD

Lyapunov's stability theory is a general theory that is applied in the study of stability of linear and nonlinear systems. It includes two methods, Lyapunov's first method (also called indirect method) and Lyapunov's second method (also called Lyapunov's direct method). Lyapunov's first method uses the linearization of a system around its equilibrium point to verify the local stability of the original nonlinear system [IS96],[MLS94]. Lyapunov's second method can be directly applied to a nonlinear system and allows verifying global asymptotic stability by examining the variations of a selected scalar function [DDV02], [MDM⁺04], [SB89].

Lyapunov's second method is a generalization of the idea that if the total energy of a system is continuously dissipating, then the system will eventually settle down to an equilibrium point. Consider, for instance, an energy-like function $V(x)$ of the state x . If its time derivative (rate of change of the energy) is negative, then the system energy is strictly decreasing over time and all trajectories are asymptotically attracted to an equilibrium point. Thus, Lyapunov's second method includes two steps: 1) find a proper Lyapunov function candidate, 2) evaluate its time derivative along the trajectory of the system [DDV02], [Haf04], [MLS94], [SB89].

Consider that there exists a scalar function $V(x)$ of the state x , with continuous first order partial derivatives. If function $V(x)$ is positive definite and if its time derivative along any state trajectory of the system is negative semidefinite then $V(x)$ is called a Lyapunov function for the system [AW95]. Additionally if:

- 1) $\dot{V}(x) = \frac{dV(x)}{dt}$ is negative definite on the entire state space and
- 2) $V(x) \rightarrow \infty$ when $x \rightarrow \infty$

then the equilibrium point at the origin is globally asymptotically stable [AW95], [DDV02], [MDM⁺04].

The Lyapunov's second method is extensively used in control design procedures. Control design requires assuming a Lyapunov function candidate and then finding the control law to make this candidate a real Lyapunov function [MDM⁺04]. Unfortunately, there is no universal method to find Lyapunov functions for a stable system but a good first attempt is to test energy-like quadratic functions [AW95].

Returning to the current design, the Lyapunov function candidate (4.49) is positive definite so it fulfills the first requirement for global stability. It is also clear that in (4.49) if $e \rightarrow \infty$ then $H \rightarrow \infty$. Thus, the second requirement is also satisfied. The last requirement is that the time derivative of H has to be negative definite. Translating this condition in equation (4.58) implies that

$$\frac{68}{\pi} f_s C_p Y - 2f_s C_p - K_I - \frac{4}{\pi} YG - 2G < 0. \quad (4.59)$$

The first term of (4.59) is positive. If this term is greater than or equal to the sum of other terms, then the derivative of H is not negative definite thus stability cannot be guaranteed. One way to solve this problem is to impose the condition that the damping injection gain K_I will be always greater than or equal the first term in (4.59). This condition is given by (4.60).

$$K_I \geq \frac{68}{\pi} f_s C_p Y \quad (4.60)$$

Substituting (4.53) in (4.60), results in

$$K_I \geq \frac{6.8 f_s C_s}{\pi \left(\left(\frac{f_s}{f_o} \right)^2 - 1 \right)} \quad (4.61)$$

In (4.61), it is observed that, after the resonant circuit is designed, the only variable parameter is the switching frequency. The lowest limit of K_I that guarantees global stability for the current design as a function of the switching frequency f_s is plotted in **Fig. 4.13**. Choosing K_I greater or equal the lowest limit for the minimum switching frequency (for example, one

has to choose $K_I \geq 0.11$ (@ 200 kHz), global stability is guaranteed for the whole switching frequency range.

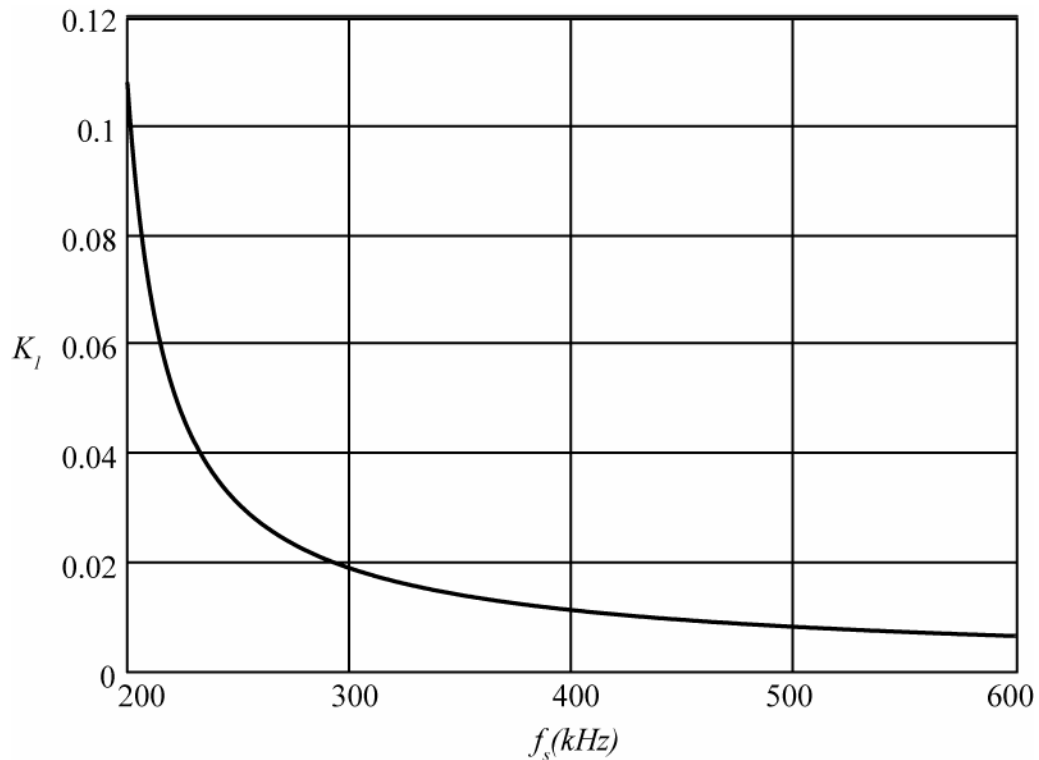


Fig. 4.13: Lower limit of K_I as a function of the switching frequency.

B. ROBUST ADAPTIVE LAW

The adaptive law developed previously is based on an ideal plant model that is free of disturbances. However a real plant may include model uncertainties, unmodeled dynamics and external disturbances.

It was shown that the adaptive controllers designed for a disturbance free plant model have serious robustness problems [IS96], [San92]. In some cases, even small bounded disturbances can cause the parameter error to increase without bound, destabilizing the system and it was also demonstrated that other perturbations, such as time-varying parameters and unmodeled dynamics, could lead to instability [San92]. Therefore it is important to modify the adaptive law such that it can preserve its stability in the presence of disturbances and uncertainties. The modified adaptive law is referred in the literature as *robust adaptive law* [IS96].

Several approaches that modify the adaptation law were proposed and one of the most popular is the *projection method*.

Projection is a method that eliminates parameter drift by keeping the parameter estimates within some a priori defined bounds [Ism98], [San92]. Projection method requires some a priori knowledge on unknown constant ψ (cf. eq. (4.56)) to define the bounded convex parameter set $\Pi(\psi_{max})$ in such a way that the actual value of ψ fits in the set. ψ_{max} is the a priori known upper bound of $|\psi|$. If an estimated parameter $\hat{\psi}$ reaches a bound, adaptation is stopped for that parameter until its gradient becomes negative. As long as the parameter estimate is within its convex set or on the boundary of its convex set with a negative gradient, adaptation proceeds unhindered. The projection method is also called *gradient projection method* because it applies a gradient algorithm in order to reduce the error of a certain function (cf. (4.56)) [IS96]. The gradient projection method retains all the properties of the unmodified adaptation law that are established in the absence of projection and in addition guarantees that $\psi \in \Pi(\psi_{max}) \forall t \geq 0$ provided $\psi(0) = \psi_0 \in \Pi(\psi_{max})$ [IS96].

In the current design, one has the following a priori knowledge of the variable G : 1) G is always positive, that means $G \geq \varepsilon > 0$, where ε is a small positive scalar and 2) The upper bound of G for a given design is also a priori known and is defined by $G_{max} = 1 / R_{o,min}$.

Consider the unmodified adaptive law given by (4.57) with an upper bound G_{max} , then the gradient projection algorithm will give us (4.62).

$$\dot{\hat{G}} = \begin{cases} -K_2 \left[\frac{4}{10\alpha\pi \left(\left(\frac{f_s}{f_o} \right)^2 - 1 \right)} + 2 \right] V_{o'D} e & \text{if } |\hat{G}| < G_{max} \\ \text{or if } |\hat{G}| = G_{max} \text{ and } V_{o'D} e \hat{G} \leq 0 \\ 0 & \text{otherwise} \end{cases} \quad (4.62)$$

Equation (4.62) ensures that $\hat{G} \geq \varepsilon > 0$. The modified adaptive law can be rewritten as (4.63).

$$\dot{\hat{G}} = Proj \left\{ -K_2 \left[\frac{4}{10\alpha\pi \left(\left(\frac{f_s}{f_o} \right)^2 - 1 \right)} + 2 \right] V_{o'D} e \right\} \quad (4.63)$$

where *Proj* represents the projection operator shown in eq. (4.62).

4.4.5.3. Fourth Step – Duty Cycle Generation

The steady-state relationship between the magnitude of the resonant current $\langle I_{Ls} \rangle_1$ and the duty cycle D is given by (4.64). For the definitions of all variables in this equation please refer to **Chapter 3**.

$$\left| \langle I_{Ls} \rangle_1 \right| = 2f_s C_s V_{in} \sqrt{\frac{2(1 - \cos(D\pi))}{\left(1 - \left(\frac{f_s}{f_o} \right)^2 + \frac{\gamma}{\pi\alpha} \right)^2 + \left(\frac{\delta}{\pi\alpha} \right)^2}} \quad (4.64)$$

The dynamical copy of this relationship is given by

$$I_{LsD} = 2f_s C_s V_{in} \sqrt{\frac{2(1 - \cos(D\pi))}{\left(1 - \left(\frac{f_s}{f_o} \right)^2 + \frac{\gamma_D}{\pi\alpha} \right)^2 + \left(\frac{\delta_D}{\pi\alpha} \right)^2}} \quad (4.65)$$

where

$$\theta_D = \cos^{-1} \left(\frac{\pi f_s C_p V_{o'D}}{I_{LsD}} - 1 \right), \quad (4.66)$$

$$\delta_D = \sin^2(\theta_D), \quad (4.67)$$

$$\gamma_D = \pi - \theta_D + \frac{1}{2} \sin(2\theta_D). \quad (4.68)$$

The next step is to evaluate (4.65) for the reference value of the resonant current I_{Lsref} . After some manipulation one obtains the expression for the control variable D as a function of the reference resonant current shown in (4.69).

$$D = \frac{1}{\pi} \cos^{-1} \left\{ \frac{1}{2} \left[2 - \left(\frac{I_{Lsref} \delta_{ref}}{2\pi f_s C_p V_{in}} \right)^2 - \left(\frac{I_{Lsref}}{2f_s C_s V_{in}} \right)^2 \cdot \left(1 - \left(\frac{f_s}{f_o} \right)^2 + \frac{\gamma_{ref}}{\pi\alpha} \right)^2 \right] \right\} \quad (4.69)$$

where

V_{in} – input voltage,

$f_o = \frac{1}{2\pi\sqrt{L_s C_s}}$ – series resonant frequency,

L_s – series resonant inductor,

C_s – series resonant capacitor,

$$\alpha = \frac{C_p}{C_s}, \quad (4.70)$$

$$\theta_{ref} = \cos^{-1} \left(\frac{\pi f_s C_p V_{o'D} - I_{Lsref}}{I_{Lsref}} \right), \quad (4.71)$$

$$\delta_{ref} = \sin^2(\theta_{ref}), \quad (4.72)$$

$$\gamma_{ref} = \pi - \theta_{ref} + \frac{1}{2} \sin(2\theta_{ref}). \quad (4.73)$$

4.4.5.4. Complete Passivity Based Controller

Finally, the complete passivity based controller is defined as

$$D = \frac{1}{\pi} \cos^{-1} \left\{ \frac{1}{2} \left[2 - \left(\frac{I_{Lsref} \delta_{ref}}{2\pi f_s C_p V_{in}} \right)^2 - \left(\frac{I_{Lsref}}{2f_s C_s V_{in}} \right)^2 \cdot \left(1 - \left(\frac{f_s}{f_o} \right)^2 + \frac{\gamma_{ref}}{\pi\alpha} \right)^2 \right] \right\} \quad (4.74)$$

$$I_{Lsref} = \frac{V_{o'ref} \pi}{2} (f_s C_p + \hat{G}) \quad (4.75)$$

$$C_o \frac{dV_{o'D}}{dt} = \frac{4}{\pi} I_{Lsref} - 2f_s C_p V_{o'D} - 2V_{o'D} \hat{G} + K_1 e \quad (4.76)$$

$$\dot{\hat{G}} = \text{Proj} \left\{ -K_2 \left[\frac{4}{10\alpha\pi \left(\left(\frac{f_s}{f_o} \right)^2 - 1 \right)} + 2 \right] V_{o'D} e \right\} \quad (4.77)$$

The closed loop system is asymptotically stable at the equilibrium point

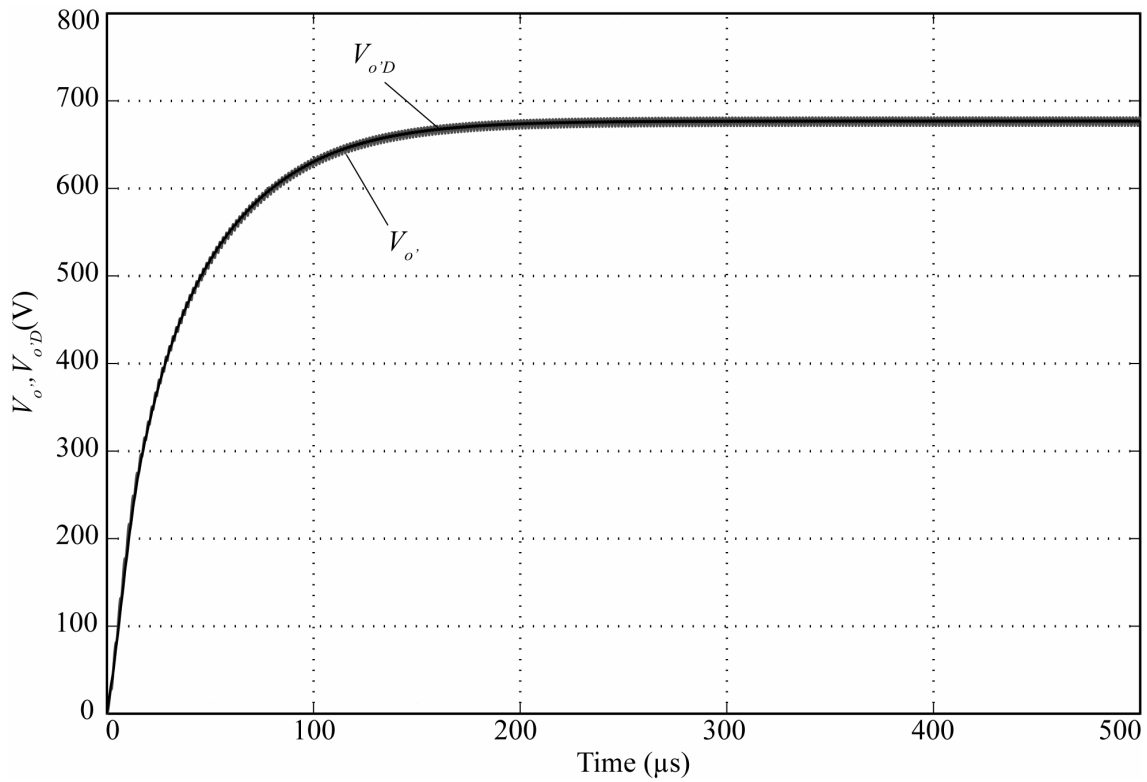
$$\begin{bmatrix} V_{o'}, & V_{o'D}, & I_{L_s}, & \hat{G} \end{bmatrix} = \begin{bmatrix} V_{o'ref}, & V_{o'ref}, & \frac{V_{o'ref}\pi}{2} \left(f_s C_p + \frac{1}{R_{o'}} \right), & \frac{1}{R_{o'}} \end{bmatrix}.$$

4.4.6. Simulation Results

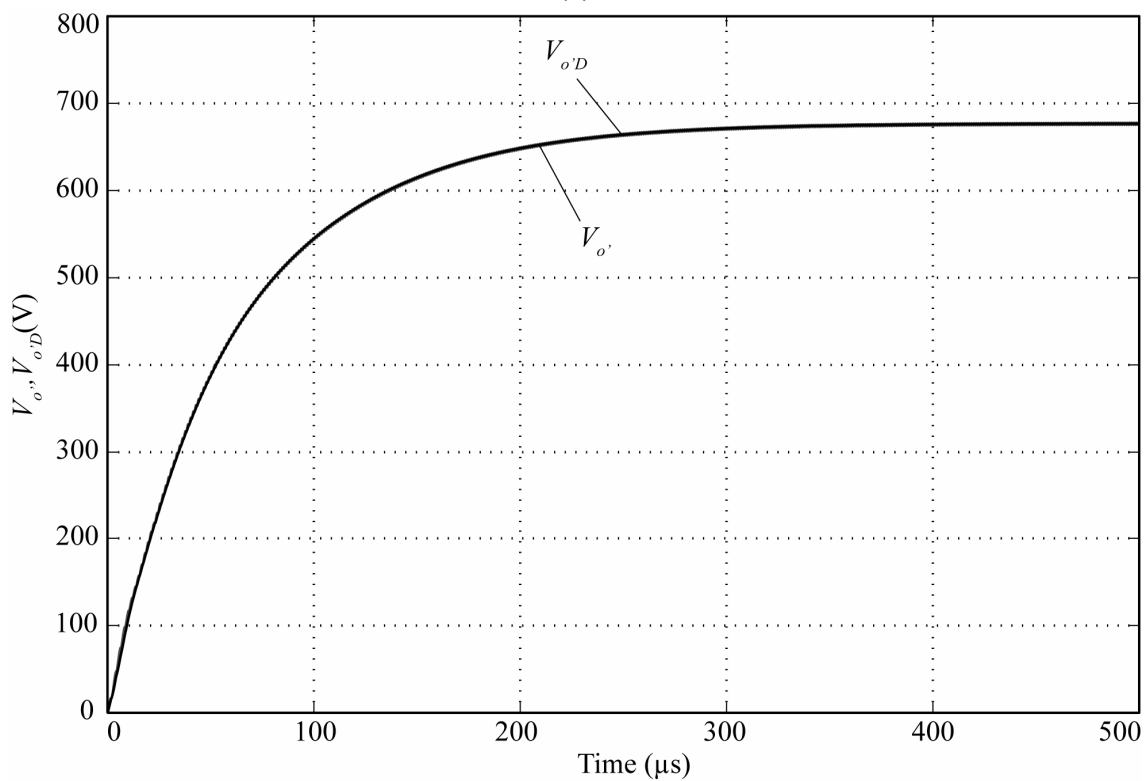
In order to validate the passivity based controller design described in section 4.4.5, digital simulations using MATLAB/Simulink are performed. The circuit is simulated without transformer as already shown in **Fig. 3.1** and all switches and diodes are simulated with ideal components. The parameters used for the simulations are: $V_{in} = 325\text{V}$, $L_s = 16\mu\text{H}$, $C_s = 48\text{nF}$, $C_p = 15\text{nF}$, $n = 17$ and $C_{o1'} = C_{o2'} = 1\mu\text{F}$. Additionally, $V_{o'ref} = 677\text{V}$ and the passivity based controller is designed with: $K_1 = 0.53$ and $K_2 = 0.02$. The values of K_1 and K_2 have been designed using simulations.

In the first simulation, the start up of the converter is simulated at rated power and at light load ($P_o = 1.15\text{kW}$). The corresponding values of $R_{o'}$ are, respectively, $R_{o'} = 99.5\Omega$ (full load) and $R_{o'} = 398\Omega$ (light load).

Fig. 4.14 shows the start up response of the measured and desired output voltage $V_{o'}(t)$ and $V_{o'D}(t)$, respectively, at rated power and at light load. One can see that in both cases, the voltages converge without overshoot very fast to the constant reference voltage $V_{o'ref} = 677\text{V}$. At rated power the output voltage achieves its steady state value within about $300\mu\text{s}$ and at light load it takes somewhat longer, namely about $400\mu\text{s}$. Normally one expects that the opposite will occur, but in PBC design the estimated parameter \hat{G} has a large influence on the rising time as will be shown later.



(a)



(b)

Fig. 4.14: Start up response of the measured and desired output voltage, V_o and $V_{o'D}$ for operation at rated power (a) and at light load (b).

Fig. 4.15 shows the start up response of the estimated parameter \hat{G} and the real value of $G = 1/R_o$.

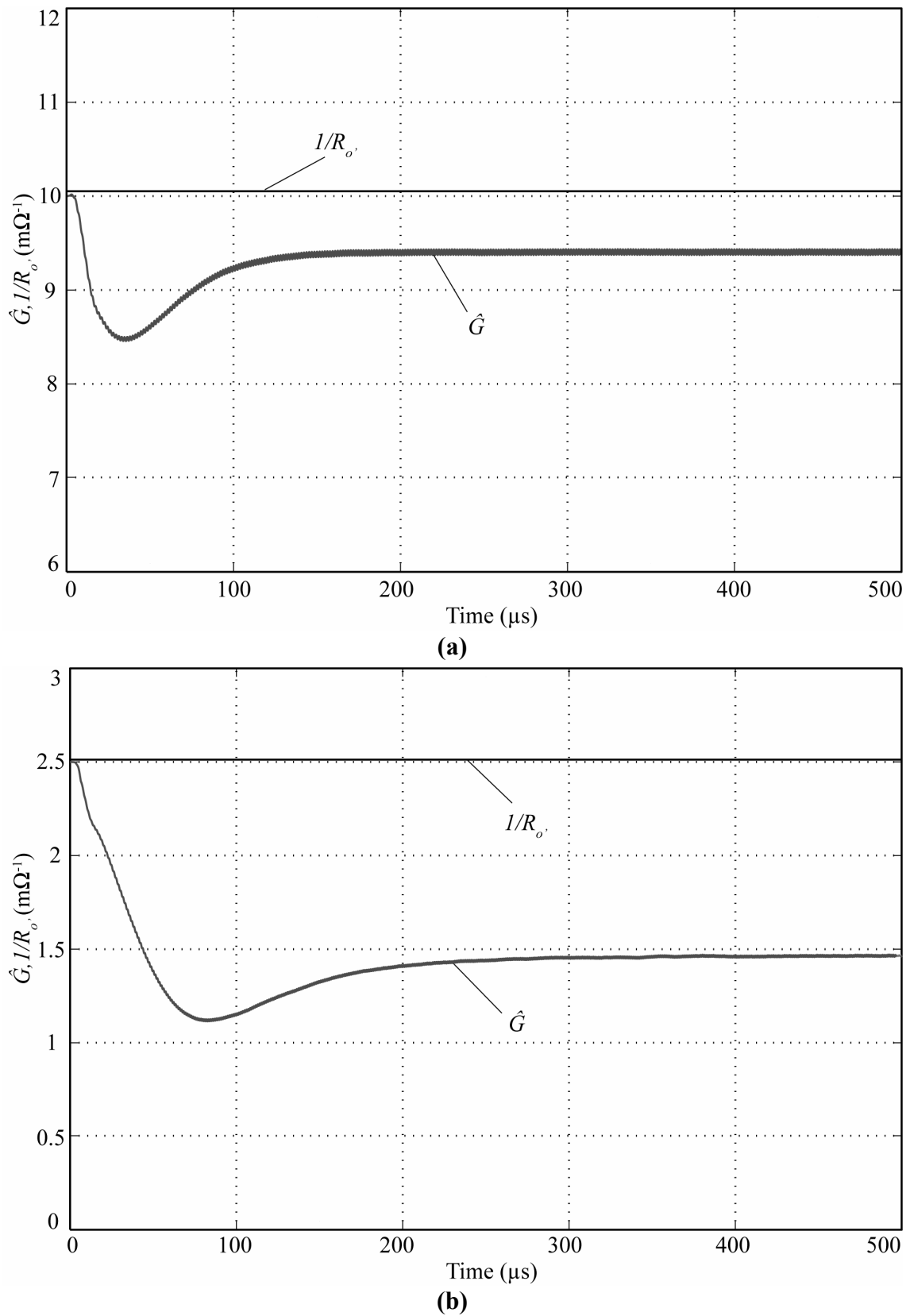


Fig. 4.15: Estimated parameter and real value of G for operation at rated power (a) and at light load (b).

The initial values of the estimate \hat{G} are chosen to be equal to the respective true values of G . It is observed that the estimator has a deviation in relation to the real value of G . At light load the deviation is larger than at rated power. This occurs because at light load the estimate \hat{G} has to converge to a very low value, so it is more sensitive to deviation of other parameters of the circuit. Even so the output voltage converges to the right steady-state value as shown in **Fig. 4.14**. But the error in \hat{G} influences the transient response because it affects the auxiliary control variable I_{Lsref} , as will be shown in the following. Higher deviation of \hat{G} with respect to the correct value of G leads to longer rising time, i.e. slower transient response. If the load resistance stays constant the error of the estimated parameter is lower for higher level of output voltage and if the output voltage is maintained in a constant level, the error will decrease as load increases.

The start up transient behavior of the resonant current i_{Ls} and of the auxiliary control variable I_{Lsref} is shown in **Fig. 4.16**. I_{Lsref} is dependent on the estimate \hat{G} (cf. eq. (4.21)) but it converges about to its right value for operation at rated power even if the estimate \hat{G} has a small error. In contrast to this case, at light load, where the relative error of the parameter \hat{G} becomes larger, I_{Lsref} does not converge to the simulated value of the resonant current but to a lower value. Thus, the passivity based controller incorrectly detects that a lower energy level has to be transferred to the output and adjusts the duty cycle to a lower value (cf. eq. (4.69)) in order to prevent overshoot in the output voltage. This fact explains why the transient response at light load is relative slow compared with the transient behavior at rated power.

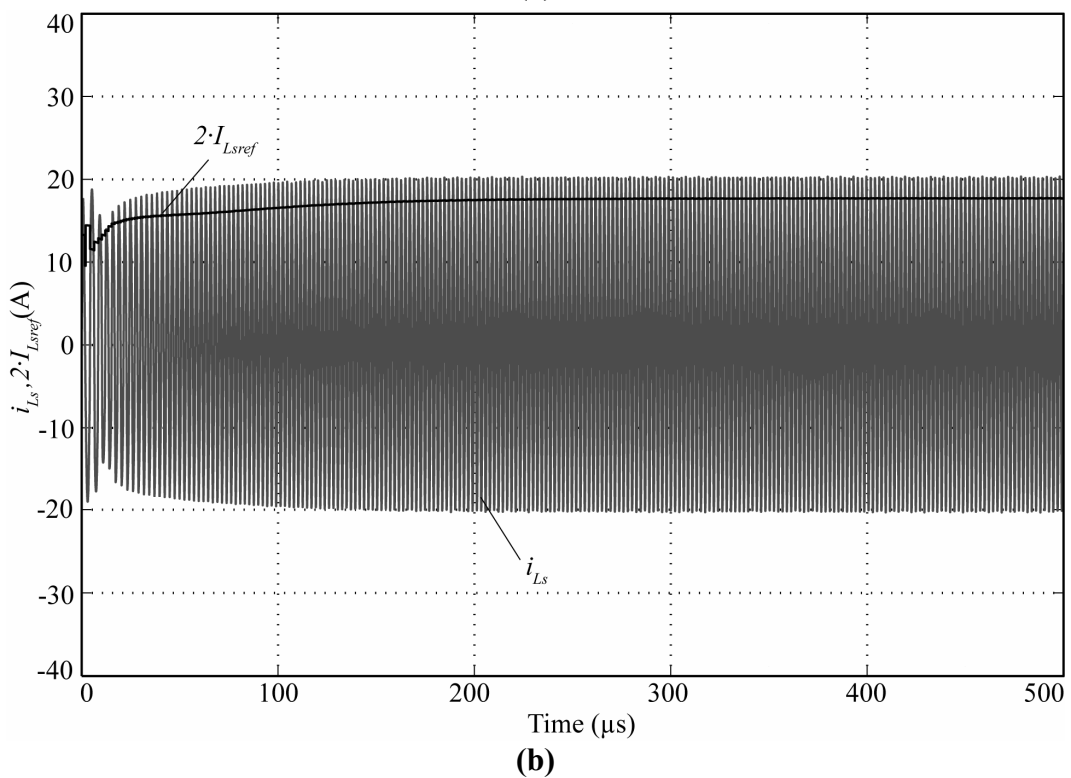
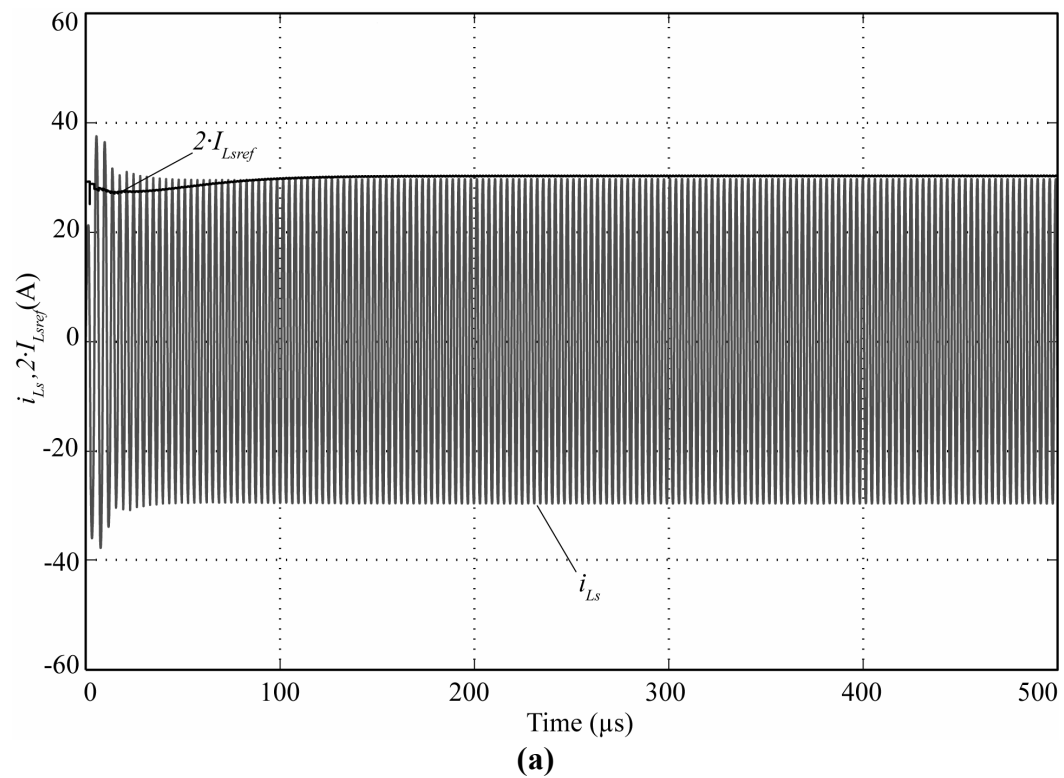
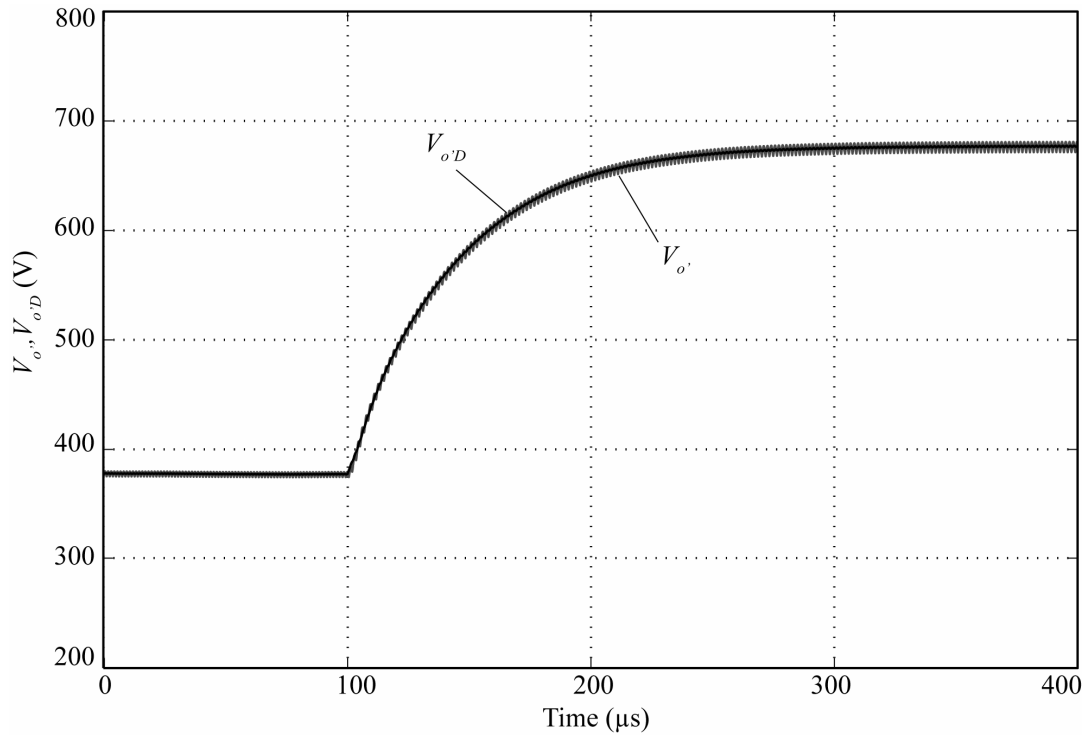


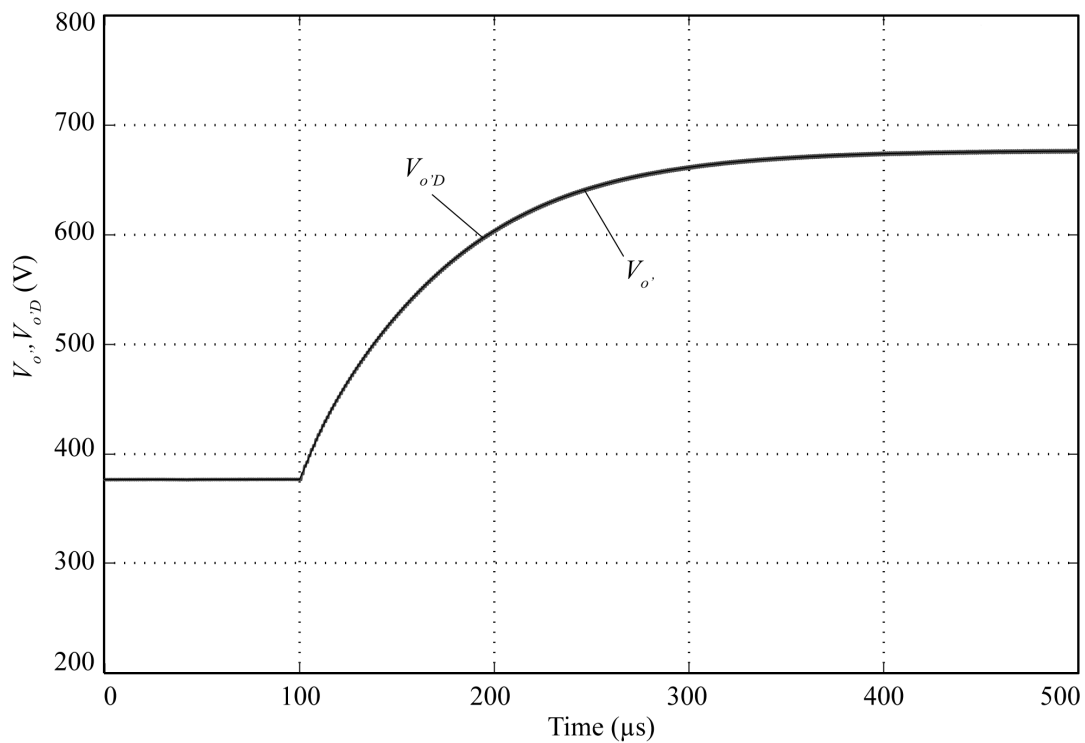
Fig. 4.16: Start up response of the resonant current and of the parameter I_{Lsref} for operation at rated power (a) and at light load (b).

Fig. 4.17 represents the closed loop response of the measured and desired output voltage V_o and $V_o'D$ respectively, at rated power and at light

load, when a step change occurs in the reference voltage $V_{o'_{ref}}$. The value of $V_{o'_{ref}}$ is started in 377V and at time $t = 100\mu\text{s}$, it is changed to 677V.



(a)



(b)

Fig. 4.17: Measured output voltage, $V_{o'}$ and desired output voltage $V_{o'D}$ with a step change in the value of reference voltage from 377V to 677V for operation at rated power (a) and at light load (b).

One can see that the controller reacts unquestionably slower to the step-like change in the reference voltage than the gain scheduled controller proposed in section 4.3. This fact does not surprise because gain scheduling control is a straightforward process where no estimation is involved. Thus, the controller parameters can be changed very fast. In contrast, the PBC has the drawback that its performance is strongly dependent on the quality of the estimate \hat{G} . One can see that at light load operation, when the error of \hat{G} increases, the transitory response of the passivity based controller is even poorer. Hence, the gain scheduled controller is the best alternative to be implemented in the high-voltage generator.

4.5. SUMMARY

In this chapter two different adaptive controller designs are presented, i.e. a gain scheduled controller and a passivity based controller. The design using gain scheduling approach is less involved than the passivity based controller design. This is due to the fact that employing gain scheduling, one is able to apply linear time invariant control techniques. In contrast, the passivity based controller is designed using the nonlinear model of the system that leads to a very involved design procedure. Comparing the step response of both controllers, the gain scheduled controller has faster transient behavior and it is also more robust against variations in the operating point so that its performance stays almost constant independent of load. For these reasons, the gain scheduled controller is preferred for the practical implementation of the converter.

CHAPTER 5

5. EXPERIMENTAL SETUP

5.1. INTRODUCTION

In order to verify the results obtained theoretically and with digital simulations a 5kW prototype is built. Since the objective of the laboratory tests is only to verify the validity of the small-signal representation and of the proposed gain scheduled controller, one does not have to construct the complete high-voltage converter. It is sufficient to build the equivalent circuit previously shown in **Fig. 3.1** Thus, the prototype is constructed without high-voltage transformer. The parasitic elements (leakage inductance and stray capacitance), which are necessary to build the resonant circuit, are replaced with external elements. This chapter shows experimental results of the steady state and dynamic behavior of the constructed prototype for different load levels.

5.2. SPECIFICATIONS OF THE PROTOTYPE

The power circuit schematic of the constructed prototype was shown in **Fig. 3.1**. This circuit was previously designed in **Chapter 2** and the main specifications and components of the power circuit of the prototype are shown in **Table 5.1**.

$V_{in} = 325V$	$V_{o'} = 23kV/2n \dots 62.5kV/2n$
$L_s = 16\mu H$	$P_o = 0 \dots 5kW$
$C_s = 48nF$	$f_o = (2\pi \sqrt{L_s C_s})^{-1} = 181.5kHz$
$C_p = 15nF$	$f_s = 260kHz - 550kHz$
$C_{o'} = 1\mu F$	$S_1, S_2, S_3, S_4 = APT \text{ MOSFETS} - 500V/57A$
$n = 17$	$D_{o1}, D_{o2} = SiC \text{ Diodes } 4 \times 1200V/10A$

Table 5.1: Specifications and components of the power circuit.

Fig. 5.1 shows two photographs of the constructed prototype. It is composed of three printed circuit boards: power board, control board and DSP board. The boards will be described in the following.

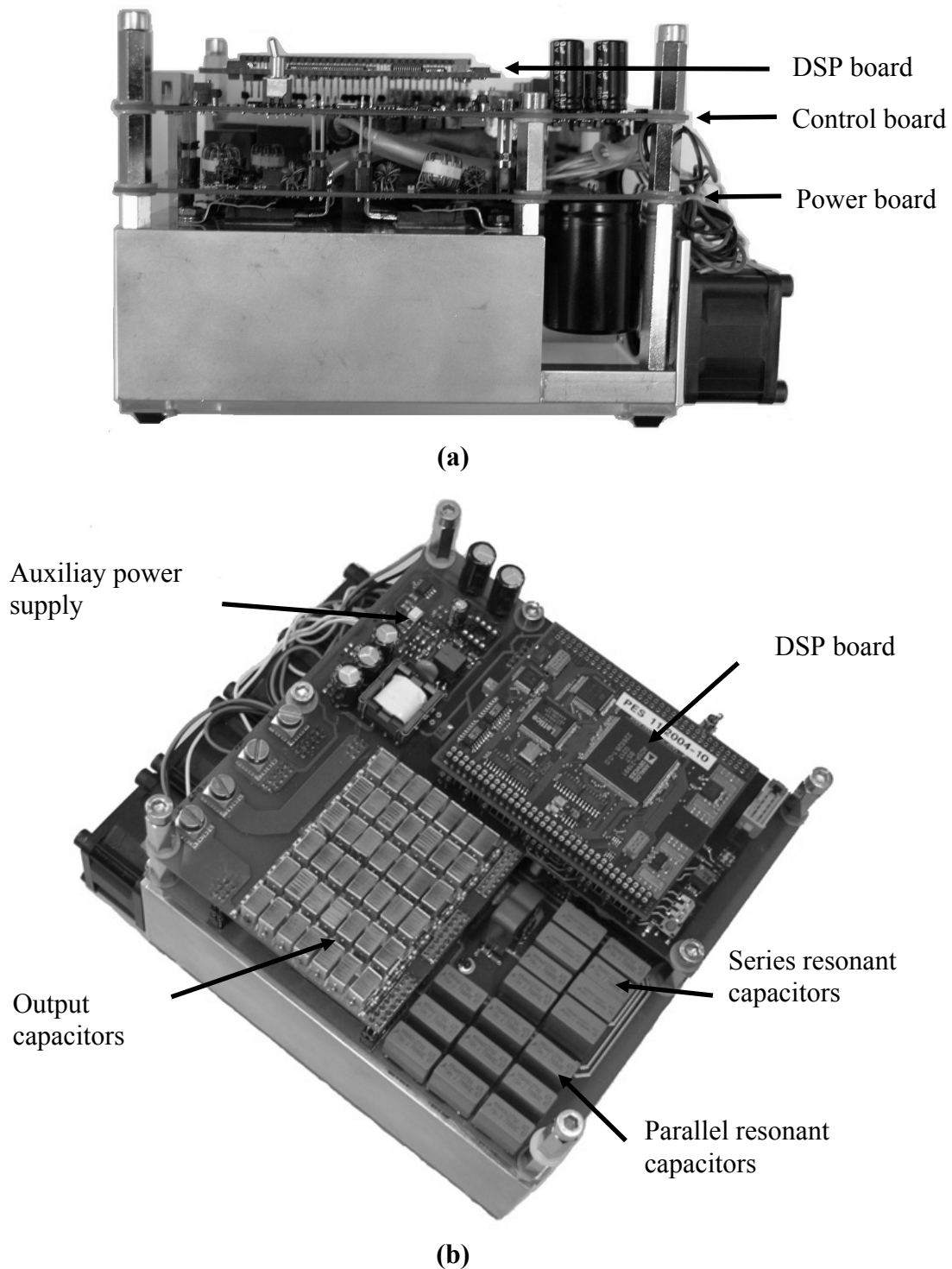


Fig. 5.1: (a) Overview of the three PCBs of the constructed prototype; (b) Overview of the main components (System dimensions: L: 19.5cm x W: 16cm x H: 11cm).

Additionally to the components indicated in **Fig. 5.1(b)**, the DC link capacitors and the power MOSFETs can be seen in **Fig. 5.1(a)**. The

resonant inductor is not visible because it is integrated into the heatsink. Its exact position can be seen in **Fig. 5.2**. Some fins of the heatsink have been removed in order to accommodate the resonant inductor. In this way the heatsink facilitate the inductor cooling.

In order to verify if the operating temperatures of the main power devices would not be excessively high, thermal simulations were performed assuming an ambient temperature of $T_a = 45^\circ\text{C}$. As said before, the switches are implemented with power MOSFETs and each output diode is implemented with four Schottky diodes, i.e. two in series and two in parallel. The power losses assumed for the simulations are following: two power MOSFETs in TO-247 package and each with 40W losses (ZCS-switches), two power MOSFETs with TO-247 package and each with 20W losses (ZVS-switches), 08 power SiC Schottky diodes in TO-220-2 package and each with 11W losses and one resonant inductor constructed with three pairs of E-cores 42/21/15 (Material N87) and total losses of 74W (25W total core losses and 49W total winding losses). The thermal resistance junction to case R_{thj-c} of the power MOSFETs is 0.22°C/W and of the power diodes is 0.48°C/W . The thermal resistance case to heatsink of the isolation between the semiconductor and the heatsink is 0.25°C/W . The heatsink used is SK416-165 with a thermal resistance of 0.5°C/W . The prototype uses four 24VDC cooling fans of the type San Ace (Sanyo Denki) with static pressure 210Pa and air flow $0.46\text{m}^3/\text{min}$. **Fig. 5.2** shows the results obtained with the thermal simulation.

In **Fig. 5.2** one can see that the maximum heatsink temperature beneath the MOSFETs is 93.8°C for one ZCS switch. Considering the thermal resistance of 0.22°C/W and the losses of 40W the maximum junction temperature is about 103°C . The maximum allowed junction temperature of the power MOSFETs is 150°C . Thus, it is guaranteed that the device junction temperature remains below the allowable maximum junction temperature under all operating conditions. For the output diodes the maximum heatsink temperature is 93.6°C . Considering the thermal resistance of 0.48°C/W and the losses of 11W the maximum junction temperature is about 99°C . According to the datasheet, the maximum

allowed junction temperature of the diodes is 175°C . Also in this case no critical temperature is present.

The resonant inductor has high losses and consequently a high temperature of 103°C . However, this is also not critical as the thermal simulations are for continuous operation and in practice the x-ray generator works in discontinuous mode. That means it is five seconds turned on and two minutes turned off. Consequently, the temperature increase will be considerably lower. Although, the prototype has been designed for continuous operation, in order to facilitate the realization of the tests.

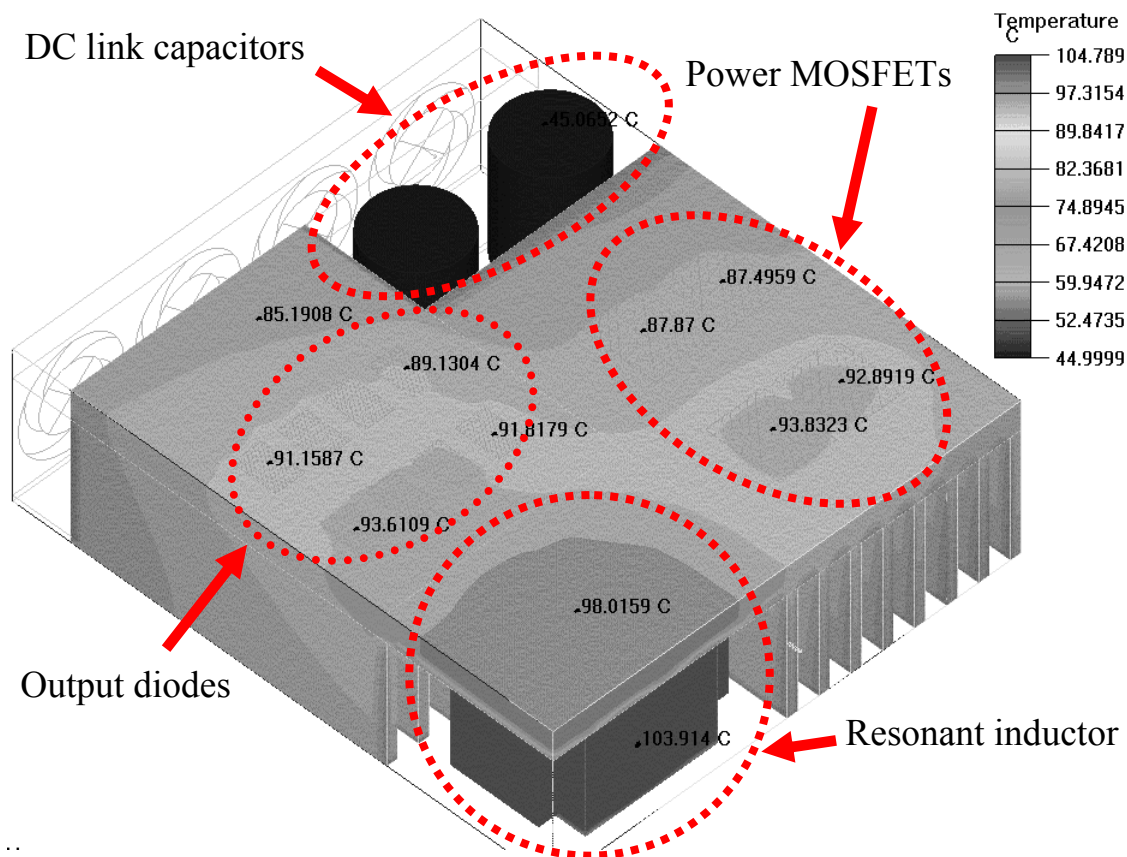


Fig. 5.2: Thermal simulation of the designed prototype.

5.3. DESCRIPTION OF THE PRINTED CIRCUIT BOARDS

5.3.1. Power and Control Boards

The power board (cf. Fig. 5.1(a)) includes the power circuit (except the output capacitors) and the gate drivers. The control board contains the output capacitors and all the control components with exception of the RMX DSP Controller Module that has its own board. The main component

of the control board is a complex programmable logic device (CPLD) where the state machine is implemented using VHSIC Hardware Description Language (VHDL).

The state machine is responsible for the generation of the gate signals of the MOSFETs and its operation was described in details in **Chapter 3**. The CPLD receives the current zero crossing synchronizing signal and the DSP signal and adjusts control frequency and duty cycle, respectively. The CPLD also protects the circuit from abnormal behavior by means of an error state implemented in the state machine. This state is entered when some irregular condition occurs, for example, when both switches of the same bridge leg are commanded to turn on at the same time. The error state turns off all the power switches and restarts the state machine. The CPLD used is of the ispMACH™4A family from Lattice, namely M4A5-192/96. It is a 5V device and it has 144 macrocells, 96 I/O user options and 144 pins [Lat03].

5.3.2. DSP Board

The RMX DSP Controller Module is a mixed signal DSP module for control of power electronic systems. A block diagram of the DSP module is shown in **Fig. 5.3**.

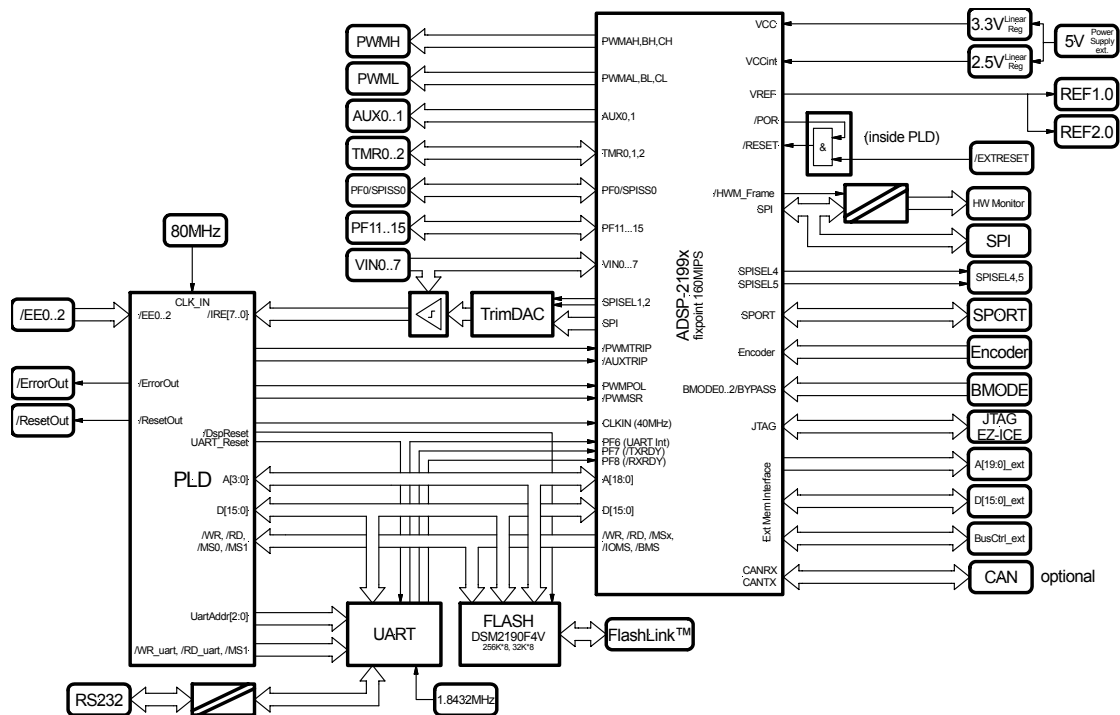


Fig. 5.3: Block diagram of the RMX DSP controller module [Pow03].

The heart of the RMX Module is the Mixed Signal DSP ADSP-21991 from Analog Devices. This DSP offers fixed point arithmetic with a maximum performance of 160 MIPS. The ADSP-21991 integrates 40K words of on chip memory configured as 32K words, 24-bit, of program RAM, and 8K words, 16-bit, of data RAM. It incorporates a variety of communication interfaces such as a serial port (SPORT), an SPI interface, an external memory interface, three programmable timers and 16 general purpose programmable flag pins, of which six are externally accessible on the RMX Module. The mixed signal architecture offers also an 8-channel, 20 MSPS, 14-bit Analog-to-Digital Converter and a 32-bit Encoder interface unit. A special PWM Generation Unit allows the generation of three phase, 16-bit center based PWM signals with a resolution of 12.5 ns, while an auxiliary PWM generation unit offers two independent auxiliary 16-bit PWM signals [Pow03].

This DSP module is used to implement the discrete adaptive controller for the resonant converter. A simple block diagram of the controller implementation is shown in Fig. 5.4.

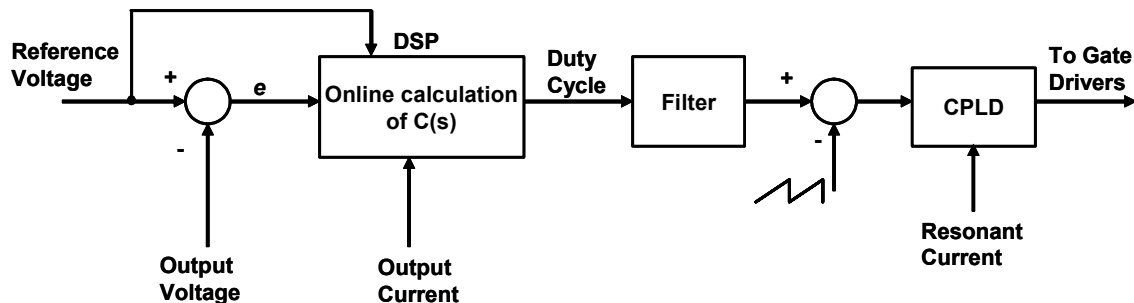


Fig. 5.4: Block diagram of the control implementation.

The output voltage V_o is measured using a resistive divider and is compared with the reference voltage $V_o'_{ref}$. Additionally the output current I_o is measured using a LEM current transducer. Both measured signals are adapted before they are sent to the DSP board because the A/D inputs of the DSP works with voltage level 0V...2V. The error e is the input of the adaptive PI controller implemented in the DSP. The controller verifies how much current is available to reach a predetermined output voltage. The adaptive proportional and integral gains are recalculated for each sampling time using the values of the reference voltage and of the measured output current so that the controller can impress a precise output voltage for any

operation point. The output of the DSP is a PWM signal that is proportional to the duty cycle. This PWM signal is filtered and is compared with a constant amplitude sawtooth (for details about the sawtooth generator see **Chapter 2**). The output is a logical signal PHI , proportional to the duty cycle that serves as one input of the CPLD, where the state machine is implemented. The resonant current is measured using a current transformer (toroidal core 1:100) and it is used to generate the input signal ILZ for the CPLD. Details about the input signals of PLD and functional description of the state machine are shown in **Chapter 2**.

5.4. EXPERIMENTAL RESULTS

In this section experimental results for low, medium and full load are depicted in order to show the behavior of the converter for different load conditions.

5.4.1. Results for $P_o = 230\text{W}$

The steady state waveforms of voltage v_{AB} and resonant current i_{Ls} for $V_{o,ref} = 677\text{V}$ are shown in **Fig. 5.5**.

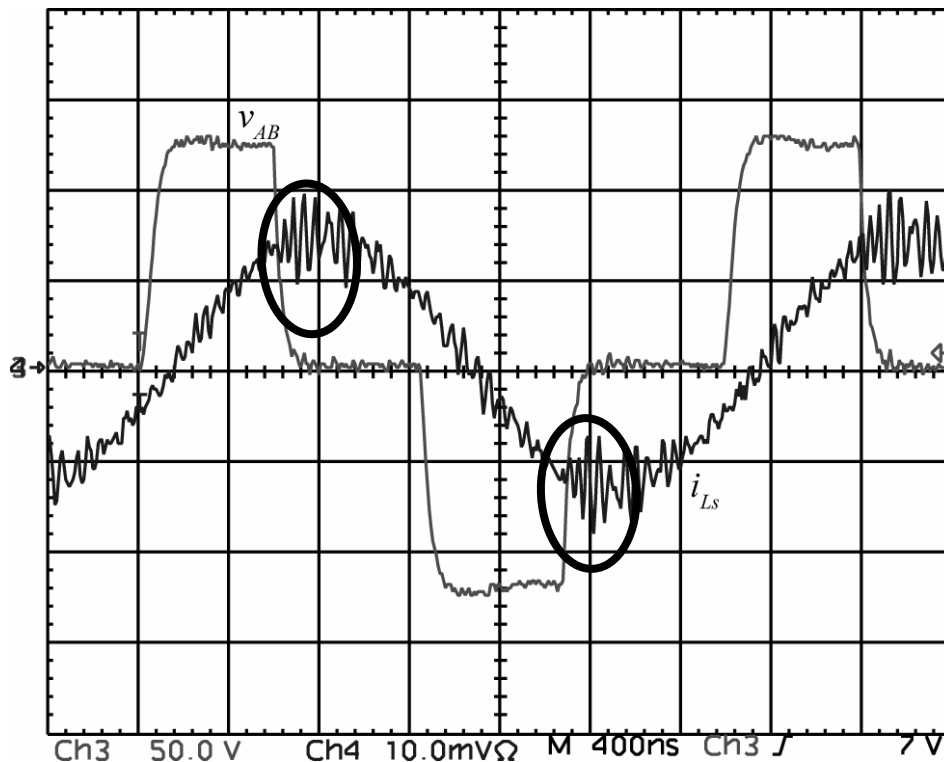


Fig. 5.5: Output voltage V_o (100V/div) and the voltage v_{AB} (50V/div) and resonant current i_{Ls} (10A/div). Time scale: 400ns/div.

The most oscillations observed in the resonant current i_{Ls} in **Fig. 5.5** are not real. They are caused by electromagnetic interference in the measurements. The only real oscillations are marked with a circle. The cause of these oscillations will be explained later.

Fig. 5.6 shows the steady state waveforms of the voltage across the parallel capacitor v_{Cp} and the output voltage $V_{o'}$ for $V_{o'_{ref}} = 677V$. The voltage v_{Cp} is clamped every half period to the half value of the output voltage. In the case of **Fig. 5.6** the voltage is clamped for a very short time because the output rectifier conducts for a very short interval in consequence of the low output power.

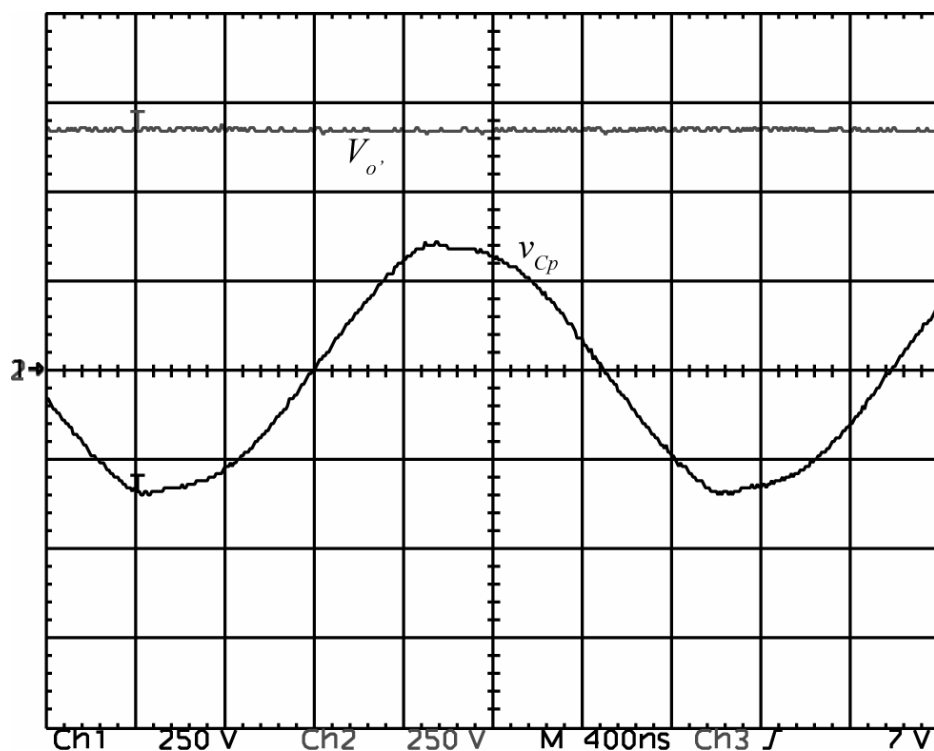


Fig. 5.6: Voltage across the parallel capacitor v_{Cp} (250V/div) and output voltage $V_{o'}$ (250V/div). Time scale: 400ns/div.

The gate voltages of the MOSFETs S_1 and S_3 are shown in **Fig. 5.7**. The positive level of the gate signal is set to 11.8V and the negative level to -3.2V. The switching frequency is 381 kHz and the switches operate under zero voltage switching (ZVS) condition.

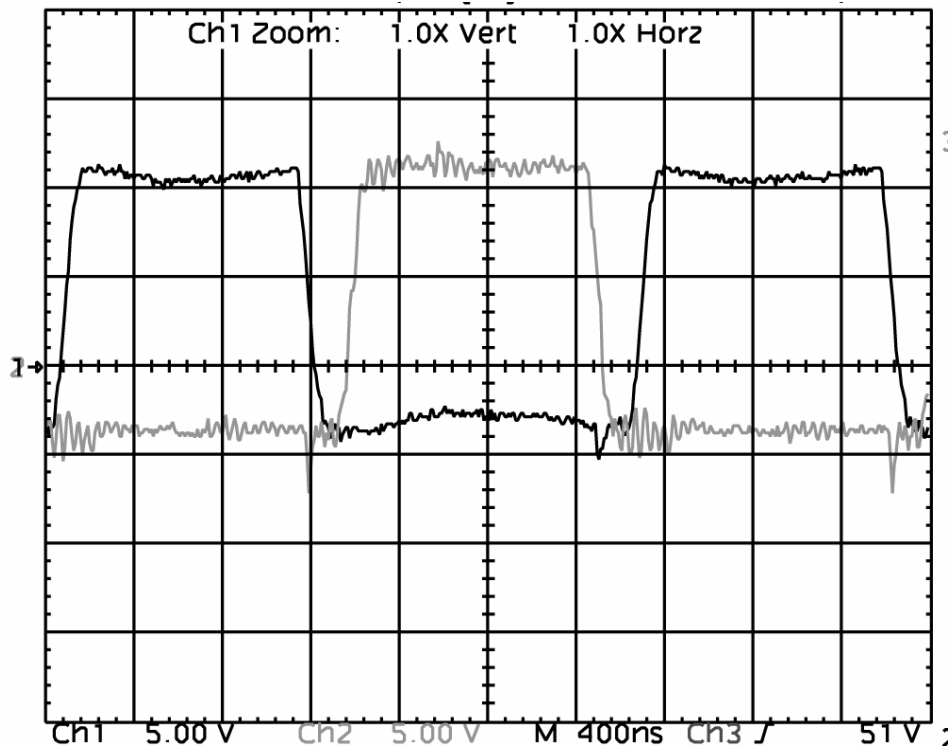


Fig. 5.7: Gate signals of the ZVS bridge leg. Time scale: 400ns/div

Fig. 5.8 shows the output voltage when a step change in the reference voltage $V_{o,ref}$ occurs.

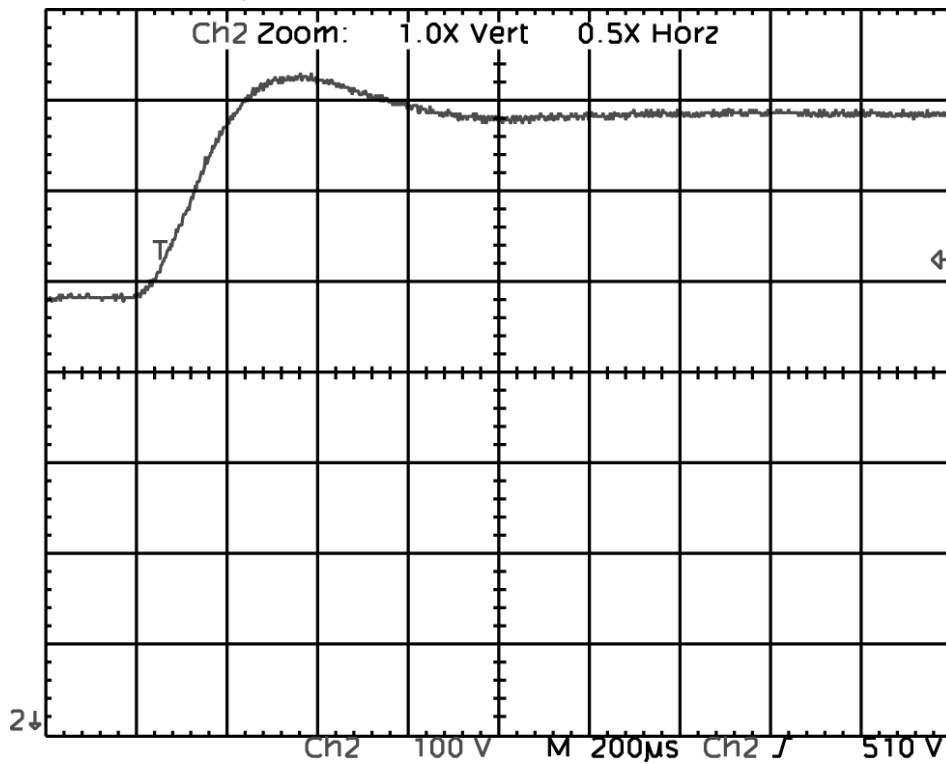


Fig. 5.8: Step response of the output voltage V_o . (100V/div). Time scale: 200μs/div.

At time $t = 200\mu\text{s}$ the reference value is changed from 477V to 677V. One can see in **Fig. 5.8** that an unexpected overshoot occurs in the output voltage. The fact is that in practice the prototype has been tested with a DC power supply. This DC power supply has a current limitation of 10A_{DC} and the controller try to compensate this limitation by setting the duty cycle to a maximum. When the input current goes to a level lower than the saturation level, the controller reacts immediately but it is not possible to avoid the overshoot anymore. Simulations with such type of current limitation show the same behavior. In order to reduce this limitation one has to increase the output capacitance.

5.4.2. Results for $P_o = 1.15\text{kW}$

Fig. 5.9 shows the steady state waveforms of voltage v_{AB} and resonant current i_{Ls} for $V_{o'_{ref}} = 677\text{V}$.

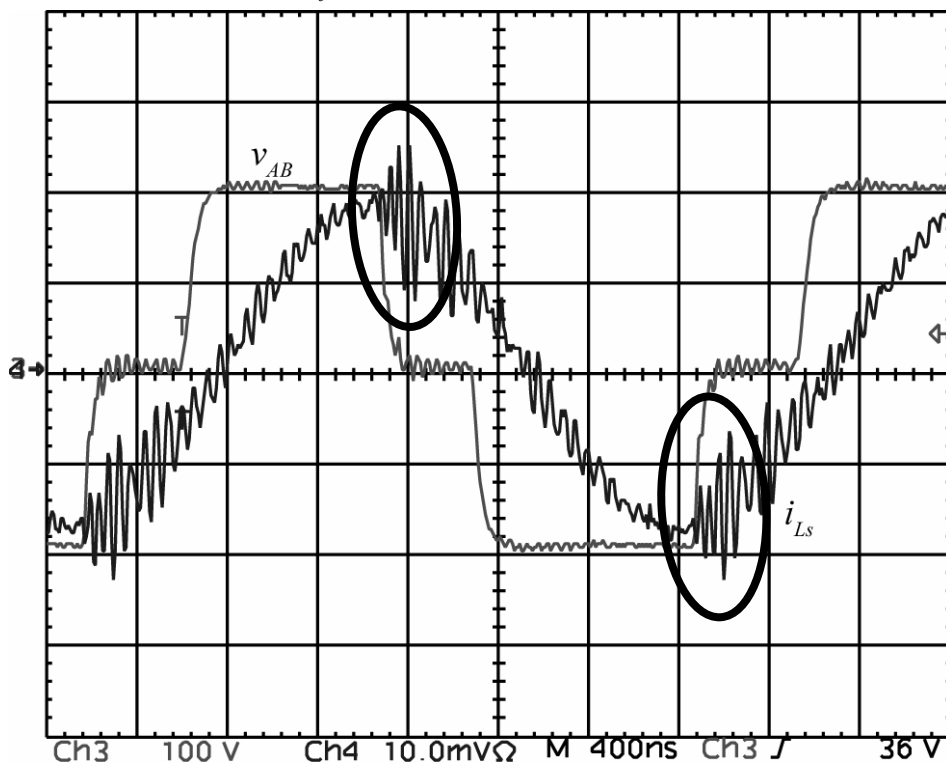


Fig. 5.9: The voltage v_{AB} (100V/div) and resonant current i_{Ls} (10A/div). Time scale: 400ns/div.

After one of the ZVS switches has turned off, parasitic oscillations occur in the resonant current with high current peak as shown in **Fig. 5.9**. These oscillations are caused by the resonance between the resonant inductor and its parasitic winding capacitance. When one of the ZVS

transistors turns off, the resonant current i_{L_s} is directed to the parasitic capacitances of the MOSFETs charging one capacitance and discharging the other one. When the voltage across the capacitance of the turned off transistor reaches the input voltage, the commutation of the switch to the anti-parallel diode of the opposite switch of a bridge leg is completed. At this moment, the resonant current starts flowing through the diode and a free-wheeling stage begins. Hence, the voltage across the resonant inductor v_{L_s} is abruptly changed. This high $dv_{L_s}(t)/dt$ excites the parasitic winding capacitance of the resonant inductor, which resonates with the resonant inductance causing the oscillations in the resonant current.

The voltage across the parallel capacitor v_{C_p} and the output voltage $V_{o'}$ for $V_{o'ref} = 677\text{V}$ are shown in **Fig. 5.10**. When the voltage v_{C_p} is clamped to the half value of the output voltage a voltage ringing can be observed in v_{C_p} . The voltage ringing originates from the hard turn-on of the output rectifier diodes.

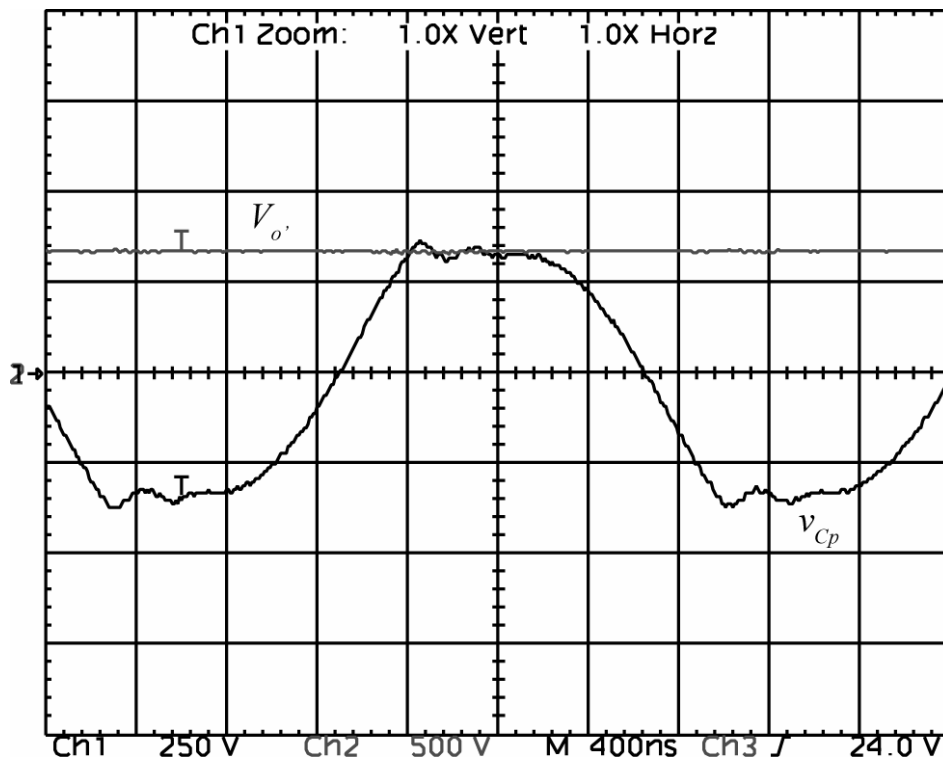


Fig. 5.10: Voltage across the parallel capacitor v_{C_p} (250V/div) and output voltage $V_{o'}$ (250V/div). Time scale: 400ns/div.

The gate voltages of the MOSFETs S_1 and S_3 are shown in **Fig. 5.11**. These switches operate under zero voltage switching (ZVS) condition and the switching frequency is 372 kHz.

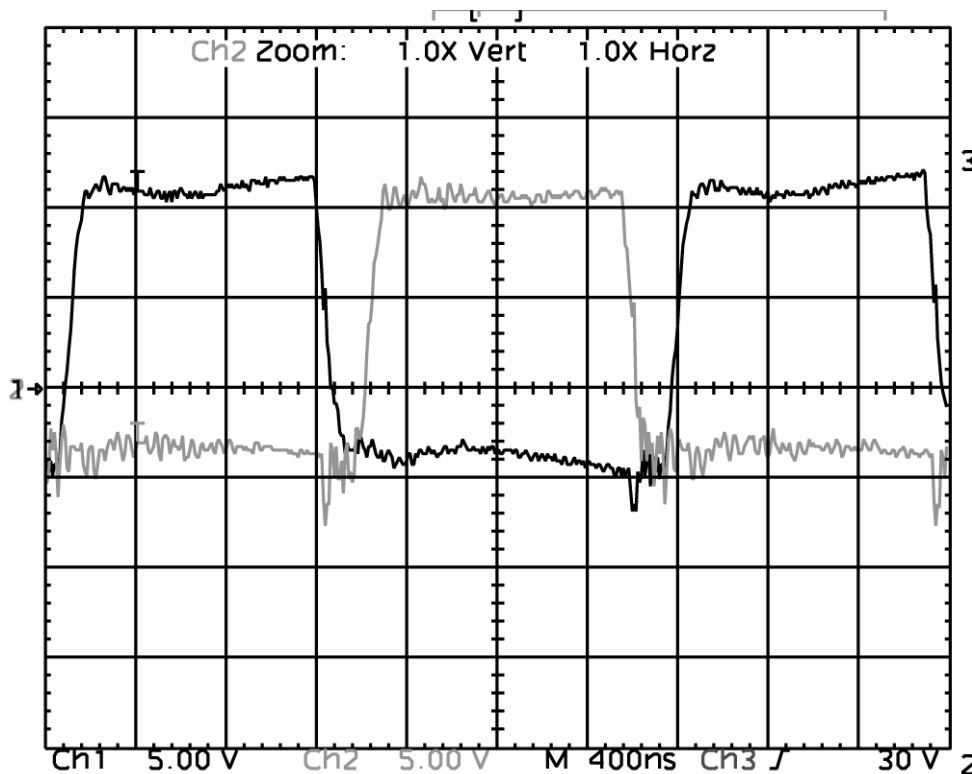


Fig. 5.11: Gate signals of the ZVS bridge leg (5V/div). Time scale: 400ns/div

Fig. 5.12 shows the output voltage when a step change in the reference voltage $V_{o'_{ref}}$ occurs. At time $t = 100\mu\text{s}$ the reference value is changed from 377V to 677V. One can see that there is no overshoot and it takes about $400\mu\text{s}$ until the output voltage reaches the new reference. The rising time is longer than expected from the simulation of the ideal circuit. This occurs due to the current limitation at start up, as explained for the measurements at 230W, and due to the losses in the practical implementation. When one adds the current limitation and a series resistance in the resonant circuit representing the losses one obtains similar transient behavior as obtained in practice. In this case, no overshoot occurs because even if the controller sets the duty cycle to its maximum value, to compensate the current limitation, the circuit is operating at higher load level, thus it takes longer to build up the output voltage.

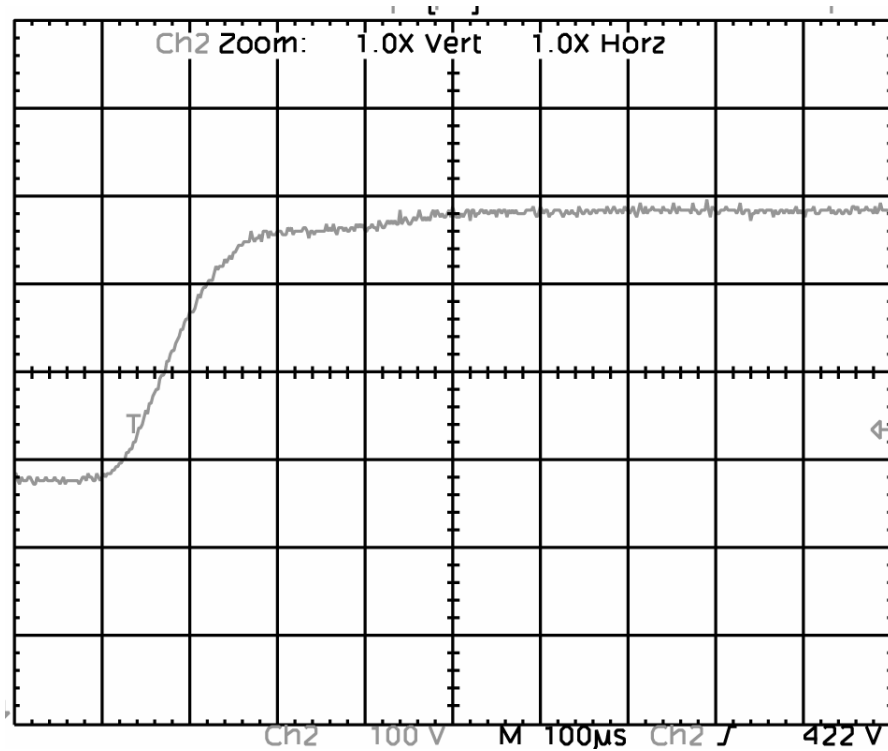


Fig. 5.12: Step response of the output voltage V_o . (100V/div). Time scale: 100µs/div.

5.4.3. Results for $P_o = 2.3\text{kW}$

Fig. 5.13 shows the steady state waveforms of voltage v_{AB} and resonant current i_{Ls} for $V_{o,ref} = 677\text{V}$.

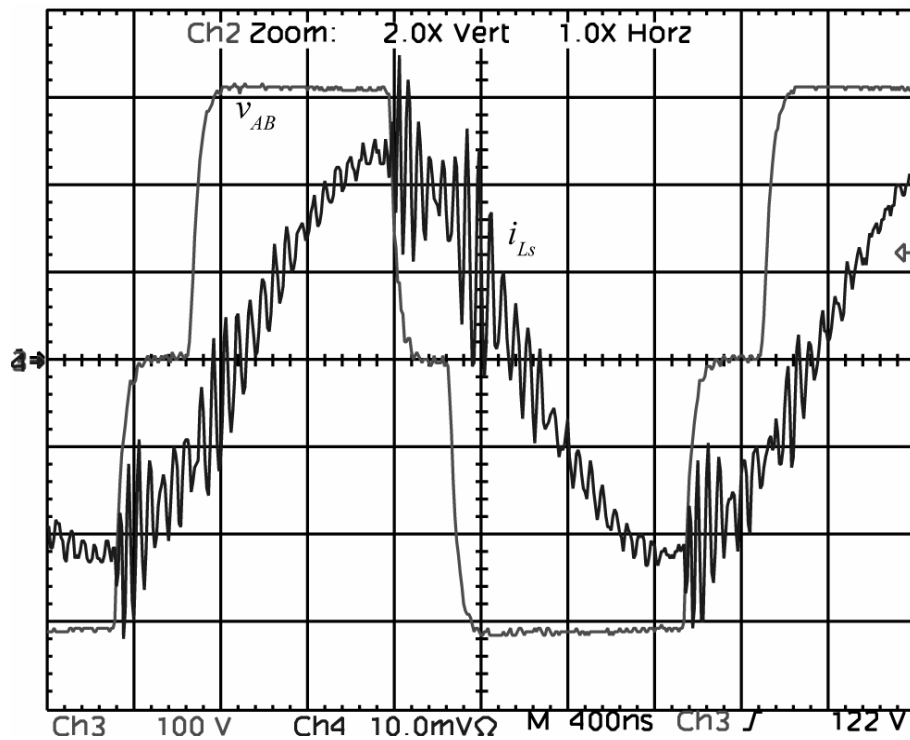


Fig. 5.13: The voltage v_{AB} (100V/div) and resonant current i_{Ls} (10A/div). Time scale: 400ns/div.

The voltage across the parallel capacitor v_{Cp} and the output voltage V_o for $V_{o,ref} = 677V$ are shown in Fig. 5.14.

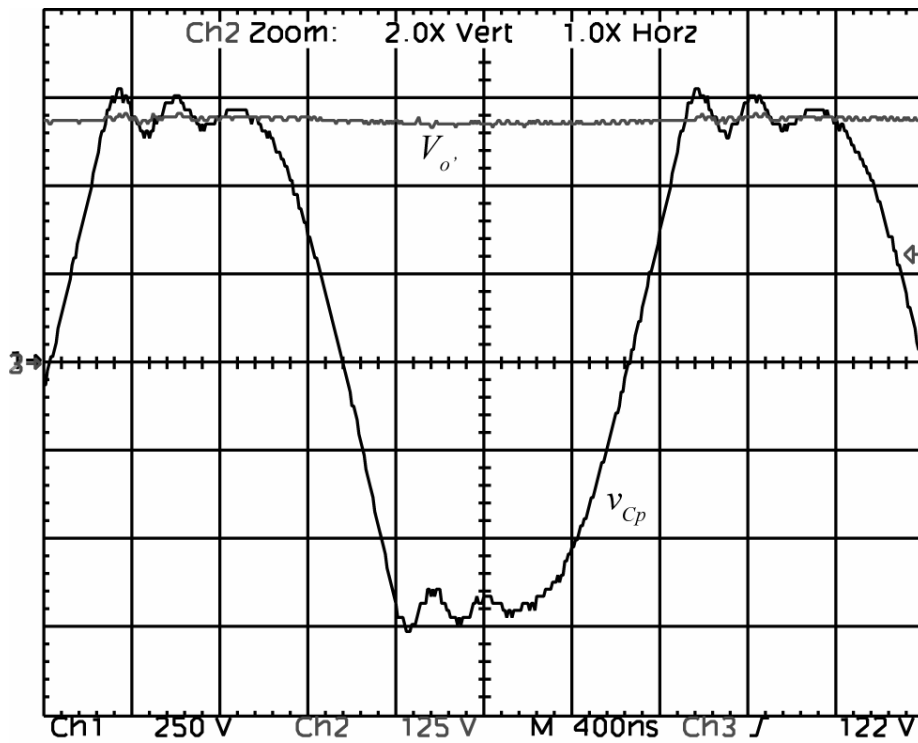


Fig. 5.14: Voltage across the parallel capacitor v_{Cp} (125V/div) and output voltage V_o (250V/div). Time scale: 400ns/div.

Fig. 5.15 shows the gate voltages of the ZCS switches S_2 and S_4 .

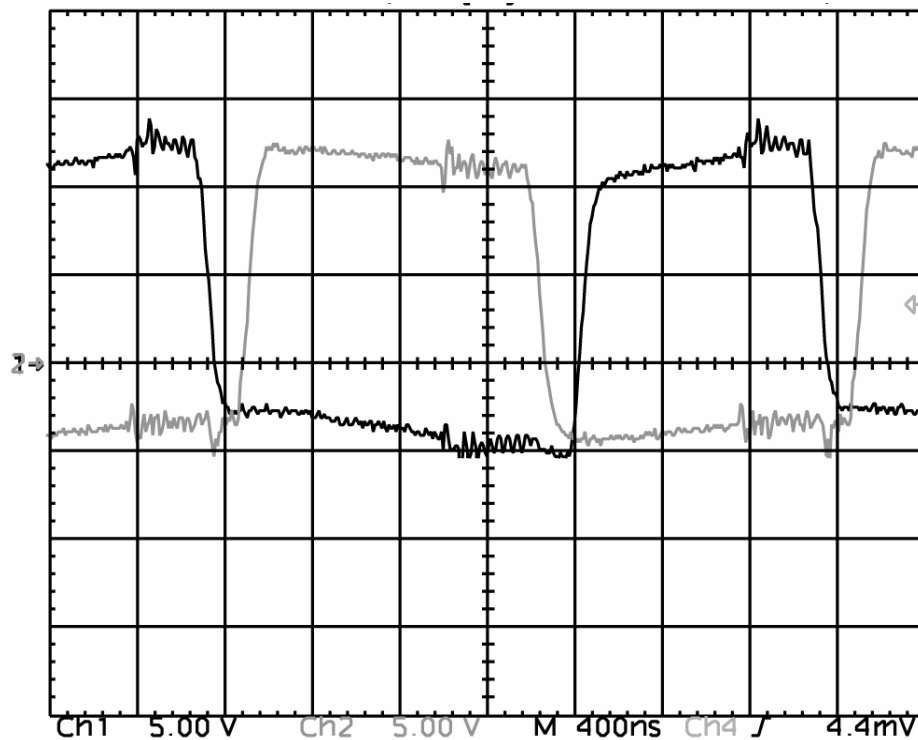


Fig. 5.15: Gate signals of the ZCS bridge leg (5V/div). Time scale: 400ns/div

5.4.4. Results for $P_o = 4.6\text{kW}$ (Full Load)

Fig. 5.16 shows the steady state waveforms of voltage v_{AB} and resonant current i_{Ls} for $V_{o'_{ref}} = 677\text{V}$ and rated power.

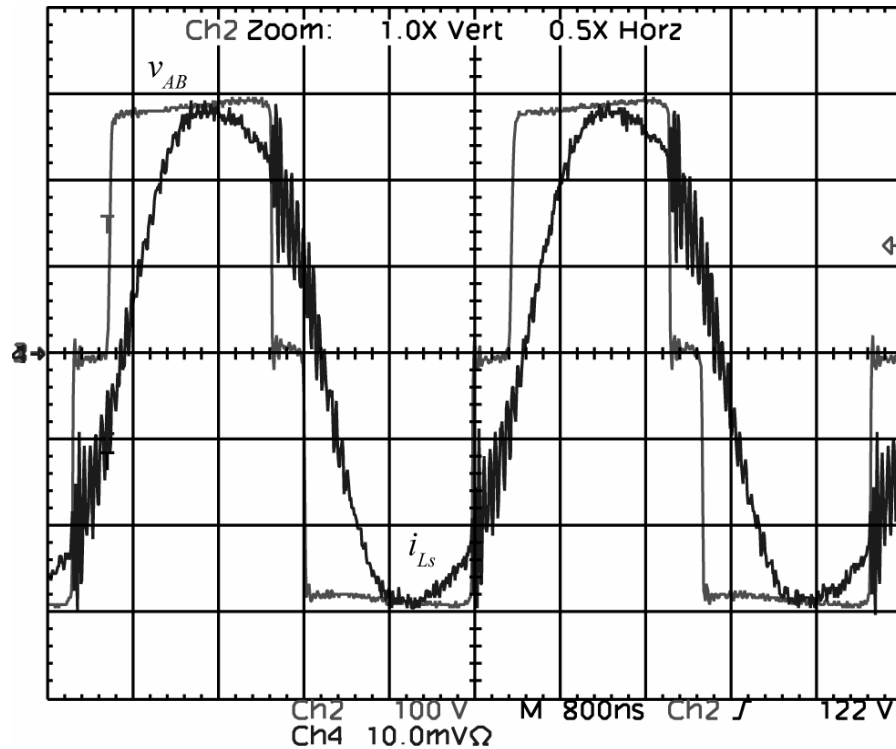


Fig. 5.16: The voltage v_{AB} (100V/div) and resonant current i_{Ls} (10A/div). Time scale: 800ns/div.

If one observes the waveforms of v_{AB} and i_{Ls} in **Fig. 5.16**, one can see that there is a delay between the end of the clamping interval and the zero crossing of the current. In this case, the ZCS switches are turned on with zero current but are turned off before the zero crossing of the resonant current. Thus, they have turn off losses. In practice this delay represents the dead time between the gate signals of both switches that is necessary to prevent short-circuit of a bridge leg and to charge and discharge the parasitic capacitances of the power MOSFETs S_2 and S_4 .

The voltage across the parallel capacitor v_{Cp} and the output voltage $V_{o'}$ for $V_{o'_{ref}} = 677\text{V}$ are shown in **Fig. 5.17**. The voltage ringing on the parallel capacitor observed in practice originates from the hard turn-on of the output rectifier diodes

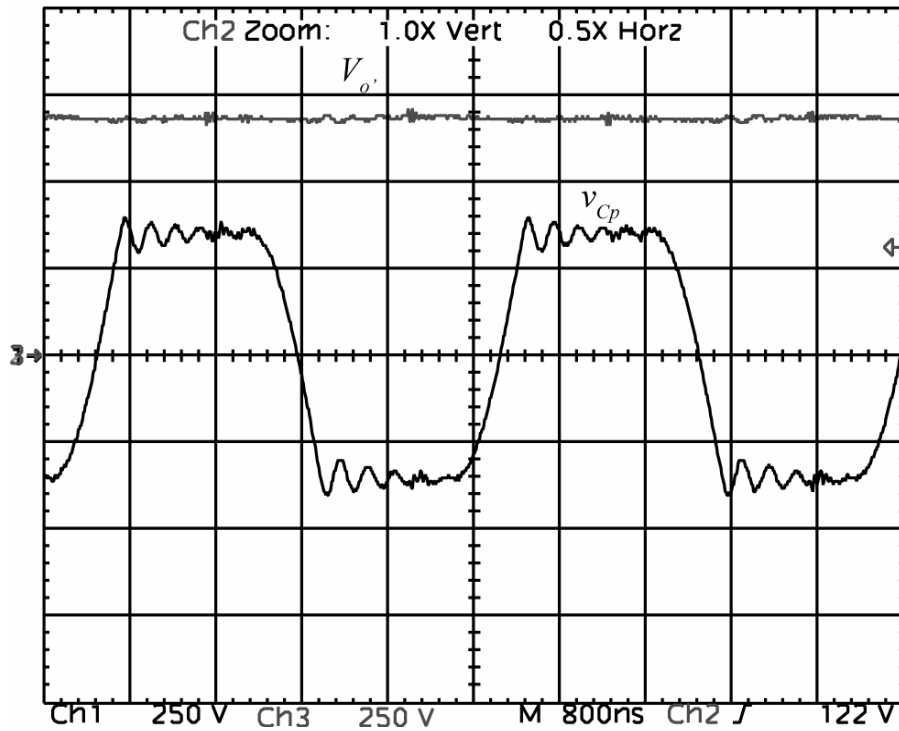


Fig. 5.17: Voltage across the parallel capacitor v_{Cp} (250V/div) and output voltage V_o (250V/div). Time scale: 800ns/div.

Fig. 5.18 shows the steady state waveforms of the voltage across the series capacitor v_{Cs} and resonant current i_{Ls} for rated power.

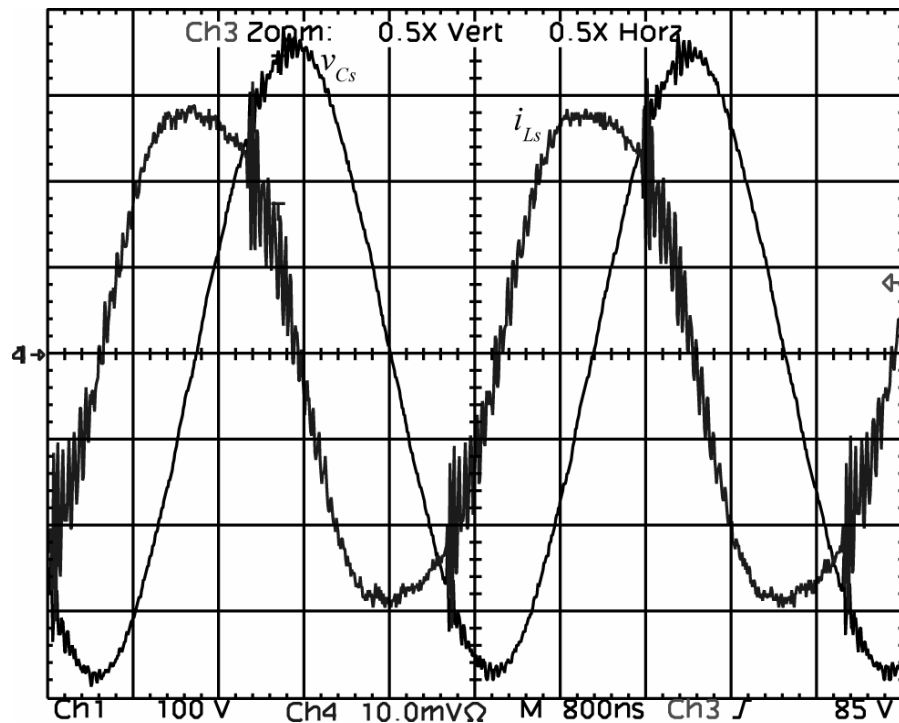


Fig. 5.18: Voltage v_{Cs} (100V/div) and resonant current i_{Ls} (10A/div). Time scale: 800ns/div.

Fig. 5.19 shows the steady state waveforms of voltage across the lower ZCS switch v_{S4} and resonant current i_{Ls} for rated power.

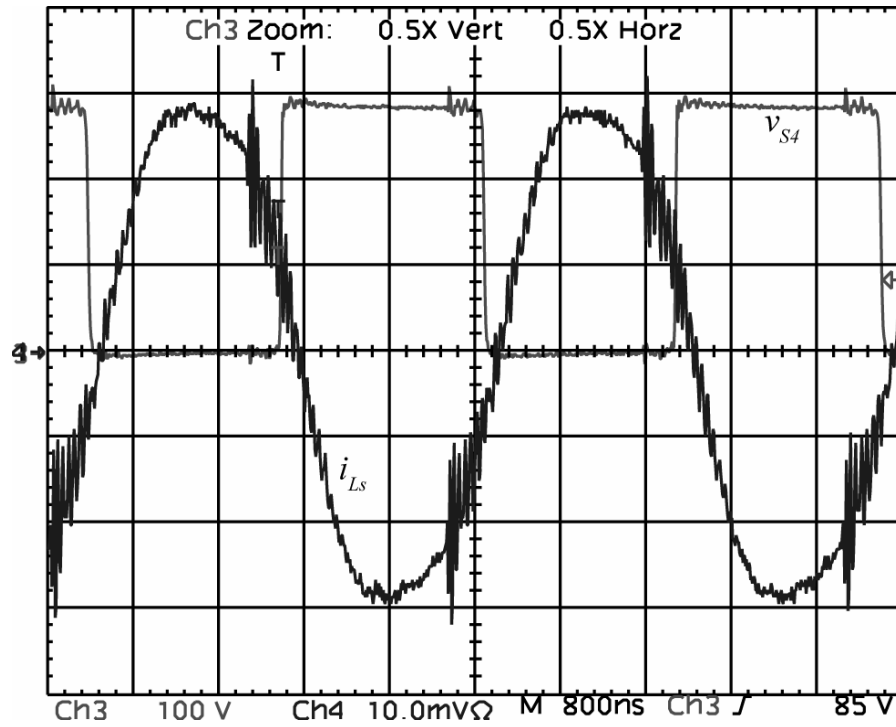


Fig. 5.19: The voltage v_{S4} (100V/div) and resonant current i_{Ls} (10A/div). Time scale: 800ns/div.

Fig. 5.20 shows the voltage across the lower ZVS switch v_{S3} and the voltage v_{AB} for full load operation.

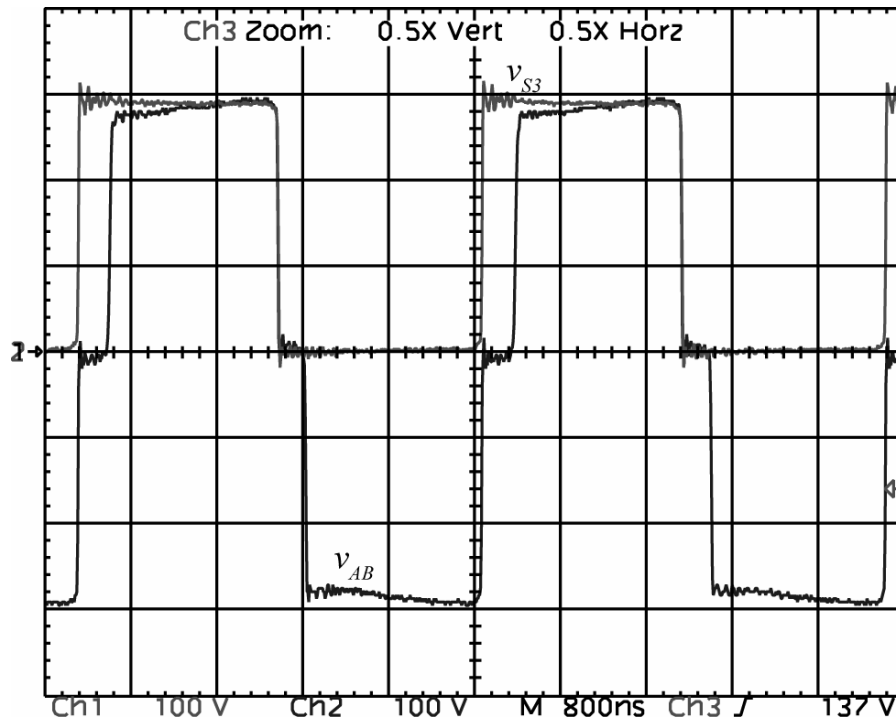


Fig. 5.20: Voltage v_{S3} (250V/div) and voltage v_{AB} (250V/div). Time scale: 800ns/div.

The measured efficiency of the converter as a function of the normalized output power ($P_{o,N} = P_o / P_{o,full_load}$) is shown in **Fig. 5.21**. The efficiency at full load is about 92%.

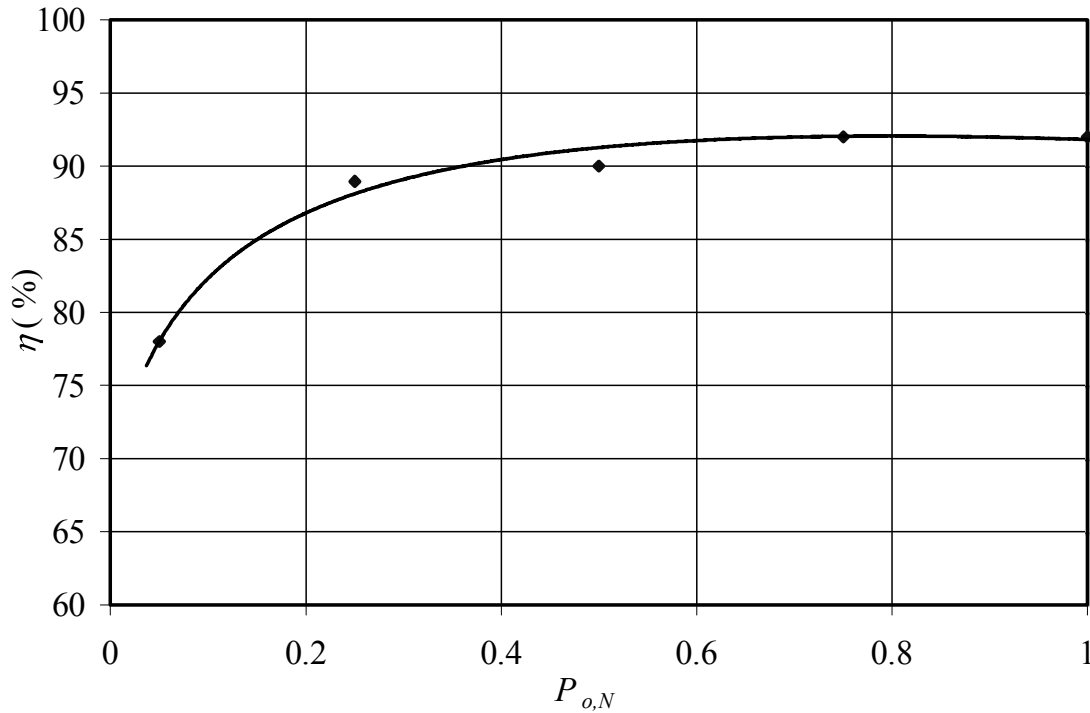


Fig. 5.21: Efficiency of the converter as a function of the normalized output power.

The efficiency decreases significantly for very low power operation because the conduction losses of the power MOSFETs are very high compared with the power supplied to the load. This is the case because for low power, the converter behaves like a parallel resonant converter with high circulating current. The losses for low power operation are considerably reduced when the converter is operated in discontinuous mode as proposed in **Chapter 2**.

	Calculated value	Measured value
Duty cycle(D)	0.74	0.82
Switching frequency (f_s)	263.5 kHz	266 kHz
Peak current of the resonant inductor (\hat{I}_{L_s})	29.7 A	29 A
Turn-off current of the ZVS switches (I_{Qzvs_off})	21.6 A	21.4A
Peak voltage of the series resonant capacitor (\hat{U}_{C_s})	373V	380V

Table 5.2: Comparison of theoretical and experimental results at full load.

In order to validate the results obtained in practice, some measured currents and voltage of the circuit have been compared with their calculated values. The results are presented in **Table 5.2**. One can see that the results agree well. Only the duty cycle has a higher value than expected. This due to the fact that the theoretical analysis is performed considering optimum commutation, that means, no reactive energy is returned from the resonant tank to the input source [GRS⁺94b]. However if one observes the waveforms of v_{AB} and i_{Ls} in **Fig. 5.16**, one can see that there is a delay between the end of the clamping interval and the zero crossing of the current. Within this delay interval reactive energy is circulating, i.e., the converter does not operate with optimum but with quasi-optimum commutation. If one considers the delay interval of 146ns, the effective measured duty cycle is equal to 0.75 that agrees well with the theoretical results.

5.5. SUMMARY

This chapter shows experimental results of the 5kW prototype of the series-parallel resonant converter. The experimental results are in good agreement with simulations proving the validity of the models developed in this thesis. The performance of the gain scheduled controller is very good and fulfills the requirements for x-ray medical imaging applications, i.e. no overshoot, small output voltage ripple and fast transient are provided.

CONCLUSIONS AND OUTLOOK

The search for new technologies in the field of x-ray medical imaging is very important because radiation can cause negative physiological effects. Thus, it is necessary to have high-efficient equipments that produce the best possible image with the smallest possible dose of radiation. The motivation of this work was to design a converter suitable for medical imaging application, more specifically for a mammograph, that is cheaper, smaller and more efficient than current solutions that are available in the market.

As explained in **Chapter 1**, good image quality is dependent on the quality of the voltage applied to the x-ray tube. This voltage should have low ripple, fast rise time and very restricted overshoot. Therefore, the control aspect is the most important feature of the x-ray generator design.

The choice of a resonant converter to implement the x-ray generator is a natural response to the requirements of this application. First of all, because resonant converters can integrate the leakage inductance and the winding capacitance of the high-voltage transformer in the converter behavior and second, because for reducing the size of the current systems, the converter has to be operated at significantly higher switching frequencies. Resonant converters can operate at higher frequencies with lower losses when compared with non soft switching converters. The series-parallel resonant is preferred because it combines the best features of the series and the parallel resonant converters.

The development of reliable models of the converter is very important because it allows the evaluation of the converter, saving time in the design process and avoiding expensive redesigns. Steady-state, large

and small-signal models of the series-resonant converter have been presented and successfully verified in this work.

Regarding the control design, in the beginning of this work, it was soon evident that an adaptive control scheme should be used in order to meet the demanding requirements concerning rise time and overshoot. In this work, two different control approaches are suggested in order to properly control the output voltage of the x-ray generator: a passivity based controller (PBC) and a gain scheduled controller. For a given reference voltage, the performance of the gain scheduled controller is relatively independent of load level. This is a major advantage compared with the PBC because for PBC the quality of the closed loop system response is dependent on the quality of the load estimate. As the load is an unknown parameter, and at light load the estimate converges to a value with a large deviation in comparison with the real load value, this characteristic is a drawback of the PBC design.

The gain scheduled controller is implemented in the prototype. The closed loop response of this controller is very fast and without overshoot, hence, agreeing with the requirements of a power supply for mammography device. This is due to the fact that no online estimation is involved in the controller, thus, the parameters of the controller can be changed very quickly. The local stability of the gain scheduled controller is investigated analytically, while the global stability evaluation is based on simulations. An idea for future research in this area is to apply the methods proposed by [SA88] to guarantee stability and robustness of the global design.

The theoretical studies proved the suitability of the series-parallel resonant converter for application as a high voltage generator for x-ray tubes and the experimental results obtained with the prototype validated the design methods and models developed in this thesis.

Most of the relevant technical questions concerning modeling and design of the series-parallel resonant converter have been clarified in this work. Nevertheless, there is still potential to develop future research work in this area. The main aspects that can be further developed are the

controller design and the optimization of the experimental setup towards high power density.

Regarding the controller design, passivity based control is a very promising approach to design robust controllers for nonlinear systems. The PBC approach handles directly with the nonlinear model of the system avoiding intrinsically non-robust operations, such as exact cancellations of nonlinearities. In the present work, the parameters of the passivity based controller are chosen by simulation. A suggestion for future works is to find tuning rules for the passivity based controller that increase the performance of the estimator. Increasing the performance of the estimator, the system will have faster transient behavior. In this work, the PBC was not implemented in practice because the gain scheduled controller has been preferred (for details, please refer to **Chapter 4**). Hence, the realization of the PBC using a digital signal processor (DSP) is suggested in order to validate the theoretical results.

Concerning the constructed prototype, a re-design towards higher power density is recommended. The first aspect that needs attention is the loss distribution of the converter. The actual efficiency of the converter is about 92%. This is a relative low efficiency for a soft switching converter. For this reason, it is important to identify which components most contribute to the increase of the power losses, and concentrate efforts on those components. The objective should be the optimization of the thermal design and power losses reduction in order to achieve converter efficiency higher than 95%.

In relation to the thermal design optimization, it should be investigated, if it is important to change the modulation technique of the converter. The main drawback of the phase-shift modulation used in this work is the unbalanced current distribution between both legs of the full-bridge inverter. This leads to higher conduction losses in the switches that are synchronized with the zero crossing of the resonant current (ZCS switches) compared with the ZVS switches of the other leg. This is due to the fact that the ZCS switches are conducting current almost 50% of the switching period while the turn-on interval of the ZVS switches is dependent on the duty cycle. An effective way to reduce this unbalance

should be the application of the switching sequence proposed by Vlatkovic et al. [VSS96]. There, the switching is sequenced in such a way, that each switch turns off low current in one switching cycle and high current in the next. In [VSS96], the main objective of the proposed switching sequence has been the reduction of the switching losses. But, it also has the desirable secondary effect of uniformly distributing the conduction losses. This is due to the fact that the ZCS and ZVS bridge legs are not fixed. They change every period, i.e. the ZCS bridge leg of the last cycle, is the ZVS bridge leg of the current cycle and vice versa. The total power losses remain constant but due to the uniform current distribution, the thermal design can be optimized.

A further outlook is the extension of the use of this converter concept to computed tomography (CT). This application requires higher output voltage and power than the mammography application, namely 40kV-150kV@100kW. For this reason, one has to analyze what has to be changed in order to meet the new requirements. The changes will affect more the practical implementation than the concept. One potential change could be the replacement of the MOSFETs with IGBTs and consequently reduction of the switching frequency range.

REFERENCES

- [Aig05] H. Aigner, *Method for Regulating and/or Controlling a Welding Current Source with a Resonance Circuit*, United States Patent 6849828, February 2005.
- [ABL⁺95] J. M. Alonso, C. Blanco, E. Lopez, et al., *Analysis and Design of a LCC Resonant Inverter for High Intensity Discharge Lamps*. Technical Proceedings of the IV IEEE International Power Electronics Congress, CIEP 95, pp. 102 – 107, 1995.
- [ABL⁺98] J. M. Alonso, C. Blanco, E. Lopez, et al., *Analysis, Design, and Optimization of the LCC Resonant Inverter as a High-Intensity Discharge Lamp Ballast*. IEEE Transactions on Power Electronics, vol.13, no. 3, pp. 573 – 585, May 1998.
- [ARB⁺95] J. M. Alonso, M. Rico, C. Blanco, et al., *A Novel Low-Loss Clamped-Mode LCC Resonant Inverter for HID Lamp Supply*. Proceedings of the 26th Annual IEEE Power Electronics Specialists Conference, vol. 2, pp. 736 – 742, 1995.
- [AW95] K. J. Astrom, B. Wittenmark, *Adaptive Control*. Second Edition, Addison-Wesley Publishing Company, Inc, 1995.
- [Bar94] I. Bartaseh, *Resonant Converter Topologies with Three and Four Energy Storage Elements*. IEEE Transactions on Power Electronics, vol. 9, no. 1, pp. 64 – 73, 1994.
- [BLL⁺90] I. Bartaseh, R. Liu, C. Q. Lee, et al., *Theoretical and Experimental Studies of the LCC-Type Parallel Resonant Converter*. IEEE Transactions on Power Electronics, vol. 5, no. 2, pp. 140-150, April, 1990.
- [BS98] R.M. Bass, J. Sun, *Large-Signal Averaging Methods under Large*

Ripple Conditions. Proceedings of the 29th IEEE Power Electronics Specialists Conference, Fukuoka, Japan, vol.1, pp. 630 – 632, 1998.

[BYR96] S. Ben-Yaakov, G. Rahav, *Average Modeling and Simulation of Series-Parallel Resonant Converters by SPICE Compatible Behavioral Dependent Sources*. Proceedings of the 11th Annual Applied Power Electronics Conference and Exposition, APEC '96, vol.1, pp. 116 – 120, 1996.

[Bha91] A. K. S. Bhat, *A Resonant Converter suitable for 650 V DC Bus Operation*. IEEE Transactions on Power Electronics, vol. 6, no. 4, pp. 739 – 748, 1991.

[Bru04] F. Bruzelius, *Linear Parameter-Varying System – an approach to gain scheduling*. PhD thesis, Department of Signals and Systems, Chalmers University of Technology, Göteborg, Sweden, 2004.

[BSL⁺02] J. T. Bushberg, J. A. Seibert, E. M. Leidholdt Jr. et al, *The Essential Physics of Medical Imaging*. Second Edition, Lippincott Williams & Wilkins, Philadelphia, PA, 2002.

[CA00] R. R. Carlton, A. M. Adler, *Principles of Radiographic Imaging: An Art and a Science*. Third Edition, Thomson Delmar Learning, Albany, NY, 2000.

[CGV⁺00] J. M. Carrasco, E. Galván, G. E. Valderrama, et al., *Analysis and Experimentation of Nonlinear Adaptive Controllers for the Series Resonant Converter*. IEEE Transactions on Power Electronics, vol. 15, no. 3, pp. 536 – 544, 2000.

[CK03] F. S. Cavalcante, J. W. Kolar, *Design of a 5kW High Output Voltage Series-Parallel Resonant DC-DC Converter*. Proceedings of the 34th IEEE Power Electronics Specialists Conference, Acapulco, Mexico, vol. 4, pp. 1807 – 1814, 2003.

[CK05] F. S. Cavalcante, J. W. Kolar, *Small-Signal Model of a 5kW High-Output Voltage Capacitive-Loaded Series-Parallel Resonant DC-DC Converter*. Proceedings of the 36th IEEE Power Electronics Specialists Conference, Recife, Brazil, June 12 - 16, pp. 1271 – 1277, 2005.

[CdL⁺03] C. Cecati, A. Dell'Aquila, M. Liserre, et al., *A Passivity-Based Multilevel Active Rectifier with Adaptive Compensation for Traction Applications*, IEEE Transactions on Industry Applications, vol.39, no. 5,

pp. 1404 – 1413, Sept.-Oct. 2003.

[CFS85] Y. Cheron, H. Foch, J. Salesses, *Study of A Resonant Converter Using Power Transistors in 25 kW X-Rays Tube Power Supply*, Proc. ESA Sessions at 16th IEEE Power Electronics Specialists Conference, Toulouse, pp. 295 – 306, 1985.

[CFG⁺01] L. S. Crawford, M. P. J. Fromherz, C. Guettier, et al., *A Framework for On-line Adaptive Control of Problem Solving*. Proceedings of CP'01 Workshop on On-line Combinatorial Problem Solving and Constraint Programming, 2001.

[CBG⁺99] V. Croulard , J. Boichot , E. Godoy , et al., *An Output Feedback Design for Series-Parallel Resonant Converters*, Proceedings of the 8th European Conference on Power Electronics and Applications EPE'99, Lausanne, September 1999.

[DDV02] M. Dahleh, M. A. Dahleh, G. Verghese, *Lectures on Dynamic Systems and Control*. Department of Electrical Engineering and Computer Science, Massachusetts Institute of Technology, 2002

[DRS00] G. D. Demetriades, P. Ranstad, C. Sadarangari, *Three Elements Resonant Converter: the LCC topology by using MATLAB*. 31st Annual IEEE Power Electronics Specialists Conference, Galway, Ireland, vol.2, pp.1077 – 1083, 2000.

[Dha03] A. P. Dhawan, *Medical Image Analysis*. First Edition, Willey-IEEE Press, New York, 2003.

[DH02] G. A. Dumont, M. Huzmezan, *Concepts, Methods and Techniques in Adaptive Control*. Proceedings of the 2002 American Control Conference, vol.2, pp. 1137 – 1150, 2002.

[EVK88] M. E. Elbuluk, G. C. Verghese, J. G. Kassakian, *Sampled-Data Modeling and Digital Control of Resonant Converters*, IEEE Transactions on Power Electronics, vol.3, no. 3, pp. 344 – 354, July 1988.

[EJW88] R. W. Erickson, S. D. Johnson, A. F. Witulski, *Comparison of Resonant Topologies in High-Voltage DC Applications*. IEEE Transactions on Aerospace and Electronic Systems, vol. 24, no. 3, pp. 263-274, 1988.

[EM01] R. W. Erickson, D. Maksimovic, *Fundamentals of Power Electronics*. Second Edition, Kluwer Academic Publishers, 2001.

- [Esc99] G. Escobar, *On Nonlinear Control of Switching Power Electronics Systems*. PhD Thesis, LSS-SUPELEC, France, May 1999.
- [FHO94] A. J. Forsyth, Y. K. E. Ho, H. M. Ong, *Comparison of Small-Signal Modelling Techniques for The Series-Parallel Resonant Converter*, Fifth International Conference on Power Electronics and Variable-Speed Drives, pp. 268 – 273, 1994.
- [FH96] A. J. Forsyth, Y. K. E. Ho, *Dynamic Characteristics and Closed-Loop Performance of the Series-Parallel Resonant Converter*, IEE Proceedings-Electric Power Applications, vol.143, no. 5, pp. 345 – 353, September 1996.
- [FM98] A. J. Forsyth, S. V. Mollov, *Simple Equivalent Circuit for the Series-Loaded Resonant Converter with Voltage Boosting Capacitor*. IEE Proceedings Electric Power Applications, vol. 145, no. 4, pp. 301 – 306, 1998.
- [GRS⁺94a] V. Garcia, M. Rico, J. Sebastián, et al., *Study of an Optimized Resonant Converter for High-Voltage Applications*. Proceedings of the 3rd International Power Electronics Congress, Puebla, Mexico, Aug. 21-25, pp. 114 –121, 1994.
- [GRS⁺94b] V. Garcia, M. Rico, J. Sebastian, et al., *Using the Hybrid Series-Parallel Resonant Converter with Capacitive Output Filter and With PWM Phase-Shifted Control for High-Voltage Applications*. Proceedings of the 20th International Conference on Industrial Electronics, Control and Instrumentation, IECON '94, vol.3, pp.1659 – 1664, 1994.
- [GGRD98] J. Garcia-Gomez, S. Rimaux, M. Delgado, *Designing a Passivity-Based Controller for the Boost Converter using Bond Graphs*, Proceedings of the 1998 American Control Conference, vol.6, pp. 3796 – 3797, 1998.
- [GSGB04] G. Garcia Soto, J. Gaysse, G. W. Baptiste, *Variable Sampling Time Serial-Resonant Current Converter Control for a High-Voltage X-ray Tube Application*. Proceedings of the 10th European Power Quality Conference, Nuremberg, Germany, 2004, pp. 972 - 977.
- [GEH05] GE Healthcare, *The Encyclopaedia of Medical Imaging – Medcyclopaedia*, 2005. Online available: <http://www.medcyclopaedia.com>.
- [GVV68] A. Gelb, W. E. Vander Velde, *Multiple-Input Describing*

Functions and Nonlinear System Design, McGraw-Hill Book Co., New York, NY, 1968.

[GMD03] J. M. Gonçalves, A. Megretskiy, M. A. Dahleh, *Global Analysis of Piecewise Linear Systems Using Impact Maps and Quadratic Surface Lyapunov Functions*. IEEE Transactions on Automatic Control, vol. 48, no.12, pp. 2089 – 2106, 2003.

[Haf04] S. F. Hafstein, *A Constructive Converse Lyapunov Theorem on Exponential Stability*. Discrete and Continuous Dynamical Systems – Series A, vol.10, no.3, pp. 657– 678, 2004.

[HBB⁺92] A. Hassan, G. Bornard, S. Bacha, et al., *Definition and Application of a Nonlinear Control Law for Series Resonant Converters*. Proceedings of the 23rd Annual IEEE Power Electronics Specialists Conference, vol.2, pp. 793 – 799, 1992.

[IN02] E. Ikonen, K. Najim, *Advanced Process Identification and Control*. Control Engineering Series, Marcel Dekker, Inc, New York, NY, 2002.

[IS96] P. Ioannou, J. Sun, *Robust Adaptive Control*. Prentice Hall, New Jersey, 1996 (out of print in 2003), electronic copy at [http://www-rcf.usc.edu/~ioannou/Robust Adaptive Control.htm](http://www-rcf.usc.edu/~ioannou/Robust_Adaptive_Control.htm).

[Ism98] J. S. Ismail, *Fixed and Adaptive Mechanical Backlash Control*. PhD Thesis, University of California, Santa Barbara, CA, 1998.

[IKBY97] G. Ivensky, A. Kats, S. Ben-Yaakov, *A Novel RC Model of Capacitive-Loaded Parallel and Series-Parallel Resonant DC-DC Converters*. Proceedings of the 28th IEEE Power Electronics Specialists Conference, St. Louis, Missouri, USA, vol. 2, pp. 958 – 964 , 1997.

[IKBY99] G. Ivensky, A. Kats, S. Ben-Yaakov, *A Novel RC Load Model of Parallel and Series-Parallel Resonant DC-DC Converters with Capacitive Output Filter*. IEEE Transactions on Power Electronics, vol.14, no. 3, pp. 515 – 521, May 1999.

[KC94] W. H. Kwon, G. H. Cho, *Optimum Quantum Sequence Control of Quantum Series Resonant Converter for Minimum Output Voltage Ripple*. IEEE Transactions on Power Electronics, vol.9, no. 1, pp. 74 – 84, January 1994.

- [LGP⁺97] J. Laeuffer, E. Godoy, T. Planas, et al., *A Control analysis and closed loop design for series-parallel resonant converters*. Proceedings of the 6th European Conference on Power Electronics and Applications EPE'97, Trondheim, pp. 4.379 – 4.384, 1997.
- [Lat03] Lattice Semiconductor Corporation, *ispMACHTM4A CPLD Family*, Technical Datasheet, 2003.
- [LL00] D. J. Leith, W. E. Leithead, *Survey of Gain-Scheduling Analysis and Design*. International Journal of Control, vol. 73, no. 11, pp. 1001 – 1025, 2000.
- [LT01] S. S. Liang, Y. Y. Tzou, *DSP Control of a Resonant Switching High-Voltage Power Supply For X-Ray Generators*. Proceedings of the 4th IEEE International Conference on Power Electronics and Drive Systems, vol. 2, pp. 522 – 526, 2001.
- [LDK⁺99] L. Lorenz, G. Deboy, A. Knapp et al., *COOLMOSTM - a new milestone in high voltage Power MOS*. Proceedings of the 11th International Symposium on Power Semiconductor Devices and ICs, ISPSD '99, Toronto, pp. 3 – 10, 1999.
- [LN02] A. Loría, H. Nijmeijer, *Passivity-based control*, in *Encyclopaedia of Life Support Systems (EOLSS), Vol. Perspectives and Overview of Life Support Systems and Sustainable Development* (Prof. Unbehauen, ed.), EOLSS Publishers Ltd., 2002.
- [MST⁺01] D. Maksimovic, A. M. Stankovic, V. J. Thottuvelil, et al., *Modeling and Simulation of Power Electronic Converters*, Proceedings of the IEEE, vol.89, no. 6, pp. 898 – 912, June 2001.
- [MRDP⁺02] J. A. Martín-Ramos, J. Diaz, A. M. Pernía, et al., *Large-Signal Modeling of the PRC-LCC Resonant Topology with a Capacitor as Output Filter*. Proceedings of the 17th Annual IEEE Applied Power Electronics Conference and Exposition, Dallas, TX, 2002, vol. 2, pp. 1120 - 1126.
- [MF99] S. V. Mollov, A. J. Forsyth, *Modelling and Control Design Issues for the Modified Series Resonant Converter*, Proceedings of the 8th European Conference on Power Electronics and Applications EPE'99, Lausanne, September 1999.
- [MDM⁺04] J. Murgaš, A. Dobrovič, E. Miklovičová, et al., *Two Level Turbogenerator Control System*. Journal of Electrical Engineering, vol. 55,

no. 3-4, pp. 83 – 88, 2004.

[MLS94] R. M. Murray, Z. Li, S. S. Sastry, *A Mathematical Introduction to Robotic Manipulation*. CRC Press, 1994.

[OCI⁺02] K. Ogura, E. Chu, M. Ishitobi, et al., *Inductor Snubber-Assisted Series Resonant ZCS-PFM High Frequency Inverter Link DC-DC Converter with Voltage Multiplier*. Proceedings of the Power Conversion Conference, PCC Osaka 2002, vol.1, pp. 110 – 114, 2002.

[OLNSR98] R. Ortega, A. Loría, P. J. Nicklasson, H. Sira-Ramirez, *Passivity-based Control of Euler-Lagrange Systems: Mechanical, Electrical and Electromechanical Applications*. Springer-Verlag, London, UK, 1998.

[PJJ97] H. Pinheiro, P. Jain, G. Joós, *Self-Sustained Oscillating Resonant Converters Operating Above the Resonant Frequency*, Proceedings of the 12th Annual Applied Power Electronics Conference and Exposition, APEC '97, vol.2, pp. 993 – 999, 1997.

[PJJ99] H. Pinheiro, P. K. Jain, G. Joós, *Self-Sustained Oscillating Resonant Converters Operating Above the Resonant Frequency*. IEEE Transactions on Power Electronics, vol. 14, no. 5, pp. 803-815, September 1999.

[Pow03] Power Electronic Systems Laboratory, *RMX DSP Controller Module*, Technical Datasheet, 2003.

[Ras01] M. H. Rashid, *Power Electronics Handbook*. Academic Press, San Diego, CA, 2001.

[RS00] W. J. Rugh, J. S. Shamma, *Research on gain scheduling*. Automatica, vol. 36, pp. 1401–1425, 2000.

[SJL⁺95] J. A. Sabate, M. M. Jovanovic, F.C. Lee, et al., *Analysis and Design-Optimization of LCC Resonant Inverter for High-Frequency AC Distributed Power System*. IEEE Transactions on Industrial Electronics, vol.42, no. 1, pp. 63 – 71, February 1995.

[SL91] J. A. Sabate, F. C. Y. Lee, *Off-Line Application of the Fixed-Frequency Clamped-Mode Series Resonant Converter*. IEEE Transactions on Power Electronics, vol.6, no.1, pp. 39 – 47, Jan. 1991.

- [SB03] T. Samad, G. Balas, *Software-Enabled Control: Information Technology for Dynamical Systems*. Wiley-IEEE Press, 2003.
- [SNL⁺91] S.R. Sanders, J.M. Noworolski, X.Z. Liu, et al., *Generalized Averaging Method for Power Conversion Circuits*. IEEE Transactions on Power Electronics, vol. 6, no. 2, pp. 251-259, April 1991.
- [San92] A. Sanei, *Towards a Performance Theory of Robust Adaptive Control*, PhD Thesis, University of Southampton, UK, 1992.
- [SB89] S. Sastry, M. Bodson, *Adaptive Control: Stability, Convergence and Robustness*. Prentice-Hall Information and Systems Sciences Series, New Jersey, 1989.
- [SA90] J. S. Shamma, M. Athans. *Analysis of gain scheduled control for nonlinear plants*. IEEE Transactions on Automatic Control, vol. 35, no. 8, pp. 898 – 907, 1990.
- [SA92] J. S. Shamma, M. Athans. *Gain scheduling: potential hazards and possible remedies*. IEEE Control Systems Magazine, vol. 12, no. 3, pp.101 – 107, 1992.
- [SA88] J. S. Shamma, M. Athans, *Guaranteed properties for nonlinear gain scheduled control systems*. Proceedings of the 27th IEEE Conference on Decision and Control, vol.3, pp. 2202 – 2208, 1988.
- [SA91] J. S. Shamma, M. Athans, *Guaranteed Properties of Gain Scheduled Control for Linear Parameter-varying Plants*. Automatica, vol. 27, no.3 pp. 559 – 564, 1991.
- [SB92] S. Shahruz, S. Behtash, *Design of controllers for linear parameter-varying systems by the gain scheduling technique*. Journal of Mathematical Analysis and Applications, vol. 168, no. 1, pp. 195 – 217, 1992.
- [SST92] K. K. Shung, M. B. Smith, B. M. W. Tsui, *Principles of Medical Imaging*. Academic Press, San Diego, 1992.
- [SRO95] H. Sira-Ramirez, R. Ortega, *Passivity-Based Controllers for the Stabilization of DC-To-DC Power Converters*, Proceedings of the 34th IEEE Conference on Decision and Control, vol.4, pp. 3471 – 3476, 1995.
- [Sta96] A. M. Stankovic, *A Dissipativity-Based Controller for Series*

Resonant DC/DC Converters, Proceedings of the 27th IEEE Power Electronics Specialists Conference, vol.2, pp. 1844 – 1849, 1996.

[SPS97] A. M. Stankovic, D.J. Perreault, K.Sato, *Analysis and Experimentation with Dissipative Nonlinear Controllers for Series Resonant DC/DC Converters*. Proceedings of the 28th Power Electronics Specialists Conference, St. Louis, MI, vol. 1, pp. 679 – 685, 1997.

[SPS99] A. M. Stankovic, D. J. Perreault, K. Sato, *Synthesis of Dissipative Nonlinear Controllers for Series Resonant DC/DC Converters*. IEEE Transactions on Power Electronics, vol.14, no. 4, pp. 673 – 682, 1999.

[Ste88] R. L. Steigerwald, *A Comparison of Half-Bridge Resonant Converter Topologies*. IEEE Transactions on Power Electronics, vol. 3, no. 2, pp. 174-182, 1988.

[Ste85] R. L. Steigerwald, *Analysis of a Resonant Transistor DC-DC Converter with Capacitive Output Filter*. IEEE Transactions on Industrial Electronics, vol. IE-32, no. 4, pp. 439-444, 1985.

[Ste01] R. L. Steigerwald, *Power Electronic Converter Technology*. Proceedings of the IEEE vol. 89, no. 6, pp. 890 – 897, 2001.

[SDN⁺00] J. Sun, X. Ding, M. Nakaoka, et al., *Series Resonant ZCS-PFM DC-DC Converter with Multistage Rectified Voltage Multiplier and Dual-Mode PFM Control Scheme for Medical-Use High-Voltage X-Ray Power Generator*. IEE Proceedings Electric Power Applications, vol. 147, Issue 6, pp. 527 – 534, November 2000.

[TK96] G. Tao, P. V. Kokotović, *Adaptive Control of Systems with Actuator and Sensor Nonlinearities*. John Wiley & Sons, Inc, New York, NY, 1996.

[TML88] F.-S. Tsai, P. Materu, F. C. Y. Lee, *Constant-Frequency Clamped-Mode Resonant Converters*. IEEE Transactions on Power Electronics, vol.3, no. 4, pp. 460 – 473, October 1988.

[VEK86] G. C. Verghese, M. E. Elbuluk, J. G. Kassakian, *A general Approach to Sampled-Data Modeling of Power Electronic Circuits*, IEEE Transactions on Power Electronics, vol. 1, no. 2, April 1986.

[VGS⁺95] C. B. Viejo, M. A. P. Garcia, M. R. Secades, et al., *A Resonant High Voltage Converter with C-Type Output Filter*. Proceedings of the 30th

IEEE Industry Applications Conference, IAS '95, vol.3, pp. 2401 – 2407, 1995.

[VSS96] V. Vlatkovic, M.J. Schutten, R.L. Steigerwald, *Auxiliary Series Resonant Converter: a New Converter for High-Voltage, High-Power Applications*. Proceedings of the 11th Annual IEEE Applied Power Electronics Conference and Exposition. San Jose, CA, USA, vol. 1, pp. 493 – 499, 1996.

[Vor84] V. Vorpérian, *Analysis of Resonant Converters*, Ph.D. Thesis, California Institute of Technology, Pasadena, May 1984.

[Vor89] V. Vorpérian, *Approximate Small-Signal Analysis of the Series and the Parallel Resonant Converters*, IEEE Transactions on Power Electronics, vol. 4, no. 1, pp. 15-24, January 1989.

[Wip05] Wipro GE Medical Systems, *X-Ray Dose Online Tutorial*. 2005, Online available: <http://www.gehealthcare.com/inen/rad/xr/education/>.

[WHE91] A. F. Witulski, A. F. Hernandez, R. W. Erickson, *Small-Signal Equivalent Circuit Modeling of Resonant Converters*, IEEE Transactions on Power Electronics, vol.6, no. 1, pp. 1 – 27, January 1991.

[WH99] T.-F. Wu, J.-C. Hung, *A PDM Controlled Series Resonant Multi-level Converter Applied for X-ray Generators*. Proceedings of the 30th Annual IEEE Power Electronics Specialists Conference, Charleston, South Carolina, USA, vol.2, pp.1177 – 1182, 1999.

[YCL⁺92] E. X. Yang, B. Choi, F. C. Lee, et al., *Dynamic Analysis and Control Design of LCC Resonant Converter*. Proceedings of the 23rd IEEE Power Electronics Specialists Conference, Toledo, Spain, vol. 1, pp. 362 – 369, 1992.

[YLJ92a] E. X. Yang, F. C. Lee, M. M. Jovanovic, *Small-Signal Modeling of LCC Resonant Converter*. Proceedings of the 23rd Annual IEEE Power Electronics Specialists Conference, vol.2, pp. 941 – 948, 1992.

[YLJ92b] E. X. Yang, F. C. Lee, M. M. Jovanovic, *Small-Signal Modeling of Series and Parallel Resonant Converters*. Proceedings of the 7th Annual Applied Power Electronics Conference and Exposition, APEC '92, pp. 785 – 792, 1992.

[YPJ03] M. Z. Youssef, H. Pinheiro, P.K. Jain, *Analysis & Modeling of a*

Self-Sustained Oscillation Series-Parallel Resonant Converter with Capacitive Output Filter Using Sampled-Data Analytical Technique. Proceedings of the 25th International Telecommunications Energy Conference, INTELEC '03, pp. 282 – 289, 2003.

[ZPv00] L. Zhao, D. Peng, J. D. van Wyk, *Analysis and Design of an LCLC Resonant Converter Suitable for X-ray Generator Power Supply.* Proceedings of the 2000 VPEC/CPES Seminar, pp. 360 – 365, 2000.

[ZCA00] S. Zouggar, H. Nait Charif, M. Azizi, *Neural Control and Transient Analysis of the LCL-type Resonant Converter.* The European Physical Journal - Applied Physics, vol. 11, pp. 21 – 27, 2000.

CURRICULUM VITAE

Fabiana da Silveira Cavalcante

- 07.09.1976** Born in Itabuna, Bahia, Brazil
- 03.1991 – 12.1994** High-School
Colégio Nossa Senhora da Glória, Itabuna, Bahia,
Brazil.
- 03.1995 – 09.2000** Electrical Engineer Degree
Department of Electrical Engineering, Federal
University of Santa Catarina, Florianópolis, Brazil.
- 09.2000 – 12.2001** Master of Science in Power Electronics
Power Electronics Institute (INEP), Department of
Electrical Engineering, Federal University of Santa
Catarina, Florianópolis, Brazil.
- 02.2002 – 12.2005** Ph.D. in Power Electronics
Power Electronic Systems Laboratory, Department
of Information Technology and Electrical
Engineering, ETH Zurich, Switzerland.

